



Project Vulcan

Final Report and System Requirements Review

Submitted: 02/05/25

Team Members

Technical Project Manager: Micle Leita

Project Systems Engineer: Joshua Moore

Mechanical Engineer Lead: Braden Hartlieb

Mechanical Engineers: Cam'Ron Valliere

Testing and Safety Engineer Lead: Abigail Smith

Testing and Safety Engineers: Victor Zaharia

Additive Manufacturing Engineer Lead: Victor Zaharia

Additive Manufacturing Engineers: Braden Hartlieb

Propulsion Engineer Lead: Cam'Ron Valliere

Propulsion Engineers: Matthew Poirier

Testing and Validation Engineer Lead: Timur Bedelbaev

Testing and Validation Engineers: Abigail Smith

Simulation and Modeling Engineer Lead: Jorge Sanchez

Simulation and Modeling Engineers: Timur Bedelbaev

Professor: Dr. Firat Irmak

Industry Mentor: Kineo Wallace



TABLE OF CONTENTS

1	EXECUTIVE SUMMARY (LEITA)	1
2	PROBLEM STATEMENT AND OBJECTIVES	2
2.1	PROBLEM STATEMENT (MOORE)	2
2.2	PROJECT OBJECTIVES (HARTLIEB, MOORE, SANCHEZ)	3
2.3	DELIVERABLES (ZAHARIA, POIRIER, LEITA)	3
2.4	BROADER IMPACT	4
3	CONCEPT OF OPERATIONS AND EXTERNAL INTERFACES	10
3.1	CONCEPT OF OPERATIONS (BEDELBAEV, MOORE, SMITH, ZAHARIA)	11
3.2	SYSTEM EXTERNAL INTERFACES (HARTLIEB, MOORE)	12
3.3	ENGINEERING STANDARDS (MOORE, LEITA)	14
4	LEVEL 1 SYSTEM REQUIREMENTS (LEITA, MOORE)	16
5	TECHNICAL APPROACH: SYSTEM DESIGN	19
5.1	SYSTEM DESIGN AND ALTERNATIVES CONSIDERED (HARTLIEB, BEDELBAEV)	19
5.2	SYSTEM DESIGN HISTORY (HARTLIEB)	32
5.3	SYSTEM DESIGN CONCLUSION (HARTLIEB, BEDELBAEV)	54
5.4	SYSTEMS ARCHITECTURE (HARTLIEB, BEDELBAEV, MOORE)	63
6	TECHNICAL APPROACH: SUBSYSTEM REQUIREMENTS AND DESIGN	67
6.1	SAFETY SUBSYSTEM REQUIREMENTS (SMITH)	67
6.2	PROPULSION REQUIREMENTS AND TECHNICAL APPROACH	70
6.3	STRUCTURES REQUIREMENTS AND TECHNICAL APPROACH	90
6.4	CONTROL REQUIREMENTS AND TECHNICAL APPROACH	146
7	TECHNICAL BUDGETS	150
7.1	MASS BUDGET (ZAHARIA, HARTLIEB)	150
7.2	ELECTRICAL POWER BUDGETS (SANCHEZ, BEDELBAEV)	151
7.3	DATA BUDGETS (SANCHEZ, BEDELBAEV)	152
8	FINANCIAL BUDGET / BILL OF MATERIALS / SCHEDULE (LEITA)	153
8.1	BUDGET/BILL OF MATERIALS	153



9 TEST PLANNING (SMITH).....	156
9.1 TEST SERIES SUMMARY (SMITH)	156
9.2 TEST RESULTS (SMITH).....	168
10 RISK MANAGEMENT (SMITH).....	248
10.1 TEAM TECHNICAL RISKS (SMITH).....	250
11 POST-CDR ANALYSIS (VALLIERE)	254
12 POST-TEST ANALYSIS (VALLIERE).....	259
12.1 PROPULSION ANALYSIS.....	259
12.2 STRUCTURAL ANALYSIS	266
14 REFERENCES (BEDELBAEV).....	271
15 APPENDIX	ERROR! BOOKMARK NOT DEFINED.

NOMENCLATURE

LITVC	= LIQUID-INJECTED THRUST VECTOR CONTROL
TVC	= THRUST VECTOR CONTROL
CFD	= COMPUTATIONAL FLUID DYNAMICS
FEA	= FINITE ELEMENT ANALYSIS
PDR	= PRELIMINARY DESIGN REVIEW
DAQ	= DATA ACQUISITION SYSTEM
HMI	= HUMAN-MACHINE INTERFACE
PLA	= POLYLACTIC ACID
CAD	= COMPUTER-AIDED DESIGN
BoM	= BILL OF MATERIALS
MoC	= METHOD OF CHARACTERISTICS



1 EXECUTIVE SUMMARY (LEITA)

This document serves as the Final Report for Project Vulcan, a 2024-2025 capstone design project at Florida Tech. Project Vulcan aims to advance propulsion technology by developing a proof-of-concept metal 3D-printed clustered aerospike engine featuring an integrated Liquid-Injected Thrust Vector Control (LITVC) system. Aerospike engines, known for their unique altitude compensation properties, offer theoretical efficiency across varying altitudes, potentially outperforming traditional bell nozzles [3]. The addition of an LITVC system promises enhanced control, making this a significant contribution to propulsion technology.

Project Vulcan is developed in partnership with Vaya Space, aligning with their small launch vehicle, Dauntless, designed for cost-effective space access. Vaya Space focuses on sustainable and affordable launch solutions, particularly in the small satellite market. This collaboration provides Project Vulcan with practical relevance, placing it within the context of industry developments and directly supporting applications in commercial and research satellite launches.

Through this effort, the team aim to gain insights into the feasibility, performance, and optimization of the LITVC system, enhancing future designs and implementation strategies. The objectives include designing, constructing, and validating an aerospike engine through static fire testing with solid rocket motors. The project will use iterative additive manufacturing, a custom-built test stand, an altitude-simulating shroud, and a tunable Ansys model to optimize performance, streamline virtual testing, and reduce the need for physical prototypes.

Safety is prioritized in alignment with Vaya Space's protocols, ensuring risk mitigation during testing. By the end of the academic year, Project Vulcan will deliver a validated prototype with comprehensive data, contributing valuable insights to next-generation propulsion systems.

2 PROBLEM STATEMENT AND OBJECTIVES

2.1 Problem Statement (Moore)

Project Vulcan focuses on the benefits of metal additive manufacturing to create an optimized monolithic aerospike geometry. This design aims to maximize efficiency with complex structures, weight factors, and integrated cooling that can only be produced with today's additive manufacturing technology.

Further emphasizing additive manufacturing complexities, Project Vulcan will print a fully integrated liquid-injected thrust vector control (LITVC) nozzle. This objective, in collaboration with Vaya Space, aims to evaluate the feasibility and benefits of LITVC for Vaya's Dauntless rocket's first stage. While traditional thrust vector control (TVC) systems rely on mechanical gimbaling, which increases mass and structural complexity, LITVC offers a potentially more streamlined solution by adjusting exhaust flow with fluid injection. This approach is expected to enhance maneuverability and control precision, reducing structural demands and improving operational efficiency.

The Dauntless rocket, designed by Vaya Space, currently lacks advanced thrust vectoring capabilities. By incorporating LITVC, Project Vulcan seeks to address this gap, providing Dauntless with enhanced flexibility and control for a broader range of mission profiles. This industry partnership ensures that Project Vulcan's findings hold direct relevance, potentially supporting future iterations of Dauntless.

Through static fire testing with solid rocket motors, Project Vulcan will generate valuable data on the operational viability of an additively manufactured aerospike engine, a fully integrated LITVC system, and an altitude-simulating shroud to validate the aerospike's performance across varying atmospheric conditions. This proof-of-concept initiative will advance propulsion control knowledge and contribute insights for the next generation of aerospace technology.



2.2 Project Objectives (Hartlieb, Moore, Sanchez)

OBJ-01: The aerospike shall withstand a 3-second static fire test with solid rocket motors, simulating real-world flow conditions. *Rationale: To assess the aerospike engine's aerodynamic efficiency and durability under operational conditions, ensuring it withstands the demands of repeated testing.* Fully Compliant.

OBJ-02: The aerospike shall be fabricated using additive manufacturing technologies. *Rationale: Leveraging 3D printing enables intricate design fidelity and rapid prototyping, ensuring optimal structural integrity and performance.* Fully Compliant.

OBJ-03: The aerospike shall be compatible with the custom-designed test stand. *Rationale: Ensuring compatibility with the dedicated test stand will streamline testing and validation, minimizing the need for additional adjustments.* Fully Compliant.

OBJ-04: An altitude-simulating shroud shall be designed and fabricated to integrate with the aerospike system. *Rationale: The shroud will simulate varying atmospheric conditions, allowing for accurate performance assessments across different altitudes, supporting data-driven insights.* Fully Compliant.

OBJ-05: The aerospike shall incorporate a LITVC system. *Rationale: Integrating LITVC will enable control over the thrust vector by injecting liquid into the exhaust flow, enhancing thrust direction precision and expanding control capabilities.* Fully Compliant.

2.3 Deliverables (Zaharia, Poirier, Leita)

Aerospike Prototype:

- A functioning prototype of the aerospike, fabricated through additive manufacturing, designed for static fire testing to validate performance.
- A demonstration model for display after testing to showcase the project's achievements.

Test Stand:



- A functioning test stand capable of recording aerospike test data during engine operation.

Altitude Simulating Shroud:

- A functioning altitude simulating shroud capable of simulating pressures correlating to atmospheric conditions up to 25 km during engine operation.

Computational Analysis:

- **CFD Simulations:** Fluid analysis of the aerospike nozzle across various operating conditions.
- **FEA Simulations:** Structural analysis to ensure the aerospike's durability under expected loads.

Design Documentation:

- Representative CAD models of the multi-engine radial aerospike, detailing the design for both manufacturing and testing purposes.

All Documentation Required by the Senior Design Class:

- PDR (November 2024)
- CDR (February 2025)
- Showcase (April 2025)
- Final Report (April 2025)

2.4 Broader Impact

Economic & Industry (Poirier):

The Vulcan multi engine aerospike design for the Dauntless vehicle aft section will greatly benefit Vaya Aerospace. The design of Vulcan will include an LITVC system, this architecture is one that allows for thrust vectoring without the added complexity of a flame deflector, the inefficiencies associated with engine throttling, or the added weight and complexity of hydraulic gimbaling [10]. The use of a flame deflecting mechanism would create more problems than it would solve due to its reduced efficiency as well as thermal management issues when compared



to LITVC and gimbaling [20]. Throttling individual combustion chambers of a rocket results in inefficiency because of incomplete combustion, as well as creating a flow that the engine is not optimized for. Lastly, hydraulic systems for gimbaling an engine are added mass that can be reduced with an LITVC system. The benefits of weight reduction, added efficiency, and reduced manufacturing complexity make LITVC an attractive design choice for a multi-engine design for the Dauntless vehicle aft section.

Comparison to Current Market (Poirier):

In the current space industry market, there are multiple space launch industry competitors to Vaya Space that have looked into, are looking into, and are designing for the utilization of aerospike technology. Among these competitors are Firefly Aerospace, Pangea Aerospace, and POLARIS Raumflugzeuge, each taking a unique approach to optimize efficiency. Firefly Aerospace investigated an aerospike design using an array of engines around a spike geometry for its Alpha vehicle shown below in Figure 1 [26]. This design was not launched by Firefly Aerospace but is one of the inspirations for the prototype system. For example, Vulcan utilizes multiple engines around a spike geometry, taking advantage of the spike effects while avoiding the complexities of creating a fully toroidal aerospike.

Aerospike technology has garnered interest because it offers significant advantages over traditional bell nozzles, making it an attractive solution for modern propulsion systems. Aerospike engines maintain high efficiency across a wide range of altitudes without the need for a variable geometry nozzle. This adaptability results from the way exhaust flow naturally adjusts to external pressure, enabling better performance during atmospheric ascent and vacuum operations. By eliminating the efficiency losses experienced by bell nozzles when operating outside their design altitude, aerospike engines provide a more versatile and effective propulsion system, which has been a key inspiration in Vulcan's design approach.

Pangea Aerospace is a rocket engine manufacturer offering two aerospike products. Their ARCOS engine is similar to Firefly's design, shown below in Figure 3; however, it is still in development [19]. The design of Vulcan benefits from having a vehicle to be designed around whereas a customer of Pangea Aerospace would need to design their vehicle around the engine

purchased. POLARIS Raumflugzeuge is another aerospace company developing a small payload lift vehicle. Their AURORA spaceplane (Figure 2) is currently in development and utilizing a multi-engine linear aerospike propulsion system [18]. As a spaceplane, this vehicle has the added complexity of thermal management that Vulcan and Vaya's systems avoid. Vulcan's design uses aerospike effects and a lightweight LITVC subsystem, reducing weight and complexity compared to the RS-25's 7,748-lb system [21]. Additional benefits of Vulcan's design are a result of the utilization of an LITVC subsystem. These benefits are increased engine efficiency due to avoiding thrust vectoring using engine throttling and reduced complexity and weight by removing the need for a flame deflecting or hydraulic gimbaling architecture that traditionally requires heavy and intricate mechanical systems, enabling streamlined operations and improved reliability in flight dynamics [20].



Figure 1: Firefly Aerospace's Alpha vehicle aft section [27]



Figure 2: POLARIS Raumflugzeuge's AURORA spaceplane [18]



Figure 3: Pangea Aerospace's ARCOS rocket engine [19]

Educational and Career Development Opportunities (Poirier):

Beyond its technical achievements, Project Vulcan serves as a practical, hands-on learning platform for the team members. By collaborating with Vaya Space, the team gains direct exposure to industry standards which also helps students learn and understand as well as prepare students for careers in aerospace. This industry partnership allows students to bridge the gap between academic knowledge and real-world applications. This project also paves the way for future Florida Tech students to seek similar partnerships, creating an educational environment that fosters both technical skills and professional growth.



Sustainable Manufacturing Practices (Zaharia):

In the field of engineering, manufacturing is an important step between a concept and its realization into a full-scale item. Before the creation of additive manufacturing, subtractive manufacturing was the main method of producing a component or part. Subtractive manufacturing includes machining, Computer Numeric Control (CNC), milling, etc. The drawback of subtractive manufacturing is the large amount of waste produced in the manufacturing process. Additive manufacturing holds a major advantage in reducing the overall waste in the creation of a part. For example, in the production of an aeronautical turbine component, subtractive manufacturing wasted 87% of the original titanium material, whereas AM drastically reduced this waste by building the part layer by layer. Furthermore, unused metal powder from the AM process, such as in electron beam melting (EBM), can often be recycled, minimizing raw material consumption [17]. Although producing the print materials, for example, titanium powder for AM is energy-intensive, the overall lifecycle material savings and waste reduction make AM a more sustainable option for complex geometries. This efficiency aligns with sustainable manufacturing goals, particularly in aerospace, where the high cost of materials like titanium amplifies the benefits of minimizing waste.

Moreover, AM's capability for on-demand and localized manufacturing transforms traditional supply chain models. By producing parts closer to their point of use, AM reduces transportation emissions and the need for extensive inventory [2]. This seamless integration of efficiency and flexibility supports industries like aerospace in adopting lighter, optimized components while maintaining a lower environmental footprint. Together, these qualities make AM a cornerstone of sustainable manufacturing strategies, providing a comprehensive solution to reduce waste, conserve energy, and modernize production logistics.

Specifically for the aerospace sector, manufacturing is the hallmark of bringing an idea to creation. They can be attributed to the following categories: functional performance, lead time reduction, lightweighting, complexity, cost management, and sustainment [6]. Meeting these points is crucial and is often the reason a project is unable to succeed. With the previously mentioned ability of additive manufacturing being able to reduce part time creation and costs,

companies are able to source or create parts that consist of complex geometries that traditional manufacturing practices would either be unable to or would leave a larger carbon footprint. Given these details, the aerospace sector is already adopting additive manufacturing and advancing it further to be more efficient overall. New standards, including ISO and ASTM are being created to create a foundation to make additive manufacturing streamlined and adhere to official guidelines.

Industry Reputation and Partnerships (Zaharia):

Project Vulcan seeks to benefit from the industry experience through mentorship from Vaya engineers. This partnership is comparable to previous CAPSTONE projects such as LAIKA's partnership with Blue Origin and the Lockheed Martin design challenge. Considering the complexities of Project Vulcan, having the proper guidance regarding which standards to reference for testing, documentation, as well as providing key insights into how to use different software to have a digital model of the aerospike structure is of great value.

Leveraging the mentorship from Vaya engineers not only enhances the technical rigor of Project Vulcan but also fosters a professional growth environment for all team members. Vaya's experience in full-scale aerospace projects ensures that the team is well-equipped to handle the various challenges of designing an aerospike structure. This collaboration aims to bridge the gap between academic theories taught in class and practical applications, ensuring that every aspect of the project aligns with industry's best practices.

Moreover, the partnership extends beyond technical guidance. It offers a unique opportunity to be immersed in a professional setting where problem-solving skills are developed. Vaya engineers can provide critical feedback on design iterations, assist in troubleshooting unforeseen issues, and offer strategic advice on project management and execution. The partnership is not just about achieving a successful project outcome; it is about cultivating a mindset geared towards continuous improvement and excellence in the field of aerospace engineering.

In addition, the collaboration will facilitate access to the tools and software used in the industry. Learning to navigate these tools under expert guidance will significantly boost the team's capability to produce high-fidelity digital models and simulations. These resources are crucial in

validating the design and ensuring that the aerospike meets all performance and safety criteria before any physical prototypes are developed. Through this mentorship, Project Vulcan aims to set a new standard in CAPSTONE projects, demonstrating how industry-academia partnerships can drive innovation and excellence. The experience gained will not only contribute to the success of the project but also prepare the team members to be future professional engineers in the aerospace sector.

Ethical and Responsible Engineering (Smith):

The team's commitment to ethical engineering practices prioritizes safety, reliability, and environmental responsibility. By rigorously adhering to Vaya Space's safety, quality, and test protocols, Project Vulcan sets an example of responsible testing practices. This is done by identifying possible risks and safety hazards then implementing mitigation measures to ensure the team mitigates these risks as well as how to verify that both personnel and the environment are safely managed. This ethical approach serves as a model for future student projects, emphasizing the importance of conscientious engineering in real-world applications.

3 CONCEPT OF OPERATIONS AND EXTERNAL INTERFACES

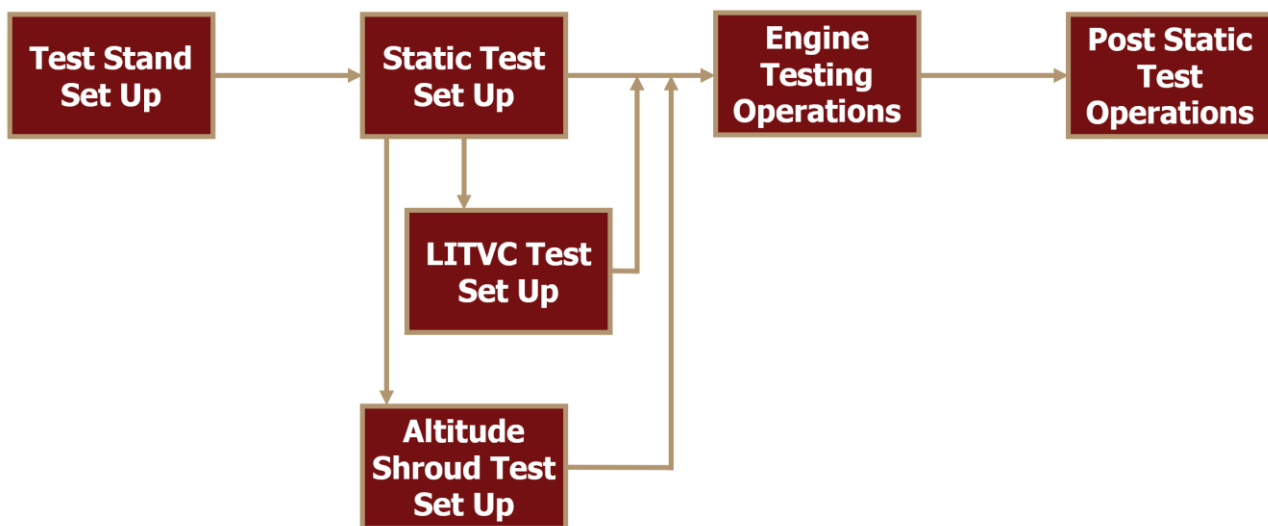


Figure 4: Concept of Operations: Static Fire Procedure Outline



3.1 Concept of Operations (**Bedelbaev, Moore, Smith, Zaharia**)

Static Test Set Up:

The radial multiengine aerospike will be produced using additive manufacturing techniques and mounted on a custom-built static test stand. Testing will be conducted at Vaya Space facilities. The engine will be outfitted with solid rocket motors, replacing the previous compressed gas setup, to simulate realistic operational conditions. Sensors, including load cells and cameras will be installed to monitor thrust, plume behaviour, and structural integrity. Imaging devices will be positioned to capture high-resolution footage for analysis after the tests. All test setup procedures will follow strict safety protocols in alignment with Vaya Space standards.

Engine Testing Operations:

Engine testing operations will commence with a thorough pre-test safety check. The solid rocket motors will be ignited, and the engine will undergo a controlled burn on the test stand. During this test, thrust and imaging data will be continuously monitored to ensure performance remains within operational limits. Once the test is complete, the motors will be safely extinguished, and the engine will be disconnected for inspection.

The testing phase will include two specialized experiments alongside the primary static fire test:

- **LITVC Test:** The LITVC system will be integrated into the aerospike design, allowing liquid injection to control thrust direction. During testing, sensors and high-speed cameras will capture vectoring behavior, assessing LITVC's effectiveness in altering thrust direction and enhancing maneuverability.
- **Altitude Simulation Shroud Experiment:** An altitude-simulating shroud compatible with the aerospike design will be placed around the nozzle. This shroud will create controlled pressure variations, simulating different atmospheric conditions experienced at various altitudes. Thrust and additional pressure data will be recorded to validate the performance of the shroud and to evaluate how the aerospike performs under reduced ambient pressure, assessing its altitude-compensating efficiency.



Post Static Fire Operations:

Following testing, all collected data—including thrust, and imaging footage—will undergo detailed analysis. This phase will involve comparing experimental results with predictive simulation models, assessing the structural integrity of the aerospike, and verifying the efficiency of LITVC within the aerospike design. The analysis will also aim to identify any discrepancies between model predictions and actual test outcomes, providing insights into areas for potential optimization.

3.2 System External Interfaces (Hartlieb, Moore)

External interface considerations for the radial multiengine aerospike prototype encompass various domains that are crucial for its design, operation, and integration. Key interface categories include:

Mechanical:

- **Solid Rocket Motor Integration:** The aerospike interfaces with six 75mm solid rocket motors. This requires precise alignment and secure attachment to ensure stable thrust and structural integrity. The top aerospike and nozzle structure will be bolted to the bottom half with the motor casings using a specially designed flange. The six M12 bolts on the outside and six M5 bolts on the inside will serve as a method of securing the two halves together. The bottom flange that is being machined will have a groove around each motor casing for an O-ring, ensuring a seal to negate pressure loss.
- **Mounting Structure:** The aerospike assembly mounts onto a custom-designed test stand that accommodates its radial configuration. The engine was designed with a dedicated flange that serves both to secure the parts together, and to be bolted to the test stand. Structural connections are reinforced to withstand forces generated during firing. The test stand integrates two steel plates serving as the base and mounting structure, clevis brackets, spherical brackets, load cells, and threaded bars for calibration and testing. The test stand base is bolted to concrete floor at Vaya's test site.

Fluid Interfaces:

- **LITVC Injection System:** The aerospike incorporates a hollow central spine to contain the fluid used for LITVC. External tubing connects the LITVC system to its fluid supply. Proper sealing and flow management are critical for an effective thrust module. Fluid is supplied to the LITVC system via a gasoline engine water pump that supplies fluid at a rate of 4 [m/s]. Entirety of the LITVC piping system will be filled with fluid prior to ignition, then once the test commences, the fluid flow will begin to flow to all LITVC orifices.

Data/Electrical:

- **Live Testing Sensors:** High-precision sensors are mounted to measure thrust and pressure. These sensors connect to a data acquisition (DAQ) system powered by an external source. Compatibility and calibration of electrical systems ensure reliable data collection during tests. Sensors present in the system include S-beam load cells, as well as a pressure transducer.
- **Data Acquisition System (DAQ):** The DAQ system will collect and transmit thrust and pressure data to a computer to then be processed using a python script. It interfaces directly with the engine's sensors for accurate, high-frequency data capture, supporting detailed performance analysis. External power sources will provide power for the sensor amplifiers and the data collection system and connected sensors, while communication links will relay the data to external monitoring stations.
- **Ignition System:** E-matches trigger the solid rocket motors. Electrical connections from the control interface enable synchronized ignition of all six motors, ensuring uniform thrust. Application of E-matches can be found in the test plans in the appendix.

Human-Machine Interface (HMI):

Operators will interact with the system via an intuitive human-machine interface. The HMI designed by the team will provide controls for motor ignition, LITVC pump, and real-time monitoring, allowing operators to maintain full oversight during the test. Fluid flow provided by Vaya Space facility will be monitored via Vaya Space control systems to ensure steady reliable flow for the entirety of each test.



Logical Interfaces

- **Simulation Integration:** Data collected during tests is compared to simulated performance models for validation and data analysis will be conducted to determine system performance.

3.3 Engineering Standards (Moore, Leita)

1. MIL-STD-1472H - Department of Defense Design Criteria Standard for Human Engineering

- **Purpose:** This standard is essential for optimizing system performance by integrating human capabilities and limitations within the total system design. Its applicability extends to all systems, subsystems, equipment, and facilities, emphasizing human-centered design to achieve mission success.
- **Application in Project Vulcan:** MIL-STD-1472H guides the design of interfaces, ensuring that operational controls are accessible and intuitive for operators during testing and data collection phases [6].

2. MIL-STD-810G - Environmental Engineering Considerations and Laboratory Tests

- **Purpose:** MIL-STD-810G addresses environmental stresses on materials throughout all phases of their service life, ensuring materials are neither over- nor under-designed. This standard is crucial for creating reliable systems that perform under various environmental conditions.
- **Application in Project Vulcan:** This standard influences material selection and structural integrity assessments for the aerospike engine and test stand, accounting for operational stresses such as temperature variations, vibration, and handling during testing [7].



3. NFPA 1125 – Code for the Manufacture of Model Rocket and High-Power Rocket Motors

- **Purpose:** NFPA 1125 provides guidelines for the safe handling, storage, and testing of model rocket and high-power rocket motors, including those using solid propellants.
- **Application in Project Vulcan:** This standard will guide the storage, handling, and testing protocols for the Rocket Motor Components 75mm Classic Propellant Grain motor. It ensures that the solid propellant motor is stored and tested in compliance with recognized safety practices, covering ignition setups, safety distances, and handling procedures [8].

4. ISO/ASTM 52927 - Additive Manufacturing – General Principles – Main Characteristics and Corresponding Test Methods

- **Purpose:** This standard outlines requirements for testing parts produced by additive manufacturing, covering feedstock quality, part integrity, and testing procedures to ensure consistent and reliable manufacturing quality.
- **Application in Project Vulcan:** ISO/ASTM 52927 guides the 3D printing and testing of the aerospike engine, ensuring that the fabricated parts meet high standards of structural and operational reliability [9].

4 LEVEL 1 SYSTEM REQUIREMENTS (LEITA, MOORE)

Table 1: Table of Level 1 System requirements

Req. #	Requirement	Rationale	Verification Method	Verification Strategy	Supporting Page #	Status
SYS.01	The system shall employ a radial multi-engine vehicle-integrated aerospike design.	The aerospike design is critical for maintaining engine efficiency across a broad range of altitudes by naturally compensating for changes in atmospheric pressure.	Inspection	The design will be inspected to meet the qualifications of a radial multi-engine aerospike design and simulated to ensure efficiency.	17, 21, 70, 90, 165, 167, 169, 176, 186	Fully Compliant
SYS.02	The system and team shall comply with all safety requirements and implement the risk mitigation measures documented in this CDR document.	Safety standards, plans, and procedures as well as risk mitigation measures are required to be followed.	Inspection	Inspection of safety procedures and plans to verify that the requirements are being followed.	17, 21, 67, 90, 165, 167, 168, 169, 171, 173, 175, 176, 181, 186, 189, 224, 241	Fully Compliant
SYS.03	The system shall be compatible with an LITVC system.	The integration of a Liquid Injected Thrust Vector Control (LITVC) system within the aerospike design enhances thrust control, potentially lowering weight and increasing control precision compared to conventional gimbals.	Analysis, Test, Demo	Comprehensive analysis and testing will confirm the system's compatibility with the LITVC system.	18, 21, 67, 88, 147, 165, 169, 173, 186, 224	Fully Compliant
SYS.04	The system shall be compatible with an altitude simulating shroud.	Simulating varying altitudes on the test stand shall provide data to further support aerospike efficiencies.	Analysis, Test	An all-encompassing shroud shall simulate a vacuum for the aerospike. Altering the shroud will dial in altitude estimations to simulate launch data.	18, 22, 58, 63, 65, 70, 138, 165, 175, 241	Fully Compliant
SYS.05	The test stand shall house the aerospike design dimensions and sensors to accurately record test data.	The test stand must be designed to accommodate the aerospike's specific dimensions and integrate sensors to accurately capture the engine's performance metrics.	Inspection	Building and testing the custom test stand will allow us to ensure compatibility with the aerospike design and proper integration of sensors to record accurate and comprehensive performance data.	18, 22, 86, 90, 147, 165, 167, 168, 169, 171, 173, 175, 176, 181, 186, 189, 224, 241	Fully Compliant



Requirement Explanations

SYS.01 - The system shall employ a radial multi-engine vehicle-integrated aerospike design.

The primary requirement for the system is the integration of a radial multi-engine aerospike design, chosen due to the aerospike's inherent altitude compensation capabilities. Unlike traditional bell nozzles, the aerospike nozzle adapts dynamically to changing atmospheric pressures, providing consistent efficiency across various altitudes. This feature is essential for improving the overall performance of propulsion systems in versatile atmospheric conditions, especially for future commercial applications that may require efficiency across a wide range of altitudes. The verification process includes an inspection and simulation of the aerospike's efficiency under different altitude conditions to confirm its operational adaptability.

SYS.02 - The team shall comply with all safety requirements and implement the risk mitigation measures documented in this PDR document.

This requirement establishes the importance of adhering to all safety standards and risk mitigation strategies outlined in this PDR document. Compliance ensures that these safety protocols are consistently followed throughout the project. These measures are vital for protecting personnel, equipment, and preserving the surrounding environment from potential harm. By implementing these documented procedures, the team not only mitigates risks associated with the project but also promotes a culture of safety and responsibility. Regular evaluations and updates to the safety protocols will further ensure that emerging risks are addressed proactively, maintaining a safe and efficient operational framework and aligning with regulatory and organizational safety expectations.

SYS.03 - The system shall be compatible with an LITVC system.

The integration of a LITVC system within the aerospike design aims to enhance thrust control without the need for conventional gimballed mechanisms. This approach offers the advantage of potentially lower weight and greater control precision, particularly valuable in aerospace applications where precise maneuvering is required. LITVC systems are relatively novel in this application, requiring rigorous analysis and testing to evaluate their effectiveness in thrust



vectoring within a confined nozzle exit. This requirement focuses on confirming the system's compatibility with the LITVC system through comprehensive analysis and testing.

SYS.04 - The system shall be compatible with an altitude simulating shroud.

To simulate high-altitude conditions, an altitude simulation shroud will be used to adjust the ambient pressure around the aerospike during testing. This compatibility is vital to validate the aerospike's efficiency under conditions it would experience during actual launch and operation. The shroud provides a controlled vacuum environment, allowing accurate performance assessments under various simulated atmospheric conditions. Testing and analysis will verify that the shroud effectively simulates different altitudes and interacts seamlessly with the aerospike, allowing for accurate data collection.

SYS.05 - The test stand shall house the aerospike design dimensions and sensors to accurately record test data.

For effective testing, a custom-built test stand is required to securely accommodate the aerospike's unique dimensions and incorporate sensors that capture critical data, such as thrust, pressure, and vector control metrics. By designing and constructing the own test stand, the team retain full control over specifications to meet the aerospike's requirements and ensure robust data acquisition. This setup not only enhances safety standards but also improves data precision, as the stand can be tailored to the precise needs of the testing parameters. Through inspection, the team will verify that the test stand is structurally sound, sensor-integrated, and fully compatible with the aerospike configuration.

5 TECHNICAL APPROACH: SYSTEM DESIGN

5.1 System Design and Alternatives Considered (Hartlieb, Bedelbaev)

The Vulcan aerospike engine prototype is centered on a radial multi-engine vehicle-integrated aerospike design. This innovative system configuration was selected after careful evaluation of its operational advantages and alignment with project goals. Aerospike nozzles are inherently capable of altitude compensation, adapting dynamically to atmospheric pressure changes and delivering consistent efficiency across various altitudes. This capability was deemed essential for improving propulsion performance in versatile environments, particularly in applications requiring efficiency across a wide range of altitudes. The design process involved an iterative evaluation of system-level alternatives and trade-offs, with the final configuration reflecting the optimal balance of performance, safety, and compatibility.



Figure 5: System Level Models & Integration Procedure

Decision-Making Process

The decision to pursue a radial multi-engine aerospike design was driven by its efficiency and adaptability. Unlike traditional bell nozzles, which are optimized for specific altitudes, aerospike nozzles provide consistent thrust efficiency from sea level to vacuum conditions. This characteristic is critical for applications that operate across variable atmospheric pressures. The team evaluated traditional bell nozzles, truncated aerospike designs, and radial aerospike configurations. While bell nozzles demonstrated simplicity and proven functionality, their lack of altitude compensation led to their exclusion. The radial aerospike configuration emerged as the



optimal solution, offering scalability and compatibility with innovative thrust control mechanisms, such as an LITVC system.

Additionally, the integration of the aerospike with an altitude simulation shroud and a custom-built test stand was factored into the system-level decision. These components enable accurate performance testing under controlled conditions, ensuring the aerospike design can be rigorously validated.

System-Level Alternatives

Several alternatives were considered during the preliminary design phase:

1. Conventional Bell Nozzle System

While reliable and well-understood, the bell nozzle was ultimately rejected due to its inefficiency across varying altitudes. Designed for peak performance at a specific altitude, it suffers from under-expansion at low altitudes and over-expansion at high altitudes, leading to significant performance losses. Additionally, achieving optimal expansion in vacuum conditions would require a much larger nozzle, increasing weight and structural complexity. These limitations made it unsuitable for the project's objectives, which required consistent thrust efficiency across a wide range of altitudes.

2. Linear Aerospike Design

The linear aerospike was considered due to its inherent altitude-compensating properties, which allow for more efficient thrust across different atmospheric conditions. However, this design introduces significant engineering challenges, including complex fuel and cooling system integration, increased structural mass, and difficulty in scaling for a multi-engine configuration. The need for precise machining and alignment of multiple combustion chambers also increases manufacturing difficulty and cost, making it less practical for the project's constraints.

3. Full Radial Aerospike Design

A full aerospike nozzle was evaluated for its ability to maintain optimal exhaust expansion across all altitudes. However, this design would require an extended spike to ensure proper



flow attachment, significantly increasing its length and structural complexity. The longer spike would be subjected to extreme heating at the tip, where exhaust gases maintain high temperatures, leading to potential material degradation or even melting. These challenges made the full aerospike impractical without advanced thermal management solutions, leading to the consideration of alternative configurations.

Design Alignment with System Requirements

The Vulcan aerospike engine prototype was carefully designed to meet all outlined system requirements, ensuring a robust, efficient, and versatile propulsion solution. Each requirement influenced key aspects of the design process, resulting in a system that addresses the complex demands of modern aerospace applications.

SYS.01 - Radial Multi-Engine Aerospike Design

The radial multi-engine aerospike design was chosen to leverage its superior altitude compensation capabilities. Unlike traditional bell nozzles, the aerospike design maintains consistent thrust efficiency across varying atmospheric pressures, from sea level to vacuum conditions. This feature directly supports the need for high performance in diverse operational environments. By utilizing this innovative configuration, the system meets the requirement for improved efficiency and adaptability, ensuring that the engine is not constrained to specific altitudes or atmospheric conditions.

SYS.02 - Safety Compliance

Safety was a top priority in the design process, as outlined in the system requirements. The decision to use AlSi10Mg, a lightweight and high-strength aluminum alloy consisting of a unique combination of aluminum, silicon, and magnesium, for the aerospike structure addresses the need for a material capable of withstanding the extreme thermal and mechanical stresses generated during operation. AlSi10Mg's exceptional thermal resistance and ideal material qualities for additive manufacturing ensures the structure remains intact during temperature cycles reaching up to 2,888 K. In addition, the incorporation of rigorous testing protocols, such as thermal and



structural analysis, ensures that potential risks are identified and mitigated, fully adhering to documented safety measures.

SYS.03 - Compatibility with LITVC

The system is designed to integrate with a LITVC system, allowing precise thrust adjustments without relying on traditional gimballed mechanisms. This compatibility reduces overall system weight while providing enhanced control precision. The aerospike's geometry and configuration were tailored to seamlessly accommodate the LITVC system, ensuring efficient integration and functionality. This innovative feature aligns with the system's objectives of advancing propulsion technology through modern control techniques.

SYS.04 - Compatibility with Altitude Simulation Shroud

Testing the aerospike design under realistic operating conditions was a critical consideration. To facilitate this, the system was designed to be compatible with an altitude simulation shroud. This shroud creates a controlled vacuum environment to replicate the low-pressure conditions the aerospike will experience during actual operation. The integration of this feature ensures accurate performance validation across varying atmospheric pressures, supporting the goal of verifying the aerospike's efficiency and adaptability in real-world scenarios.

SYS.05 - Custom Test Stand Integration

The system's dimensions and mounting features were specifically designed to integrate seamlessly with a custom-built test stand. This stand is equipped with sensors to capture critical performance metrics, such as thrust, pressure, and vector control data. The tailored design ensures structural stability and precise data acquisition during testing. By incorporating these features, the system aligns with the requirement to support rigorous testing and validation, which are essential for refining the design and confirming its compliance with operational objectives.

Final Configuration and Justification

The selected radial multi-engine aerospike system integrates key innovations, such as compatibility with an LITVC system and an altitude simulation shroud. These features address the

dual goals of high-efficiency propulsion and precise thrust control. The compatibility with LITVC allows for enhanced maneuverability without the added complexity of traditional gimballed systems. The altitude simulation shroud ensures accurate data collection during testing, replicating real-world atmospheric conditions.

The custom test stand was also a critical consideration in system design. By designing a stand specific to the aerospike's dimensions and integrating sensors for thrust, pressure, and vector control data, the team ensures both structural reliability and high-fidelity data acquisition.

Prototyping and Verification

The system-level design has been translated into detailed CAD models (Figure 5), providing a comprehensive visualization of the aerospike configuration and its integration with auxiliary systems. Physical prototypes have been created, with initial testing focused on validating model completeness and 3D printing capabilities with the design. Inspections and simulations are ongoing to confirm alignment with the outlined system requirements.

Test Stand

Previous designs considered were a linear stand which measures the thrust, and another axial test stand that would measure the deflection (Figure 6). Design alterations for the first stand were considered for measuring momentum by having load cells on four of the legs of the stand and measuring the momentum from the difference between the front and back legs.

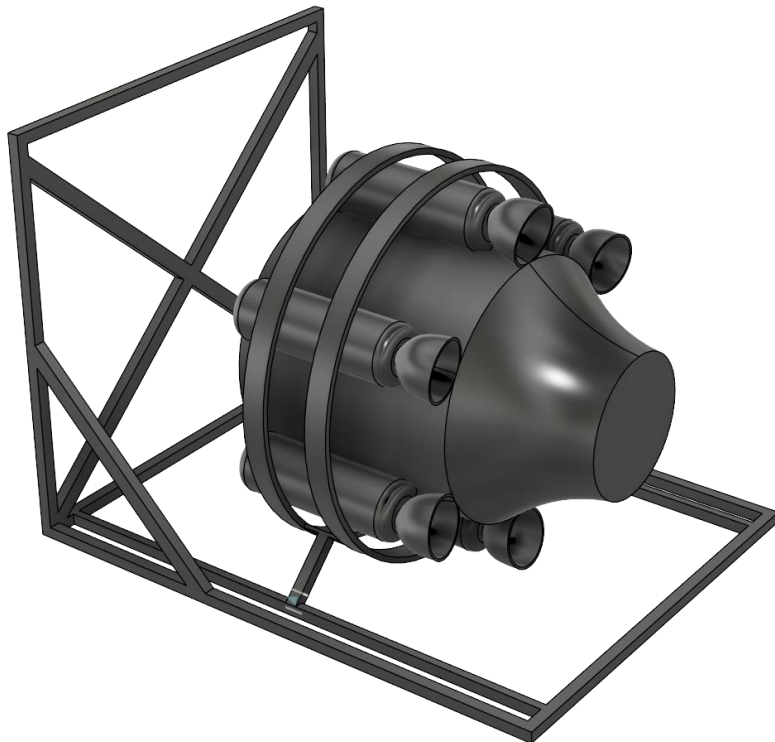


Figure 6: Linear Test Stand Design

Some other design alternatives were considered before settling on the final design. One of which was an experiment with creating an omnidirectional test stand (Figure 7). The main issue with this design was the complexity of the math required to decompose the forces and general flimsiness of the design.

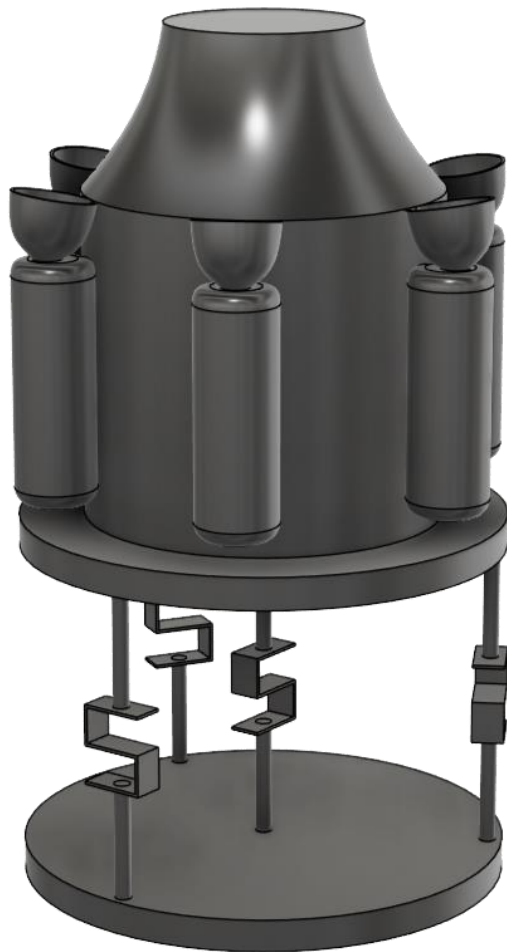


Figure 7: Omni-Directional Stand First Concept

Similar design alternatives were looked at from various papers and other external sources on the subject of measuring omni-directional thrust or thrust together with thrust vectoring.

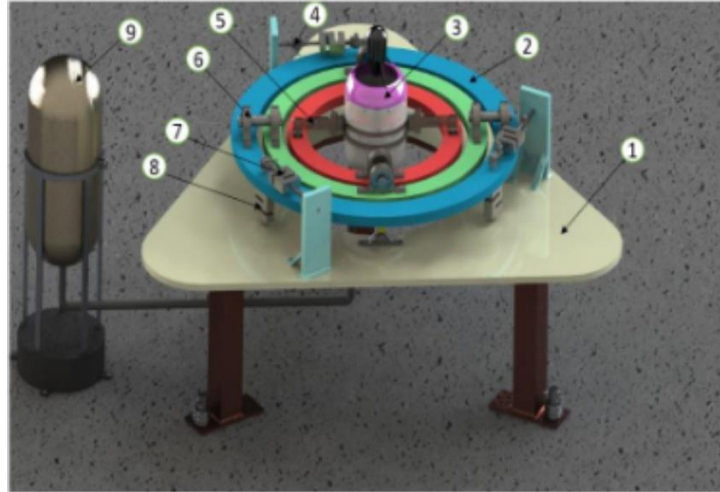


Figure 8: Design Inspiration 1 [20]

Design inspiration 1 came from a paper for designing a test stand for this exact purpose [20]. The design was rejected due to high complexity and questionable compatibility with other systems, mainly the LITVC and Altitude Shroud systems.

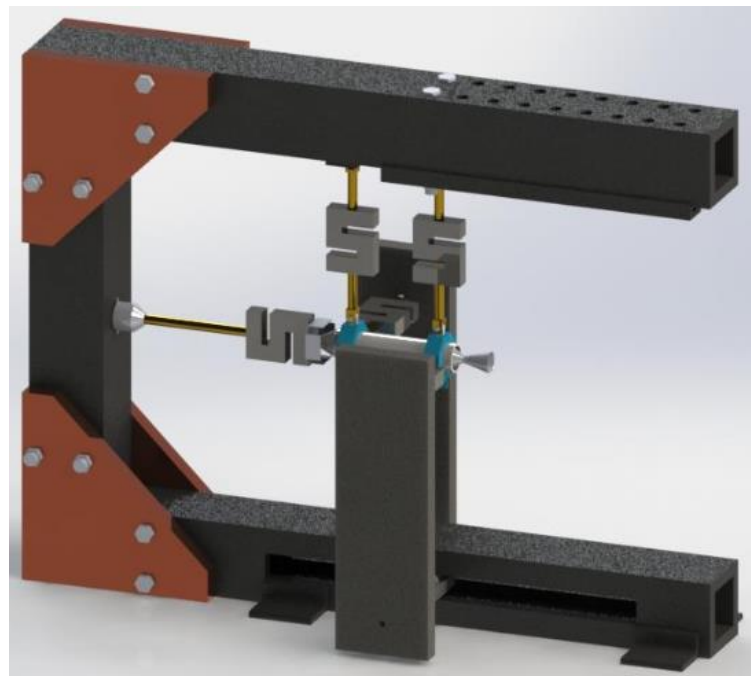


Figure 9: Design Inspiration 2 [12]

Design inspiration 2 was a more robust design and was also based on a thrust vectoring system [12]. This design was also rejected due to the high complexity of math, and the questionable compatibility with other systems.

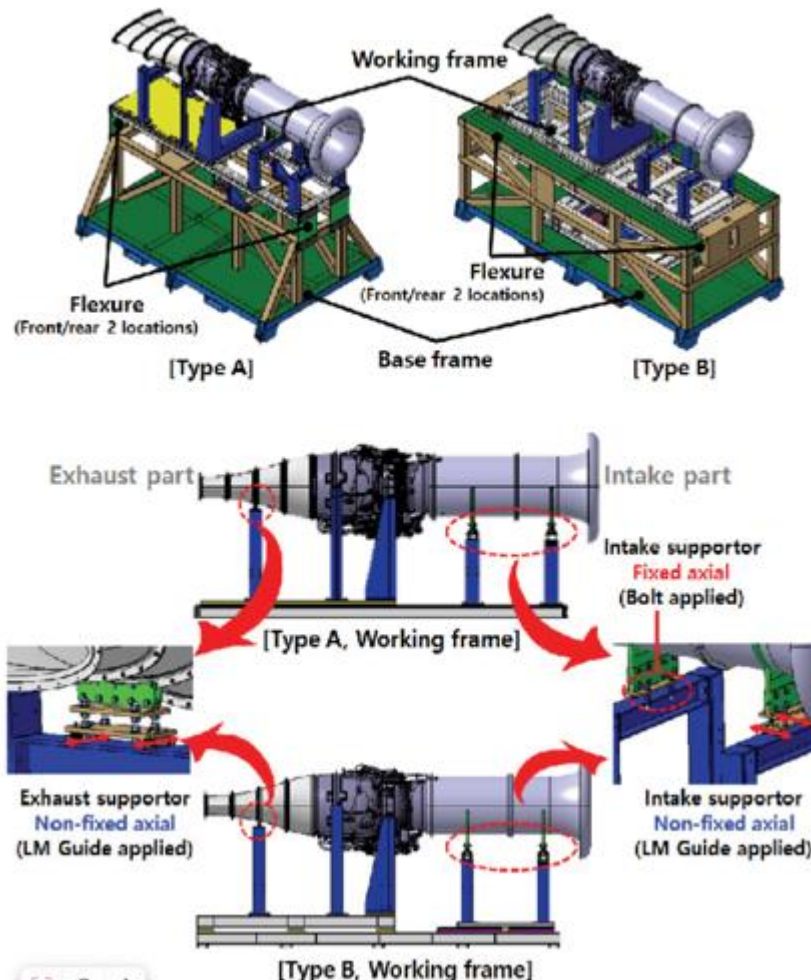


Figure 10: Design Inspiration 3 (Jin et al., 2021)

The third design inspiration came from a Korean journal that focused on thrust vectoring a jet engine (Jin et al., 2021). The design was rejected due to construction complexity and general confusion on the design implementation, which led us to finding a much simpler design alternative.

Table 2: Pugh-Matrix for Test Stand Design

Test Stand Pugh Matrix							
Solution Alternatives							
Concept Selection Legend		<i>Importance Rating</i>	Linear Stand	Omni-Directional Stand	Design Inspiration 1	Design Inspiration 2	Design Inspiration 3
Better	+						
Same	S						
Worse	-						
Key Criteria							
Data processing Complexity	3		-	+	-	+	-
Mechanical Complexity	2		+	+	+	-	+
Part Cost	5		+	+	S	-	+
Compatibility	5		+	-	-	-	+
Structural Integrity	4		-	-	S	S	+
Sums of Positives				3	3	2	1
Sums of Negatives				2	2	1	3
Sums of Sames				0	0	2	1
Weighted Sums of Positives				12	10	2	3
Weighted Sums of Negatives				7	9	8	12
Totals				5	1	-6	-9
							13

Table 2 details a Pugh-Matrix selection method process that was used to select the best option for the stand. The decision matrix main factors were both regarding the compatibility of the test stand with the engine, as well as the cost of the parts to make the test stand. Compared to a standard linear test stand the final design inspiration outperformed the other variants by a significant margin. Scoring in all aspects of design except in the complexity of data processing.

Altitude Simulating Shroud

Previous designs considered were shrouds made of PVC and of CPVC. These designs utilized a 55-gallon drum for support. This design was decided against due to the uncertain quality of the separation of ambient air from the internal volume of the shroud. A rendering of this design can be seen below in Figure 11.

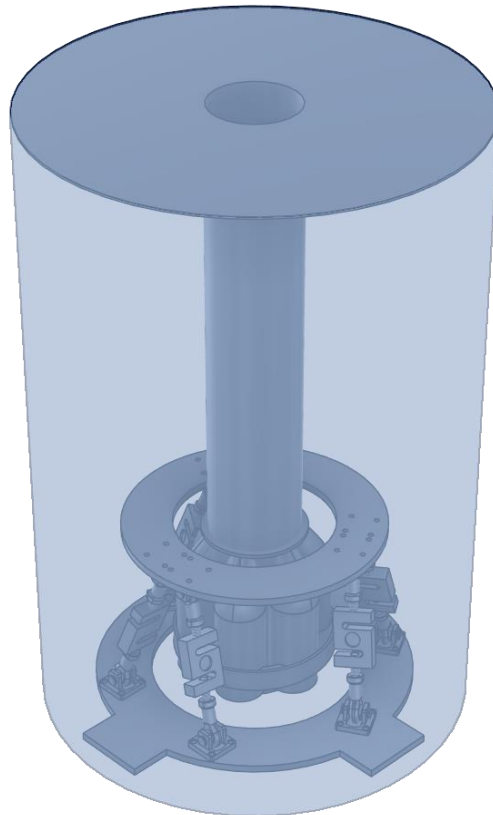


Figure 11: 55-Gallon Drum and PVC Design

The team decided against PVC because it was unfit for pressure-based applications, so the team instead looked into the pressure rated variant CPVC. This type of PVC satisfied most of the subsystem's needs but had the drawback of a much greater price and delivery time when compared to normal PVC. While weighing available options, the team were offered a section of

the shock tube from Dr. Kirk's lab that possessed superior qualities to both types of PVC as seen in the Pugh matrix below.

Table 3: Pugh-Matrix for Shroud Selection

Altitude Simulating Shroud Pugh Matrix					
		Solution Alternatives			
Concept Selection Legend		<i>Importance Rating</i>	PVC	Steel	CPVC
Better	+				
Same	S				
Worse	-				
Key Criteria					
Price	4		+	-	
Structural Capability	5		+	+	
Compatability	3		S	S	
Delivery Time	2		+	-	
Weight	4		-	+	
Sums of Positives			3	2	
Sums of Negatives			1	2	
Sums of Sames			1	1	
Weighted Sums of Positives			11	9	
Weighted Sums of Negatives			4	6	
Totals			7	3	

Table 3 details a Pugh-Matrix selection method process that was used to select the best option for the altitude simulating shroud. The matrix details the shroud materials considered. The matrix prioritized material properties and cost. Weighing these criteria, it is evident that the steel tube was the best option by far. Scoring in all aspects of design except in the weight of the material.

5.2 System Design History (Hartlieb)

To determine the optimal nozzle contour for the aerospike, the team resorted to using MATLAB and creating a MoC code. When given the initial pressures and flow rate, the code would give us X and Y coordinates for points along the nozzle contour. The contour that was generated from the MoC code was a long accumulation of points that represent the diverging section of the nozzle. The team then cut this curve of points at the 25% mark from the nozzle throat. The first 25% of the contour would be the diverging section of the nozzle, where the other 75% would be the aerospike contour (Separated by the white dot in red circle in Figure 12).



Figure 12: MoC Points Obtained from MATLAB Code

With these points, the team were able to import them into Autodesk Fusion and begin modeling out aerospike design. A CD nozzle was modelled based on the contour, seen above in Figure 12. The architecture for the design was based on Vaya's Dauntless rocket, where you have the tanks and combustion chamber going along the outside of the rocket itself, with the nozzles pointed off the back. The team opted to cant/angle the nozzles inward toward the aerospike at an angle of 10 [deg] to allow the flow to better utilize the aerospike capabilities. With the nozzles pointing straight out and not angled, the flow does not get a chance to push against the aerospike due to the plume expansion not reaching. By giving the flow the aerospike to push off, thrust and efficiency of the rocket propulsion system is increased.

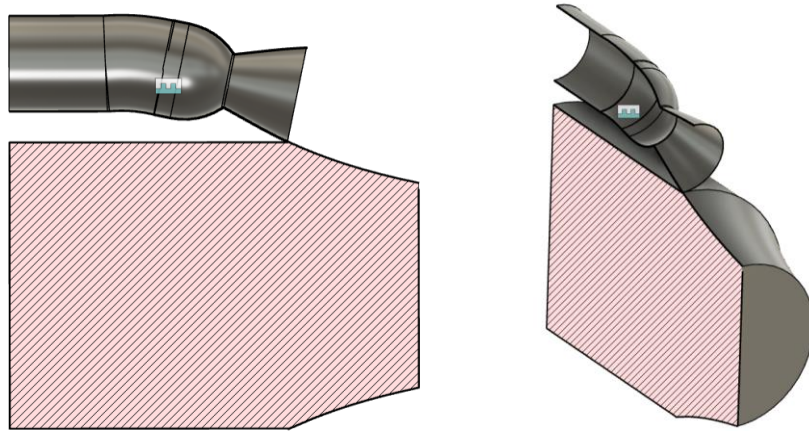


Figure 13: Cross Section View of Aerospike and CD Nozzle

In Figure 13, you can see a cross section of the aerospike, with the chamber to nozzle angled at 10 degrees and then the aerospike directly after the exit of the nozzle. The radius of the CD nozzle and the aerospike itself was also determined from the MoC. Initially, the team chose to use only 4 nozzles for the engine, seeing that the feasibility of manufacturing this design out of metal at the time would be difficult and costly. Also, without the completed CFD and FEA simulations, the thickness of each aspect of the design was arbitrary and undefined.



Figure 14: Radial Aerospike design with 4 & 6 Nozzles

Initial designs had only 4 nozzles going around the aerospike, but with a newfound connection with Vaya Space, the team opted to switch to 6 nozzles. This was due to Vaya Space's Dauntless Rocket which employs a 6-nozzle configuration. Initial arbitrary supports were added in between the combustion chambers and the aerospike spine itself.

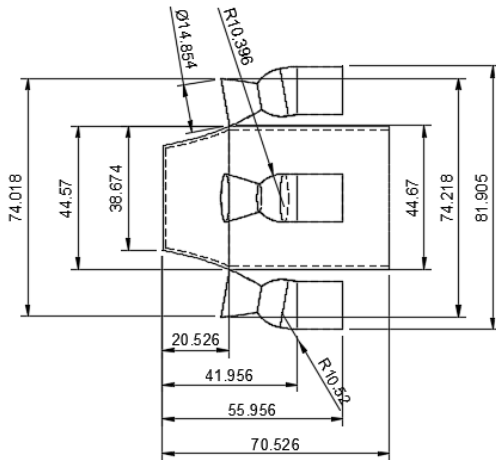


Figure 15: Part Drawing of Aerospike Design with 4 Nozzles

Part drawings were created for this design to help the team and Vaya visualize the current concept, aiding in problem solving and justification. This initial design had a major diameter of 81.905 [mm] or 3.22 [in], with a height of 70.526 [mm] or 2.77 [in]. Initial chamber walls were set at 1 [mm] thick, a thickness the team would later determine was unsafe and insufficient for the amount of heat and pressures. Through research in the small world of radial aerospikes, the team came across the firefly design, which employed plume channels around the aerospike to guide the flow more axially [27]. These channels would come up from the aerospike contour, around where the plume was expected to be. This channel would guide the flow more horizontally, ensuring less thrust is lost to the sides and is instead directed axially off the back.

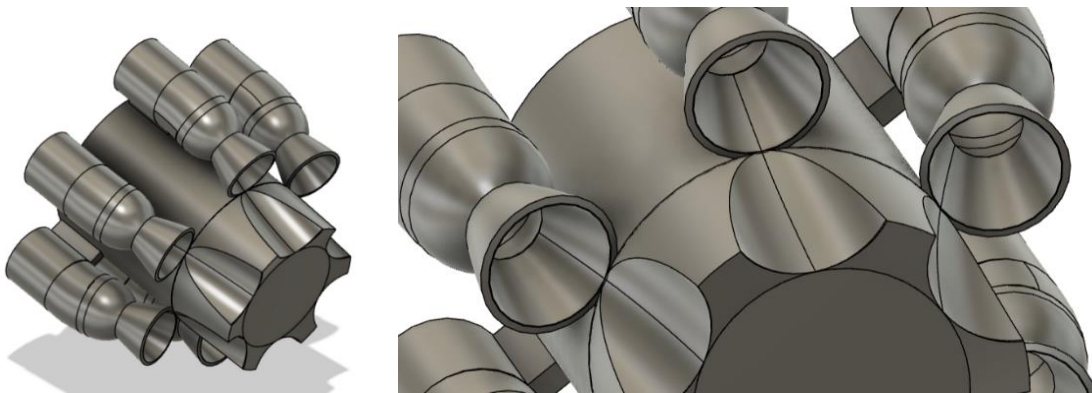


Figure 16: Fly Spike Design Channels

More work had gone into the nozzle and chamber contour to try and make it as smooth as possible for optimized flow direction. While the chamber wall thickness was also being worked on to determine possibilities/capabilities of the Fusion software to thicken a surface.

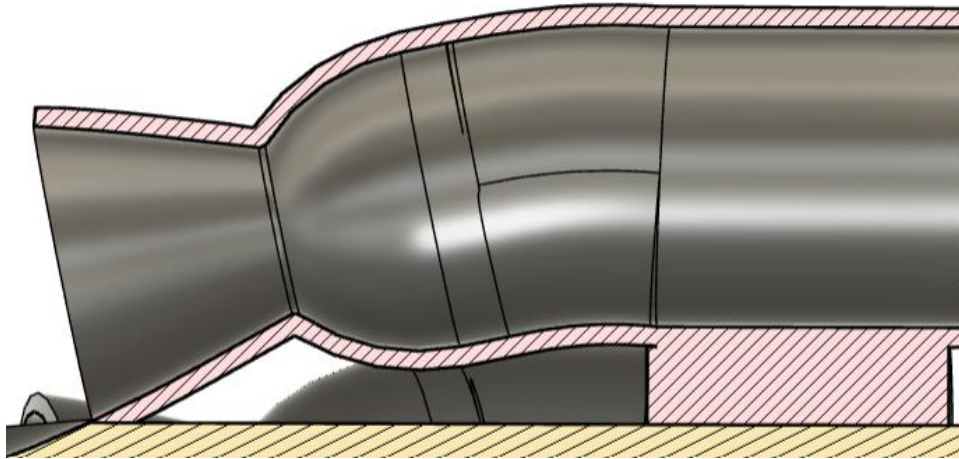


Figure 17: Thickened Chamber-Nozzle Walls

New part drawings were made for this new design with the fly spike variant. General dimensions remained the same, with the only addition being the fly spike attachment. This fly spike concept was for a removable attachment onto the general aerospike contour, that could be added or removed based on the test the team were playing on doing. This would also give us a realistic look into the difference in thrust from the generic aerospike model with the new fly spike model.

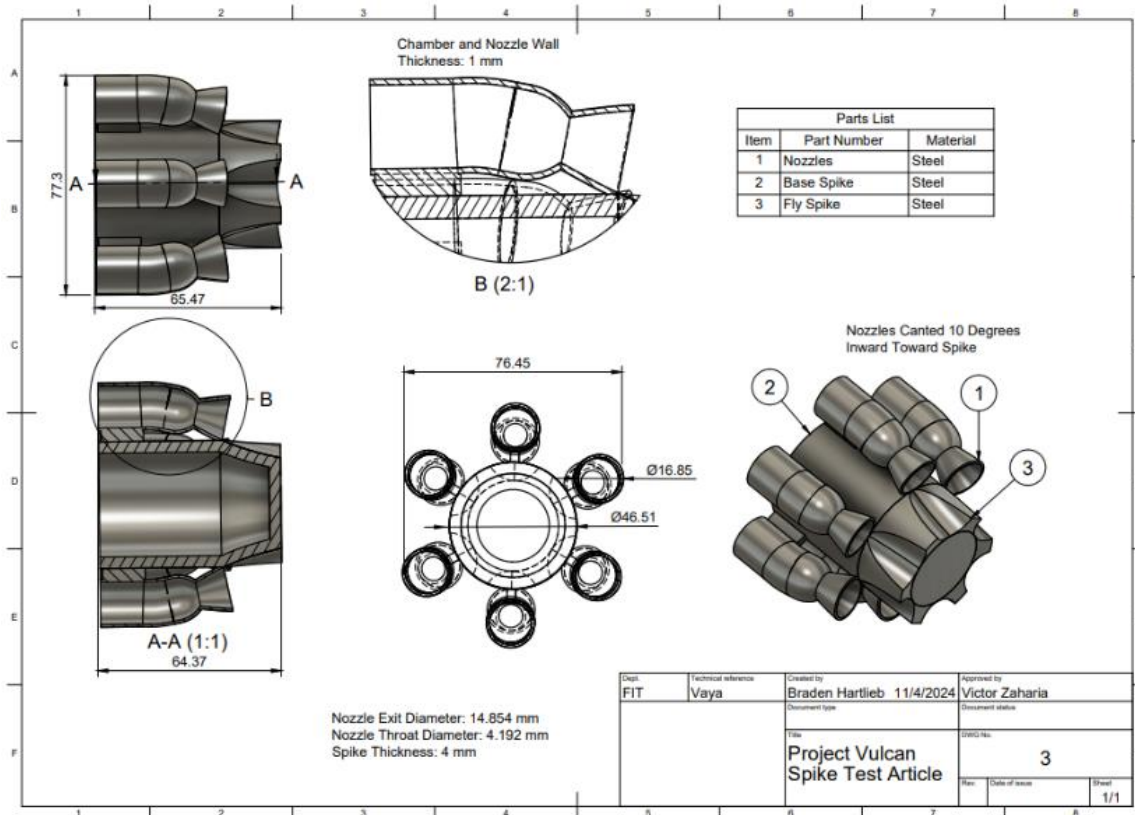


Figure 18: Part Drawing of Fly Spike Design

At this point, development into the LITVC system had started. Working closely with Vaya space on feasibility and design architecture, a new model had been developed incorporating LITVC piping. The LITVC port itself would sit 25% down the aerospike contour, in line with the deepest most point in the fly spike channel. Then coming from that port on the inside of the hollow spike structure, a pipe system would go all the way to the back of the model.

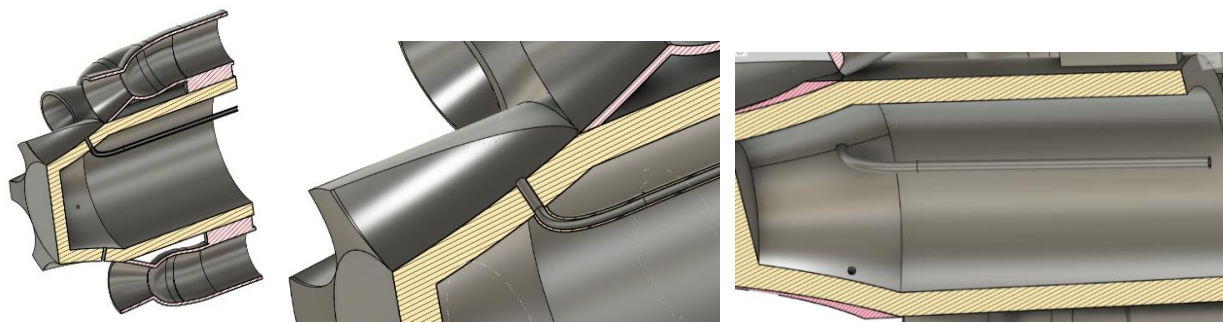


Figure 19: LITVC Port and Piping

Most of these design considerations and alterations come mainly from brainstorming and research within the team, then proposing these design concepts to Vaya, where they would help guide us with tips or industry knowledge that can be applied. An additional part drawing was made with the LITVC system in each of the 6 fly spike contours, giving us the ability to apply a thrust vector in any direction.

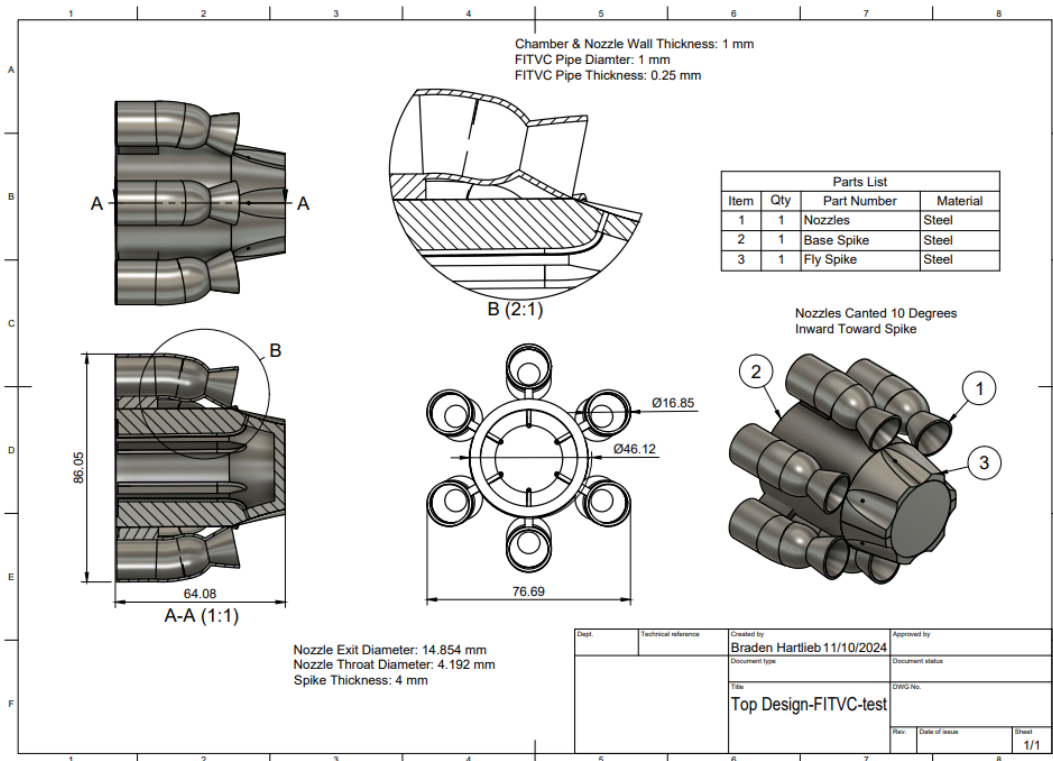


Figure 20: Part Drawing of Fly Spike Model with LITVC



With the major dimensions not changing, the main addition is the 1 [mm] or 0.0393 [in] LITVC port and the 0.25 [mm] or 0.0098 [in] LITVC pipe diameter. Now, these values are small and would require the most precise 3D printing technologies to produce. This model was going to be used with the compressed air design, which would aim to simulate the characteristics and flow of the aerospike engine without the need for solid rocket fuel and its complexities. The compressed air tanks that would be needed to produce the desired flow rates of this design far exceeded the team budgets for the class. The team came together and worked out what the project's goals would be with this monumental roadblock, and after days of research into possible other options, a decision was made to redesign the system to use solid fuel.

This new design architecture would require a complete rework of the model in Fusion to be modeled from scratch. So, going back to the MoC code in MATLAB, an ideal nozzle-spike contour was determined and imported into Fusion. This contour given by the code was greatly larger in length compared to the contour gotten for the compressed air design. Using this contour, the spike and converging section of the nozzle could be modeled. Following this would be the casings/housing for the solid propellant grain. After research was conducted into possible solid propellants that were out on the market, the team decided to use “75mm Classic Propellant Grain”. This grain was chosen due to its affordability solid fuel grain that gave us a burn duration high enough to produce the thrust the team were trying to get. This grain comes in a paper casing and when removed it has an outer diameter of 64.9 [mm] or 2.55 [in]. Being that this grain is vastly larger than the spike model itself, some unique design philosophies had to be implemented. An initial sloped chamber-nozzle shape was modeled to connect the motor casings, that houses the grain to the CD nozzle itself. This was a difficult task to do in Fusion, due to the little information or guidance on the internet, but working with the team, the team were able to get a smooth connection path.



Figure 21: New Solid Fuel Design

Now, this connection path was forcing the flow to make a sharp re-direction against the inside of the chamber walls. These chamber walls, at the time, were only 1 [mm] thick and would not be able to withstand the immense amount of heat during engine test firing. Extra material could be added to the walls of the nozzle but with the casings being so close to each other, the method would not be realistic, and the addition of a lot of material would increase the weight and print cost drastically. To fix this, the model had to be restarted from scratch again, while keeping the same MoC points from the MATLAB code. With the prior concept having three changes in direction, that went from a -10 [deg] canted nozzle to a small 0 [deg] section to the sloped chamber-nozzle section, the new design would need to increase the fluid dynamics.

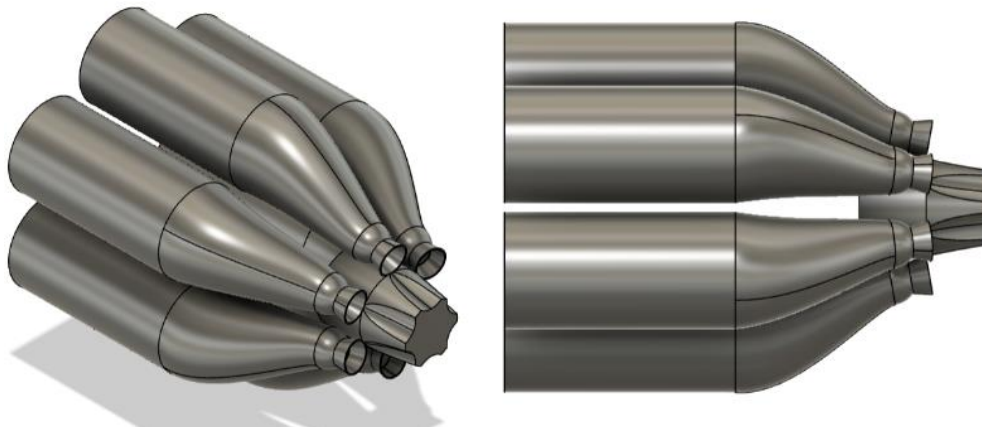


Figure 22: Optimized Solid Fuel Design

The new design contour would allow the flow an easier transition from the fuel grain to the nozzles, with the model going from the -10 [deg] canted nozzles directly into the chamber-nozzle sloped connection section. In other words, just removing the flat 0 [deg] section and change the changes in direction from 3 to 1 (right after the grain). This new design concept would prove to be a great alternative and was approved by Vaya Space.

The next task was to determine connection points to the test stand; therefore, a circular ring was embedded into the print itself just before the nozzles. This adds structural integrity to the nozzles when firing as well as provides room for any connection points such as bolts or welding that may connect the test stand. An external supporting ring was also added to the design to support the end of the motor casings when firing and reduce the possible destructive vibrations.

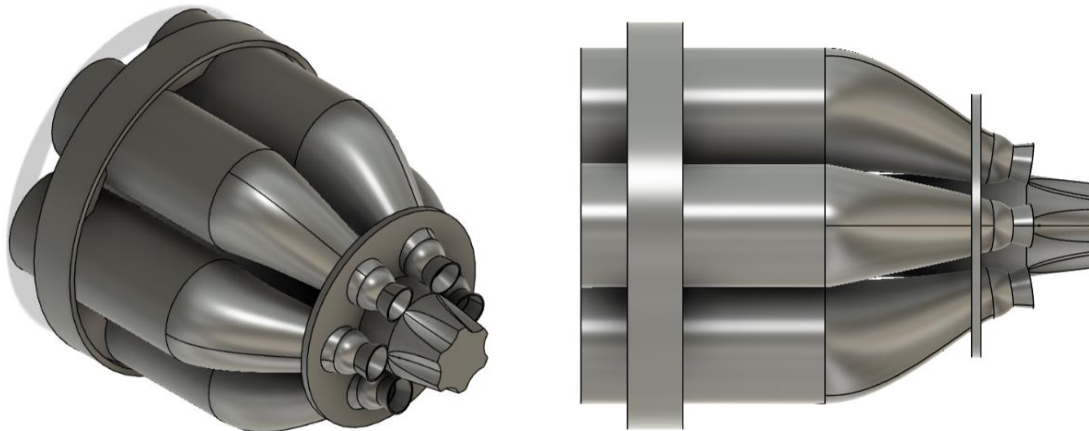


Figure 23: Fly Spike Design with Supporting Structures

With the test stand modeled and ready for integration, connection concepts needed to be created. There are two concepts for the connecting points, Tension arm and C-clamps.

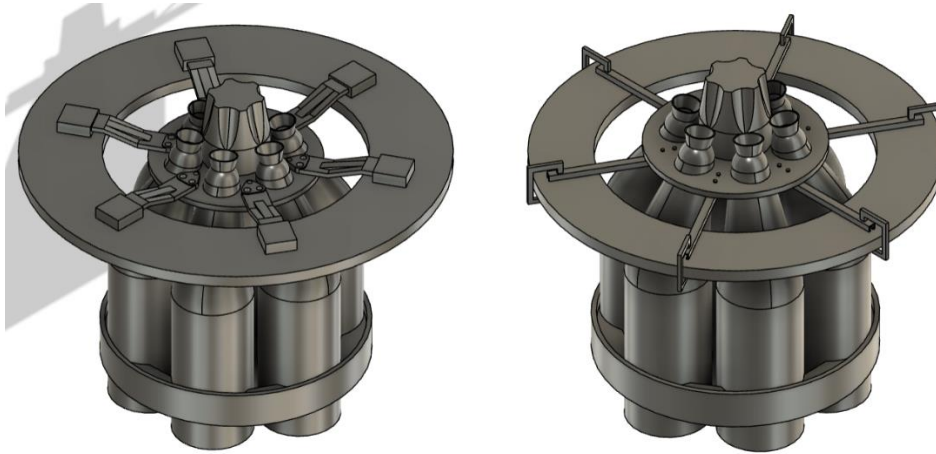


Figure 24: Tension Arm & C-clamp Test Stand Connection Concepts

The large ring around the aerospike is the top plate on the test stand to scale. This allows for ideal visualization of new connection concepts. The tension arm concept demonstrates the use of tension and compression in materials and acts as a sturdy structure when thrust loads are trying to force the aerospike downward. The tension arm design would utilize metals found in the machine shop on Florida Tech campus and would be manufactured using the equipment there, then would be bolted to the circular disk and test stand using bolts that are later to be determined. The C-clamp concept utilizes off the shelf C-clamps and U bars that securely hold the aerospike. The U bars would sit upside down and would be bolted to the aerospike's circular disk, whereas the C-clamps would secure it to the test stand.

The next iteration of the design has thickened walls for the combustion chamber and nozzles. These thickened walls were in response to the large amount of heat flux going into the walls of the chamber. Other design changes include the addition of threads to the motor casings as well as to each of the nozzles on the 3D printed section. These threads will securely hold each motor casing to the printed section. The motor casings themselves will have end caps welded on to the aft end before the grain is installed. Then the supporting ring will slide on to the back side. The following information dives into the design that was selected prior to the PDR submission, and all information pertains to the design concepts and architecture. Current model design can be found later in the document and alters slightly since PDR submission.

Front Aerospike Section:

The front aerospike is integral to the design, serving as the central spine of the rocket's thrust system. The aerospike is a metal 3D printed component, the metal being ALS10MiG. The aerospike is designed with a hollow interior to house the LITVC fluid injection system, which provides thrust vectoring by injecting fluid into the flow path. This design choice eliminates the need for traditional movable nozzles, increasing simplicity and reliability.



Figure 25: Metal 3D Printed Radial Aerospike Section

Aerospike Structure: The main structure is printed in metal (likely using Laser Powder Bed Fusion (LPBF) or Direct Energy Deposition (DED) techniques) to ensure high precision and durability under extreme thermal and mechanical loads. The aerospike had a circular disk embedded in the print to offer structural support during firing, as well as serve as the connection point to the test stand.

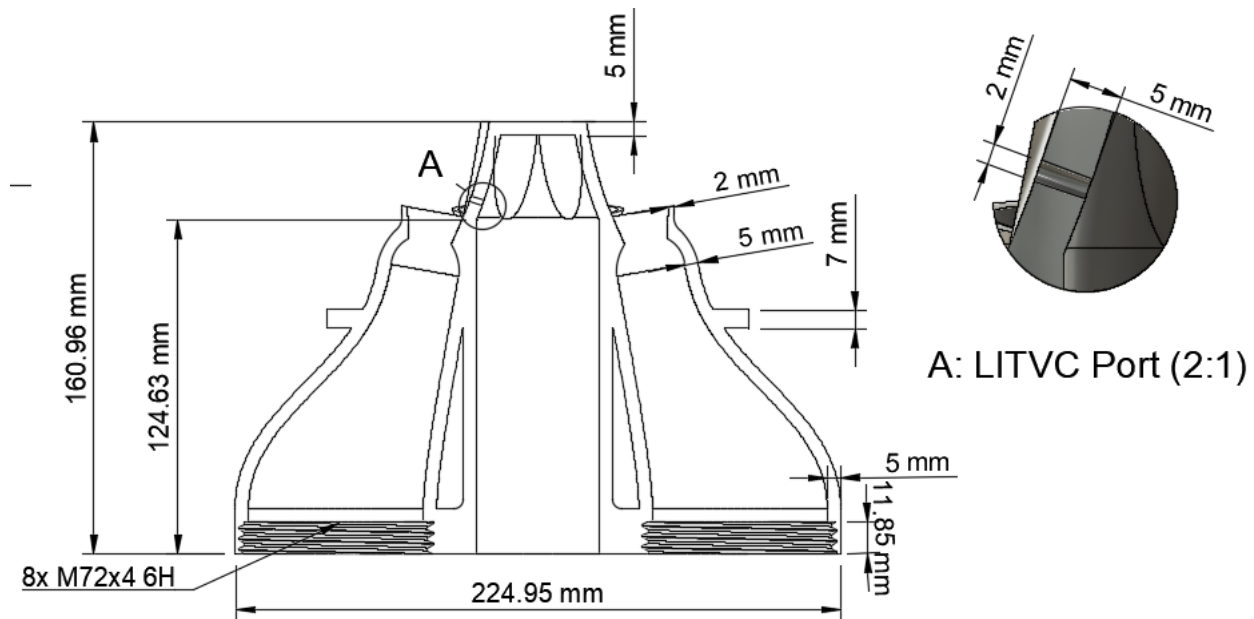


Figure 26: 3D Printed Cross Section Part Drawing

The design had a major diameter of 224.95 [mm] and a height of 160.96 [mm], with the top aerospike section being 36.33 [mm] in height. The combustion chambers for each nozzle have a wall thickness of 5 [mm] for all the converging sections and most of the diverging section, to give added heat resistance to areas where large amounts of heat concentration are expected. The aerospike contour had a thickness of 5 [mm], with the LITVC port located 25% along one of the aerospike contours. This LITVC port had a diameter of 2 [mm] and goes the entire thickness of the aerospike. Each nozzle was going to be threaded at the start of the combustion chamber using M72X4 6H imbedded into the print itself. Post-processing techniques will need to be utilized to ensure effective thread tolerance. The aerospike features conventional CD nozzles that help accelerate flow to supersonic speeds, which is critical for the vehicle's performance at high altitudes.

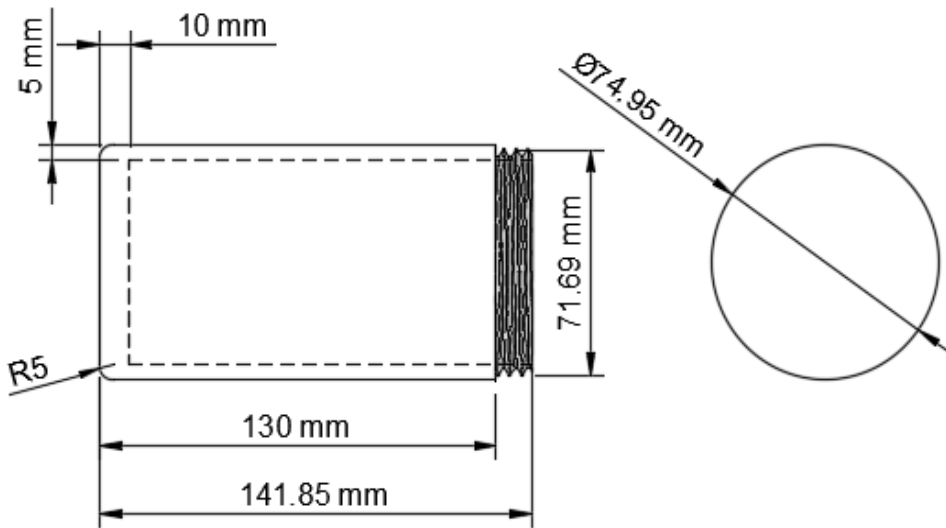


Figure 27: Motor Casing Part Drawing

Motor Casings: The motor casings, most likely made of stainless steel at the machine shop of Florida Tech's campus. These casings will house the solid rocket fuel, or “75mm Propellant Grain” that will be used for all test firings. One end of the casings will have a metal end cap welded on, whereas on the other side, M72X4 6H threads will be input to connect seamlessly and tightly to the printed section.

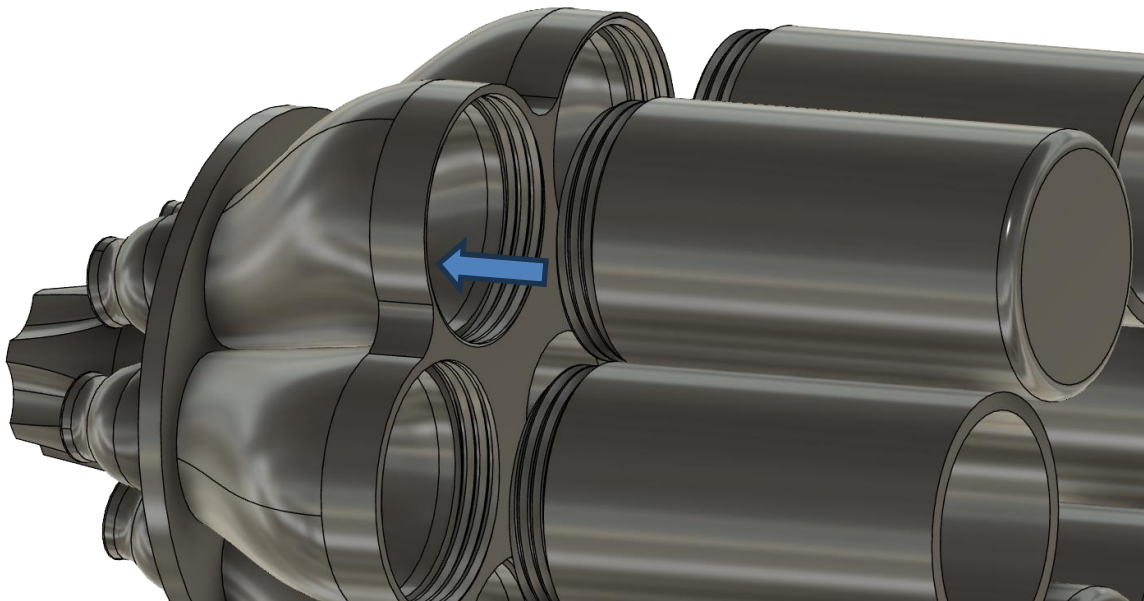


Figure 28: Motor Casing – Aerospike Print Integration

After threading and welding of the motor casings, the propellant grain will be loaded into each one, based on the test being conducted. Then, each motor casing will be screwed into the 3D print.

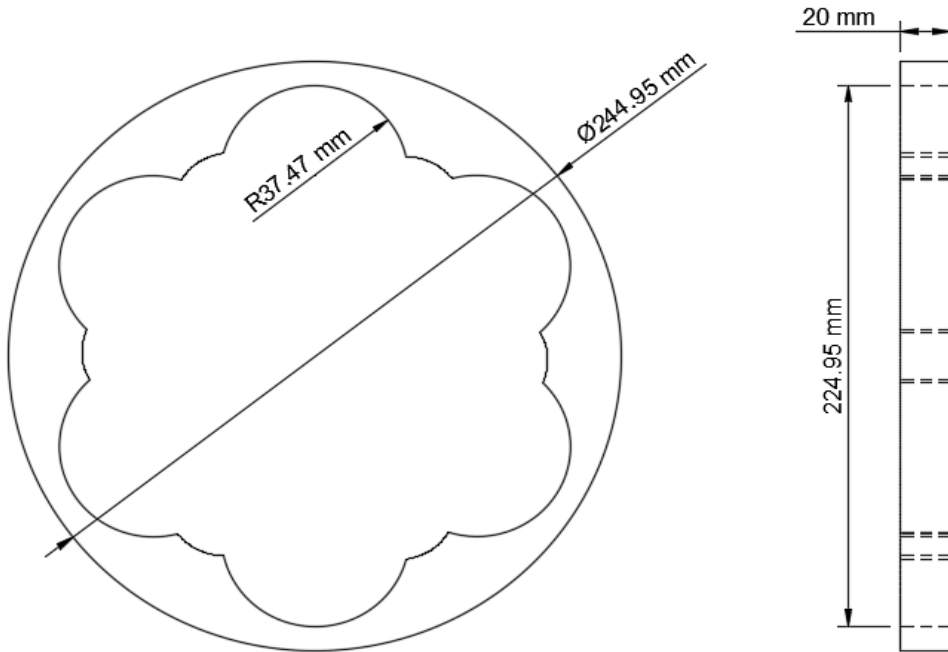


Figure 29: External Supporting Ring Part Drawing

To secure these motor casings and ensure no destructive vibrations occur, a metal external support ring will slide on to the back end over top of the motor casings. This ring will be made from metal and fabricated at the machine shop on Florida Tech's campus. The ring will be manufactured to secure the casings tightly, with the inner radius around the casings being 37.47 [mm]. The ring itself has an outer diameter of 244.95 [mm] and has a thickness of 20 [mm]. These values were chosen to ensure the structure will withstand the expected loads.

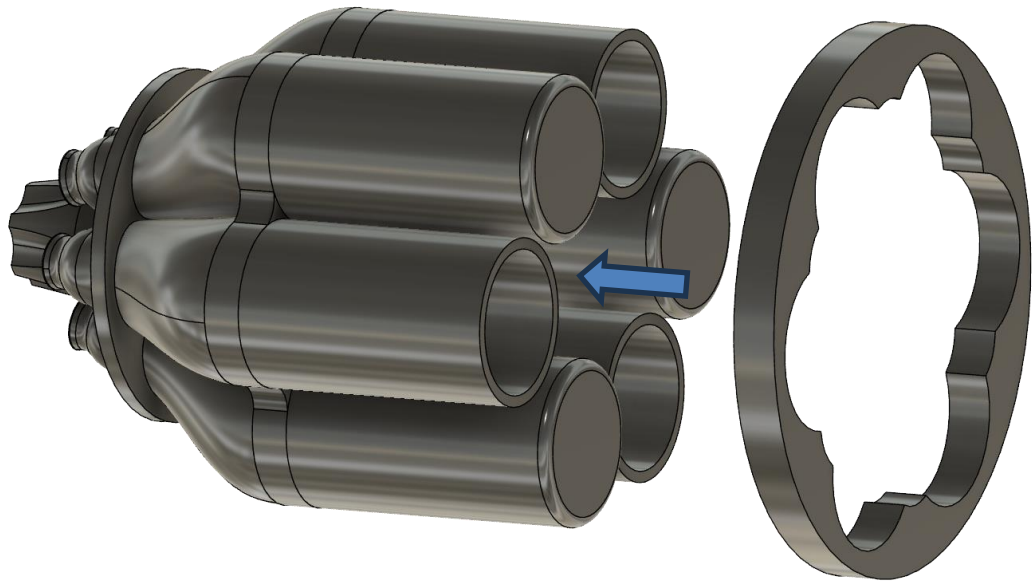


Figure 30: Support Ring – Aerospike System Integration

With each motor installed and the supporting ring securing each motor, the total system is ready to be placed in the custom test stand for testing.



Figure 31: Final Radial Aerospike System

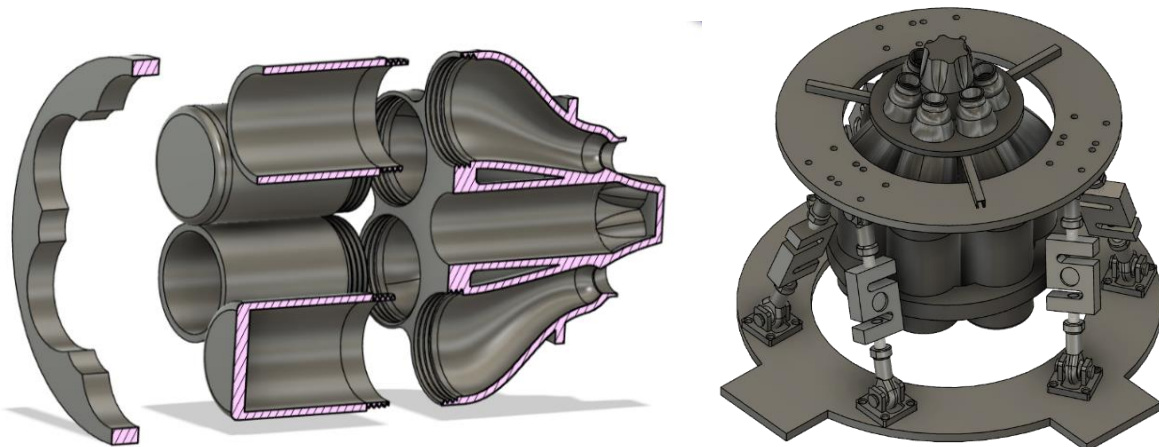


Figure 32: Radial Aerospike Model & Integration with Test Stand

With this design concept selected and finalized for the PDR submission, the aerospike and test can stand can be added together, fitting perfectly to allow space for the altitude simulating shroud to rest on the circular disk of the print. This print demonstrates that the design will integrate with the custom test stand, LITVC system, and the altitude simulating shroud. Physical to-scale

PLA prints could be created and printed from Florida Tech's HSDC 3D printing farm. Using these physical prints, validation of the design architecture can be completed to ensure the model print finish is physically possible.



Figure 33: Physical 3D Print of Aerospike Model

Constant communication with the HSDC is being used to determine the correct and most ideal print specifications for the surface finish. Prints of the motor casings have also been printed out at the HSDC center, one with an end cap and one without. It's important to note that the motor casings are not going to be printed for the actual system, PLA prints are being made now to confirm easy integration with the radial aerospike section.



Figure 34: Physical 3D print of the Motor Casings

The one major change that happened to the model was the transition from threaded connections to bolted flange connections. Communication with the manufacturer and Vaya led us to the conclusion that metal 3D printing threads would pose some difficulties with resolution and tolerances, ultimately pointing us in the direction to determine a new connection method, so no analysis was completed for the threads.

The next task for the model was to design the internal piping system that would supply fluid to the nozzles, acting as cooling channels in hopes of ensuring the nozzle would be able to withstand the immense temperatures that were expected. The cooling lines would need to go along the entire length of the combustion chamber and into the CD nozzle, going along the complex curve of the nozzles. This is a difficult task to do in Fusion or any modeling software, where the lines must keep the same diameter throughout the entire nozzle curve, as well as keeping the same distance from the nozzle walls. On top of this, the lines need to go from the larger motor casing diameter to the very small CD nozzle diameter, causing the lines to be largely dispersed by the motor casings but then completely bunched up towards the CD nozzle.

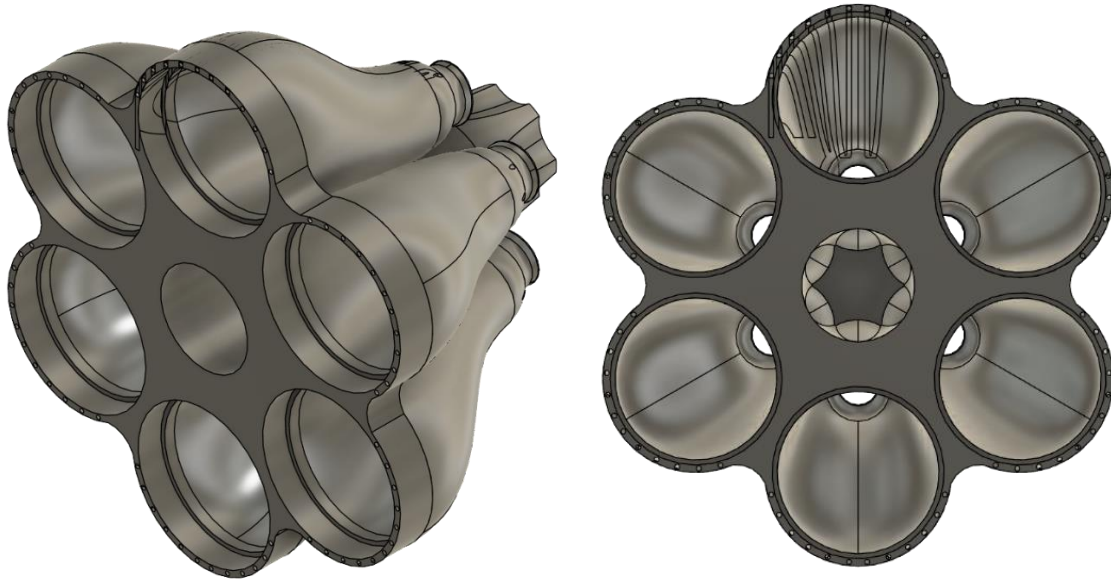


Figure 35: Initial Cooling Line Model

Initial attempts to model this very complex geometry ended in failure, where the modelling approach was to determine tracks that the lines would follow from above. This would make the lines on the outer sides of each nozzle not have a continued geometry, and they would curve upward rather than proportionally along the chamber curve. 12 cooling channels were initially modeled in each nozzle, with 6 inlet and 6 outlet lines connected to each other after wrapping around the CD nozzle.

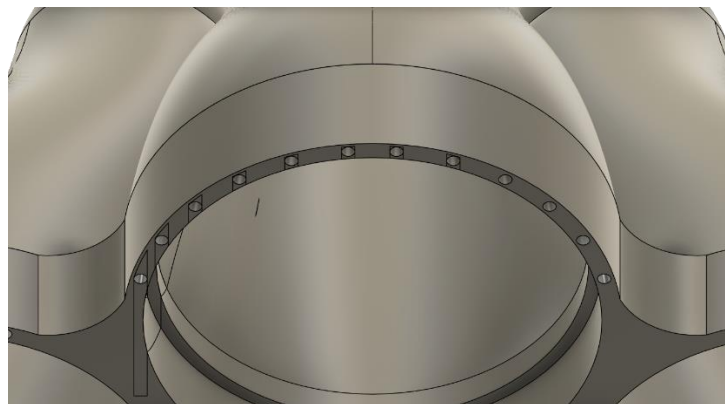


Figure 36: Close up Top view of Initial Cooling Lines

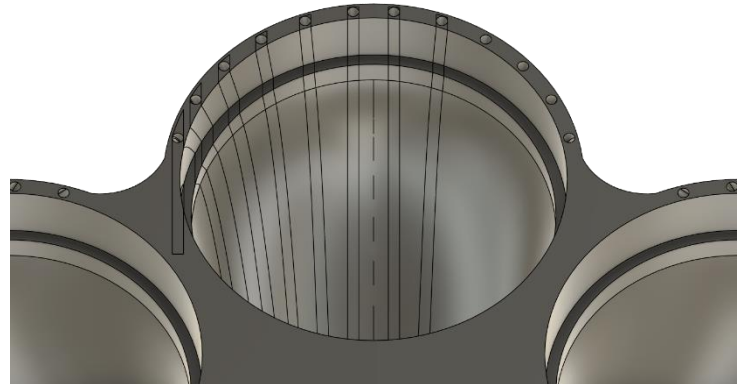


Figure 37: Close up Bottom view of Initial Cooling Lines

The goal of the cooling lines was to encompass as much internal area along the combustion chamber walls so that fluid could be evenly distributed across the chamber walls, bettering the chances of the model sustaining the thermal impact.

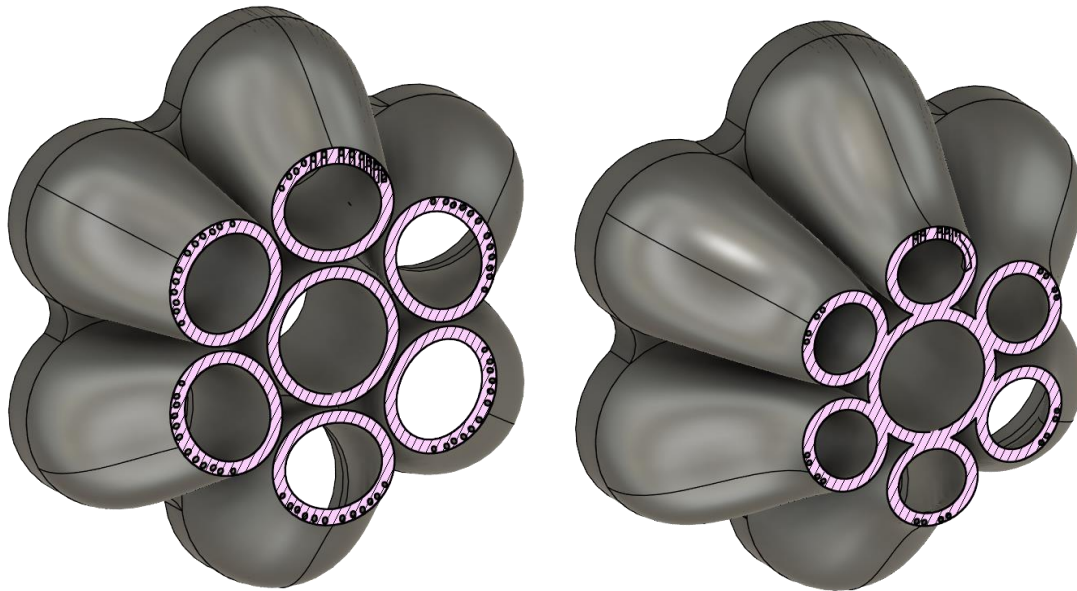


Figure 38: Cut view of Internal Cooling Lines

With the cooling lines becoming closer and closer together as they approached CD nozzle, the amount of room for each nozzle was drastically decreasing. This led to the outer lines of each nozzle stopping at different stages as they moved along the CD nozzle, so that once the nozzle was reached, only four lines were left to fill the walls. In figure 38 on the left demonstrates the cooling lines as they are around halfway down the aerospike contour, with the figure on the right demonstrating the lines as they are right before the CD nozzle.

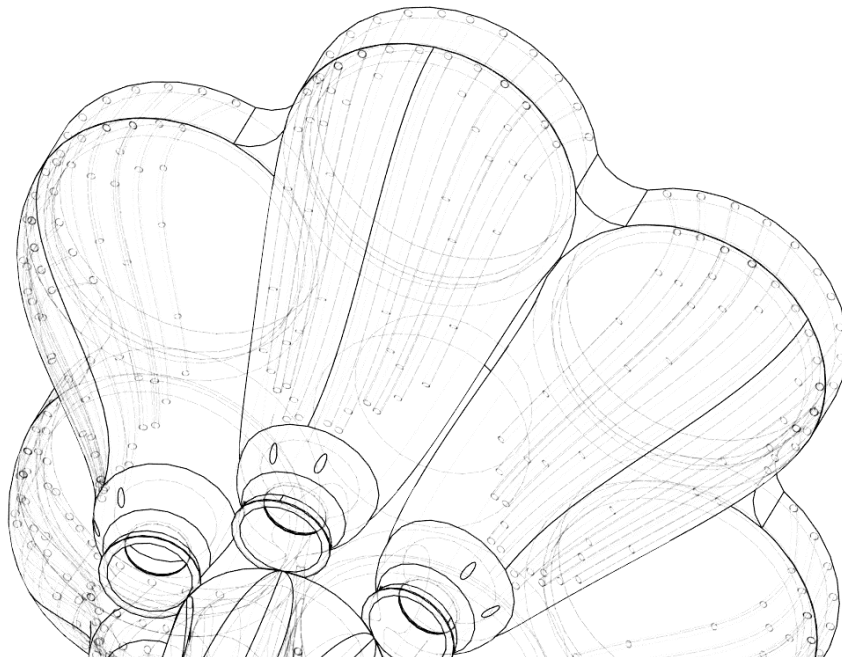


Figure 39: Wireframe of Aerospike and Internal Cooling Lines

A wireframe demonstration of the model and the cooling lines can be seen in Figure 39 above help to visualize the cooling lines as they are in the model. This model concept was eventually trashed due to the inconsistency with the cooling lines, with the replacement model concept being currently used in the system design. The system design history entails all previous design choices within the Radial Aerospike Engine print section and walks the reader along the long process of designing such a complex system. The final system design model for the aerospike can be seen later in the document.

5.3 System Design Conclusion (Hartlieb, Bedelbaev)

The metal 3D-printed radial aerospike engine represents a complex integration of advanced manufacturing, fluid dynamics, structural resilience, and data acquisition, culminating in a system designed for high-temperature, high-pressure static fire testing. The system-level components have been carefully developed to ensure a seamless and controlled testing environment at the Vaya Space facilities.

Aerospike Design and Fabrication

The aerospike, the core component of the engine, will be manufactured using AlSi10Mg. Additive manufacturing techniques, such as Directed Energy Deposition (DED) or Laser Powder Bed Fusion (LPBF), facilitate the fabrication of its intricate geometry. Post-processing, including surface finishing inside the nozzle, ensures minimal turbulence and enhanced flow properties. The manufacturing process incorporates thermal analysis to validate its ability to withstand combustion temperatures reaching 2,888 K. Use of the school's student design center and machine shop will aid in the fabrication of the solid motor casing structure.



Figure 40:Aerospike and Nozzle Structure (Top View)

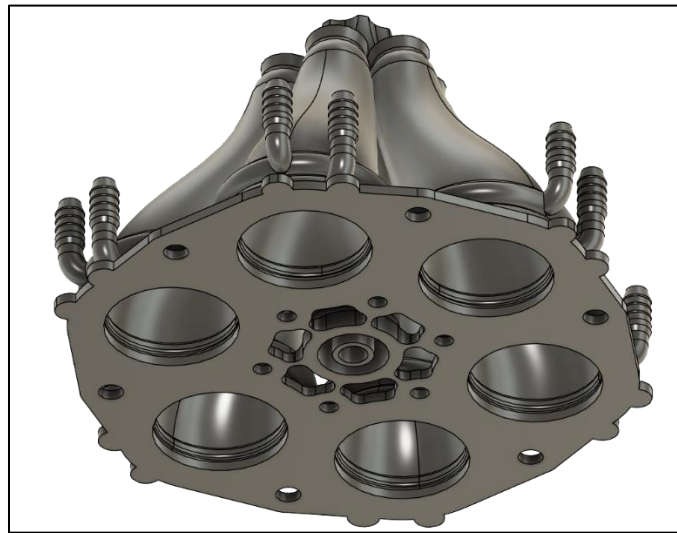


Figure 41:Aerospike and Nozzle Structure (Bottom View)

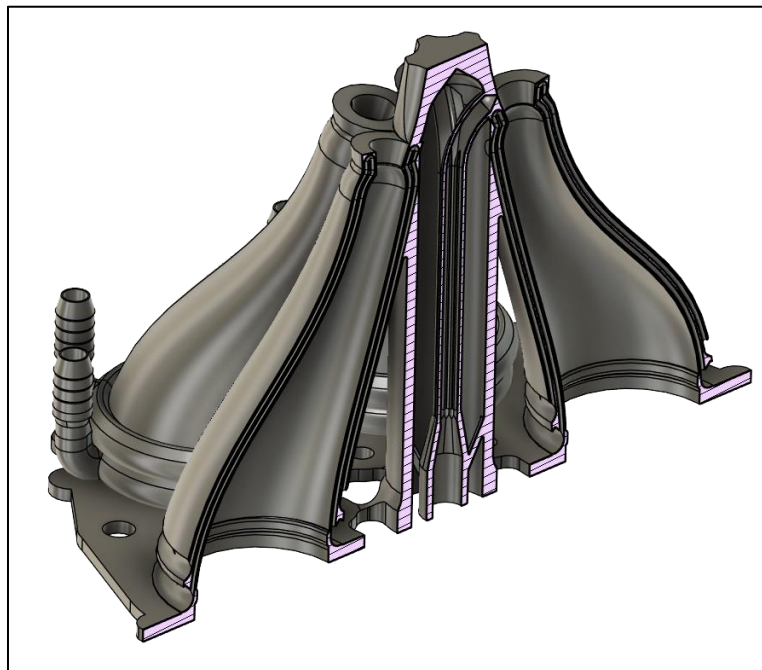


Figure 42:Aerospike and Nozzle Structure (Sliced View)



Figure 43: Solid Motor Casing Structure

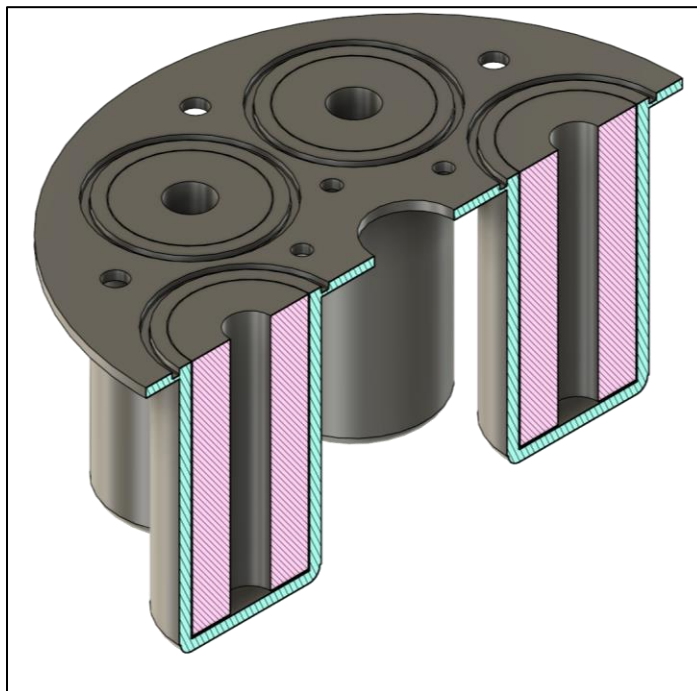


Figure 44: Cross-section Solid Motor Casing Structure (with Propellant Grain)



Figure 45: Fully Assembled Model Aerospike Structure

Test Stand and Integration

The custom-built test stand replicates a Stewart Platform and serves as the structural foundation for the aerospike engine, securing it against thrust forces up to 1.5 kN. The stand incorporates two steel plates, clevis brackets, spherical brackets, and load cells, ensuring accurate force measurement and stability. Two rings of M12 and M5 bolts are used to secure the model flange to the test stand for maximum structural integrity. The base is then bolted to the concrete floor at the Vaya Space test site during firings to ensure secure stabilization. The test stand was specifically designed to take measurements in 6 DOF. This is done to avoid constructing two different test stands for thrust and for LITVC.



Figure 46: Integrated Test Stand with Aerospike Design

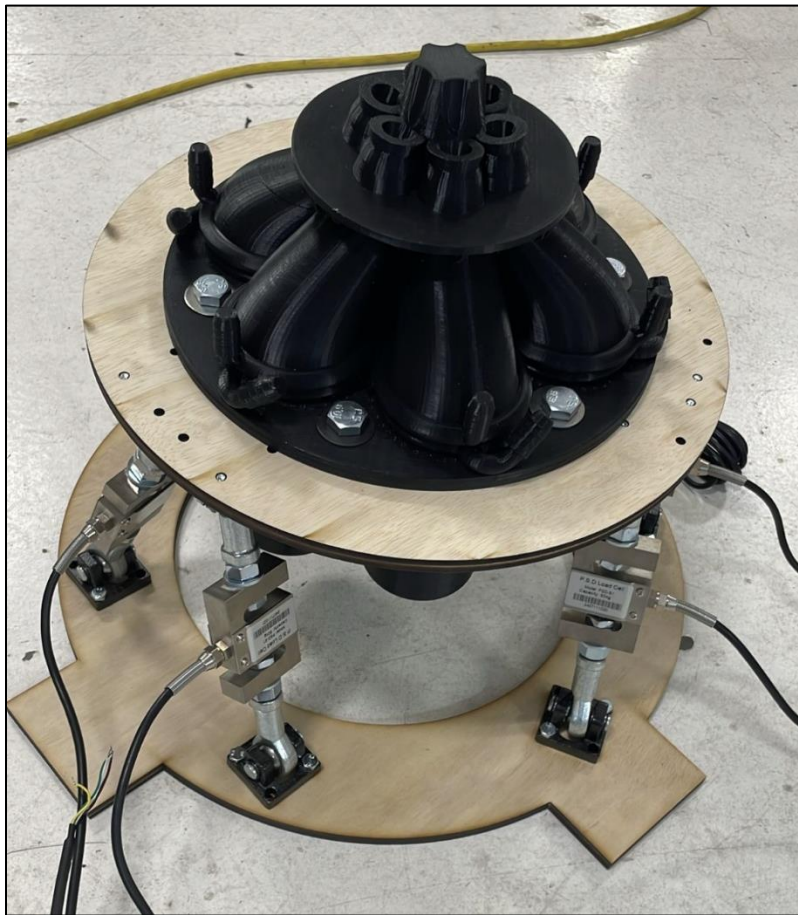


Figure 47: Fully Integrated Test Stand (Previous PLA Model & Wooden Plates)

Fluid Connection Techniques

The LITVC system integrates external tubing to manage and regulate fluid flow through the hollow central spine of the aerospike. Proper sealing mechanisms, including O-rings at each motor casing groove, prevent pressure loss. Fluid control is monitored through Vaya Space's external systems, ensuring steady and controlled flow for vectoring operations. The cooling system incorporates dedicated piping and supply equipment to maintain operational integrity during combustion testing.

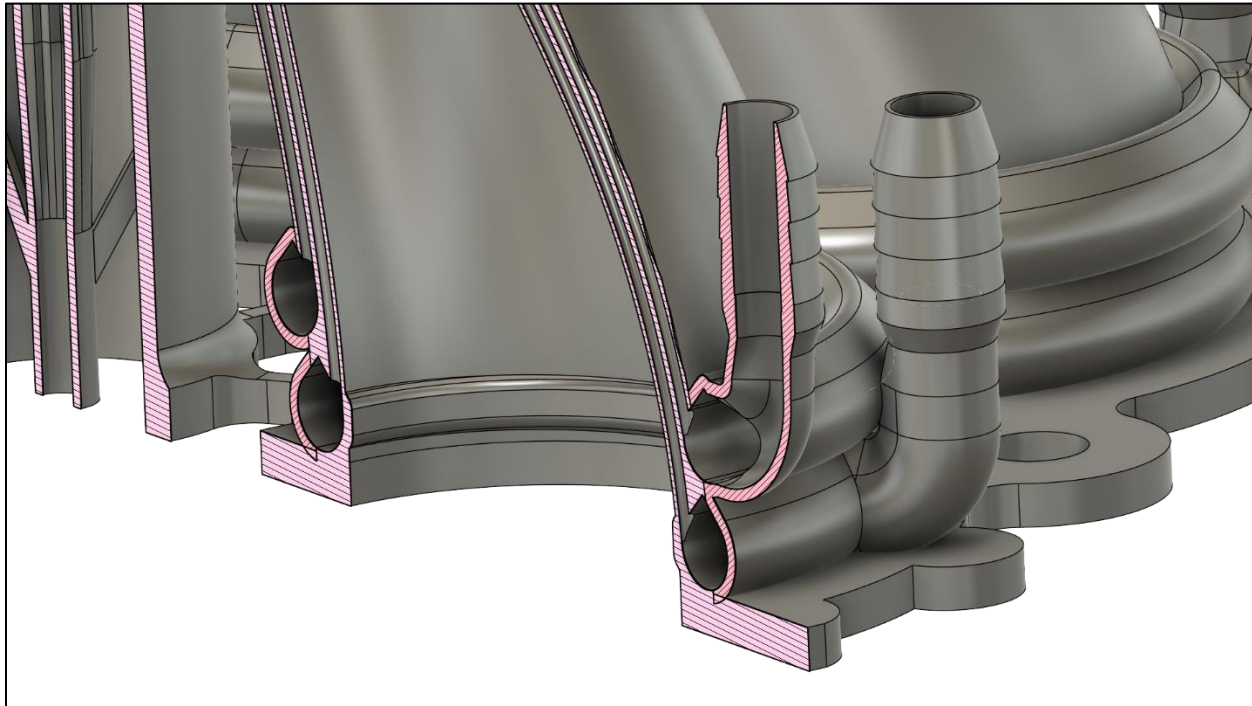


Figure 48: Cut-out view of Cooling Channels Piping System

Propellant Integration and Ignition

The aerospike engine incorporates six 75mm solid rocket motors, securely mounted via a specialized flange design. The sim results of the 75mm Classic™ grain with the design throat diameter of 12.7 mm gives a burn duration of 4.61 seconds, satisfying PROP.01. Integration ensures precise alignment for stable thrust and controlled combustion. E-matches serve as the ignition mechanism, triggering simultaneous ignition across all motors to maintain uniform thrust. Electrical connections from the control interface enable synchronized activation, monitored through high-speed imaging and live sensor feedback.

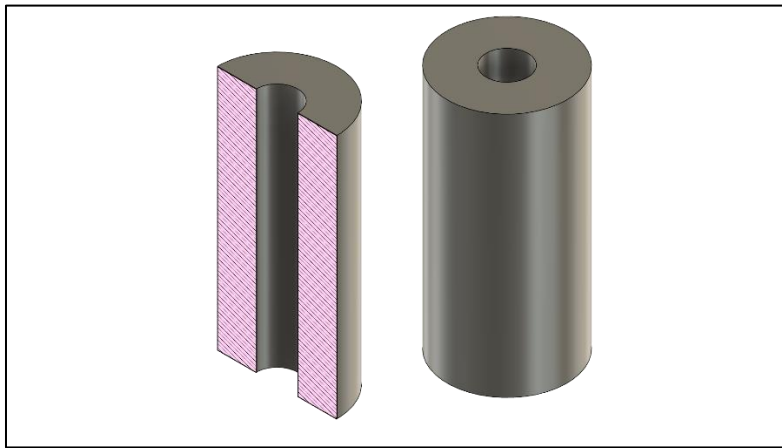


Figure 49: Propellant Grain Model

Data Acquisition and Sensor Installation

A robust Data Acquisition (DAQ) system facilitates real-time monitoring of thrust, pressure, and structural response. S-beam load cells and pressure transducers relay data to an external processing system powered by amplifiers and control electronics. The DAQ system is designed to interface seamlessly with Python-based analysis tools, allowing for post-test validation against predictive simulation models. Takes raw output from the Arduino and automatically calculates the total forces and moments applied to the Stewart platform structure. High-speed cameras capture plume behavior and LITVC effectiveness, providing critical visual data for maneuverability assessments.



Figure 50: Early Electronic Amplifier or DAQ System

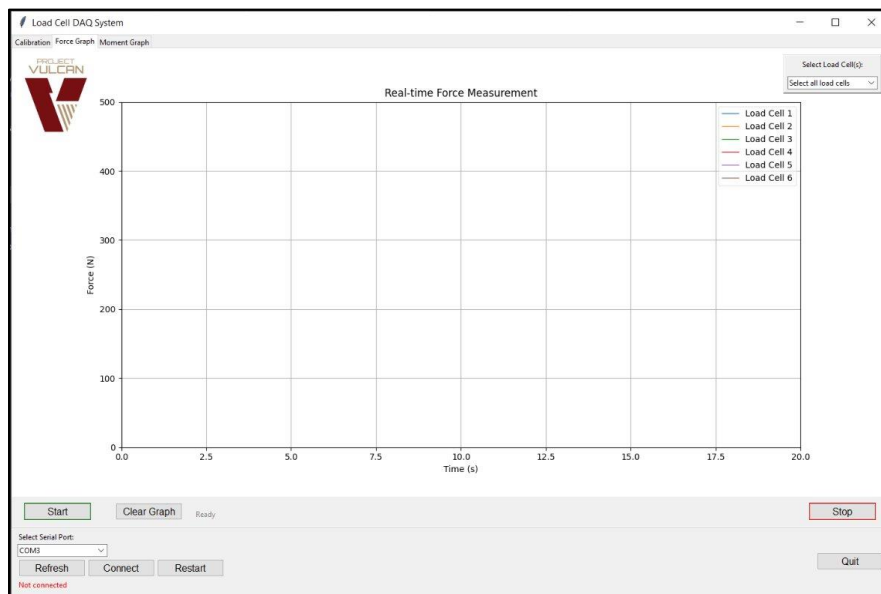


Figure 51: DAQ Interface

5.4 Systems Architecture (Hartlieb, Bedelbaev, Moore)

The system architecture for the Vulcan project can be explained using the provided details, refined by the associated requirements, testing protocols, and fabrication phases. The architecture comprises four main columns—Structures, Mechanisms, Control Systems, and Propellant—each addressing critical subsystems and their role in the aerospike engine's operation and testing. Here's how each column and its elements are connected to the project goals

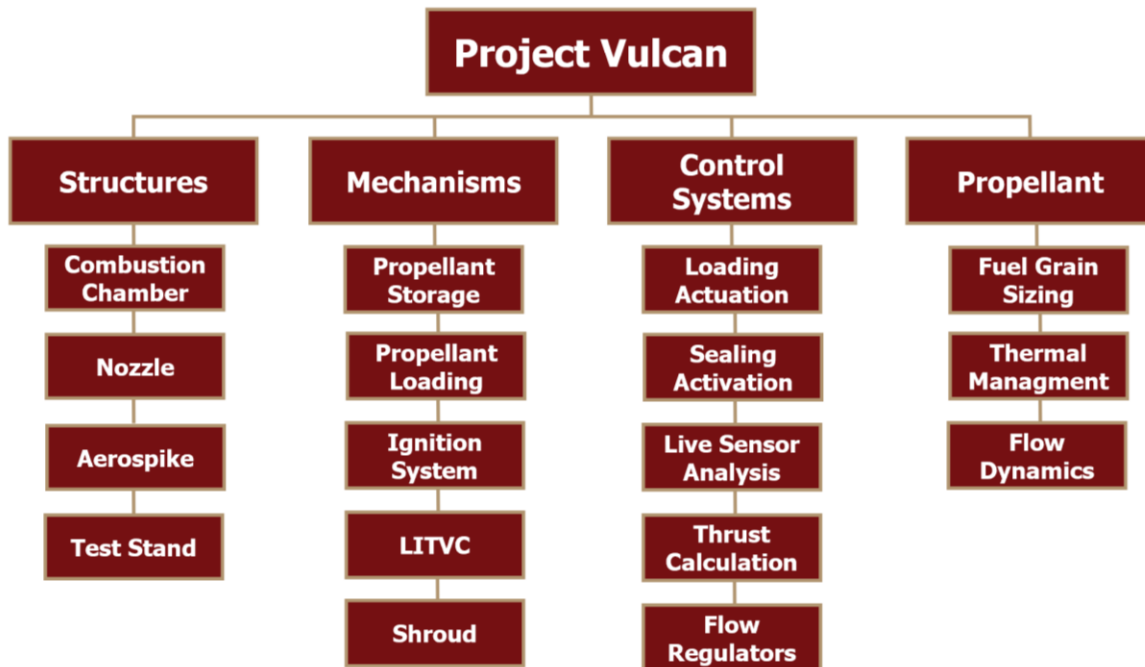


Figure 52: Project Vulcan System Architecture

The structures column provides the physical framework and thermal resilience required for high-stress, high-temperature testing of the aerospike engine. Each structural component must withstand the extreme conditions produced by solid propellant combustion.

- Combustion Chamber: Houses the propellant burn and contains extreme pressures and temperatures. Design validation includes thermal analysis to ensure the chamber withstands cycles up to 2,888 [K] and maintains integrity during solid propellant burns (STRUCT.01).

- Converge-Diverge Nozzle: Directs exhaust gases to generate thrust. Temperature generated from the motors enters the combustion chamber section of the nozzle, then is converged to a smaller diameter before it diverges or expands outward into the ambient air. The exhaust plume also exits out into the surface of the aerospike channels as well as the plume-plume interaction between nozzles.
- Radial Aerospike: The centerpiece of the design, providing consistent thrust efficiency across altitudes. Additive manufacturing techniques, such as DED or LPBF, enable its complex geometry. Post-processing ensures smooth surfaces to minimize turbulence (STRUCT.03). The aerospike contour itself matches the diverging section contour as if the nozzle was continued, yet only the aerospike surface is used as the extended diverging section. Its integration with the aerospike leverages altitude compensation capabilities, crucial for the aerospike's efficiency across varying pressure conditions.
- Test Stand: A custom-built structure capable of accommodating the aerospike, sensors, and thrust loads up to 1.5 [kN] (STRUCT.02, STRUCT.04). The stand ensures secure mounting and data collection compatibility.

Mechanisms enable the functional operation of the aerospike engine, facilitating ignition, propellant management, and advanced experiments.

- Propellant Storage: Safely houses solid propellant grains (e.g., RCS 75mm Classic™). Designed for compatibility with the propulsion subsystem requirements and ease of integration during test operations.
- Propellant Loading: Ensures controlled transfer of propellant into the combustion chamber, emphasizing repeatability and safety.
- Ignition System: Activates the propellant burn to achieve consistent test conditions, initiating supersonic exhaust flow through the CD nozzles for at least 3 seconds (PROP.01).

- LITVC: Introduces liquid injection thrust vector control, enabling precise adjustments to thrust direction. Testing includes high-speed imaging to evaluate its maneuverability improvements.
- Shroud: Simulates reduced ambient pressures for altitude testing. It works in tandem with sensors to validate the aerospike's altitude-compensating performance (SYS.04).

The following control systems manage the aerospike's operation, ensuring precision, safety, and robust data collection during tests.

- Loading Actuation: Allows a seamless and efficient process for installing and securing the 75mm Propellant Grain into the individual motor casings.
- Sealing Activation: Ensures the combustion chamber remains sealed to handle high pressures and prevent gas leaks during tests.
- Live Sensor Analysis: Monitors thrust, pressure, and thermal loads in real time, facilitating immediate adjustments or shutdowns if anomalies occur (HMI).
- Thrust Calculation: Processes sensor data to calculate thrust during supersonic exhaust flow, verifying compliance with PROP.01 and PROP.02.
- Flow Regulators: Controls the flow dynamics within the LITVC section to maintain controllable flow rates and pressure, preventing unexpected surges or drops in liquid injection.

The propellant subsystem focuses on optimizing the solid propellant's performance and ensuring compatibility with the aerospike engine's design.

- Fuel Grain Sizing: Determines the solid propellant's dimensions to achieve desired burn duration (3 seconds for steady-state conditions) and chamber pressure stability (PROP.01).
- Thermal Management: Ensures that structural components can handle thermal stresses from combustion. This involves selecting materials that resist thermal fatigue and maintaining proper cooling or heat dispersion.



- Flow Dynamics: Simulates and validates the exhaust's supersonic flow properties, ensuring smooth interaction with the aerospike nozzle and optimal altitude compensation.

6 TECHNICAL APPROACH: SUBSYSTEM REQUIREMENTS AND DESIGN

6.1 Safety Subsystem Requirements (Smith)

Table 2: Safety Subsystem Requirements

Parent	Req. #	Requirement	Rationale	Verification Method	Verification Strategy	Supporting Page #	Status
SYS.02	SAF.01	The team shall meet all the safety requirements for Vaya Space and Florida Tech's Environmental, Health, and Safety Department (EHSD), the Cocoa Fire Department, and the City of Cocoa regarding safety training, PPE, hazardous material handling, and hot firing.	Required per Florida Tech EHSD and Vaya Space's safety procedures.	Inspection	Inspection of safety procedures and plans to verify that the requirements presented by Florida Tech EHSD and Vaya Space are being followed.	69, 167, 169, 170, 171, 172, 174, and 175.	Fully Compliant.
SYS.02	SAF.02	The system shall be constructed with a safety factor of 1.5.	The structural integrity under high-pressure and thermal loads associated with solid propellant combustion, a safety factor of 1.5 is applied.	Inspection, Test, Analysis	Demonstrate the system's capability to transmit accurate thrust data to the ground station during engine operations.	69, 86, 127, 128, 167, 169, 170, and 174.	Fully Compliant
SYS.02	SAF.03	The system shall be tested in a safe operating zone at Vaya Space.	To prevent potential injuries or harm to any personal or surrounding environment.	Inspection	All personnel shall wear welding masks when directly viewing the test or remain in Vaya's control room.	69, 167, 172, and 174.	Fully Compliant.
SYS.02	SAF.04	The system shall include immediate containment protocols, including the availability of appropriate fire suppression equipment, to manage potential hazards during ignition.	Ensures rapid response to anomalies, providing containment measures to limit risk if an unexpected issue arises during burn.	Procedure Test	Verify the availability and readiness of fire suppression equipment and protocols through simulated emergency drills.	70, 167, 171, 174, and 175.	Fully Compliant.
SYS.02	SAF.05	The safety system shall comply with regulatory standards and use the required personal protection equipment (PPE).	To prevent potential injuries or harm to any person as well as adherence to safety expectations.	Inspection	Documentation that specifies the required PPE that needs to be used and defined safety standards.	70, 167, 169, 170, 171, 172, 174, and 175.	Fully Compliant.

Explanations of Safety Subsystem Requirements:

SAF.01 - The team shall meet all the safety requirements for Vaya Space and Florida Tech's Environmental, Health, and Safety Department (EHSD) regarding safety training, PPE, hazardous material handling, and hot firing.

This is required by Florida Tech's EHSD as well as Vaya Space to ensure that the established safety protocols are being followed. Having this requirement guarantees that all personnel involved are adequately trained in safety practices and are familiar with the procedures necessary to maintain a secure working environment. By adhering to these protocols, the risks are minimized, thereby preventing potential injuries to individuals, damage to equipment, or harm to the surrounding environment. It also promotes a culture of accountability and diligence, ensuring that all operations align with industry standards and regulatory compliance.

SAF.02 - The system shall be constructed with a safety factor of 1.5.

A safety factor of 1.5 is applied to ensure the structure can withstand the high pressures and extreme thermal loads produced by solid propellant combustion. This margin of safety accounts for material imperfections, unexpected stress spikes, and thermal expansion, minimizing the risk of deformation, material degradation, or catastrophic failure. Aligning with aerospace industry standards, this factor enhances structural reliability in high-stress environments. Through rigorous inspection and testing, materials and structural designs will be verified to maintain dimensional stability and withstand operational extremes. This requirement ensures that the system remains intact and performs reliably during testing and operational phases [16].

SAF.03 - The system shall be tested in a safe operating zone at Vaya Space.

Vaya Space's testing facilities provide a controlled and secure environment specifically designed for conducting tests involving solid rocket motors. These facilities are equipped with the necessary safety infrastructure and protocols to minimize risks during testing operations. By utilizing these facilities, the project benefits from the oversight and expertise of industry professionals who ensure that all test procedures are executed in accordance with established safety standards and best practices. This collaboration not only guarantees the safety of personnel and



equipment but also enhances the reliability and validity of the test results. Furthermore, conducting tests in a dedicated safe operating zone demonstrates the team's commitment to upholding the highest levels of safety and compliance throughout the project's development.

SAF.04 - The system shall include immediate containment protocols, including the availability of appropriate fire suppression equipment, to manage potential hazards during ignition.

This requirement is essential for ensuring a fast and effective response to any anomalies that may occur during ignition or operation of the solid rocket motors and fuel. Immediate containment protocols are designed to mitigate risks by addressing potential hazards such as fire, debris, or unintended system failures in real-time. By incorporating fire suppression equipment and other containment measures, the system ensures that any unexpected issues that may occur during ignition or operation are promptly controlled. This will reduce the likelihood of escalation and minimize any potential harm to personnel, equipment, and the surrounding environment. Regular maintenance and testing of containment systems further ensure their reliability and effectiveness when needed, reinforcing a robust safety framework throughout the project.

SAF.05 - The safety system shall comply with regulatory standards and use the required personal protection equipment (PPE).

This requirement emphasizes the importance of aligning with established regulatory standards and ensuring the consistent use of personal protective equipment (PPE) to maintain a safe working environment. Compliance with these standards is critical for minimizing risks of injury or harm to personnel. The use of appropriate PPE, such as helmets, gloves, safety glasses, and fire-resistant clothing, acts as an essential barrier against potential hazards, including physical, chemical, and thermal risks. Moreover, adherence to these protocols ensures that the project meets industry expectations, protects personnel, and reduces liability. Regular training and test procedures will help reinforce the proper use of PPE and compliance with safety standards, further supporting a culture of safety and accountability throughout the project's execution.

6.2 Propulsion Requirements and Technical Approach

6.2.1 Propulsion Subsystem Requirements (Valliere)

The propulsion subsystem of Project Vulcan is critical for achieving controlled, repeatable, and precise engine test results. The requirements ensure that the aerospike engine, LITVC system, and custom-built test stand are appropriately validated to handle the conditions created by the RCS 75mm Classic™ Propellant Grain. These requirements support the project's goals of advancing high-performance aerospike and thrust vectoring technology through rigorous testing and data acquisition. Table 4 below outlines the propulsion subsystem requirements, including the parent requirements, rationale, and verification methods.

Table 4: Propulsion Subsystem Requirements

Parent	Requirement #	Requirement	Rationale	Verification Method	Verification Strategy	Supporting Page #	Status
SYS.01	PROP.01	The propulsion system shall be capable of supporting a burn duration of at least 3 seconds.	A continuous 3 second test duration provides sufficient time to observe and analyze steady-state plume interaction with the aerospike geometry, ensuring the system can withstand the propulsion environment.	Test	Verify that chamber pressure remains stable throughout the test, ensuring steady exhaust flow for the entire duration.	166, 172, 174, 176, 176, 190, 225, 242	Fully Compliant.
SYS.03	PROP.02	The LITVC system shall produce a thrust deflection of at least 3 degrees.	A lateral thrust deflection of 3 degrees provides directional control precision typical in aerospace applications without significantly impacting overall propulsion.	Test	Conduct controlled burns with the LITVC system to measure thrust vectoring effectiveness.	150, 166, 170, 174, 187, 225, 241	Fully Compliant.
SYS.04	PROP.03	The altitude-simulating shroud shall be capable of simulating atmospheric pressure up to 25 km altitude.	Simulating up to 25 km altitude pressures is critical for evaluating the aerospike's performance in near-vacuum conditions, supporting efficiency studies at high altitudes.	Test	Measure static pressure during operation within the shroud, ensuring it matches the target pressure to replicate high-altitude conditions.	86, 166, 176, 242, 269	Fully Compliant.



Explanations of Propulsion Requirements

PROP.01 - Continuous 3-Second Test Duration

The propulsion system's ability to sustain a continuous 3-second burn is critical for observing steady-state conditions, enabling an in-depth analysis of exhaust interactions with the aerospike nozzle. This duration ensures that transient effects have settled, allowing for meaningful data collection on plume behavior and potential thermal stresses on the aerospike structure. Testing will confirm that chamber pressure and exhaust flow remain stable, signifying the propulsion system's resilience under prolonged operational stresses.

PROP.02 - LITVC System Lateral Thrust Capability

The LITVC system must demonstrate the ability to generate lateral thrust equivalent to a 3-degree thrust vector deflection. This minimal yet precise thrust vectoring ensures the aerospike's maneuverability without engine throttling or gimbaling. The team chose the value of 3-degrees of deflection because it was an obtainable and measurable quantity for the proof of concept. In a flight ready-configuration, the industry partner Vaya Aerospace would utilize a deflection range of 8-9 degrees and NASA's RS-25 engines are capable of a gimbaled plus or minus 10.5 degrees of thrust vectoring [28]. Testing the LITVC will involve controlled burns to assess lateral force generation, validating that thrust vector adjustments are smooth, predictable, and effective for directional control. This requirement cannot be validated via analysis and will only be verified post-testing.

PROP.03 - Altitude Simulation up to 25 km Pressure

To simulate near-vacuum conditions encountered up to 25 km altitude, the altitude-simulating shroud is designed to reduce ambient pressure around the nozzle during tests to a desired pressure. The shroud does this by preventing the atmosphere from interacting with the flow while the exhaust gas entrains and removes air within the shroud, thus creating a lower ambient pressure and simulating a higher atmosphere. This simulation allows for the examination of exhaust flow patterns and aerospike adaptability at high altitudes, offering insights into efficiency gains. The shroud is designed for a target altitude by treating it as the exit area of the nozzle in the

isentropic flow relation. Tests will verify that the shroud maintains the target low pressure to accurately replicate these conditions [24].

Equation 1: Equation to Determine Shroud Area Using Isentropic Relations [24]

$$\frac{A_d}{A_t} = \frac{1}{M_1} \left[\frac{2}{\gamma + 1} \left(1 + \frac{\gamma - 1}{2} M_1^2 \right) \right]^{(\gamma+1)/2(\gamma-1)}$$

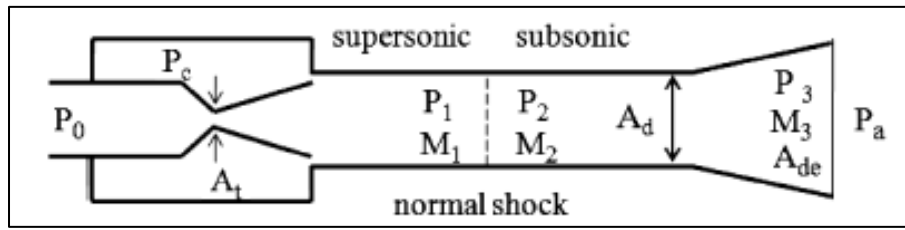


Figure 53: Picture Describing Shroud Set Up [24]

6.2.2 Propulsion Design (Valliere)

The fuel chosen for the propulsion system is the 75mm Classic™ Propellant Grain from Rocket Motor Components. This fuel has satisfactory burn characteristics such that for the chosen throat diameter of 12.7 [mm], the chamber pressure is high enough for a pronounced nozzle geometry, low enough that structural integrity is not the largest concern, and the burn time is high enough to meet the requirement for burn duration. The throat diameter of 12.7 [mm] was chosen to ensure the system is not so large that the peripheral and material requirements cause costs to shoot up, but not so small that the geometry's smallest feature size is smaller than the printer's resolution.



Propellant Data

Part Number:	8441C
Propellant Type:	AeroTech Classic™ (84% solids version)
Visual Effect:	Yellow-orange flame, no smoke
% Solids:	84
Density:	0.0595 lb/in ³
I_{sp} at 1000/14.7 PSI:	248.2 seconds
Burn Rate Exponent:	0.323
Burn Rate Coefficient:	0.0304

Thermodynamic Properties at 1000/14.7 PSI:

ENTHALPY = -46.75623 DENSITY = 1.652
 CSTAR = 5048.21

	CHAMBER	THR(SHIFT)	EXH(SHIFT)
PRESSURE (PSIA)	1000.000	565.092	14.700
EPSILON	.000	1.000	8.355
ISP	.000	106.210	248.188
ISP (VACUUM)	.000	194.877	267.458
TEMPERATURE(K)	2887.981	2639.329	1345.096
MOLECULAR WEIGHT	24.145	24.231	24.316
MOLES GAS/100G	4.142	4.127	4.113
CF	.000	.677	1.582
PEAE/M (SECONDS)	.000	88.667	19.270
GAMMA	1.225	1.227	1.261
HEAT CAP (CAL)	44.843	44.342	39.521
ENTROPY (CAL)	246.320	246.318	246.319
ENTHALPY (KCAL)	-46.756	-59.715	-117.518
DENSITY (G/CC)	6.93284E-03	4.30207E-03	2.20363E-04
ITERATIONS	6	3	4

Information represents typical values and is believed to be correct, however no warranty is expressed or implied as to the accuracy of any of the information contained herein nor is any warranty implied as to the fitness of the device described herein for any particular application. This document is not to be used for design or specification purposes. This document is uncontrolled and all information on this document is subject to change without notice or obligation.

Figure 54: 75mm Classic™ Propellant Grain Data Sheet (RCS, 2024)

The propellant data sheet is organized so users can easily input the fuel characterization values into BurnSim, a solid rocket steady-state internal ballistics simulation software, which can predict burn behavior like duration, chamber pressure, and thrust. The resulting burn behavior for one of these grains in each of the six nozzles with a 12.7 [mm] throat diameter is displayed in the following plot.

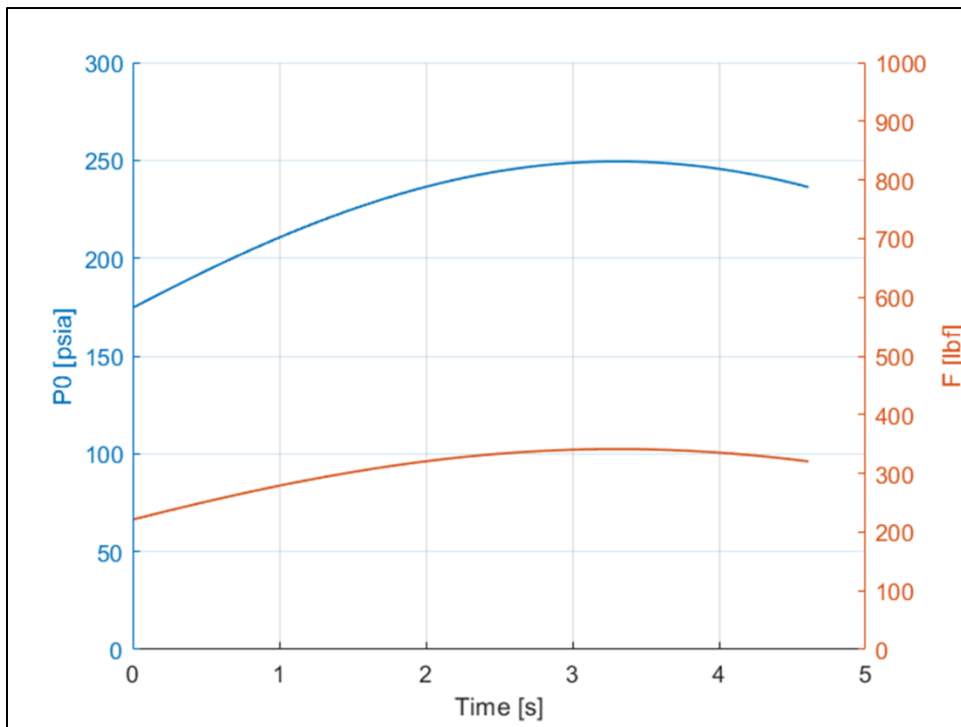


Figure 55: Pressure and Thrust Curves from BurnSim Analysis

The predicted burn duration for this grain at the selected throat size is 4.61 seconds. The maximum chamber pressure for this burn is 249.4 [psi] and the maximum predicted thrust for all six nozzles is 341.4 [lbf]. The predicted thrust is calculated from a simple area ratio assigned by the user, which in this case was the area ratio for the bell nozzle portion. Therefore, the predicted thrust only applies to the bell nozzles and does not consider the addition of thrust contributed by the spike. Testing data should show how significant the addition of a spike contour is to this propulsion system through comparisons of measured thrust data and the theoretical thrust prediction. In choosing a design chamber pressure for the nozzle it would make sense to pick the

lowest chamber pressure so that mass flow is always choked, however, 200 [psi] was chosen to lessen the wasteful effects of under-expansion from the max pressure point.

The design of the nozzle is an axisymmetric minimum length nozzle contour designed for a 1379000 [Pa] (200 [psi]) chamber pressure and a 101325 [Pa] exit pressure. The nozzle contour profile was generated using the axisymmetric MoC MATLAB code written by Ludovico Fossà [9].

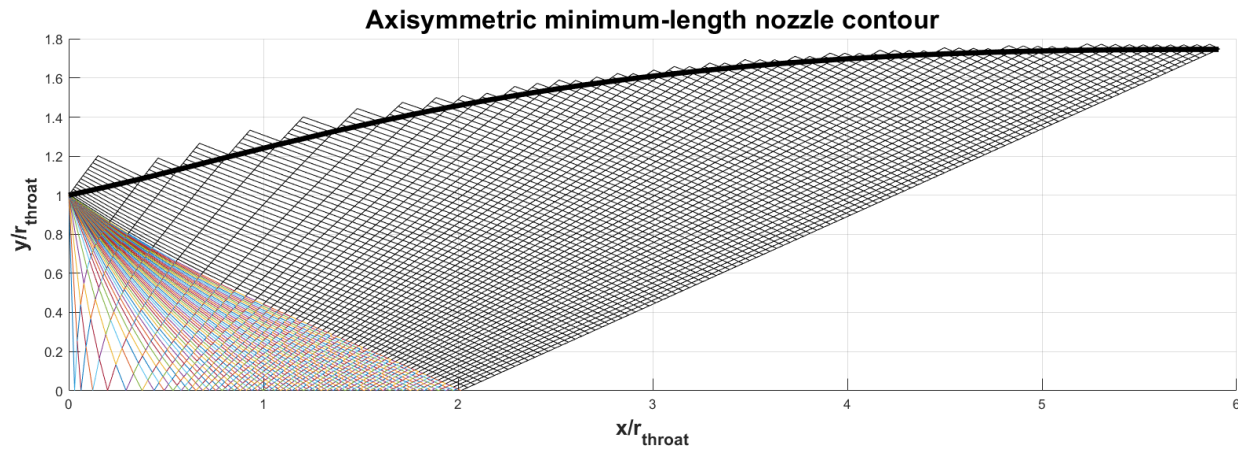


Figure 56: MATLAB Generated Axisymmetric MoC Contour

The first 25% of points in the wall coordinate array make up the contour of the bell nozzle and the rest of the contour makes up the spike.

For the initial design, the flow delivery system for the nozzles used the assumption that compressed air would still be viable to provide ample thrust to measure deflection from engaging the LITVC. The design thrust that dictated the dimensions of the nozzle was set at 400 [N], based on the total mass of air available in a tank, to allow for a measurable change in thrust from deflection. As mentioned in section 5.1, the nozzle contour design for a 2D planar case was created using MATLAB, which exports into Excel as a list of points that can be imported into CAD, where the first 25% of points are used for the bell nozzle and the rest of the contour is implemented as the spike contour. The nozzle design works as expected during a 2D simulation in Ansys Fluent. However, as the simulations became more intensive, the CFD analysis focused on a 3D simulation to visualize the interaction of the flow with the spike. When adding the spike contour to the fluid

domain, there was no interaction between the end of the bell nozzle exit area and the contour of the spike. It was here that the expected behavior breaks down due to the difference between 2D planar and 3D axisymmetric flow expansion.

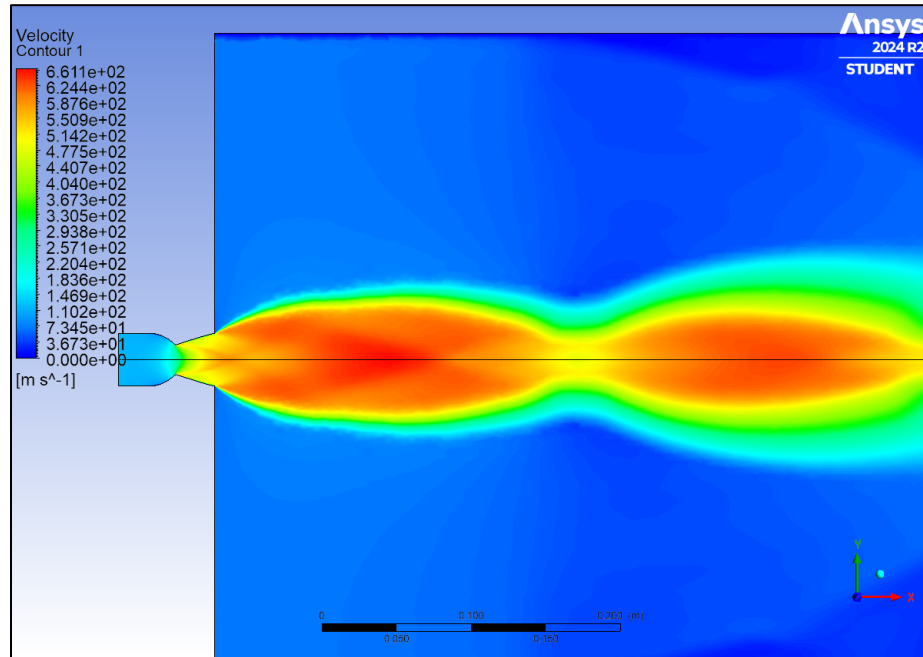


Figure 57: Velocity Contour in a 2D Planar Case

In Figure 57 above, as boundary conditions, the pressure-inlet is at 1,379 [kPa] of total pressure and a total temperature of 300 [K]. The free stream is pressure-far-field at 101.325 [kPa], 0.05 Mach, and 300 [K]. Lastly, the outlet is a pressure-outlet at 95 [kPa] and 300 [K]. These conditions are set to mimic sea-level conditions. In this case, the fluid domain was a 2D plane and was set up as a planar case in Ansys Fluent. From Figure 57, the result shows that the nozzle is under-expanded, which is what is expected, since there is no spike contour to make it ideally-expanded. As mentioned, when attempting the first test with a 3D fluid domain that contained the spike contour there was no flow interaction. At first, it was assumed this was an issue with the capabilities of the student version of Ansys, which only allows a mesh of the model with a maximum amount of one million elements, but now a check was needed to test if the nozzle would still behave the same in a 3D space.

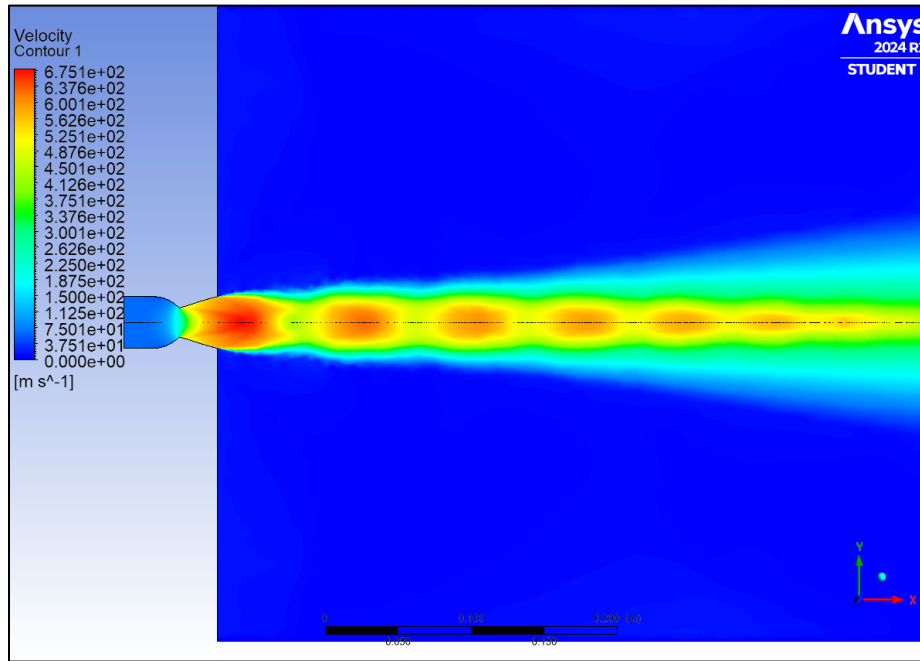


Figure 58: Velocity Contour in a 3D Axisymmetric Case

In Figure 58, the boundary conditions are the same as those set in Figure 57, and the only difference now is that this simulates a 3D axisymmetric rather than a 2D planar case. Here, the velocity contour is a 2D slice from the 3D fluid domain. In this case, the nozzle is slightly over-expanded, so there is no interaction when the spike is added to the 3D fluid domain. This discovery highlighted a key issue with the nozzle contour that needed to be fixed using axisymmetric MoC, which was later found in an online MATLAB library [9]. Although the nozzle design assumed that the fluid would be cold compressed air, the change in using the 3D MoC would still be incorporated into the main design involving the 75mm Classic Propellant Grain combustion. This is because the same issue of over-expansion would have arisen if the team had continued to use 2D MoC, which is why it applies to the new flow delivery. As a result of this change, the nozzle expansion behaves as desired in the following analysis.

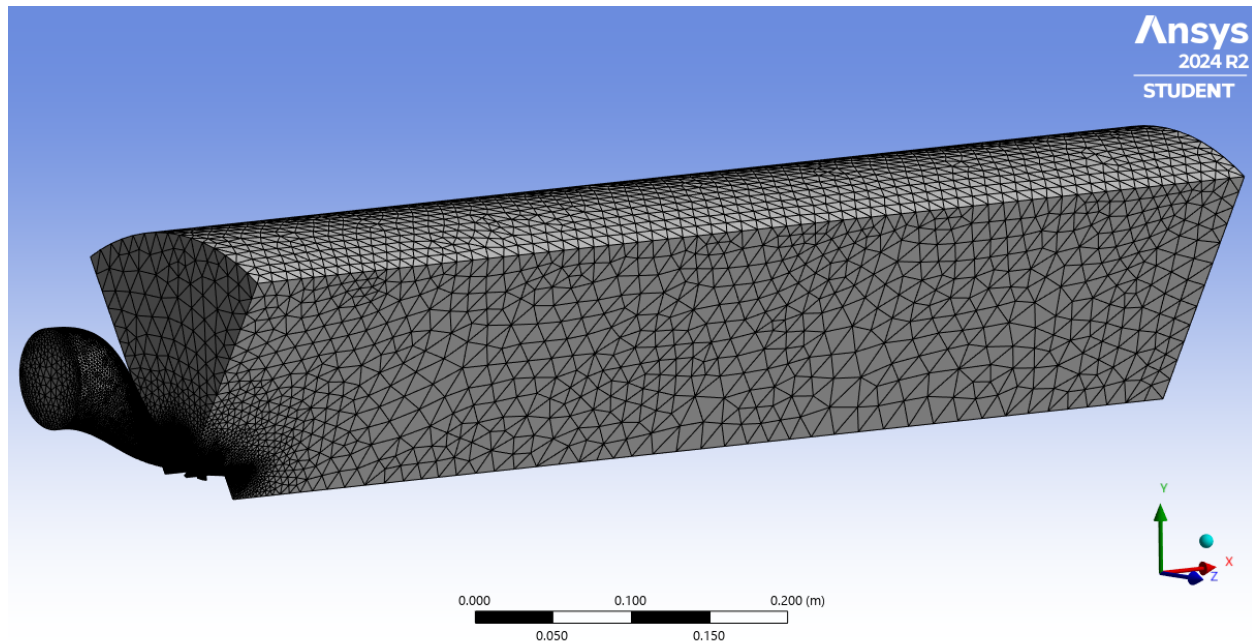


Figure 59: 1/6 Slice of Entire Fluid Domain

Using what was applied before but for the relevant solid propellant design, a 3D fluid domain was created using the new geometry for the fluid analysis shown in Figure 59. Figure 59 is the slice of the model used for the mesh. This refined mesh focuses on the areas close to the nozzle and spike geometry to capture flow behavior close to the walls. Additionally, the benefit of slicing the model is that the amount of mesh elements per unit volume of the fluid domain can be greatly increased while staying under Fluent's student version limitation of 1,048,576 elements. Since each nozzle should behave the same due to the geometric axisymmetry of the engine, a periodic boundary condition allows Fluent to effectively simulate the entire model's fluid domain with the benefits included in post-processing. For the boundary conditions, the model needs to replicate the conditions of the exhaust based on the 75mm Propellant Grain combustion, which are shown as the following:

User defined fluid:

- Density set to ideal gas
- $c_p = 1,874.7 \text{ [J/kg}\cdot\text{K]}$
- Viscosity set to Sutherland's Law
 - **Approximation for a mixture of major exhaust constituent gases:**
 - Reference viscosity (μ_0): $1.01\text{e-}05 \text{ [Pa}\cdot\text{s]}$
 - Reference temperature (T_0): 248.71 [K]
 - Sutherland Constant (S): 118.95 [K]
 - **Later improved approximation for a more detailed composition:**
 - Reference viscosity (μ_0): $1.30\text{e-}05 \text{ [Pa}\cdot\text{s]}$
 - Reference temperature (T_0): 283.60 [K]
 - Sutherland Constant (S): 107.90 [K]
- k- ϵ Realizable viscous model
- Molecular weight = 24.145 [g/mol]

Pressure Inlet:

- $P_0 = 1,719,613 \text{ [Pa]} (249.4 \text{ [psia]})$
- $T_0 = 2,887.981 \text{ [K]}$

Pressure Far-field:

- Pressure = $101,325 \text{ [Pa]}$
- Mach = 0.05 in x-direction
- Temperature = 300 [K]

Pressure Outlet:

- Pressure = $101,325 \text{ [Pa]}$
- Temperature = 300 [K]

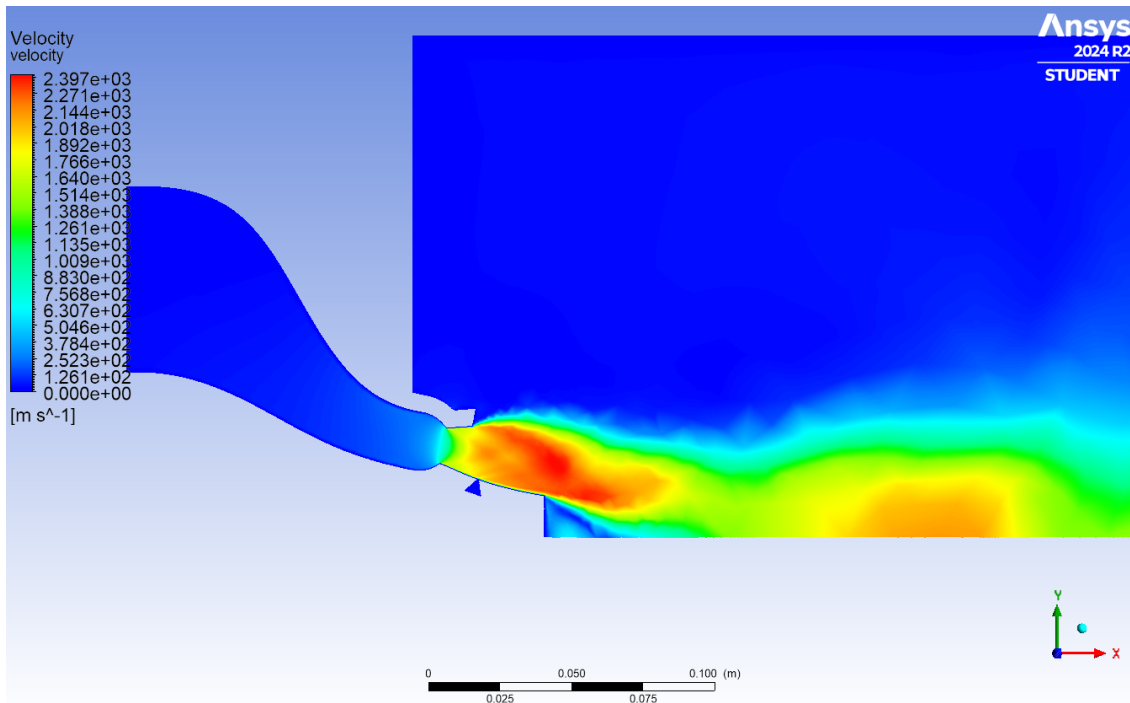


Figure 60: Velocity Contour of Exhaust Gas in XY-plane

From these boundary conditions, mesh size, and iteration count of 10,000-15,000, the simulation takes, at minimum, ten hours to run. The velocity contour in Figure 60 shows that the previous issue involving a lack of flow interaction with the spike is no longer present. The nozzle exit Mach (CFD) and spike exit Mach (CFD) are 1.951 and 2.914, respectively, compared to theory, which yields 1.944 and 2.460 (see Appendix A.2). Therefore, there is a 0.36% error for the bell nozzle, and the error increases to 18.45% for the spike. There is one main reason for this discrepancy: the predicted spike exit Mach is based on isentropic calculations assuming a full nozzle contour, whereas the only portion to have a full contour in the model is the 25% truncated bell nozzle. This is why the bell nozzle values align closely, and for the spike, this partial contour leads to under-expansion, which accounts for the higher Mach number downstream of the bell nozzle exit plane.

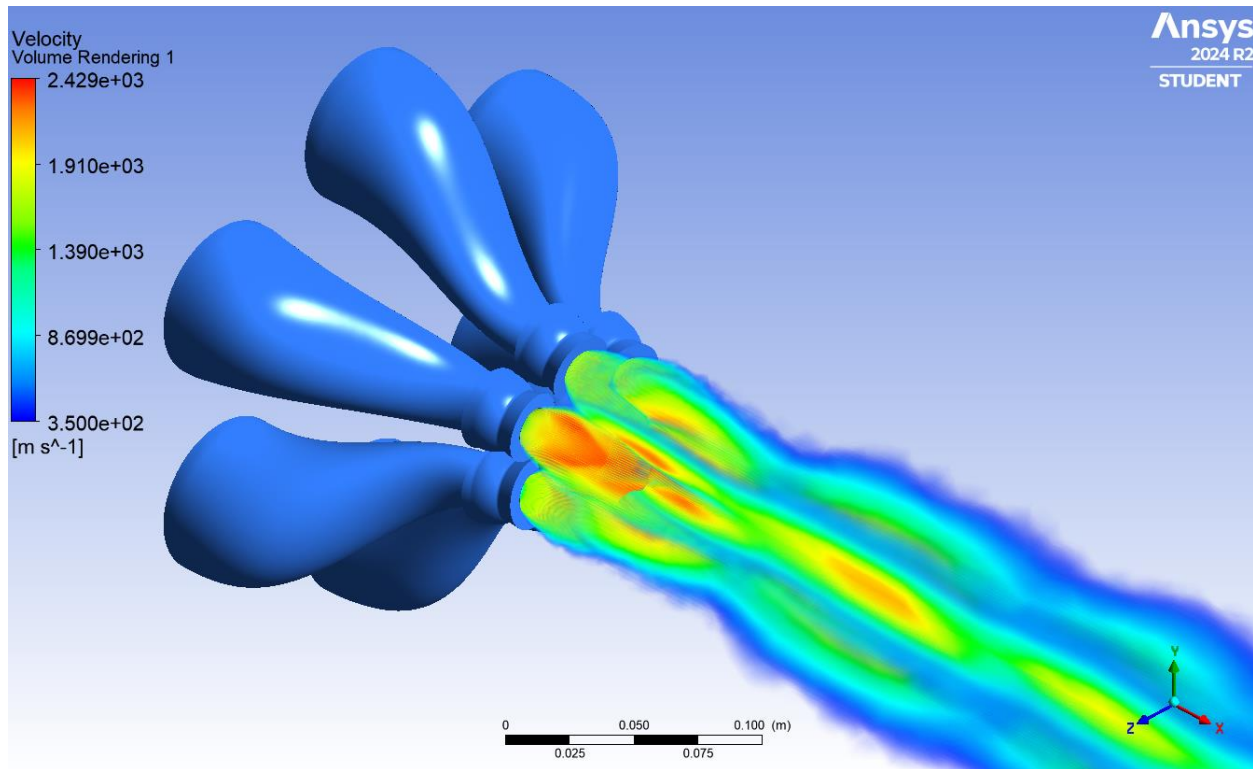


Figure 61: 3D Volume Rendering of Exhaust Plume

The power of slicing the model for meshing is illustrated perfectly in Figure 61. From post-processing, it is easy to visualize the model by creating a rendering of the 3D volume and including the other five nozzles from the periodic boundary conditions. Now, this allows for visualization of the plume interaction from all combined nozzles and gives an idea on how the model may perform in real conditions.

The only CFD results needed for the thermal and structural analyses are convection coefficients and pressures. Because Fluent does not export heat transfer quantities in an adiabatic simulation, custom field functions will have to be written into Fluent to create a contour of convection coefficient. This will need to be done for different locations because convection coefficient is a function of diameter which changes along the length of the thrust chamber. The general method used for calculating convection coefficient involves using the Dittus-Boelter equation to solve for Nusselt number and relating that to the convection coefficient.

Reynolds number:

$$Re = \frac{\rho UD}{\mu}$$

Prandtl number:

$$Pr = \frac{c_p \mu}{k}$$

Nusselt number (Dittus-Boelter equation):

$$Nu = 0.023 * Re^{0.8} * Pr^{0.3}$$

Convection coefficient:

$$h = \frac{Nu * k}{D}$$

Because Reynolds number and convection coefficient are dependent on diameter, multiple custom field functions were written for each quantity in Fluent for three locations: inlet, start of converging section, and throat. Therefore, three separate contours for convection coefficient were used to pull values for the thermal analysis.

Altitude Simulator Design (Poirier)

The desired simulated altitude chosen for this subsystem is about 10 km. This altitude was chosen because it is equivalent to a simulated 91,000 [Pa] drop in ambient pressure and is a significant measurable and achievable test case with the available time and resources, while also fulfilling the requirement for altitude simulation. To create this simulated altitude, a 152.4 [mm] (6 inch) inner diameter tube made of 316 stainless steel is being borrowed from Dr. Kirk's lab.

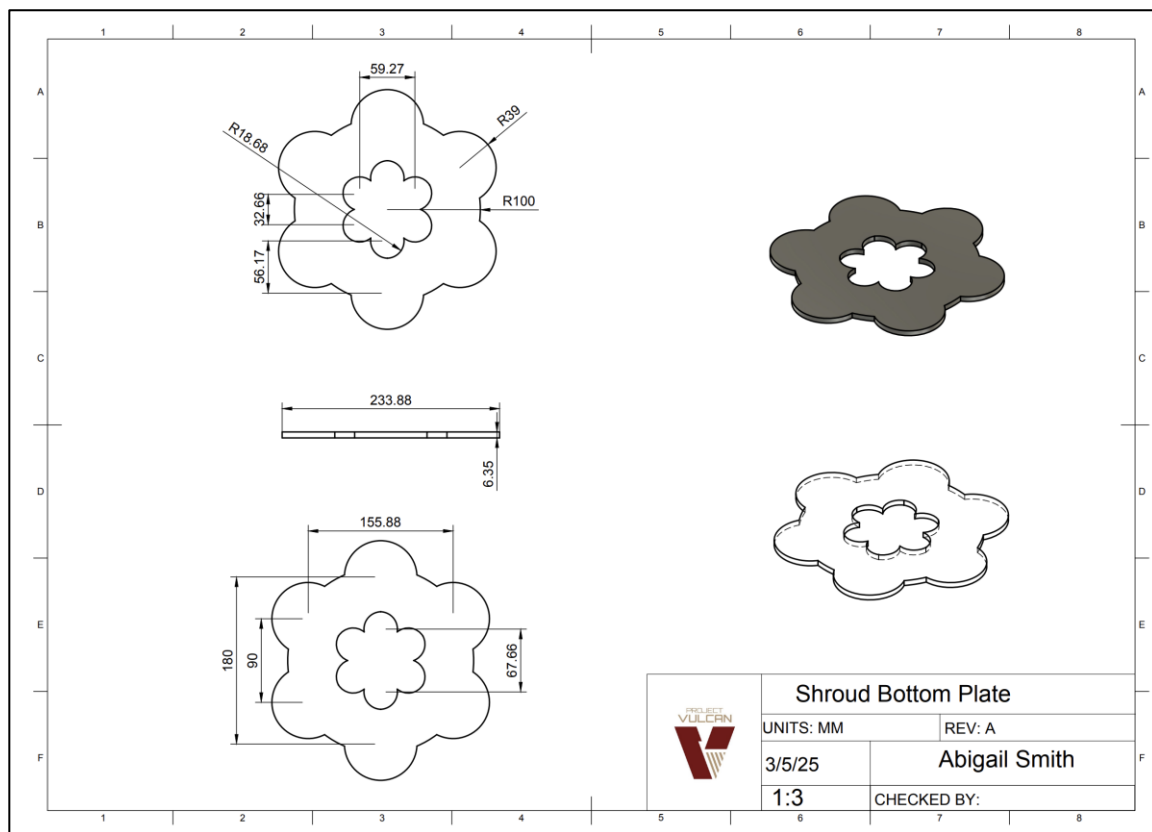


Figure 62: CAD Drawing of the Altitude Simulating Shroud's Bottom Plate

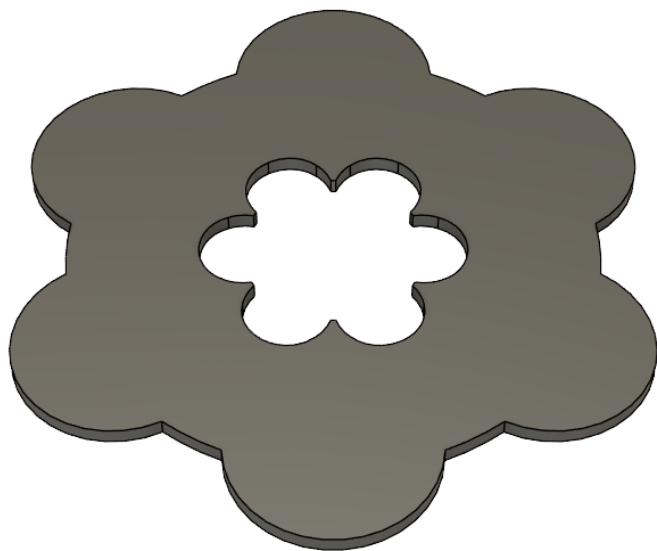


Figure 63: Altitude Simulating Shroud's Bottom Plate Mode

To prevent the open atmosphere from replacing the air removed from the shroud, the end closest to the engine is closed off with a plate and sealed to the engine itself as seen in Figure 63 above as a part by itself and below in Figure 65 as an assembly integrated with the system. This plate utilizes the material removed from the top plate of the test stand made of $\frac{1}{4}$ inch (6.35 mm) A36 steel seen in section 6.4.3 later in the document. This material is then cut using a water jet to create the geometry seen in Figure 63 that will follow the nozzles of the main system. When in the testing configuration, this plate will be sealed to the flange of the shroud using gasket material and clamps that will attach to the aluminum extrusion support structure.

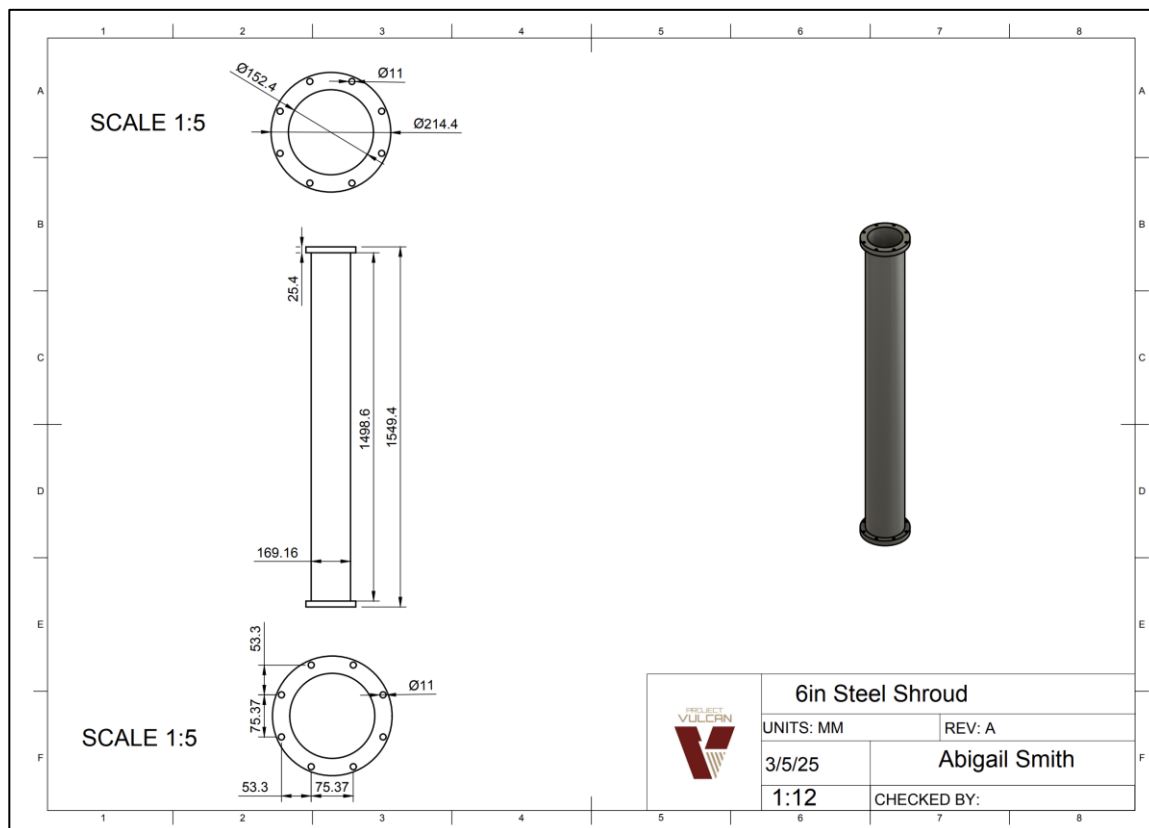


Figure 64: CAD Drawing of the Altitude Simulating Shroud Tube

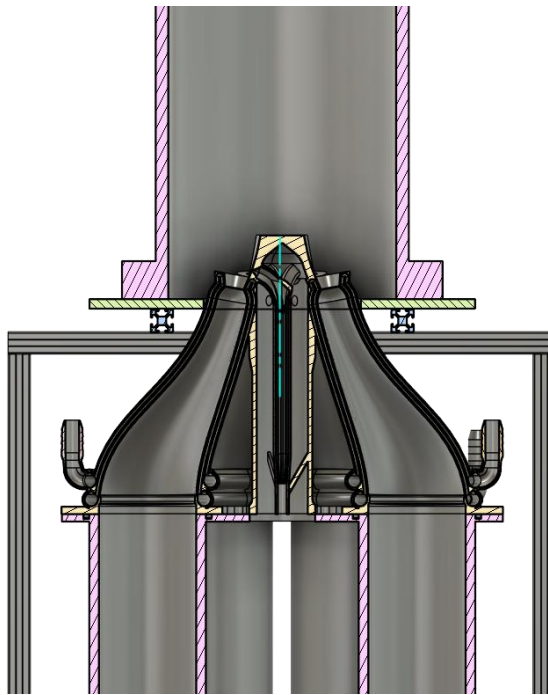


Figure 65: Cut-Away View of Altitude Simulating Shroud and Aerospike System

The additional measures to create a seal around the system's exhaust are done to mimic the conditions set in the fluent simulation done in Ansys below (Figure 66). This simulation in conjunction with MATLAB code, was used to estimate the pressures achievable with this system. Utilizing the isentropic flow equations, the MATLAB code predicted a shroud ambient pressure of 6333.93 [Pa] or 19 [km] assuming that the six nozzle throat areas were combined into a single throat area (see Appendix A.1). This value was then compared to the Fluent simulation seen below where a pressure of only about 10000 [Pa] or 16 [km] was created. This 44.9% difference is due to the assumption of isentropic conditions as well as one large central nozzle made in the MATLAB code. As a result of this, the team are using the value obtained through Ansys fluid analysis as an estimate of the altitude that can be simulated because it utilizes less assumptions and results in a more conservative estimate. This analysis fulfils PROP.03.

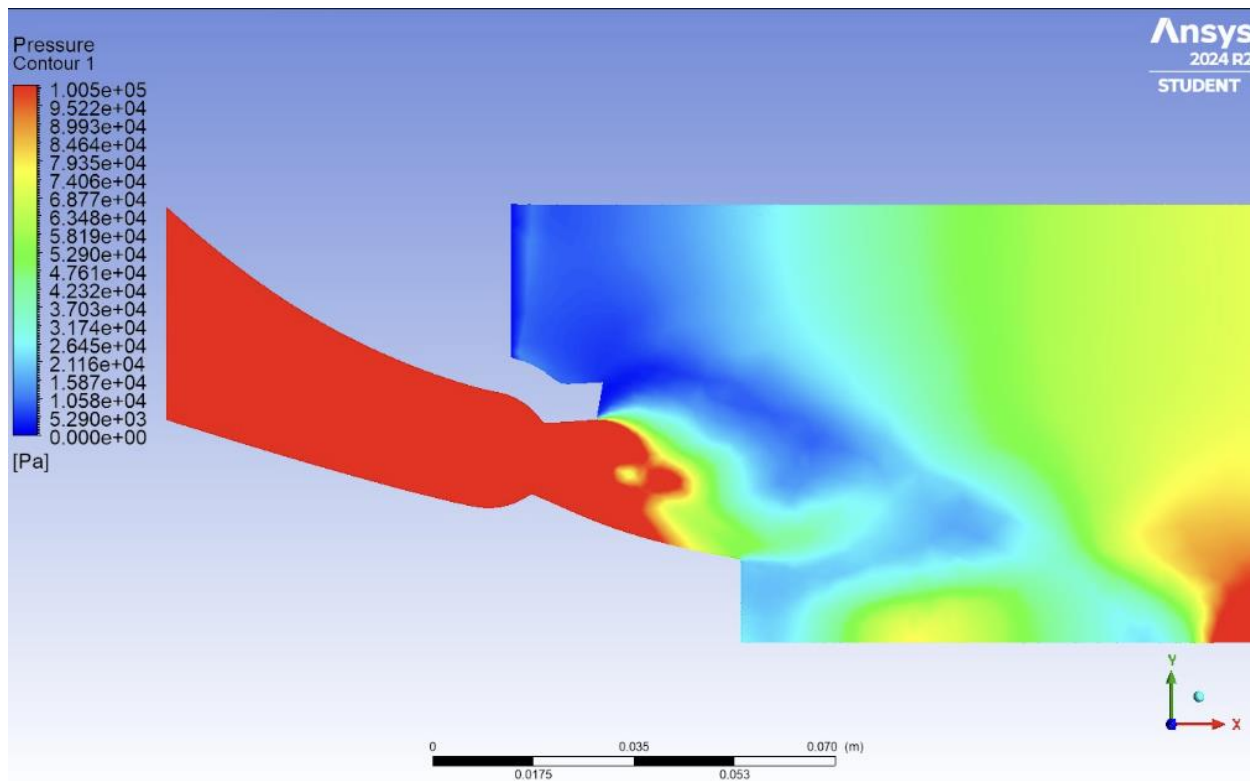


Figure 66: CFD of Altitude Simulating Shroud and 1/6th Aerospike Cutout

To ensure compliance with SAF.02, finite element analysis was also conducted on the shroud as seen in Figure 67 below. The loading case for this analysis was a pressure of -101,325 [Pa] on the internal surface with a fixed support applied to the bottom surface of the flange on the right. This loading condition simulates a complete internal vacuum to account for all possible operational conditions. The material of the shroud is 316 stainless steels with a modulus of elasticity of 193 GPa, a Poisson ratio of 0.26, and a yield strength of 240 MPa. The resulting maximum von mises stress was 1.4727 MPa using 69441 elements in Ansys. The result of this analysis was a factor of safety of 332, ensuring that this design is compliant with SAF.02.

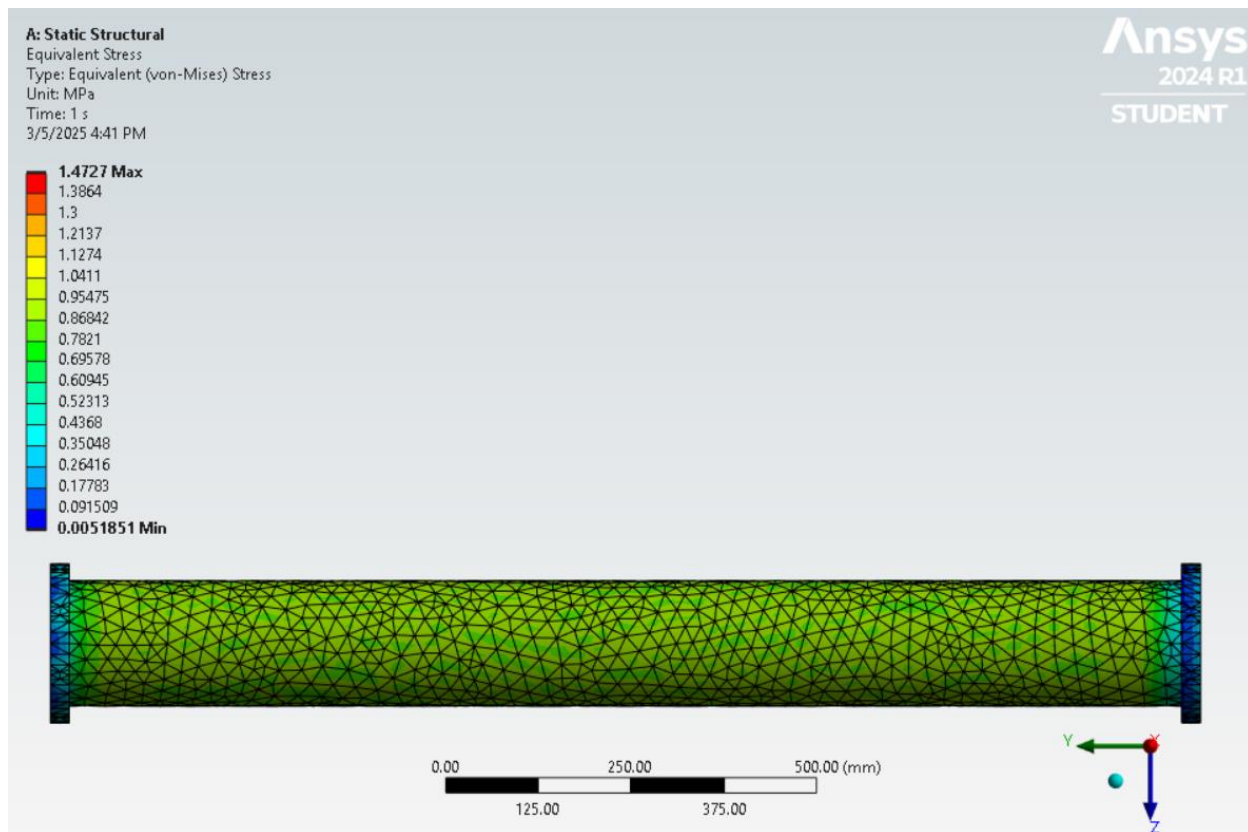


Figure 67: 316 Stainless Steel Shroud Tube

To communicate how the fully integrated system will look when constructed, a model of the system can be seen below (Figure 68). This system consists of the 316 stainless steel tube, a A36 bottom plate, aluminum extrusion, fasteners, and a pressure sensor rated for 0-200 KPa. The aluminum extrusion will act as a support structure for the shroud and will attach to the bottom plate of the shroud with L-brackets and bolts. The successful construction of this subsystem will fulfill the SYS.04 requirement for this project.



Figure 68: Altitude Simulating Shroud Fully Integrated into the Test Stand Configuration

6.2.3 Propulsion Fabrication (Zaharia)

The aerospike assembly consists of two main components, the bottom section, which houses the fuel grains, and the metal printed top section. The complex geometry of the top section makes its fabrication with traditional subtractive manufacturing difficult to achieve. This is the primary motivating factor in selecting additive manufacturing for the project as well as satisfying SYS.03 as well as STRUCT.01 through STRUCT.04. The design of the top section will be driven by the need to meet the four structural subsystem requirements. The bottom section will be manufactured using the tools and machinery available at the HSDC and its design will also be in compliance with section 6.3.1. Having the design simplified into two parts rather than a collection of parts makes the design more efficient from a structural perspective. This simplification allows for the design to be tailored to the pressures and temperatures that are



expected in the testing environment. The fabrication will be assigned to MIMO Technik, a California-based company that specializes in LPBF additive manufacturing. Their experience with printing thin-walled components is aligned with the requirements for the cooling lines in the top section. The decision to select MIMO Technik as the manufacturer was fully based upon the ability of their services to satisfy the structural system requirements.

6.3 Structures Requirements and Technical Approach

6.3.1 Structural Subsystem Requirements (Hartlieb)

The structure of the Vulcan aerospike engine prototype must be capable of withstanding the extreme loading conditions and thermal stresses generated by solid propellant combustion. This includes managing the unique operational challenges posed by solid rocket motor testing, with maximum temperatures reaching 2,888 [K] and thrust forces up to 1.5 [kN]. The structural subsystem requirements are shown below in Table 5.

Table 5: Structural Subsystem Requirements

Parent	Req. #	Requirement	Rationale	Verification Method	Verification Strategy	Supporting Page #	Status
SYS.01	STRUCT.01	Spike structure shall withstand temperature cycles from ambient to operational extremes (up to 2,888 K).	The engine must withstand repeated cycles experienced during solid propellant ignitions without material degradation.	Inspection, Analysis	Thermal analysis and visual inspection will verify material integrity across repeated cycles, preventing potential failure from temperature-induced stresses.	145, 165, 171, 173, 175, 189, 241, 242	Fully Compliant.
SYS.02	STRUCT.02	Spike to engine/thrust stand mounting points shall maintain structural integrity under maximum expected thrust loads (up to 1.5 kN).	Mounting points must endure the full thrust of the engine to prevent structural failure during operation.	Analysis, Test	Load testing and finite element analysis (FEA) will confirm that mounting points can sustain these forces without deformation, ensuring operational safety.	93, 145, 165, 171, 173, 175, 186, 224, 241	Fully Compliant.
SYS.01	STRUCT.03	All structural components shall be fabricated from materials compatible with solid propellant combustion byproducts.	Material incompatibility could lead to corrosion or weakening of structural elements, compromising safety and performance.	Inspection, Test	Material compatibility tests will be conducted with propellants and oxidizers to verify durability against exposure to combustion gases and residues.	165, 171, 173, 175, 189, 224, 241	Fully Compliant.
SYS.05	STRUCT.04	Aerospike structure shall integrate with the propulsion system and custom test stand.	Ensuring compatibility with the custom test stand and propulsion equipment allows for smooth integration and reduces the need for modifications.	Inspection	A finite element load analysis will confirm the secure attachment and support of the six motors.	165, 167, 168, 169, 171, 173, 175, 176, 181, 186, 224, 241	Fully Compliant.

Explanations of Structural Subsystem Requirements

STRUCT.01 - Spike structure shall withstand temperature cycles from ambient to operational extremes (up to 2,888 [K]).

The engine structure is designed to endure the high-temperature cycles induced by solid propellant combustion, with peak operational temperatures reaching up to 2,888 [K]. This resilience is essential, as each ignition and burn period exposes the material to intense thermal fluctuations, potentially causing thermal fatigue or material degradation over time. To ensure structural integrity across these repeated cycles, inspection and thermal analysis will confirm that the materials can withstand the thermal stresses without compromising performance or safety. Temperature values of 2888 [K] were acquired from thermal analysis on the model.

STRUCT.02 - Spike to engine/thrust stand mounting points shall maintain structural integrity under maximum expected thrust loads (up to 1.5 [kN]).

Ensuring structural stability at mounting points is critical for safely supporting the engine during high-thrust operations. This requirement verifies that the mounting points can withstand the full thrust force, reaching up to 1.5 [kN], generated by solid propellant combustion. Given the high stress exerted by these operations, FEA will validate that these points can sustain the forces without deformation or failure, thereby preserving the safety and functionality of the propulsion system. Thrust values of 1.5 [kN] were acquired from fuel burn simulation and CFD of engine model.

STRUCT.03 - All structural components shall be fabricated from materials compatible with solid propellant combustion byproducts.

Material compatibility with combustion byproducts is crucial to prevent corrosion, degradation, or weakening of structural components. The structure must resist adverse effects from exposure to combustion gases and residues, maintaining durability and reliability over multiple test cycles. Testing for material compatibility with the specific environment created by solid propellant combustion will ensure that the structural components can withstand these conditions without compromising integrity. AlSi10Mg is ideal for this requirement due to its exceptional



resistance to oxidation, corrosion, and thermal degradation in extreme environments. Its high nickel and chromium content forms a stable oxide layer, protecting against chemical attack from reactive combustion byproducts. The alloy maintains mechanical integrity at high temperatures (~980°C / 1,800°F / 1,250 K), preventing weakening from thermal fatigue or creep. Additionally, its resistance to hot gas erosion ensures durability over multiple test cycles. Using AlSi10Mg in Project Vulcan minimizes material degradation and failure risk, with testing validating its compatibility with solid propellant combustion conditions.

STRUCT.04 - Aerospike structure shall integrate seamlessly with the propulsion system and custom test stand.

Seamless integration with the propulsion system and custom-built test stand is essential for safe, reliable, and efficient operation. This requirement ensures that the aerospike and related structural components can be mounted and aligned accurately, minimizing the need for adjustments during setup and enhancing operational readiness. Compliance will be verified through physical inspection, fit checks, and test stand trials, ensuring that the integrated system functions as intended under real conditions.

6.3.2 Structural Design (Hartlieb, Bedelbaev)

The system-level design of Project Vulcan revolves around the creation and testing of an aerospike engine integrated with a LITVC system. The design approach is focused on achieving a balance between performance, reliability, and manufacturability, ensuring that the engine meets the requirements for propulsion in high-altitude, variable-pressure conditions. The system is also designed with scalability in mind, to allow for future iterations or adaptations based on the results of testing.

The decision-making process for the system design began with identifying the primary goals of the project: ensure the testing infrastructure and aerospike can handle the extreme conditions generated during rocket propulsion, integrate LITVC for enhanced maneuverability, and validate the aerospike's performance in varying atmospheric conditions. A core part of the



design was selecting a configuration that could meet these goals while adhering to constraints related to material properties, manufacturing techniques, and testing requirements. Key factors influencing the design included:

Performance Requirements: The aerospike engine needed to optimize thrust distribution and altitude compensation. Ensuring these factors led to the choice of a radial multi-engine configuration with a nozzle capable of leveraging the unique properties of an aerospike. The integration of the LITVC system to allow for precise thrust vectoring further informed the nozzle design.

Material Selection: Given the high temperatures and stress involved in the rocket propulsion process, materials had to be thermally resistant and capable of withstanding extreme conditions. The use of metal 3D printing allowed to produce complex geometries while maintaining the strength needed for the aerospike, providing a key advantage over traditional manufacturing methods. AlSi10Mg was chosen for Project Vulcan due to its exceptional properties for rocket engine components. Its high-temperature resistance (up to approximately 980°C / 1,800°F / 1,250 K) enables reliable performance in extreme thermal environments, such as combustion chambers and nozzles. With the use of cooling channels and heat dissipation, the structure will withstand operation temperatures up to 2,888 K, satisfying STRUCT.02. Additionally, AlSi10Mg exhibits outstanding oxidation and corrosion resistance, ensuring durability in chemically reactive and high-stress conditions, satisfying STRC. 03. Its superior mechanical strength, including excellent creep resistance and fatigue performance, provides the necessary structural integrity under extreme loads. Furthermore, AlSi10Mg's weldability and suitability for additive manufacturing allow for efficient production of complex geometries. While more costly than stainless steel, its performance advantages make it a preferred choice for high-performance aerospace applications.

Printing Material Pugh Matrix						
Solution Alternatives						
Key Criteria	Importance Rating	Stainless Steel 316		Inconel 625		Copper Alloy
		S		S		+
		+		+		S
Thermal Conductivity	3	S		S		-
Yield Strength	3	+		+		S
Printability	5	S		S		-
Cost	2	-		-		-
Availability	10	-		+		S
Sums of Positives		1		2		1
Sums of Negatives		2		1		2
Sums of Sames		2		2		2
Weighted Sums of Positives		3		13		3
Weighted Sums of Negatives		12		2		7
Totals		-9		11		-4

Figure 69: Material Selection for Aerospike Print

AlSi10Mg was selected for Project Vulcan due to its favorable properties for lightweight aerospace structures and compatibility with metal additive manufacturing. This aluminum alloy offers a strong balance of mechanical performance, corrosion resistance, and thermal conductivity, making it ideal for components not subjected to the extreme temperatures of combustion zones. AlSi10Mg provides good strength-to-weight ratio, making it particularly advantageous in applications where mass reduction is critical without compromising structural integrity.

Compared to stainless steel 316, AlSi10Mg is significantly lighter and more suitable for additive manufacturing. While stainless steel offers better high-temperature strength, it lacks the weight efficiency and ease of processing provided by AlSi10Mg. The aluminum alloy is also less prone to residual stresses and warping during printing, improving manufacturability and dimensional stability.



When compared with high-temperature nickel-based alloys such as Inconel 625 or 718, AlSi10Mg cannot match their mechanical performance at elevated temperatures. However, for structural elements that are not exposed to direct combustion or extreme thermal cycling, AlSi10Mg offers more efficient printing, simpler post-processing, and reduced cost. Its mechanical strength is sufficient for non-critical load-bearing components and provides the added benefit of corrosion resistance in ambient conditions.

In contrast to copper alloys like CuCr1Zr or GRCop-42, which are chosen for their superior thermal conductivity in actively cooled regions, AlSi10Mg offers superior structural rigidity and is less prone to thermal softening under moderate heat loads. While copper alloys excel in heat dissipation, they lack the mechanical stability required for structural support in uncooled zones.

By selecting AlSi10Mg, Project Vulcan achieves a design that is optimized for lightweight performance, cost-effective manufacturing, and adequate structural capability in areas not subject to peak thermal loading. This makes it a practical choice for parts printed using laser powder bed fusion.

The top section of the system is being manufactured using metal additive manufacturing, specifically laser powder bed fusion. As mentioned, this component is printed entirely from AlSi10Mg as a monolithic structure, meaning all its geometries are produced in a single print operation. This eliminates the need for assembly and ensures dimensional accuracy and material continuity throughout the printed part. All design choices were made to ensure all the system and subsystem requirements were met and complaint by showcase.



Figure 70: Aerospike and Nozzle Structure (Top View)

The design concept for the project aims to place a radial aerospike section right after a set of nozzles to determine the added benefits and effects of the aerospike on the thrust of the rocket. So, the team chose to mimic the Firefly rocket aerospike design mentioned before in the report, that sees a channel continuation of the diverging section of a CD nozzle, where only the inner portion of each diverging section is engraved into the aerospike. This allows the exhaust plume to have additional flow direction as well as more surface to push from, increasing the thrust of the rocket. Having the exhaust plume reacting off the aerospike surface while exposed to the ambient air, allows for the exhaust to always be ideally expanded, and always produce the maximum amount of thrust at any altitude. With the nozzles placed so close together, this allows for plume-plume reactions to occur in between each nozzle, aiding the force created by the rocket to be more directed in the axial direction, losing less thrust in the horizontal directions.

Cutting the model just before the throat of the nozzle, the team see cooling channels that run up and down the entirety of each nozzle. As well as the aerospike spine, which is hollow to allow room for the LITVC piping.



Figure 71: Aerospike and Nozzle Structure (Top Sliced View)

Each nozzle contains 20 cooling lines, with each line coming from the base of the model to the diverging section, wrapping around, and then coming back down the nozzle. The pipes wrap over top of one another and have a diameter of 2 [mm]. Notice how the LITVC pipe does not resemble a generic circular pipe, where this pipe has ridges that aid in fluid flow and structural integrity. LITVC system will be mentioned in more detail later in the section.

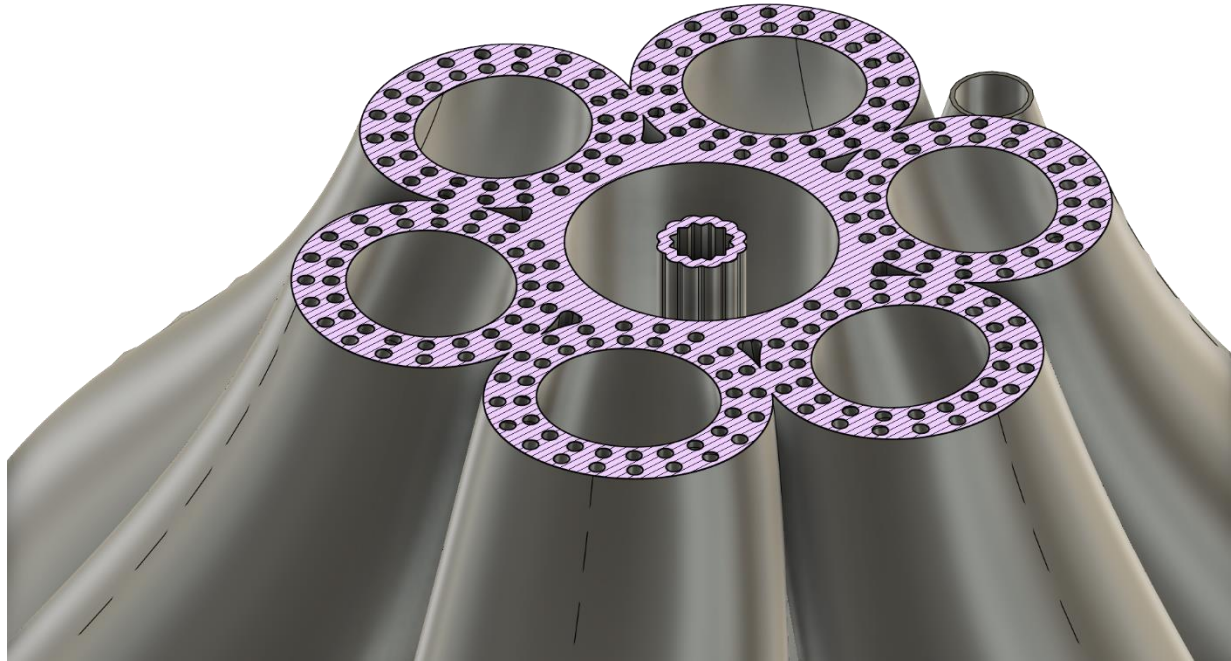


Figure 72: Figure 71 - Zoomed in

Seen in Figure 73 is another image of the cooling lines that are inside each of the nozzles, that are placed over top of themselves to allow for lower temperature fluid to be closer to the inner walls of the combustion chamber aiding greater in the cooling of the material being more directly exposed to the heat of the combustion chamber, and then the fluid that has already passed through here, loops around the diverging section of the nozzle and comes back down the outside of the walls. The thickness of the combustion chamber walls varies through the nozzle, with a thickness of almost 7 [mm] at the exit of the nozzle. A thickness of 7.5 [mm] at the throat, a thickness of 6.5 [mm] at the beginning of the converging section, and an equal thickness of 6.5 [mm] for the rest of the chamber going to the manifold/flange.

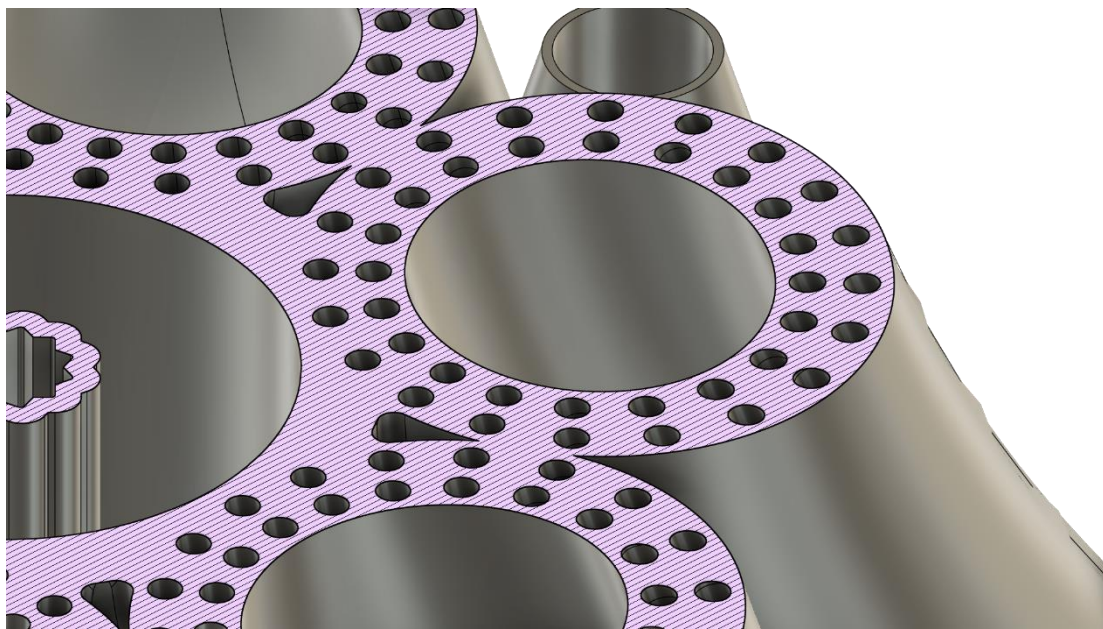


Figure 73: Figure 72 – Zoomed in more

The negative bodies in Figure 74 demonstrate the internal piping system for one of the nozzles that supplies the cooling fluid. Notice the manifold at the base of the cooling lines, these manifolds connect each of the inlet and outlet flows and will be covered later.



Figure 74: Internal Cooling Piping Lines – Negative Bodies

Figure 75 is an image demonstrating the cooling lines wrapping over themselves in the diverging section of the nozzle. The lines have a consecutive diameter of 2 [mm] for the entire system. A distance of 1 [mm] of material is kept in between the overlapping cooling lines, and a minimum of 3 [mm] distance is kept in between each of the lines. This distance of 3 [mm] is the closest the lines ever get to one another, which is located at the diverging section where they wrap back around. The furthest they are apart is at the base of the aerospike section right after the motor casings, with a distance of 9 [mm].

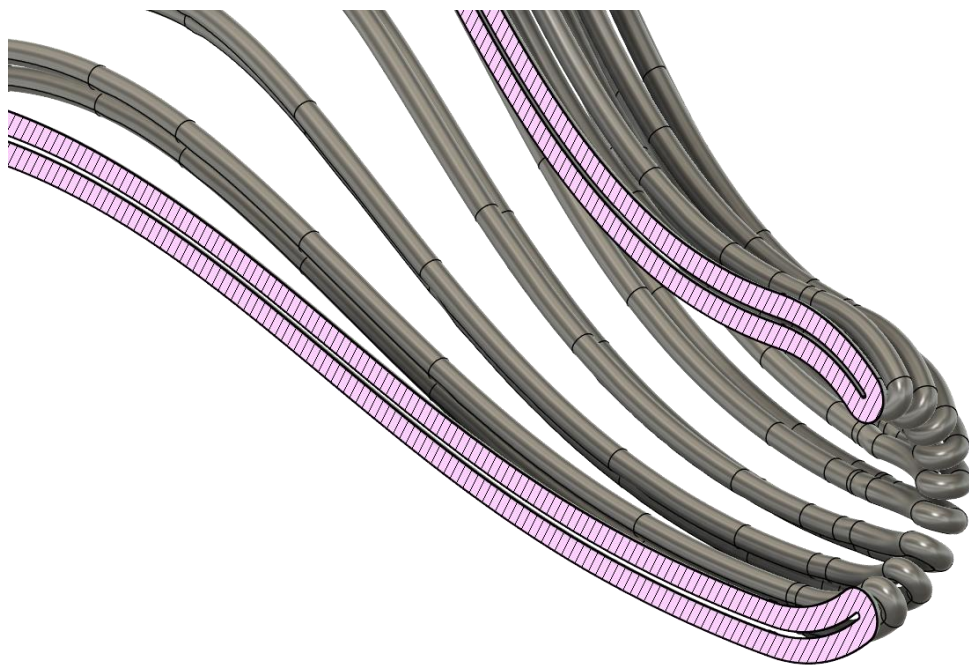


Figure 75: Cut view of Internal Cooling Lines

Now moving on to the LITVC orifices that are located in the aerospike section right after the exit of the nozzles. The orifices are placed on the center line of the nozzle and aerospike channel contour at three side-by-side nozzles.



Figure 76: Three LITVC Orifices

Top view of only three aerospike nozzle channels having LITVC exit orifices. The goal of placing the orifices all at sequential nozzles is to aid in testing the vectoring of thrust of the aerospike, whereas placing the orifice evenly spaced out would increase the complexity of the system and require shut off valves for each individual orifice. A single orifice design was also considered but not chosen because a single LITVC orifice would not demonstrate a meaningful enough thrust vectoring that the project was trying to achieve.

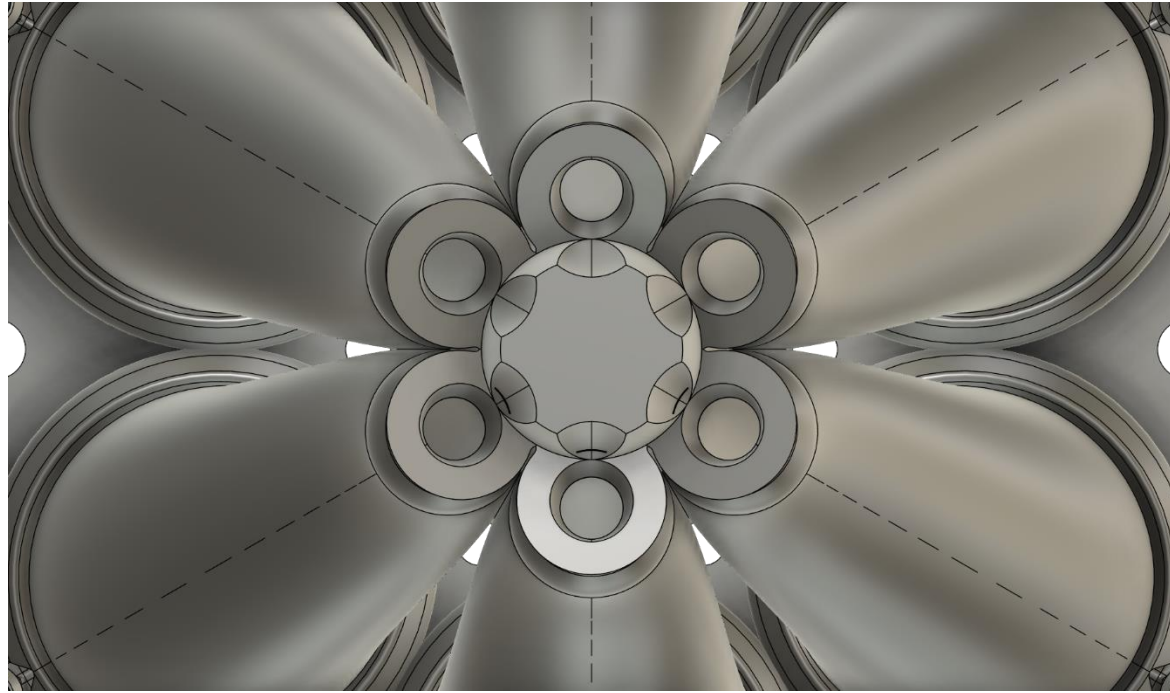


Figure 77: Top View of Three LITVC Orifices

Closer look at LITVC exit orifices can be seen in Figure 78. The rectangular slit of the LITVC orifice was chosen to increase fluid flow supply to a velocity that would induce an acceptable shock against the exhaust plume of the nozzles, where a circular port would not get the required velocities and would cause inadequate shock formations, disturbing the exhaust plume. These rectangular orifices are placed 25 % along the aerospike channel contour and are 6 [mm] long by 0.5 [mm] wide.

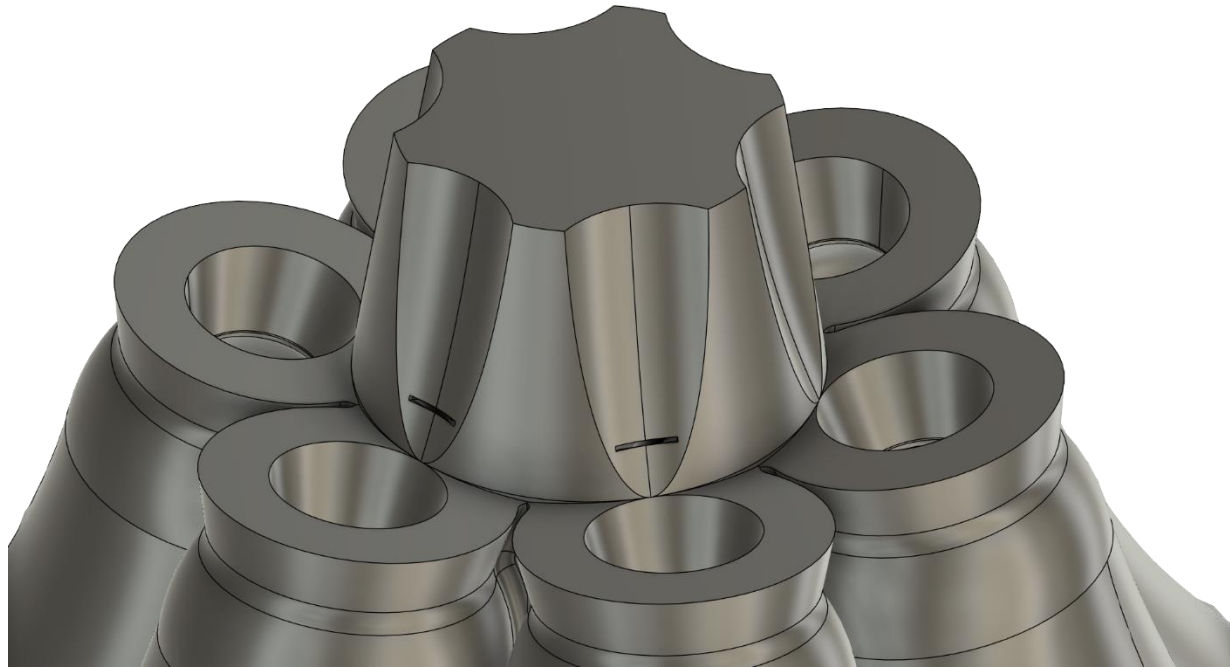


Figure 78: Close view of LITVC Orifices

To supply fluid to these LITVC orifices, a design was needed to ensure fluid flow could be obtained at this section without interfering with the nozzle and its high temperatures and pressures. So, to solve this problem, the inside of the aerospike section was hollowed out to act as a spine to house the LITVC piping. Seen below is a cut out view that aids in visualizing the LITVC orifices, as well as the piping that supplies the fluid.



Figure 79: Cut view of Aerospike Section and LITVC Piping

This pipe goes all the way from the aerospike to the base of the bolted flange. A cross-section view of aerospike in Figure 80 aids in visualizing the whole piping system from the LITVC orifice to the flange section inside the aerospike spine. The underside of the aerospike contour section was modeled to come to a point to allow for the increase in manufacturability. The roof of the aerospike spine was initially flat to decrease the amount of material that was in this section, but this needed to be changed. The flat roof was at an angle of 0 [deg] compared to the horizontal plane, making it almost impossible to print without the necessary supporting structure, which would increase the print cost by a large portion. To fix this, a pointed roof was modeled so that the angle of the roof was at least 45 [deg], and in this case the angle is around 51 [deg], satisfying the printer capabilities.



Figure 80: Cross-section view of Printed Model

A single pipe inside the spine produces the fluid flow to all three of the LITVC orifices, with three-way splitter located in the piping system, right before the fluid is released out of the orifice. Another view of the LITVC system inside spike can be seen below, with a section of the nozzles removed.



Figure 81: Cross-section view of LITVC system

To better demonstrate the three-way splitter of the piping, the image below has more of the aerospike section removed to give a top-down view. The ridged-circular pipe molds into a rectangular exit orifice using a loft command in Fusion to allow for a seamless connection between the two complex geometries.



Figure 82: Cut view of LITVC Orifices

Another close-up view of the LITVC orifice can be seen below. The fluid flow of the LITVC system will be released perpendicular to that of the exhaust flow, inducing a shock wave that will vector the thrust force vector of the nozzle in another direction. This new thrust force will change from going axially out of the nozzle, to being angled outward from the aerospike contour, enough to induce a change in thrust vector of the entire system.

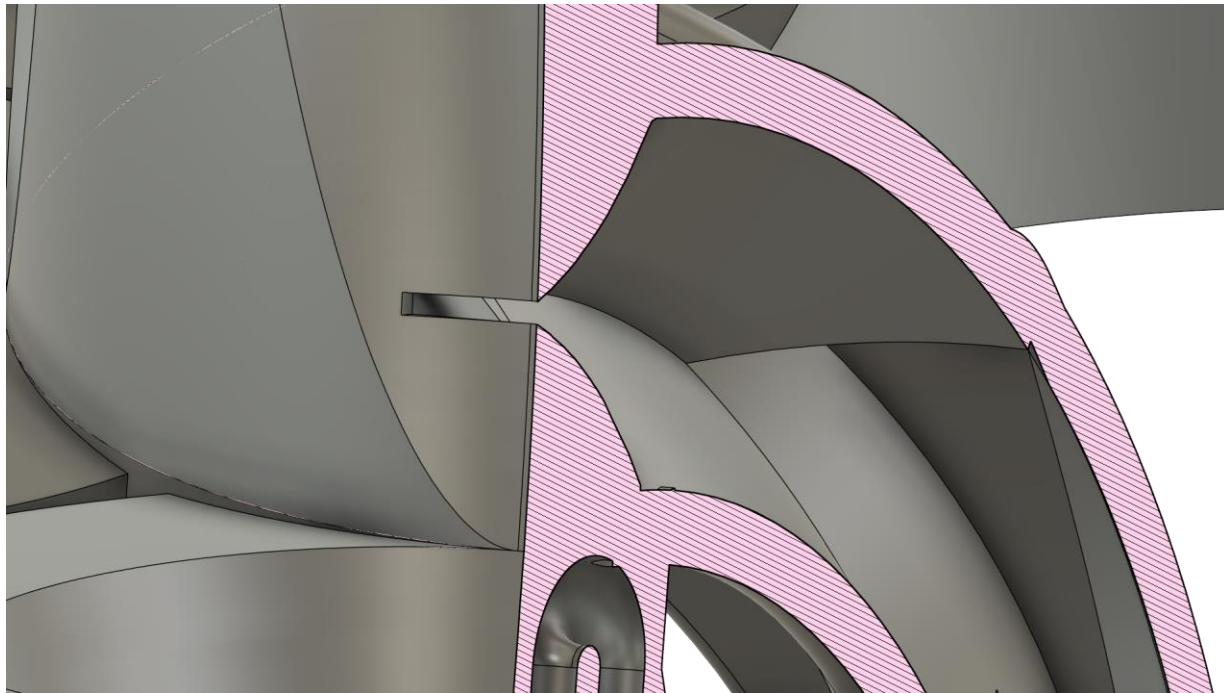


Figure 83: Close up Cut view of LITVC Orifice

Each of the three LITVC orifices look like the image above, and all three converge from a circular pipe to a rectangular slit. Now that the orifice has been covered in detail, the team will move back to the LITVC system as a whole and focus more on the bottom section. Going back to the image displayed before, the LITVC pipe and external pipe can be visualized.

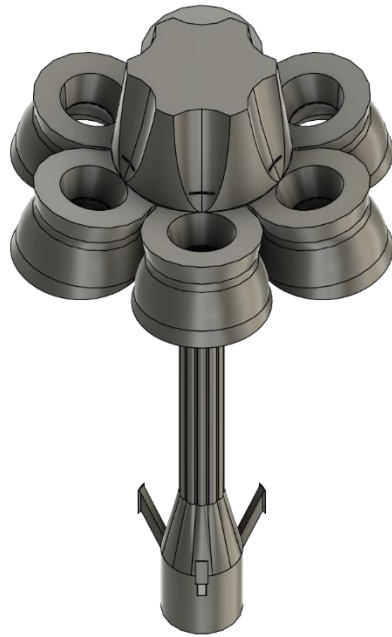


Figure 84: Cut view of Aerospike Section and LITVC Piping

As stated before, this piping system goes along the entire inside of the aerospike spine and has an external port towards the bottom or flange face of the design. Figure 85 visualizes this port from an underneath view.



Figure 85: Bottom Cut views of LITVC Piping

The LITVC piping system takes many shapes through its travel inside the aerospike spine, with a large circular pipe being at the very external portion and a rigged circular pipe taking up most of the length of the pipe. The image below shows this LITVC piping system in a side cross-section view, demonstrating the location of the external port related to the nozzles and aerospike section.



Figure 86: Sides Cut views of LITVC Piping

The external port of the LITVC system takes the shape of a 14.1 [mm] inner diameter pipe that meshes smoothly from the ribbed pipe section. The external port has a wall thickness of 3 [mm] and once the model is printed, the inner diameter of this pipe will be threaded to allow connection to the water pump. The diagonal supports on the port connect to the inner walls of the aerospike spine and allow for structural integrity. These supports were initially straight across, but due to 3D printing limitations mentioned before, the supports had to be moved to be over 45 [deg] angle from the horizontal plane.

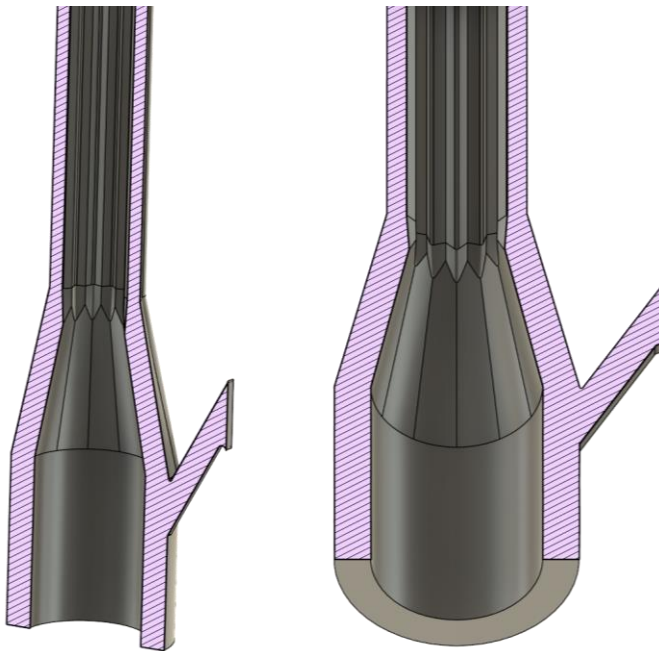


Figure 87: Close up Cut view of LITVC Port

Moving away from the LITVC section and towards the cooling channels, the figures below compare a model with the cooling manifolds and a model with some manifolds missing. To introduce manifolds, the team must understand their purpose. With the 20 cooling lines there needs to be a way to deliver fluid to each of them, while also allowing for a path for the already used fluid to be released back out of the system. To accomplish this challenge, two separate manifolds were created for each nozzle, with one of those controlling the inlet fluid into the lines and the other controlling the outlet from out of the lines.

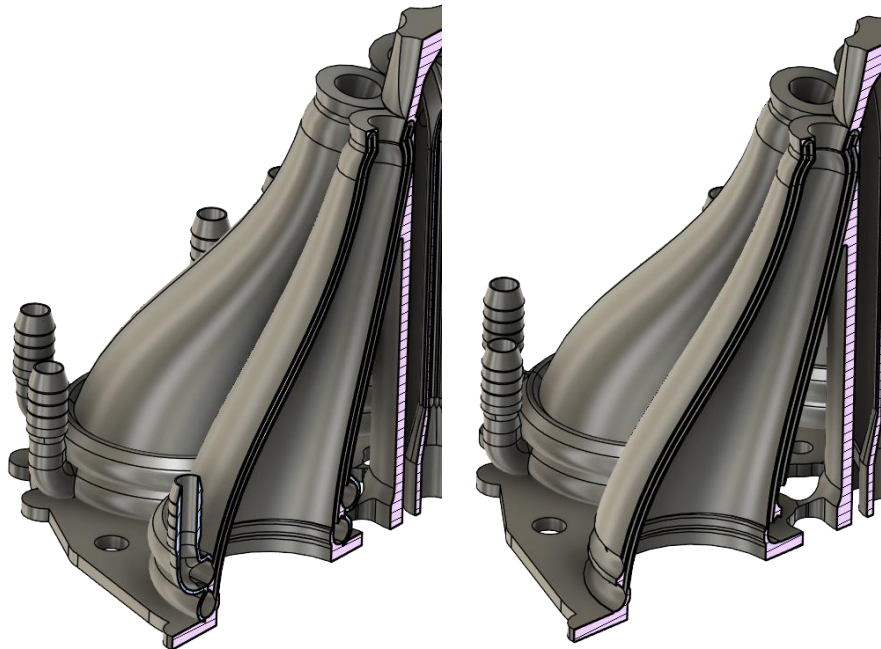


Figure 88: Comparison with and without Cooling Manifold

All 20 of the inlet lines continue further down the combustion chamber walls than the outlet lines, allowing for a large circular manifold to fit within the system. This circular manifold wraps around the entirety of the nozzle and connects to each of the inlet lines. Similarly, all the outlet lines connect in the higher manifold.



Figure 89: Top Aerospike Section with Manifolds Removed

Manifolds for the inlet and outlet lines are placed around all 6 nozzles. The manifolds that connect these lines are included in the monolithic print of the aerospike section.



Figure 90: Cut views of Cooling Manifolds

Cut out views of just the manifolds can help better visualize their geometries, with two external ports connecting the manifolds to the fluid supply. The water pump will be connected to the lower manifold to supply the fluid flow at 4 [m/s], then after the fluid makes its way into each inlet line up to the diverging section of the nozzle and back down through the outlet lines, the fluid can be released out of the external port connected to the top manifold. Manifolds have a wall thickness of 1.5 [mm].



Figure 91: Cut views of Cooling Manifolds

This circular manifold takes the shape of a teardrop as it goes around the nozzle, due to a similar problem mentioned before with the aerospike spine roof. This teardrop shape allows for the printability of this section, where a regular cylindrical pipe causes an increase in print failure probability. All areas within the model that had a cylindrical surface parallel to the horizontal axis or had a rounded ceiling needed to be changed. An important consideration is metal printers struggle in rounded areas of any overhangs less than 45 [deg] angle. A cylindrical roof creates an area at the very top that is completely flat to the horizontal plane or 0 [deg] parallel to the floor, and with a hard requirement that nothing can be below 45 [deg], this was a problem. By bringing the manifold to a point where the teardrop has a point, the roof gets a greater overhang angle. In the case, the top pointed section of the teardrop manifolds is a perfect 45 [deg] angle, satisfying the printer capabilities. With the manifolds being the last geometric detail to the design, the main aerospike section is completed and ready to be printed by the manufacturer.



Figure 92: Top Aerospike Section

Where the top section is going to be metal printed, the bottom section is going to be fabricated using materials and machines found on campus. The bottom flange section connects to

the top aerospike section using a system of bolts in a flange system that also secures it to the test stand. Motor casings for each nozzle need to be placed in this bottom section and held securely during the intense pressures and temperatures expected during firings.



Figure 93: Manufactured Motor Casing Section

The flange system on this motor casing section resembles that of the top aerospike section, with the same placement of holes for the respected bolts. The 6 motor casings will house the “75 mm Propellant Grain”, which when removed from its casing, has the following dimensions:

- Outer Diameter = 65 [mm]
- Core Diameter = 22 [mm]
- Length = 131 [mm]
- Net Propellant Weight = 1.3 lbs

Off the shelf motor casings were purchased and will be used to house the propellant grain. Additional material will be sourced and used to manufacture the flange and end caps on this section. Slits in the flange are placed to house O-rings during each firing to ensure the combustion is completely sealed within the flange system.



Figure 94: Bottom view of Motor Casing Section

With a bottom view of the motor casing section, the bolt system can be visualized, with an inner ring of M6 bolts initially securing the two flanges together, and then an outer ring of M12 bolts securing the flanges together as well as securing the system to the test stand. With both sections fully manufactured, a fully assembled aerospike structure can be produced for testing.



Figure 95: Fully Assembled 3D Printed Aerospike Structure

Engineering drawings for the completed 3D printed aerospike structure as well as the motor casing's structure can be developed to indicate important dimensions and scale. With the amount of components and individual geometries of the 3D aerospike structure, multiple drawings needed to be created to fully demonstrate the shape of the printed structure.

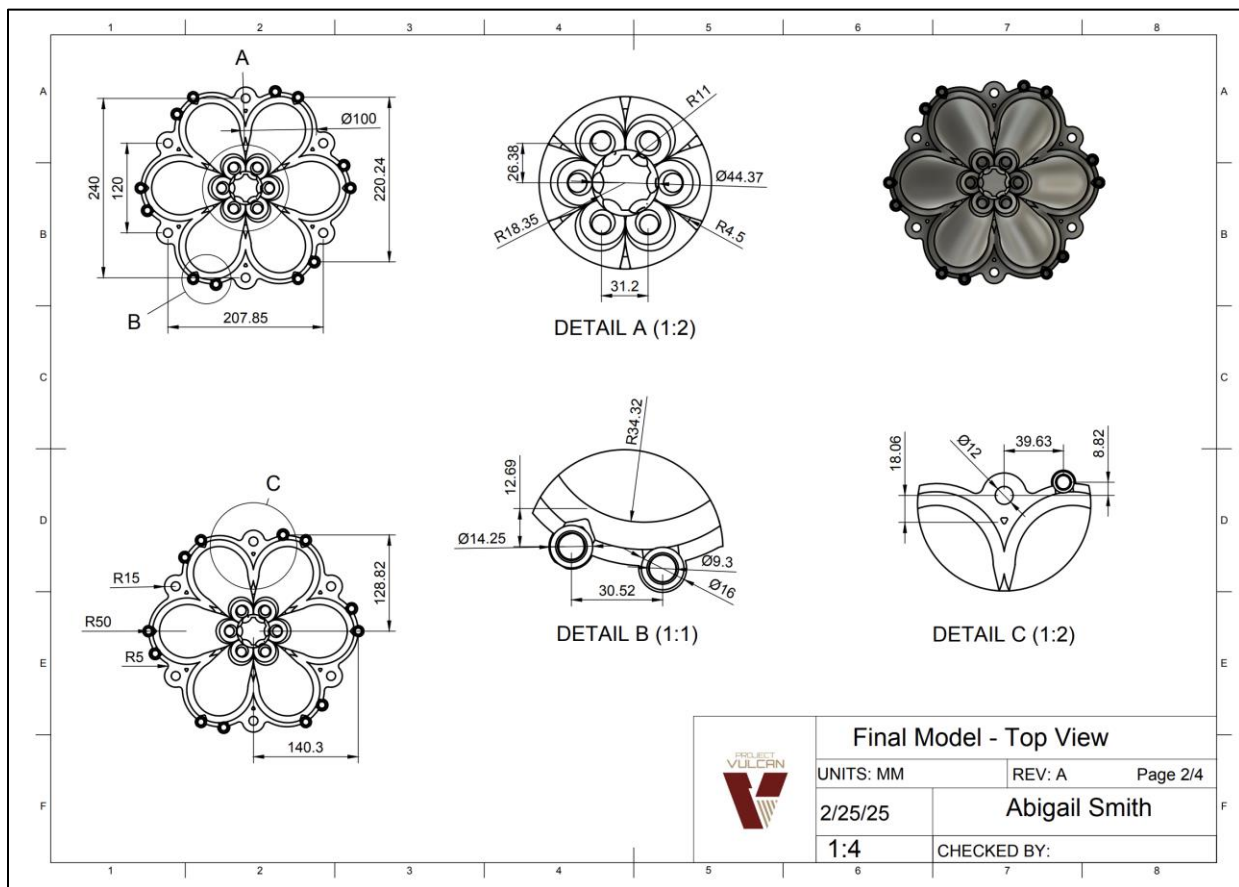


Figure 96: Top View Drawing of Top Portion of the Aerospike Model

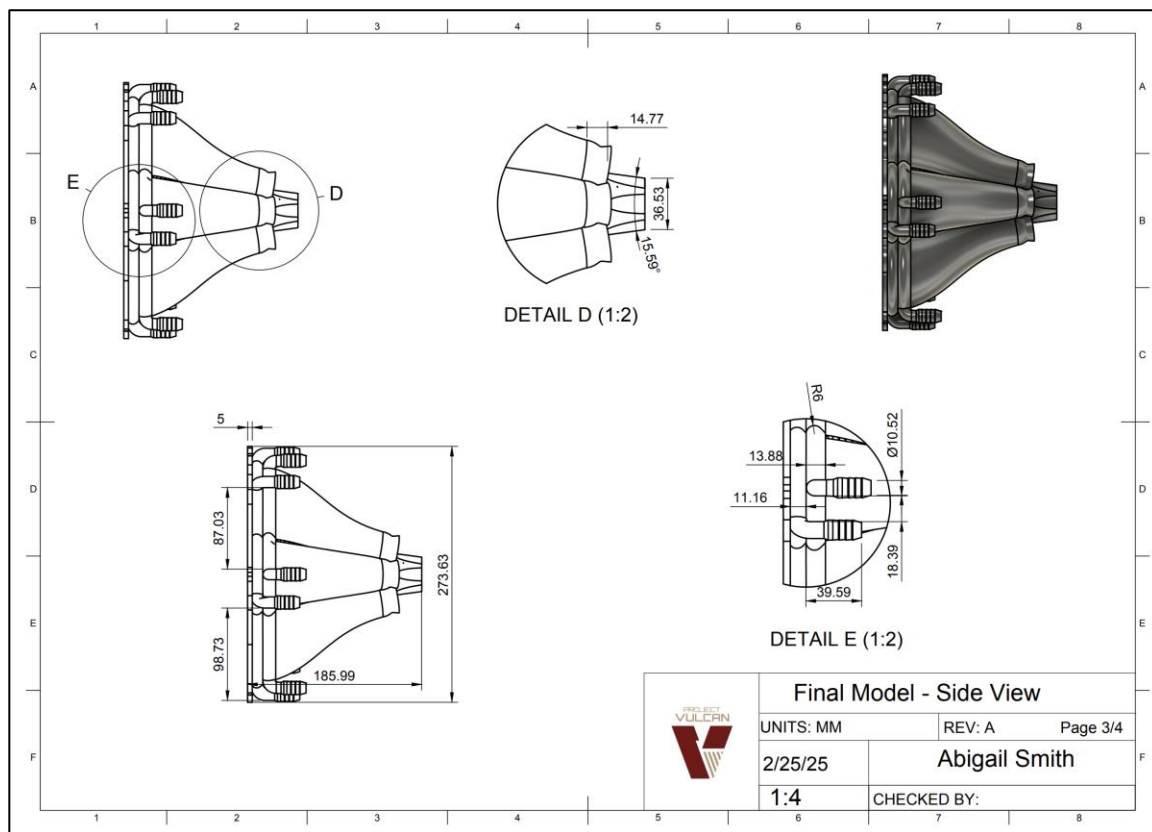


Figure 97: Side View Drawing of the Top Portion of the Aerospike Model

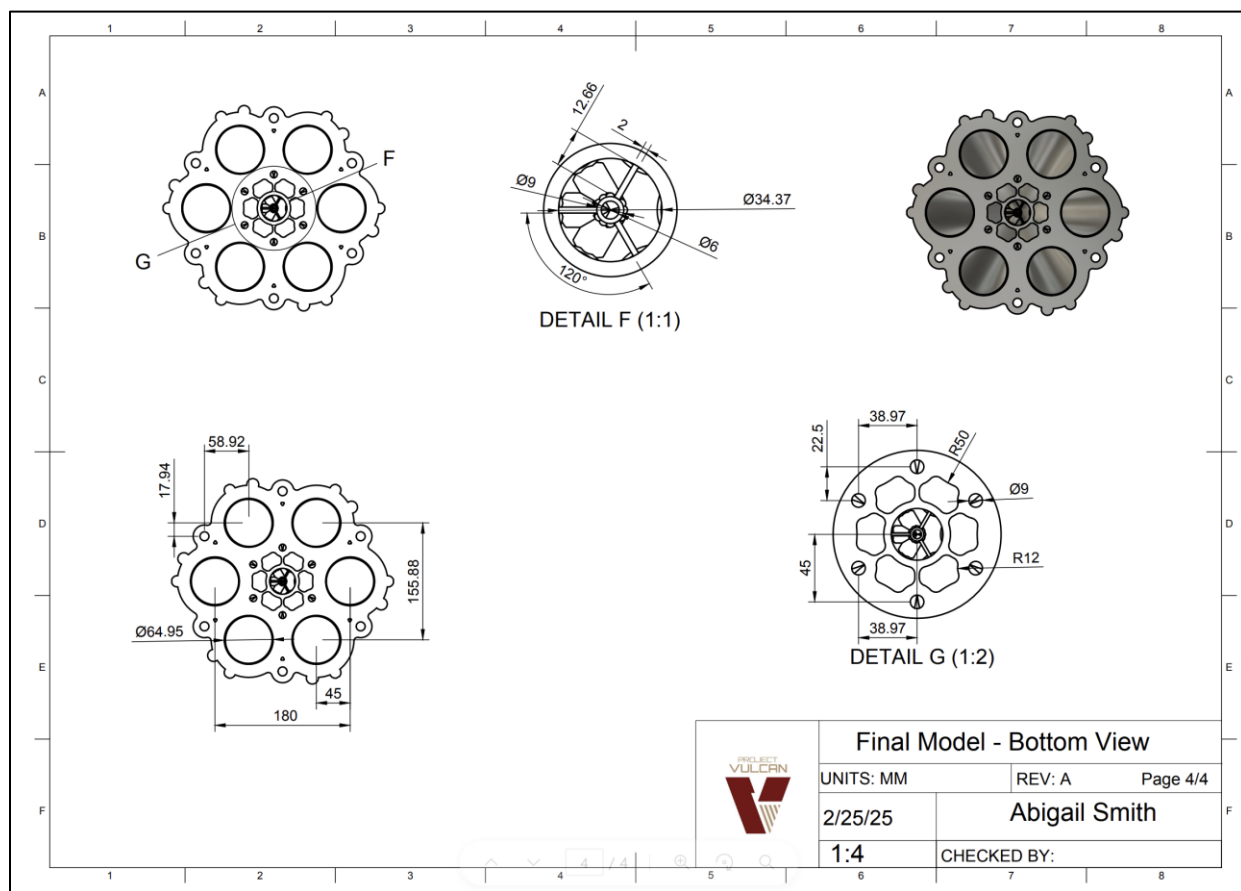


Figure 98: Bottom View Drawing of the Top Portion of the Aerospike Model

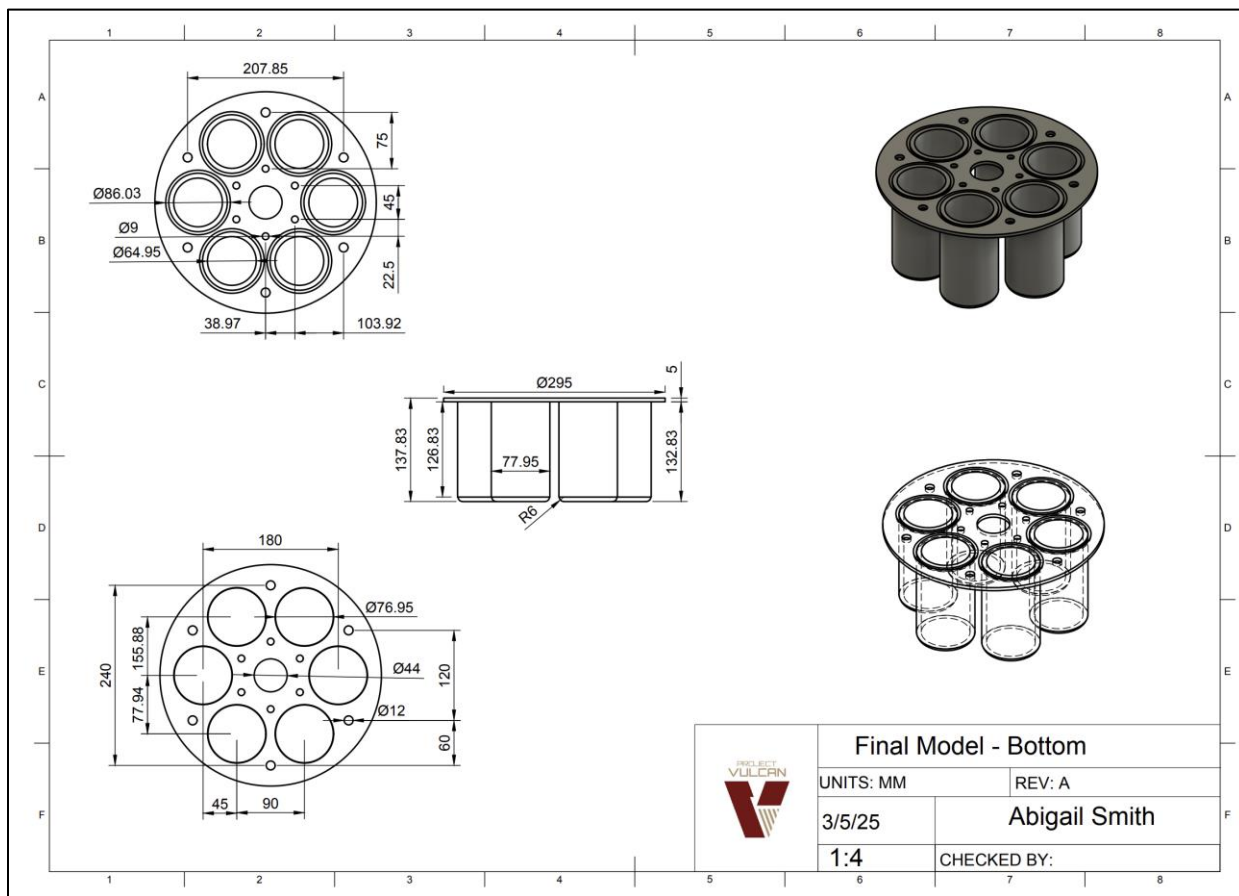


Figure 99: CAD Drawing of the Bottom Portion of the Aerospike Model

6.3.3 Structural Design Analysis (Sanchez, Valliere)

The combustion chamber and bell nozzle are the most critical thermal and structural analysis parts. The spike of the model is also important; however, it is in the combustion chamber and bell nozzle where the highest pressures and convection coefficients result from the CFD.

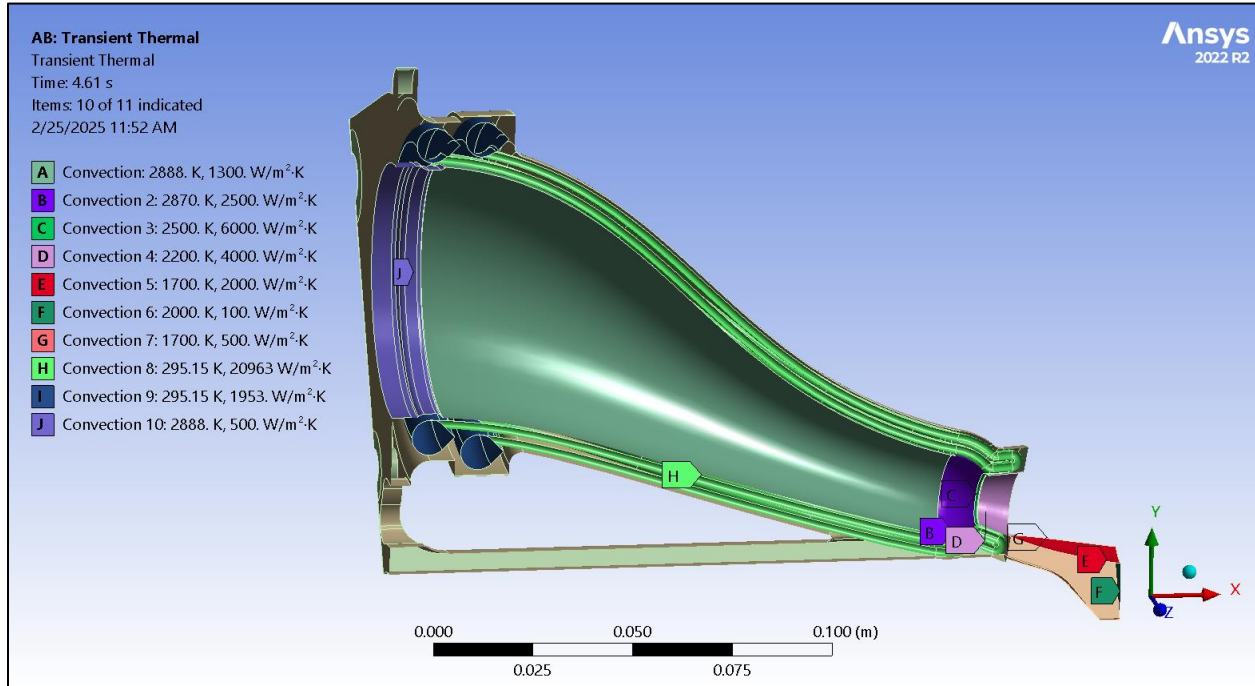


Figure 100: Thermal Boundary Conditions

In Figure 100, the geometry uses the entirety of the top half of one of the nozzles. Since PDR, the cooling channels have been fully integrated into the design, leading to a more accurate representation of the thermal response. The boundary conditions for the thermal analysis are imported from the CFD resulting from the mesh in Figure 59. On the internal walls, the convection coefficient varies from 500 to 6,000 [W/m²K] (the highest coefficient occurring at the throat), with temperatures up to 2888 [K]. In the cooling channels, the convection coefficient applied is 20,963 [W/m²K], which is a value obtained from running a CFD analysis on the internal volume of the channels, assuming water is pumped through the inlet manifold at 4 [m/s]. Lastly, a coefficient for stagnant air convection is applied to the outer walls.

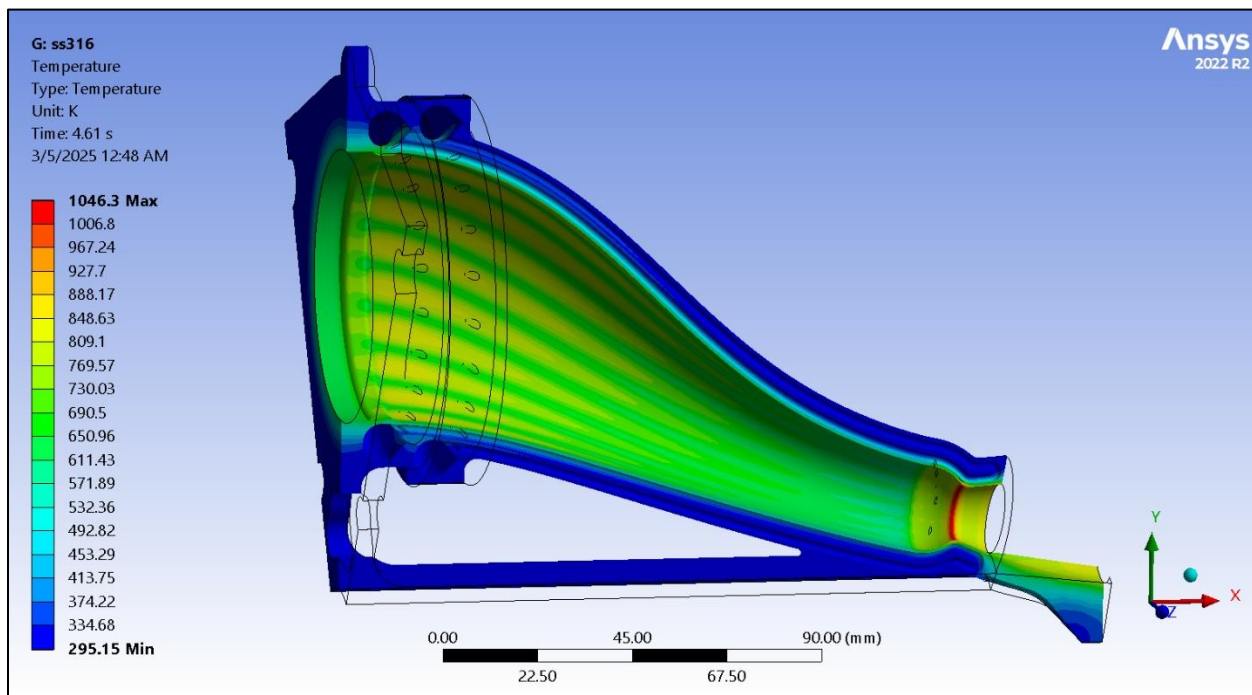


Figure 101: Stainless Steel 316 - Thermal Results on the Sliced Nozzle

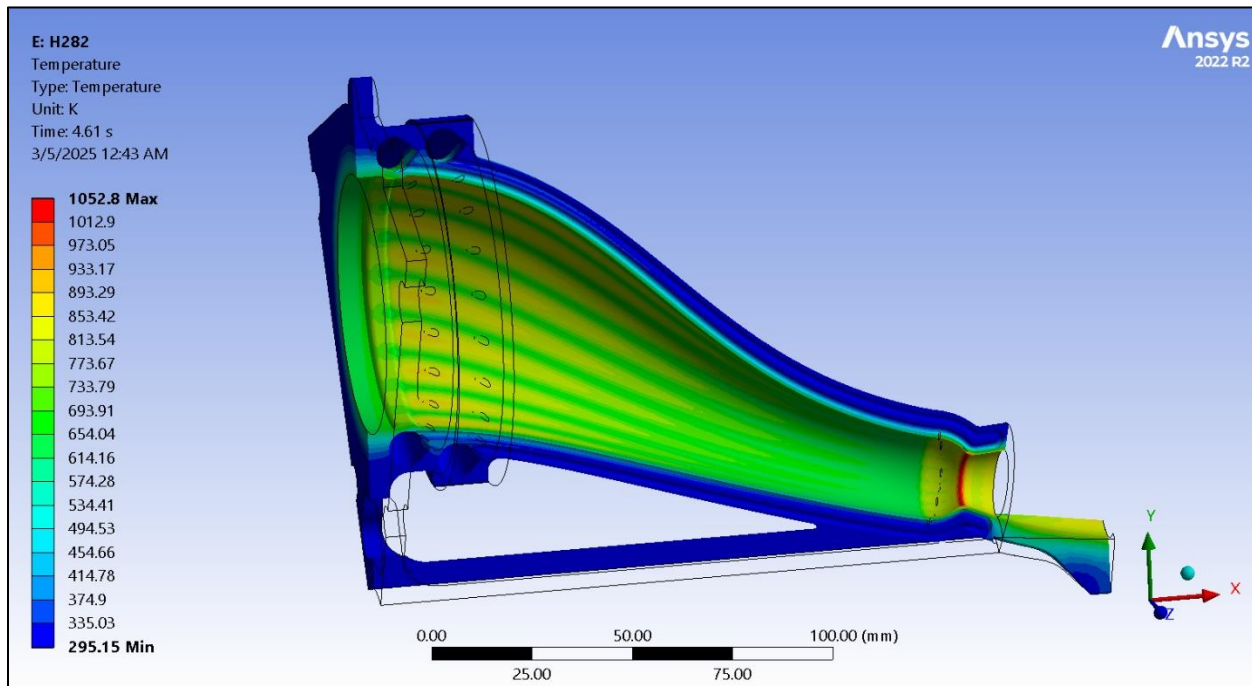


Figure 102: Haynes 282 - Thermal Results on the Sliced Nozzle

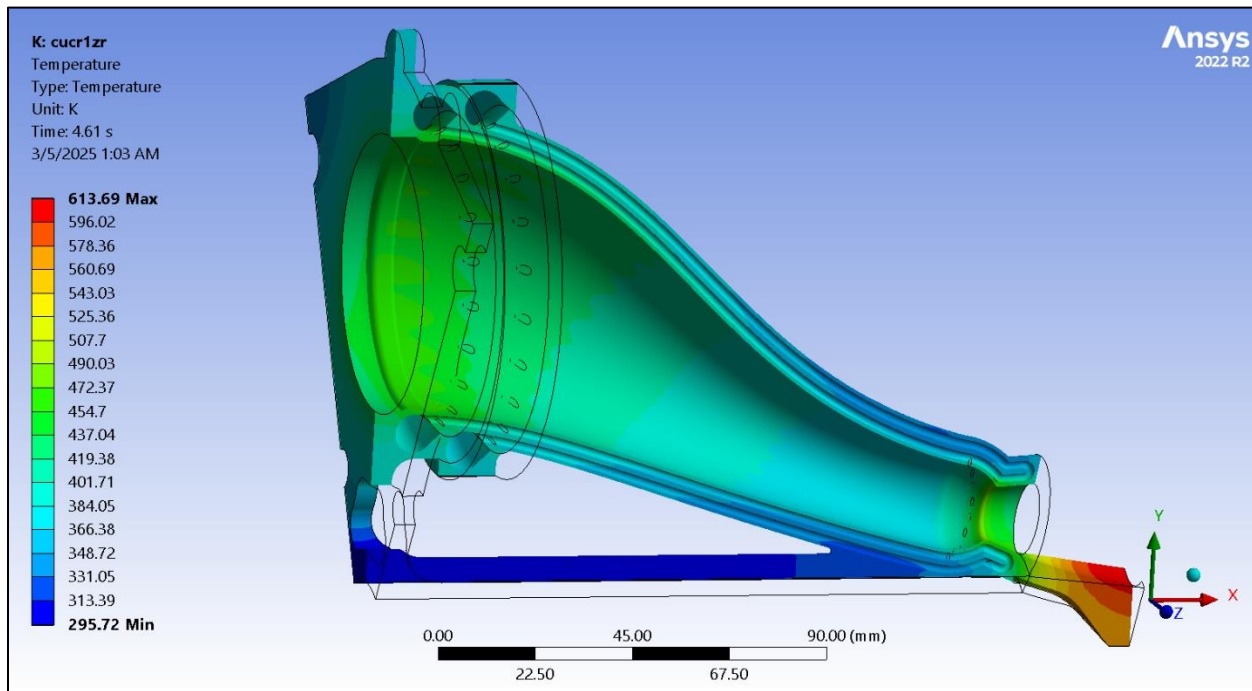


Figure 103: CuCr1Zr - Thermal Results on the Sliced Nozzle

The simulation for Figure 101 - Figure 103 is set at 4.61 seconds to simulate the burn time of the propellant grain. Three analyses were done on materials using the same boundary conditions established in Figure 100: Stainless Steel 316 (SS316), Haynes 282 (H282), and Copper Chromium Zirconium Alloy (CuCr1Zr). From the analysis, the highest temperatures occur directly under the manifold, where the velocity of the coolant is at a minimum, and at the throat, which is caused by the increased heat flux in that section. Examining the temperature gradient reveals that the cooling lines effectively dissipate heat from combustion. This is particularly evident where the cooling lines pass directly above the surface, as these areas exhibit lower temperatures than the adjacent surfaces.

SS316, H282, and CuCr1Zr melting temperatures are 1643.2, 1572, and 1338.2 [K]. However, the maximum temperatures reached from the simulations were 1173, 1063, and 613.6 [K], respectively. Active cooling is crucial for the design, without any cooling channels, any of these materials would quickly reach to their respective melting points (not explicitly shown but instead self-checked by applying no cooling coefficient).

Although none of the materials reached their melting point, the increase in temperature does lead to a reduction in the overall material strength. For example, CuCr1Zr yield strength decreases from 267 [MPa] at room temperature to 174 [MPa] at 400 °C. This reduction in strength must be considered when deciding the value and integrity of a material.

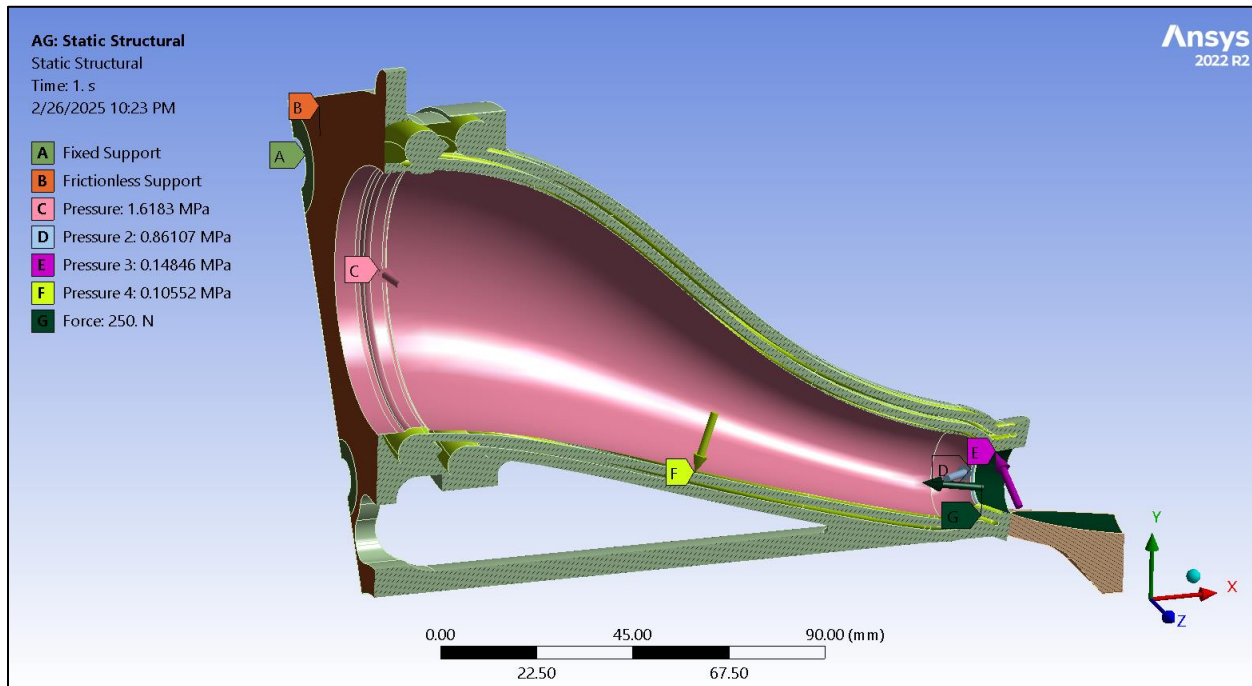


Figure 104: Structural Boundary Conditions

For the structural analysis, there are four primary boundary conditions. The first two are a fixed support located on the area of the bolted flange along with a frictionless support on the surrounding surface. Next, in the inner walls, the internal pressures are manually taken from CFD results and applied to the faces of the thrust chamber geometry where the magnitude varies from 1.6183 [MPa] in the converging section to 0.86107 [MPa] at the throat and is the smallest in the diverging section at 0.14846 [MPa]. The pressure in the cooling system is about 30 [psi] based on the pump curve at 30 [GPM], so 0.10552 [MPa] is applied to the cooling channels and manifolds. It is important to note that all pressure boundary conditions are gauge pressures, so they will appear to be different values with respect to the CFD analyses, which are all absolute pressures. Lastly,

the total thrust of the engine is 1,500 [N], so for only one out of the six nozzles, this thrust is applied as 250 [N].

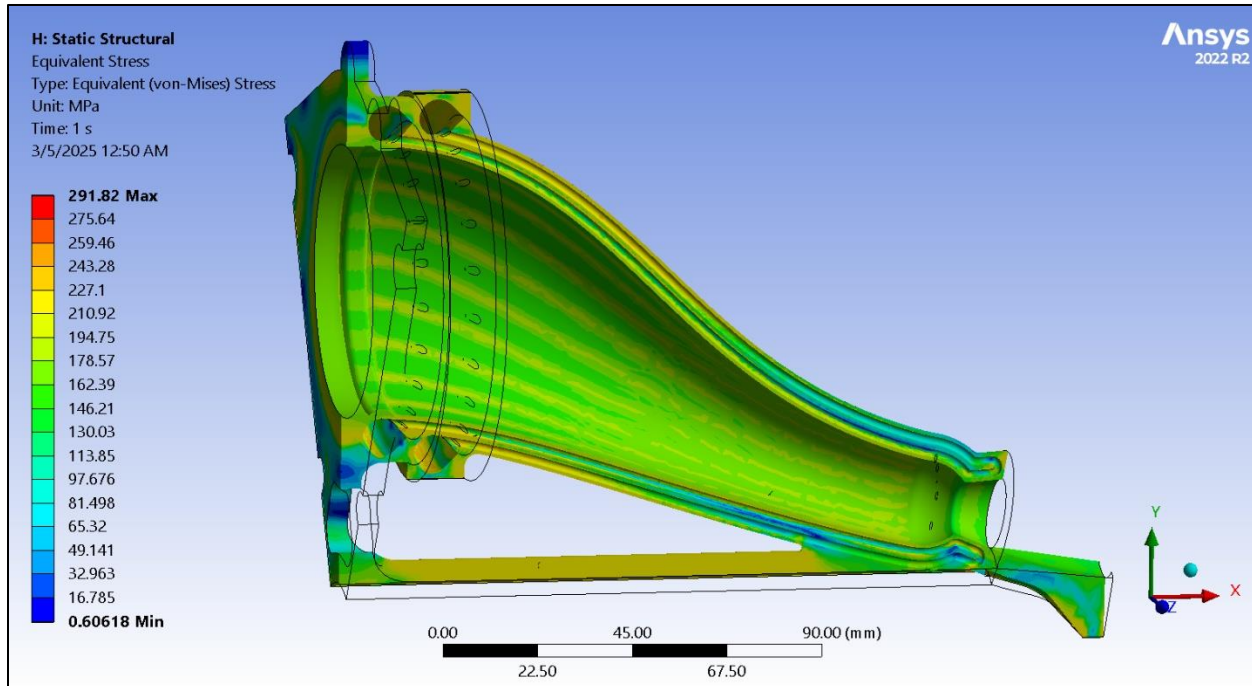


Figure 105: Stainless Steel 316 - Structural Results on the Sliced Nozzle

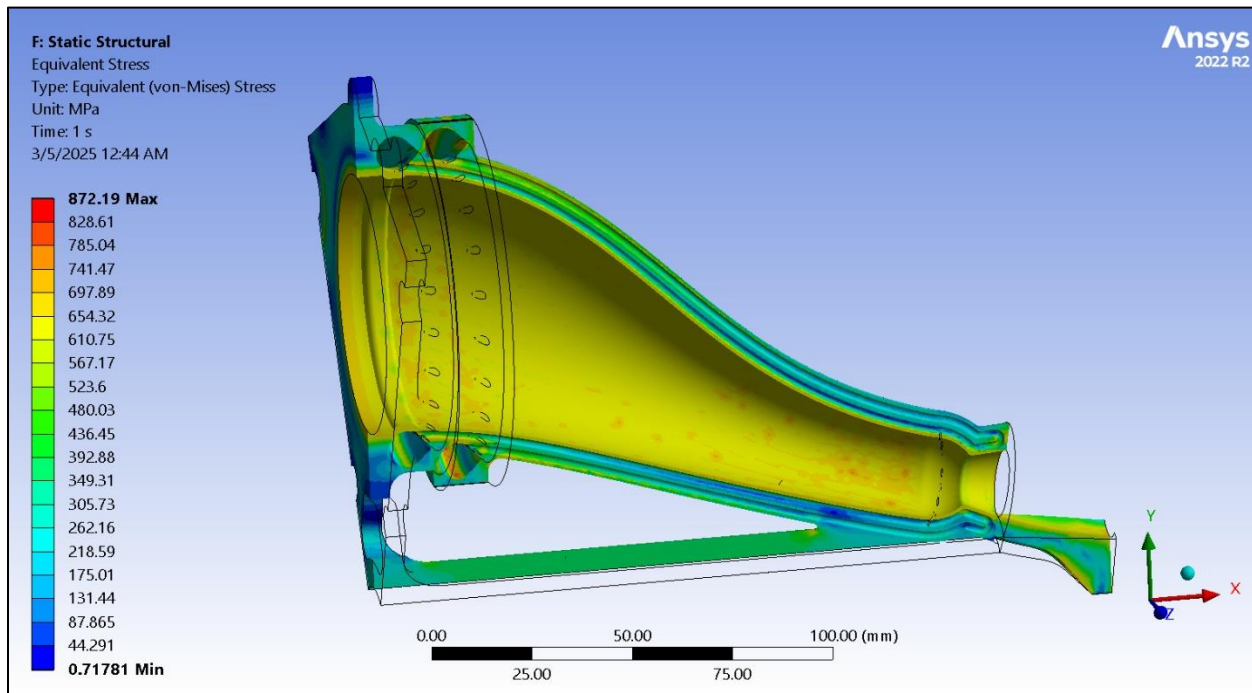


Figure 106: Haynes 282 - Structural Results on the Sliced Nozzle

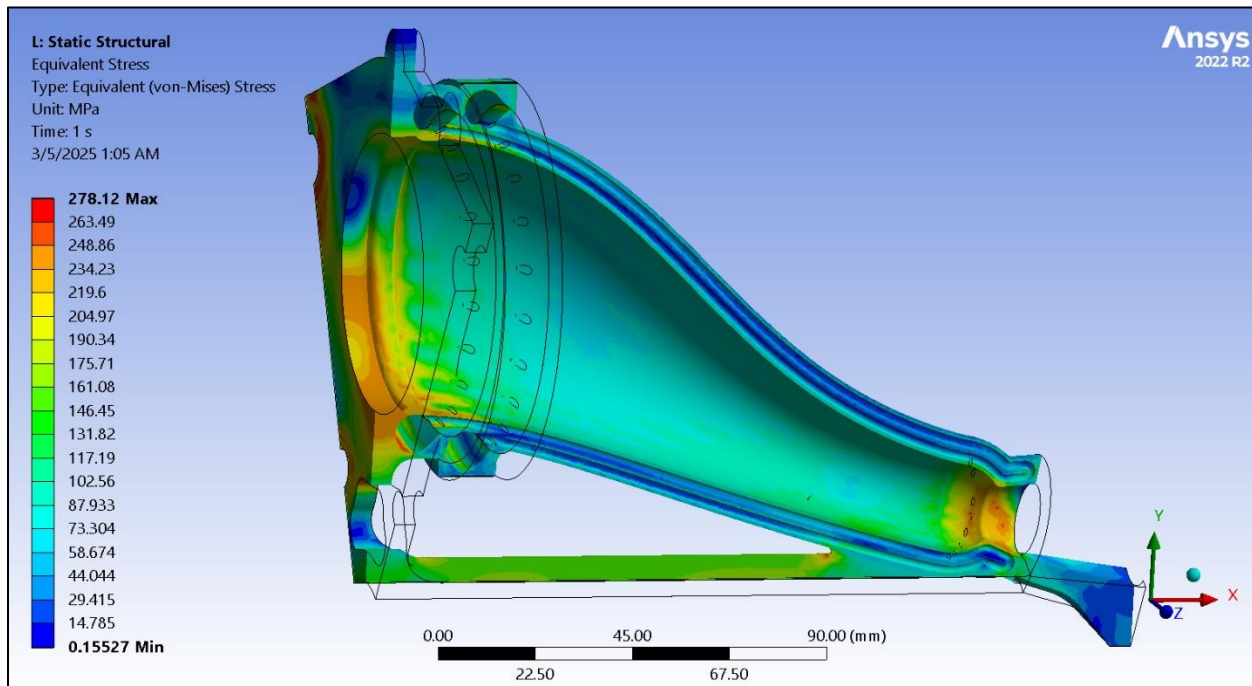


Figure 107: CuCr1Zr - Structural Results on the Sliced Nozzle



Ansys enables simultaneous structural and thermal analyses within a single instance of Mechanical, allowing the same mesh used for the thermal analysis to be directly applied to structural simulation. This approach simplifies the process of importing temperature loads throughout the model. Because the model assumes isotropic material properties, the team use the von Mises stress to reduce complex loads into an equivalent stress. By comparing this equivalent stress to the yield strength, the team can determine the safety factor and identify which sections of the material experience the highest stress relative to temperature.

In Figure 105, the first material, SS316, exhibits a minimum safety factor of 0.24. The significant temperature difference between the model's external and internal surfaces creates stresses that exceed SS316's capacity at the operating temperature. Evidently, a much stronger material is needed to survive the applied stresses. This thought is reinforced in Figure 106; notably, even H282 - a much stronger material than SS316 - struggles to achieve an adequate safety factor, as indicated in SAF.02. At 1000 [K], the yield strength of H282 decreases to 613 [MPa]. From the resulting simulated 4.61 second burn time, the maximum equivalent stress reaches 872 [MPa]. Although this high stress occurs at a lower temperature in the manifold (roughly around 600 [K]), the minimum safety factor on the part is still around 0.8 which means yielding does occur.

Similar behavior is observed with CuCr1Zr. Unlike H282, CuCr1Zr boasts a much higher thermal conductivity, making it ideal for managing temperature intensities on the internal walls. However, even with higher transfer, the copper alloy still experiences temperature ranges that significantly reduce its yield strength. As shown in Figure 107, the maximum stress is 278 [MPa] resulting in a safety factor of only 0.82. Overall, for these three materials, the safety factor remains below the SAF.02 requirement with respect to the yield stress. No matter which material is used, under operating conditions, the material to some extent will yield because of the extreme temperature gradients. Instead, going forward the factor of safety will be relative to the equivalent strain required for fracture.

One issue with this simulation is that it only contains 600,000 elements. Although a higher amount than the student Ansys limitation, the mesh count between the thin walls of the model is still too coarse for accurate results. Since the model is so geometrically complex, attempting to



refine the mesh even further becomes very difficult. Additionally, since the model begins to yield in an elastic simulation, the analysis does not take any nonlinear properties past the yield point into effect. Therefore, the stresses indicated by the simulation are more than likely higher than expected. The next step is to continue with a refined mesh and focus on a plastic and low cycle fatigue analysis of the material to ensure that even if the material yields, it can still survive multiple firings.

6.3.4 Final Test Infrastructure: Stewart Platform Test Stand

The test stand for Project Vulcan employs a Stewart platform design, a six-degree-of-freedom (6 DOF) system that allows for precise and dynamic measurement of forces and movements in multiple directions. This approach is critical for capturing a comprehensive range of test data without the need to construct separate test stands for thrust measurement and lateral, longitudinal, and vertical force control (LITVC). By using a single versatile test stand, the project maximizes both space and resources, streamlining the testing process and enabling more efficient integration of test results. Calculations for the mathematics of a Stewart platform can be found in Appendix E.

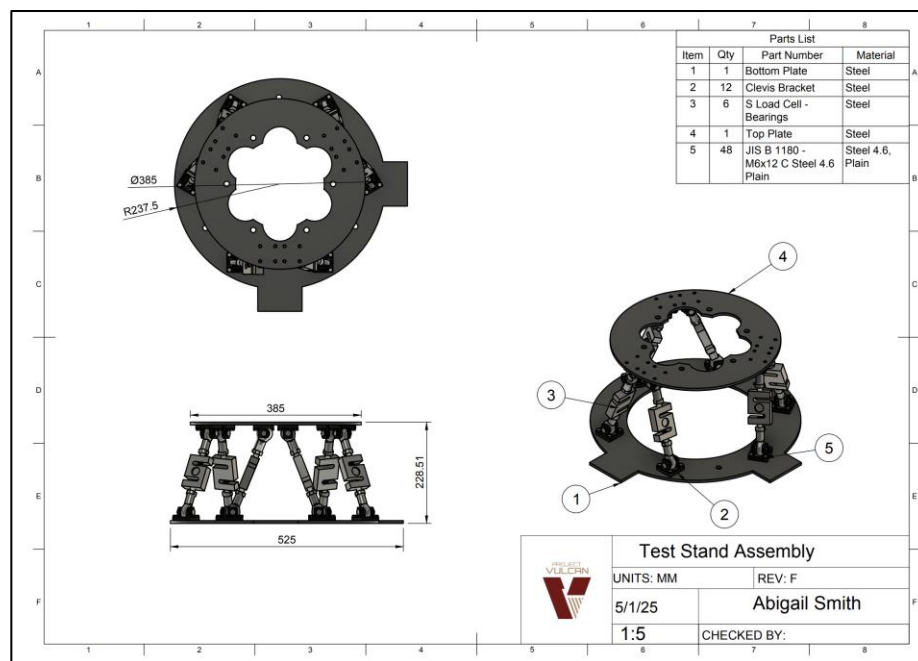


Figure 108: Test Stand Assembly CAD Drawing



Figure 109: Test Stand Assembly CAD Model

Key Components and Design Features:

The Stewart Platform design is a modular and scalable solution, ensuring flexibility and reliability. The primary components of the test stand include:

Standard 50 [kg] S-Beam Load Cells: These load cells are integral to measuring forces applied during tests. The S-Beam configuration is chosen for its ability to measure forces in both tension and compression with high precision. Each load cell is capable of handling up to 50 [kg], providing the necessary accuracy and sensitivity for thrust and force measurement in 6 DOF tests.

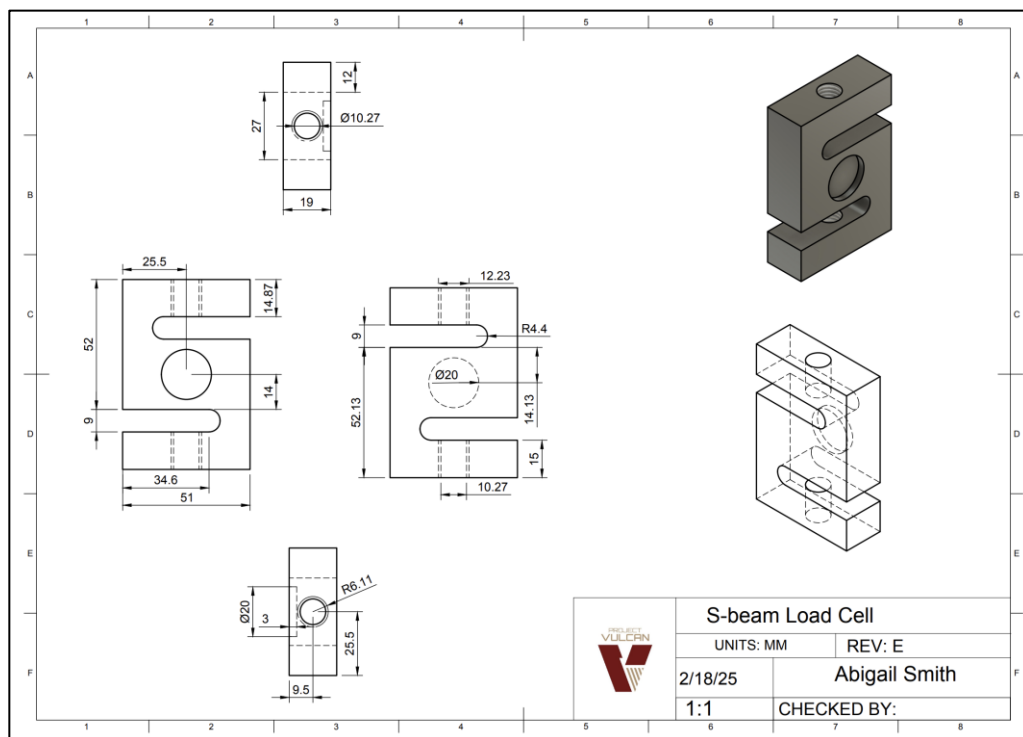


Figure 110: S-Beam Load Cell CAD Drawing

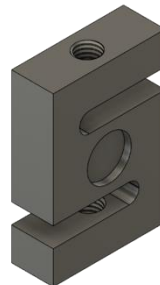


Figure 111: S-Beam Load Cell CAD Model

12 [mm] All-Thread Rods: The all-thread components act as connecting elements between various parts of the stand, ensuring structural integrity and enabling easy adjustments during the setup.

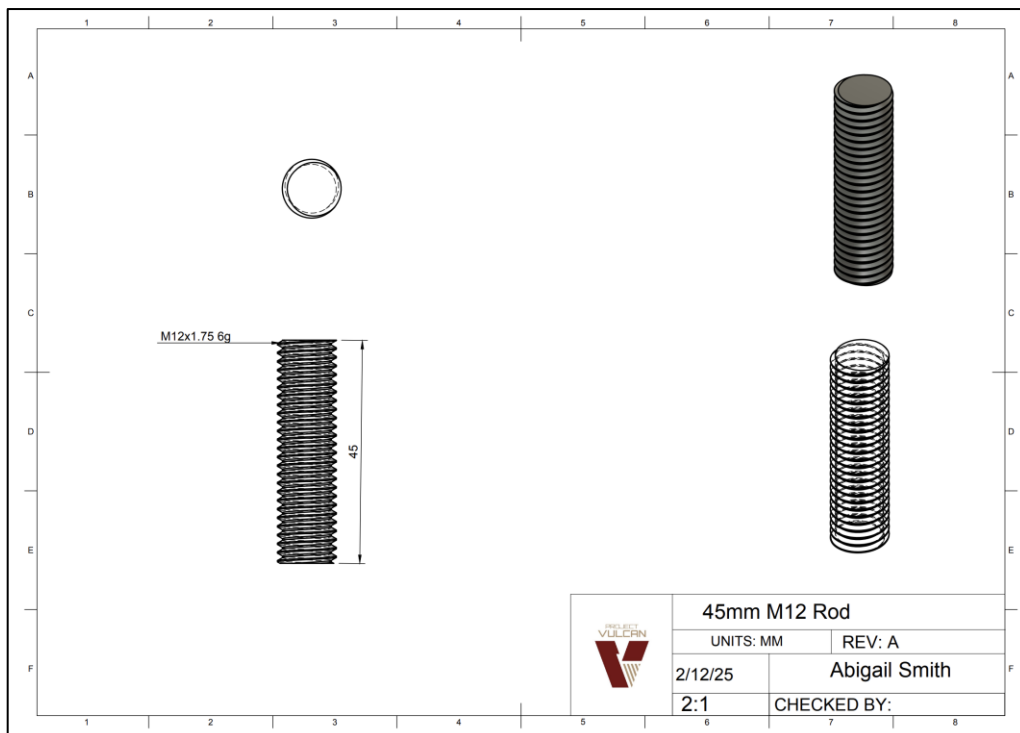


Figure 112: 12 [mm] all-thread CAD Drawing

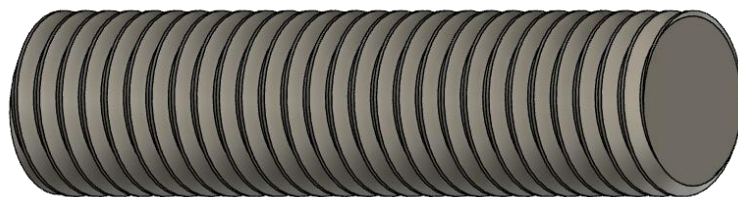


Figure 113: 12 [mm] all-thread CAD Model

Plain Spherical Bearings: Spherical bearings are used in the Stewart Platform to allow free movement between connected parts, ensuring that the system can adjust in multiple axes without introducing friction or misalignment. These bearings provide smooth motion while minimizing wear and maintaining alignment throughout testing, which is critical for accurate data collection.

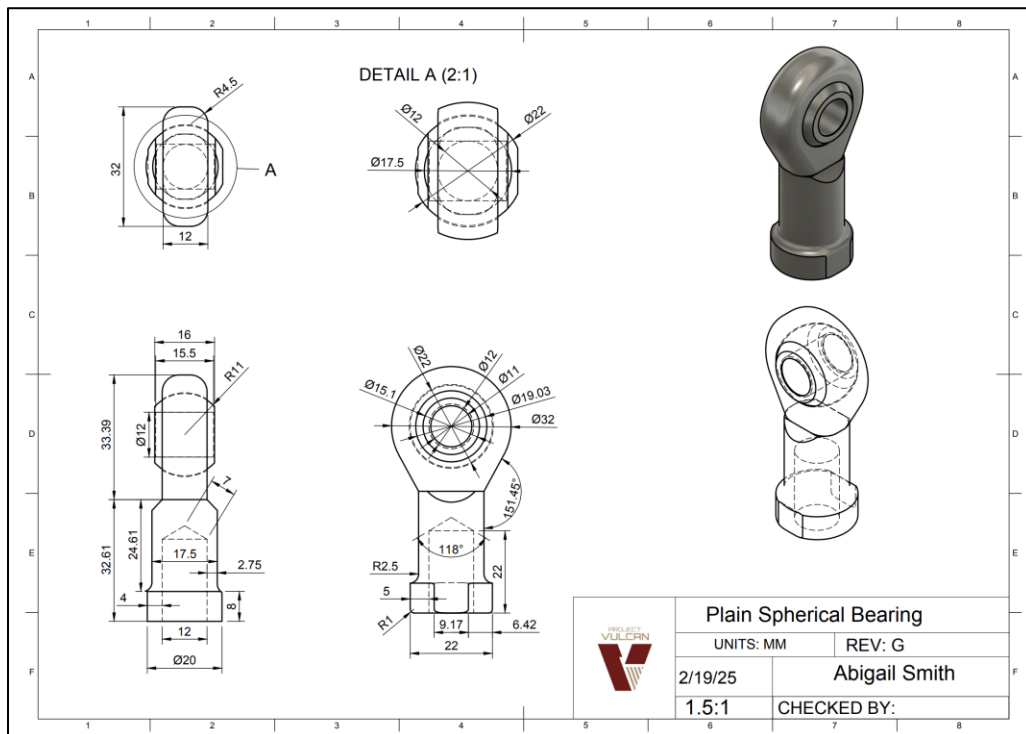


Figure 114: Plain Spherical Bearing CAD Drawing

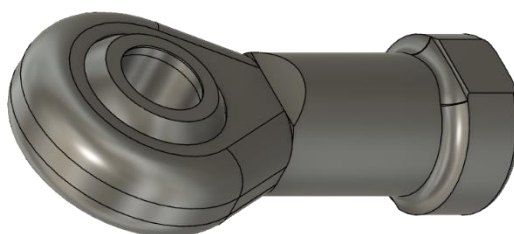


Figure 115: Plain Spherical Bearing CAD Model

12 [mm] Hydraulics Clevis Brackets: These brackets are used to mount and secure the hydraulic actuators, which play a central role in adjusting the platform's positioning. The clevis design ensures secure attachment to the actuators while allowing for easy adjustments to the test platform's position, aiding in dynamic force measurement and simulation.

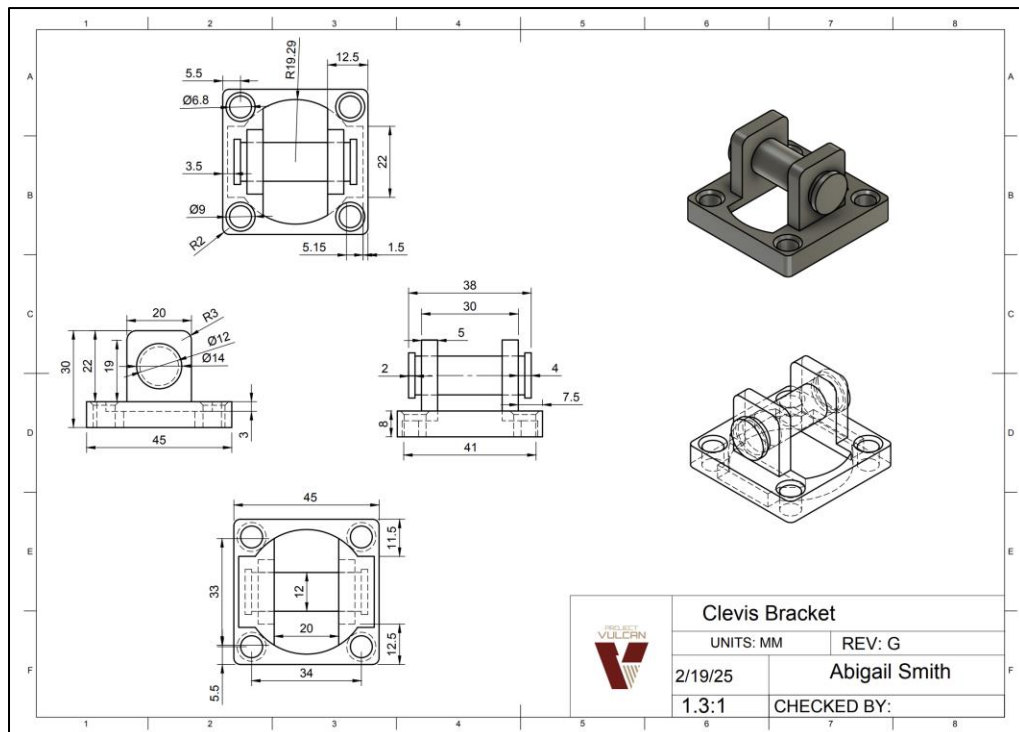


Figure 116: Clevis Bracket CAD Drawing

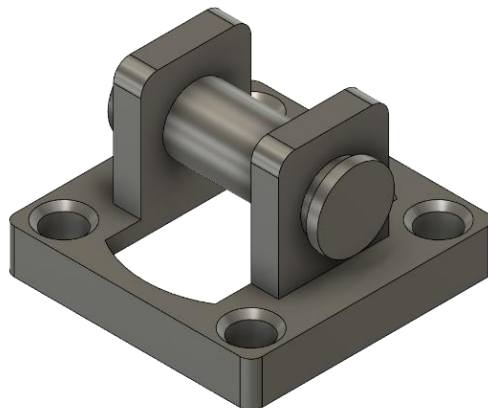


Figure 117: Clevis Bracket CAD Model

1 [cm] Steel Plates: The steel plates used in the construction of the test stand contribute to its overall rigidity and stability. These plates form the base of the platform, providing a solid foundation that withstands the forces applied during testing and ensures consistent measurements. The thickness of the steel plates is optimized to provide both strength and durability.

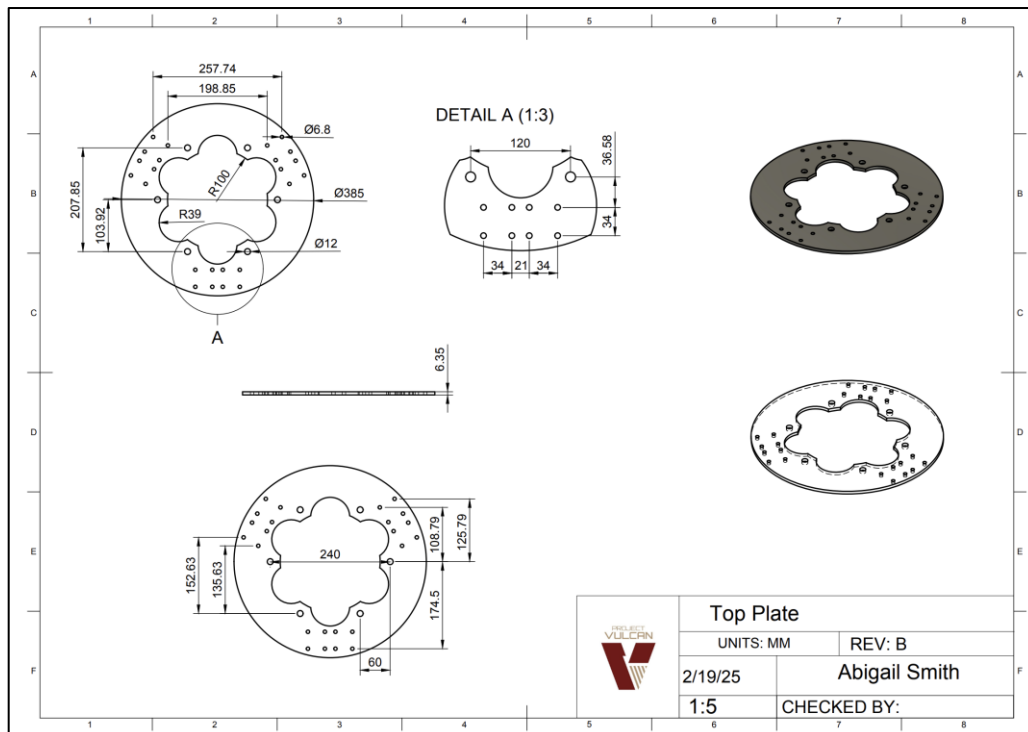


Figure 118: Top Plate CAD Drawing

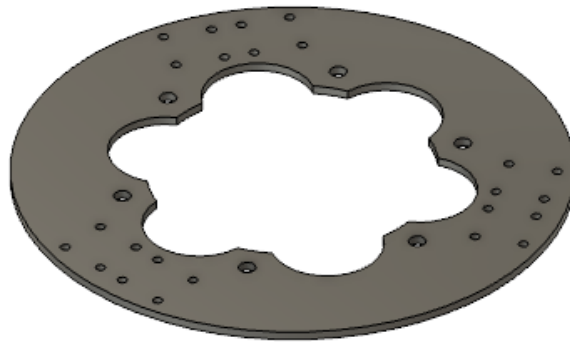


Figure 119: 6.35 [mm] Steel Plate Ring Cut Out CAD Model

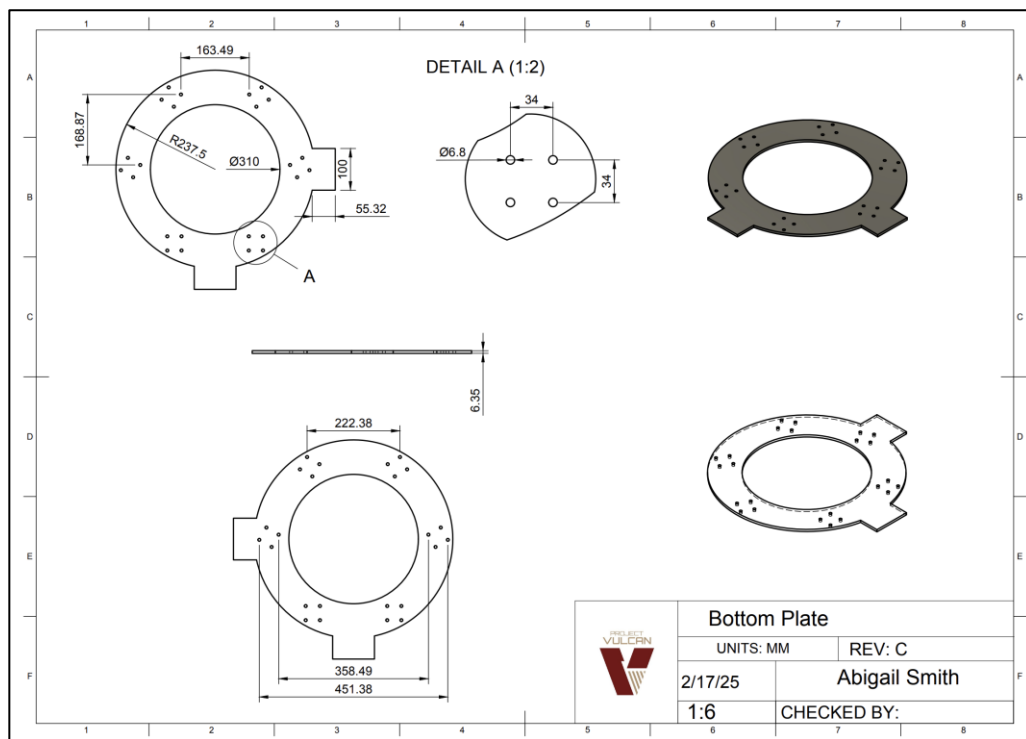


Figure 120: Bottom Plate CAD Drawing

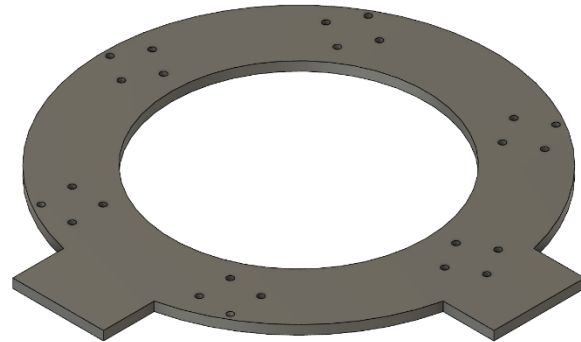


Figure 121: 6.35 [mm] Steel Plate Ring Cut Out CAD Model

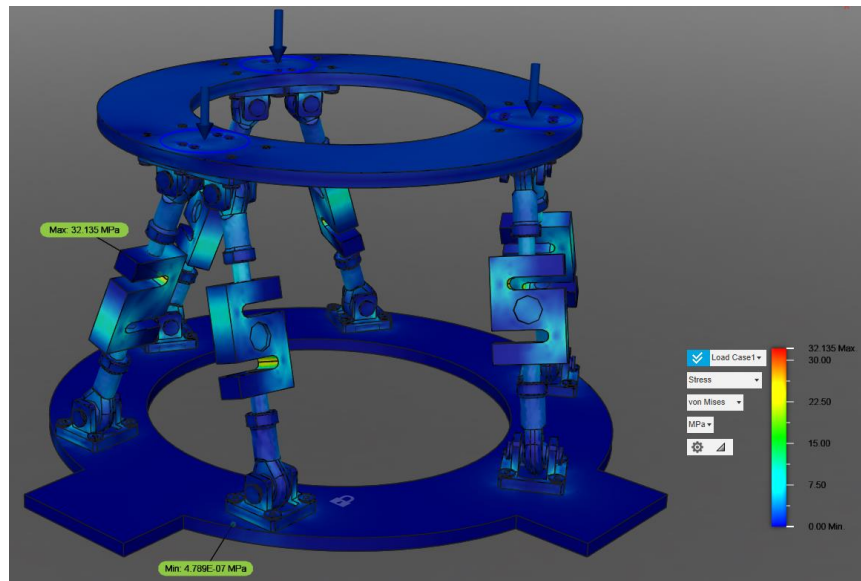


Figure 122: Structural Results on the Test Stand

The preliminary simulation on the test stand was performed in Autodesk Fusion 360. Figure 122 shows stress concentration due to three 670 [N] forces that are placed at the support points with the bottom plate fixed. This force distribution mimics the mounting mechanism for the engine as well as totals at about 2 [kN] which is the maximum thrust predicted to be generated by the engine. Material used for the simulation is Stainless Steel 316. Maximum stress concentration results at about 32 [MPa] at the load cells, which is much less than the yield strength of steel. Maximum deformation is about 0.014 [mm] and the factor of safety is approximately 6.4, indicating that the stand can withstand the engine operation. The number of mesh elements for the following simulation totaled to 256,351.

After the redesign of the top plate for the mounting mechanism a new simulation was performed with the same boundary conditions. To simulate the engine mounted on the test stand a solid bottom piece of the engine was made and the 2000 [N] were applied to it. Maximum stress was concentrated on the load cell bends and resulted in about 32 [MPa] as before. All other results were the same as the previous simulation. Number of elements for the final simulation totaled to 258,844. Results for stress and safety factors are shown below. The successful construction of this subsystem will fulfill the SYS.04 requirement for this project.

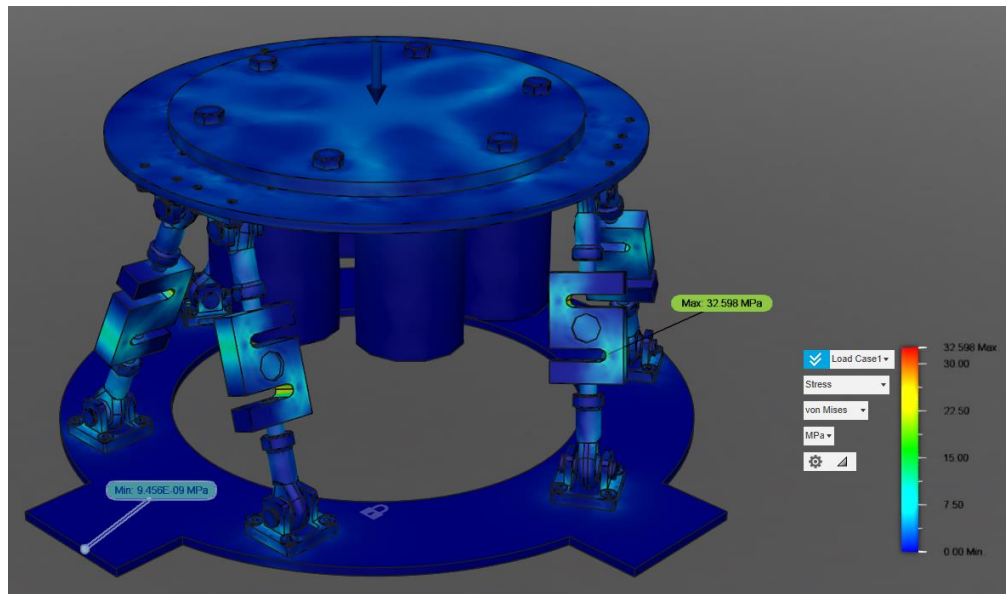


Figure 123: Final Simulation (Stress)

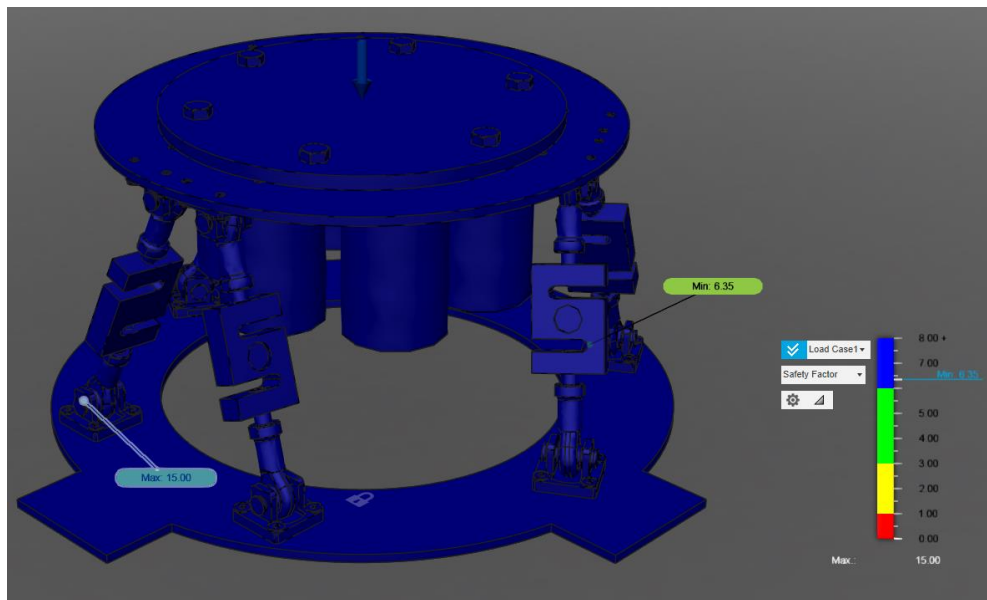


Figure 124: Final Simulation (Safety Factor)

Design Inspiration and Principles:

The design was inspired by the Stewart Platform (Hexapod), which is a type of parallel manipulator with six linear actuators which allow for all 6 degrees of motion needed to record the data required from the system (thrust force and moment/deflection induced by the LITVC). After looking at previously done research, a design inspiration was found in a paper titled “A Novel 6 DOF Thrust Vectoring Control Test Stand” [16].

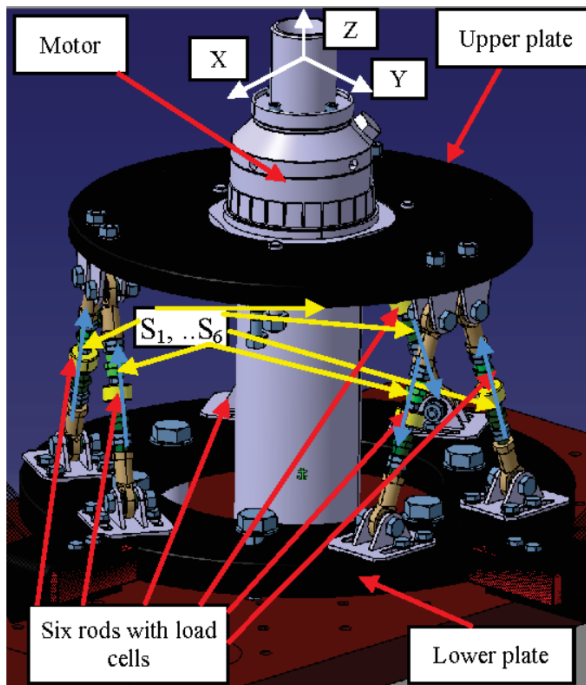


Figure 125: Final Design Inspiration [16]

The paper details the calibration process as well as the confirmation data of the design's functionality. This design presented the least complexity in both construction and mathematical decomposition of data. The greatest appeal of this design was that it would be easily made to be compatible with other systems that connect to the engine (LITVC and Altitude Simulating Shroud). This made the design clearly superior to other design considerations. Due to these positive attributes the hexapod design was chosen to be the final test stand design as the aerospike data collection apparatus.

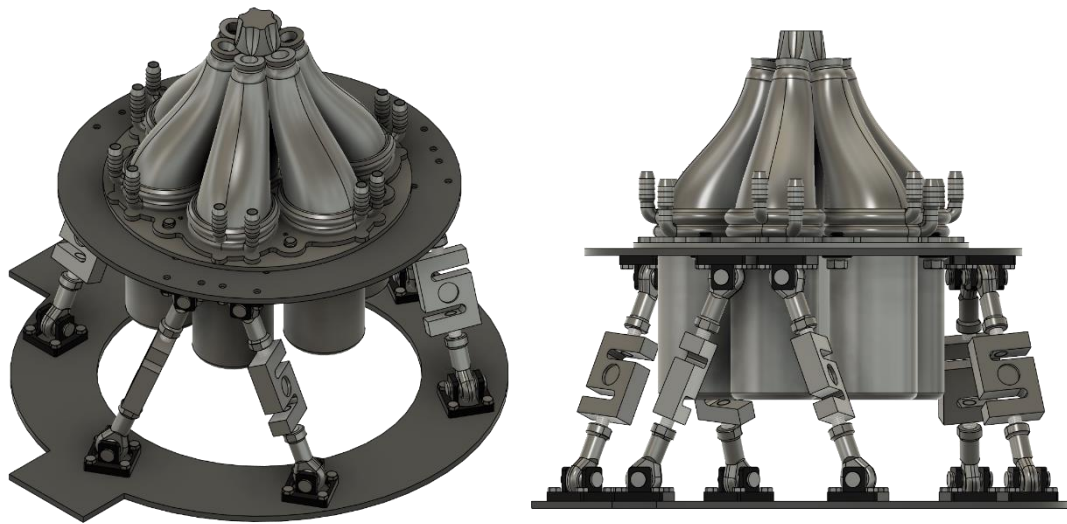


Figure 126: Fully Integrated Assembly

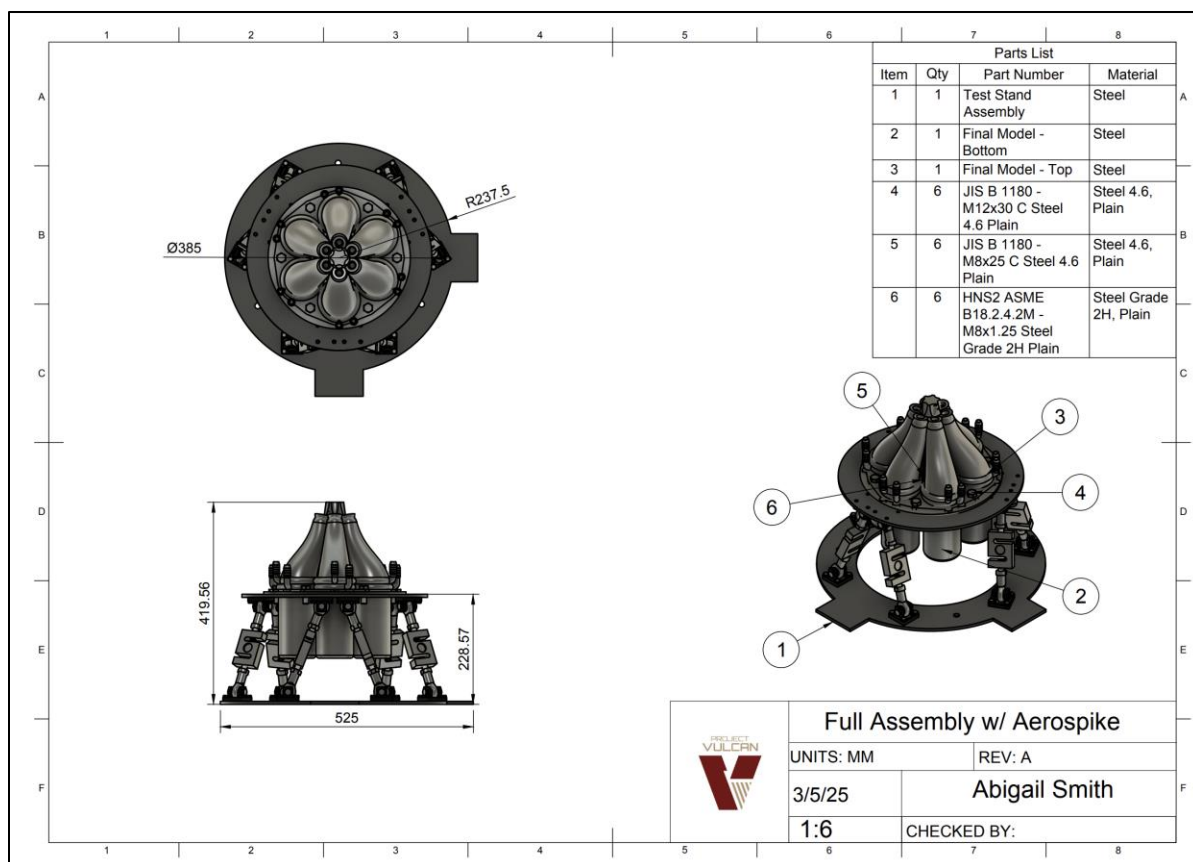


Figure 131: Integrated Aerospike with Test Stand Assembly



6.3.5 Structural Fabrication (Zaharia)

The process of acquiring, manufacturing, and integrating the system's hardware components will be broken down into different phases. These phases align with the project timeline and aim to minimize development costs. Each phase serves as a milestone to validate the progress of the system design, ensuring that once a phase is completed, there is little to no revision needed. This approach streamlines the development process and helps maintain cost-effectiveness and efficiency.

Phase 1 introduces additive manufacturing using PLA/PETG as a material for rapid prototyping. Due to the complex nature of integrating an aerospike structure with a radial nozzle configuration, having a physical model is beneficial for visualizing how components occupy space as well as what improvements can be made after visual inspection. The Harris Student Design Center (HSDC) offers a 3D printing farm which allows students to send in models that can be printed for no cost. This facility will be used extensively to have newly developed CAD models printed to gain physical and visual ability to determine if the new design is capable of being integrated with other artifacts of the project. The most important artifact, other than the spike itself, is the thrust stand that will be used for all the testing that will be performed to verify and validate the aerospike design. It is critical to ensure that with each revision of the spike design, there is the ability to determine what changes need to also be made concurrently to ensure the spike fits within the test stand's allowable range of dimensions.

Numerous meetings were held with the staff at the HSDC to ensure the proper protocols are followed to request a model to be printed. The process to request a print is via the L3HSDC 3D Print Form listed on the Florida Tech website (L3harris Student Design Center: Florida tech 2024). These meetings also helped with understanding the capabilities of the HSDC, specifically to determine what method of printing will be used as well as what material for rapid prototyping. At present state, the HSDC offers Fused Deposition Modeling (FDM), which is one of the most common types of plastic additive manufacturing. Stereolithography (SLA) printing is another available option that is being considered due to the surface finish and accuracy of the print. As this project is heavily dependent on manipulating high-speed fluid, it is imperative that the surface



finish is manufactured in a way that matches the operational environment to minimize losses due to unintended turbulence. Extensive use of the PLA printers allowed for the necessary rapid prototyping of the design and served as a method to physically interact with the model. Having the physical models also serves as a baseline to keep track of design changes as well as conduct fitting tests to ensure the design is compatible with the other systems.

While in the process of Phase 1, research will be done into finding a company that is capable of printing using metal as a material. A company of interest is Solideon, a California-based additive manufacturing company [25]. Their ability to use Direct Energy Deposition (DED) as a manufacturing technique is in line with the goals of this system. DED is a manufacturing process that uses metal feedstock and a laser to fabricate parts [27]. A second type of metal printing that is also of interest, due to its high degree of precision and accuracy, is Laser Powder Bed Fusion (LPBF) printing. LPBF uses a laser to selectively melt metal powders in a powder bed [13]. The design challenge of the aerospike and nozzle structure is the complex geometries that are difficult to achieve using traditional manufacturing techniques. By making use of the advances in additive manufacturing, these difficulties are resolved. The drawback of additive manufacturing is the need to apply post processing to the created part and the cost associated with it. A major concern of using additive manufacturing is the overall finish of the print allows for even flow with minimal turbulence caused by imperfections. Post-processing techniques have been investigated, and a selection will be made depending on the cost and time needed to perform those techniques to ensure the timeline is being followed.

Phase 2 of fabrication will consist of communicating with the selected manufacturer to have the aerospike structure printed and delivered ready to be integrated with the rest of the spike design as well as the thrust stand. As mentioned previously, post processing is a necessary step in preparing the printed artifact for later integration and testing. Talks with the manufacturing company will include a plan for post processing as well as other options to ensure the structure can operate in the anticipated testing conditions. An important design choice is the selection of material for the spike. After further talks with the selected manufacturer, the material that will be chosen for the manufacturing of the aerospike structure as well as the post-processing procedures



will be determined based on the system requirements. The selected post-processing technique will ensure the metal printed article is capable of operating in the anticipated test conditions for multiple firings.

Phase 3 will be full assembly of the spike which includes the shroud and LITVC subcomponents. The manufacturing process for this phase will focus on finding an interface between the fluid reservoir, using a pump to move the fluid, and an interface to the aerospike structure where the selected area is. Further research will be conducted to evaluate the best process for accomplishing this task while remaining within the allocated budget the team has access to. The fabrication of the shroud will be assembled according to CAD model.

Phase 4 is the construction of the custom test stand. Once all the materials for the test stand are acquired the manufacturing process for this item can begin. The two square steel plates will be waterjet cut at the HSDC into rings according to the CAD drawings. The rings mounting holes will be threaded and the clevis brackets will be attached. The struts will be assembled by screwing 12 [mm] all thread bars together with plain spherical bearings and onto an S-beam load cell from both sides. The ring steel plates then will be connected using the struts. The calibration mechanism will then be welded together from square steel pipes according to the CAD drawings.

Numerous meetings have been held with MIMO Technik regarding refining the model and preparing it for their Model SLM 280 LPBF printer. Changes from the old model seen in PDR to CDR have been discussed in Section 6.3.2, but the most critical changes lie in the following items. The first deals with ensuring the aerospike having a minimum thickness of 0.75 [mm]. This was to ensure during the manufacturing process, when the power is melted, there is a reduced chance of warping due to the part's low thickness. The second item was changing the cooling line connection to a teardrop shape to avoid overhang, which is a limitation of metal printers. The third item is having the entirety of the aerospike have a minimum 45 [deg] with respect to the horizontal plane. All the listed design considerations were done in the interest of ensuring the aerospike structure is given the highest chance of print success on the first attempt.

After the extensive meetings with MIMO Technik and their manufacturing team, a formal agreement was reached to have two aerospikes printed using AlSi10Mg as the material. The



discussions also included post processing measures such as support removal as well as heat treatment to ensure the right internal crystal grain structure to allow for STRUCT.02 to be compliant. The decision to utilize AlSi10Mg as the material was driven by the cost associated with other material choices as well as the ability to obtain two aerospike instead of one. The high heat transfer of the material ensured STRUCT.01 was satisfied when integrated with the water pump cooling system. Another key negotiated feature during the discussions with MIMO Technik was the option to obtain a student discount, which was negotiated to a 30 percent reduction in cost for the second aerospike. The aerospikes were also shipped overnight by MIMO Technik, which greatly reduced the logistical challenges of the project.

6.4 Control Requirements and Technical Approach

6.4.1 Control Subsystem Requirements (Smith, Zaharia, Leita, Bedelbaev)

The control system is a critical component of Project Vulcan, overseeing essential operational parameters and ensuring the safe and precise functionality of the propulsion system. In this context, the control subsystem fulfills multiple roles: it initiates and monitors engine operations, facilitates real-time data capture, and regulates the flow of liquids to the LITVC system. By enabling controlled, remote ignition and shutdown capabilities (where applicable), recording performance data, and managing thrust vectoring mechanics, the control system ensures that testing protocols meet both safety standards and functional requirements.

The requirements detailed in Table 6 outline the specific controls needed to safely operate the propulsion system and support thrust vector control during testing. Each requirement is designed to address a unique aspect of engine control, from remote start capabilities to real-time performance monitoring and precise liquid management for the LITVC system. Collectively, these controls ensure the system's stability, responsiveness, and compliance with operational protocols throughout all phases of testing.

Table 6: Control Subsystem Requirements

Parent	Requirement #	Requirement	Rationale	Verification Method	Verification Strategy	Supporting Page #	Status
SYS.05	CONTR.01	The control system shall be capable of initiating the engine start sequence remotely.	Remote start capability is crucial for operational safety, allowing controlled ignition initiation while ensuring personnel are safely distanced from the propulsion system.	Test	Perform remote ignition tests to verify the control system's start capability and operational safety.	165, 169, 171, 173, 175, 184, 189, 224, 241	Fully Compliant
SYS.05	CONTR.02	The control system shall record thrust data for engine performance parameters to a ground station.	Real-time thrust data is essential for monitoring engine performance and making informed decisions for post-flight analysis, enhancing system reliability.	Demonstration, Test	Demonstrate the system's capability to transmit accurate thrust data to the ground station during engine operations.	149, 165, 168, 169, 171, 173, 175, 181, 186, 189, 224, 241	Fully Compliant
SYS.03	CONTR.03	The control system shall regulate liquid supply to the LITVC system during engine operation.	Precise control over the LITVC liquid supply is necessary to maintain stable and responsive thrust vectoring, ensuring effective maneuverability and control during testing.	Demonstration, Test	Verify liquid flow control functionality by testing system responses at various thrust vectoring angles.	165, 169, 173, 186, 224	Fully Compliant



Explanations of Controls Subsystem Requirements

CONTR.01 - The control system shall be capable of initiating the engine start sequence remotely.

Remote ignition capability is a fundamental safety feature for handling solid propellant engines. By enabling a remote start, the system ensures personnel can be distanced from the engine at the moment of ignition, significantly reducing risk. This feature also aligns with autonomous testing protocols, allowing precise control over the ignition sequence. The requirement will be verified through remote ignition tests to confirm operational safety and reliability.

CONTR.02 - The control system shall record thrust data for engine performance parameters to a ground station.

Recording thrust data in real time is vital for assessing the engine's operational state and overall performance. This data allows engineers to evaluate thrust fluctuations, performance consistency, and any unexpected deviations during testing. This requirement will be validated through demonstration and testing, ensuring the data is accurately captured and transmitted to the ground station for subsequent analysis.

CONTR.03 - The control system shall regulate liquid supply to the LITVC system during engine operation.

For effective thrust vectoring, the control system must manage the precise injection of liquid into the LITVC system, directly influencing the thrust vector and thereby affecting the vehicle's directional control. This requirement ensures that the control system can modulate liquid flow according to the vectoring demands, allowing for accurate steering and stability. This functionality will be verified by testing the system's response across various vectoring scenarios, confirming that the control system can maintain stable thrust direction.

6.4.2 Control Design (Bedelbaev)

The control system integrates hardware and software systems to manage all operational aspects of the aerospike. Remote ignition capabilities are implemented through an ignition module, ensuring controlled activation capabilities. To facilitate effective thrust vectoring, the system employs a flow actuator that manages liquid injection into the LITVC system. And a data acquisition system (DAQ) captures critical sensor data such as thrust, pressure, and video transmitting it in real-time to a ground station for processing and analysis.

Ignition System

The ignition system consists of ignitors connected to long wires, allowing the engine to be started from a safe distance. The wires are linked to switches housed in a control box and powered by an external battery, ensuring reliable operation during tests. This setup enables precise ignition control while keeping participating members of the team and any other personnel away from the engine at the moment of activation. The switches are designed for straightforward operation, integrating seamlessly with the broader control system.

LITVC Control

The LITVC control system regulates the liquid injection into the aerospike's thrust vectoring system using a pump control switch. This switch is housed within the same control box as the ignition system, offering a consolidated interface for ease of use. The pump control switch ensures precise modulation of liquid flow to the LITVC system, enabling activation of thrust vectoring during testing. This integration simplifies operations, as both the ignition and LITVC controls can be managed from a single unit, enhancing operational efficiency and safety.

Data Acquisition System (DAQ)

The DAQ system is built around microcontroller boards connected to sensors attached to the aerospike engine. These sensors monitor thrust, pressure, and other critical parameters, transmitting the data to a laptop running MATLAB for data acquisition and analysis. The microcontroller units serve as the interface between the sensors and the laptop, ensuring sufficient



frequency and accurate data collection. This setup enables efficient monitoring of engine performance, supporting both immediate oversight and post-test evaluations.

By organizing these components within a unified framework, the control system is optimized for functionality, safety, and ease of operation. Each subsystem will need to be rigorously tested and calibrated to meet the project's requirements, as well as ensuring reliable performance during all testing phases.

6.4.3 Control Fabrication (Zaharia, Bedelbaev)

The fabrication of the control system does not require complex circuitry for operation. The ignition system will be used to send a current through wires that are connected to electronic matches. The LITVC control system will feature a simple on/off switch to operate the water pump. Lastly, the DAQ control system will rely on a laptop running Python data acquisition code (Appendix E) to manage and process data, therefore no fabrication is required. The data acquisition code ensures CONTR.02 is satisfied by having all the thrust data collected for further analysis. The DAQ system was able to collect each static fire test data as well as allow for the results to be visualized in the form of a thrust vector. Having this ability allowed PROP.02 to be satisfied.

7 TECHNICAL BUDGETS

7.1 Mass Budget (Zaharia, Hartlieb)

The mass budget for this project falls under the need to ensure the test article, in this case the aerospike structure in the test configuration is compatible with the test stand's operating ranges. Since the fabrication will be outsourced to a selected company, there are concerns about the cost associated with the amount of material that will be required for the structure as well as the associated shipping costs. The design of the spike will reference the system/subsystem requirements for factor of safety to ensure the part can operate in the desired test conditions while minimizing the need for excess material unless required by the design. The projected mass values can be seen in Table 7. An important item to note is the difference between the dry and wet mass of the system. The dry mass refers to the assembly of the 3D printed portion and the motor housing without the propellant grains whereas the wet mass includes the mass of the propellant grains.

Table 7: Mass Budget

System Component	Mass (kg)
Aerospike 3D Print	3.40
Motor Housing	11.59
Propellant Grain (x6)	3.54
Test Stand	15.27
Total Dry Mass	30.26
Total Wet Mass	33.80

7.2 Electrical Power Budgets (Sanchez, Bedelbaev)

The following electrical power budget defines the power requirement for Project Vulcan during all operational phases. During the testing phase of the project the system's primary power consumption comes from the data acquisition and processing unit as well as load sensors for running the test stand. The budget accounts for both the power requirements of these components and the total energy requirement for a full calibration and testing sessions. The system also technically does not require a power budget as there are no units that operate independently or exceed power consumption.

7.2.1 Power Budget

The Table 8 shows below the summarized power consumption for each component during a typical testing session.

Table 8: Power Budget

System Component	Power Provided/Consumed (Watts)
Laptop Power Supply	+ 250.0
Laptop	- 180.0
Load Cells (6 units)	- 1.5
Load Cell Amplifiers (6 units)	- 3.0
Margin	+ 65.5

The load cells and amplifiers consume minimal power during operation. The laptop, which acts as the data acquisition/processing unit and serves as the primary control interface, consumes most of the power demand. The power supply selected for the system exceeds power requirements of the operation, giving a margin of 65.5 [W].

The LITVC pump is not included in the power as it is not a part of a regular testing procedure.

7.3 Data Budgets (Sanchez, Bedelbaev)

The data budget for this project estimates the total storage and processing requirements for collecting sensor and video data during a 5-second static fire test. This includes contributions from load cells, high-resolution video recordings, and data acquisition overhead.

Table 9: Data Budget

Component	Parameters	Data Per Test (5 second Duration)
Load Cells	6 units, 16-bit resolution, 1 [kHz] sample rate	60 [kB]
Pressure Transducer	1 unit, 16-bit resolution, 1 [kHz] sample rate	10 [kB]
DAQ Overhead	Metadata, headers, and system-level overhead (~10% of sensor data)	6 [kB]
Video Recording	4k resolution, 60 [fps], H.264 encoder (~30 [MB/sec])	150 [MB]
Total (Per Test)		150.076 [MB]

With a load cell sample rate of 1 kHz per sensor, each load cell produces 10 [kB] of data during a 5-second test, amounting to 60 [kB] for six load cells. Additionally, there will be a pressure transducer installed for the altitude simulation shroud to validate its performance. The dominant contributor to the data budget is the 4K video recording at 60 [fps], which generates approximately 150 [MB] per test due to the increased frame rate and high resolution. The DAQ overhead, calculated as 10% of the sensor data, accounts for metadata such as time stamps, packet headers, and synchronization information, ensuring accurate and organized data collection for post-test analysis. While small in size, the overhead is essential for aligning sensor data with video and maintaining the integrity of the dataset.

8 FINANCIAL BUDGET / BILL OF MATERIALS / SCHEDULE (LEITA)

8.1 Budget/Bill of Materials

Table 10: Bill of Materials

Item	Item Dimensions	Quantity	Unit Cost (\$)	Total Cost (\$)	Status
Clear Vinyl Tubing	1/2" ID x 5/8" OD x 10 ft	1	6.83	6.83	Arrived
Hose Clamp	3/8" - 7/8"	14	1.98	25.74	Arrived
Clevis Brackets	45 mm x 45 mm x 30 mm	6	9.99	59.94	Arrived
S-Beam Load Cells (50 kg)	50.8 mm x 19 mm x 76.2 mm	6	41.15	246.90	Arrived
Steel Plate (Small)	15.5" x 15.5" x 1/4"	1	77.36	77.36	Arrived
Steel Plate (Large)	21" x 21" x 1/4"	1	77.36	77.36	Arrived
Aluminum 80/20 Extrusions	Varying	8	0.00	0.00	Arrived
1 st Metal 3D Printed Spike	273.6 mm x 295 mm x 186 mm	1	9,884.24	9,884.24	Arrived
2 nd Metal 3D Printed Spike	273.6 mm x 295 mm x 186 mm	1	7,128.91	7,128.91	Arrived
Plain Spherical Bearings x4	32 mm x 19 mm	3	9.59	28.77	Arrived
Load Cell Amplifiers x4	33 mm x 20 mm	2	6.99	13.98	Arrived
290 GPM Water Pump	18" x 22" 18"; 6.5 hp	1	399.99	399.99	Arrived
Pressure Sensor 0-0.5 MPa	3.94" x 1.97" x 1.18"	1	25.72	25.72	Arrived
High Temp Silicone O-Rings	0.139" WD x 3.109" ID x 3.387" OD	60	13.63	81.78	Arrived
Classic Propellant Grain	75 mm	54	31.99	1,727.46	Arrived
Electric Matches	1 ft	1	56.80	56.80	Arrived
Steel Tube	65 mm ID x 5 3/8" OD	6	34.61	207.63	Arrived
Shroud Tube	6" ID x 6.75" OD x 5 ft	1	0.00	0.00	Arrived
Hose Barb	1/2" ID x 3/8" MIP	2	5.05	10.10	Arrived
Vinyl Tubing	3/8" x 10 ft	1	2.96	2.96	Arrived
Barb Adapter	3/8" ID x 3/8" MIP	1	5.48	5.48	Arrived
Barb Adapter	3/8" ID x 1/4" MIP	1	4.48	4.48	Arrived
Engine Cylinder Hone	2" to 7"	1	26.99	26.99	Arrived
Stainless Steel Barb Fittings	1/2" Barb x 3/4" MNPT	1	22.99	22.99	Arrived
High P Braided Vinyl Tubing	1/2" ID x 3/4" OD - 50 ft	1	37.66	37.66	Arrived
Probe Camera w/ Light	7.72 x 5.39 x 3.19 in	1	35.99	35.99	Arrived
Pressure Transducer	30 PSI	1	21.79	21.79	Arrived
Generator	15 kW	1	840.00	840.00	Arrived
Water Pump	GRUNDFOS	1	0.00	0.00	Arrived
Manifold (Flow Diverter)	1" NPT in, 1/2" NPT Out	1	126.97	126.97	Arrived

Vermiculite Gasket	24" Wd. 0.064" thick	2	74.27	148.54	Arrived
Subtotal				21,347.34	
Contingency (1%)				213.47	
Shipping				108.40	
Total (Estimate)				21,669.21	
Provided Funds				1,750.00	
Raised Funds				19,936.22	
Budget (Right Now)				21,686.22	
Difference				17.01	

8.1.1 Resource Strategy and Procurement Framework

The material acquisition strategy for Project Vulcan was shaped by a hybrid model that blended conventional procurement with institutional partnerships, in-kind donations, and resource reuse. This multifaceted approach enabled the team to meet ambitious design and testing objectives while staying within 99.92% of its \$21,686.22 budget. The team maintained operational readiness throughout the design, integration, and static fire phases by aligning procurement with technical criticality and lead-time sensitivity.

8.1.2 Strategic Donations and Institutional Partnerships

Key components of the propulsion and test infrastructure were provided through generous donations from academic and industry collaborators. Foremost among these were the two AlSi10Mg 3D-printed clustered chamber aerospikes, manufactured by MIMO Technik and fully funded via sponsorship from Solideon, Educate the Children Foundation, Vaya Space, and Panther Works. These contributions eliminated nearly \$17,000 in direct manufacturing costs and allowed financial bandwidth for thrust sensing instrumentation, DAQ systems, and combustion hardware.

In addition to additive-manufactured components, the structural backbone of the altitude-simulating shroud mount was constructed using aluminum 80/20 extrusions provided at no cost by the L3Harris Student Design Center (L3HSDC). This modular hardware facilitated iterative integration and was central to the project's just-in-time strategy. Dr. Kirk further supported the project by supplying the large-diameter steel pipe used to fabricate the shroud structure. This high-

value donation enabled the team to simulate nozzle backpressure conditions for atmospheric stand-in testing without incurring additional material costs or machining delays.

8.1.3 Procurement Philosophy and Risk Mitigation

Procurement was executed with a tiered criticality model: components essential to propulsion functionality or long-lead fabrication were prioritized in early funding cycles. At the same time, auxiliary items were ordered closer to integration milestones. The Classic Propellant Grains from RCS, identified as both cost-intensive and schedule-critical, were ordered proactively. Despite potential shipping uncertainties, strong supplier communication and built-in schedule flexibility ensured their timely arrival before the first firing window.

The net effect of this procurement framework was a streamlined integration pipeline that minimized idle time, prevented hardware starvation during test prep, and supported nine successful static fire tests. The financial and material strategy behind Project Vulcan reflects a synthesis of Lean supply chain thinking and tactical academic resource utilization, offering a replicable model for complex undergraduate engineering programs.



9 TEST PLANNING (SMITH)

9.1 Test Series Summary (Smith)

To verify that the design and prototype will meet the specified requirements, the five test procedures outlined below in Table 11 will be executed. This table includes a short summary of each test that was conducted. This includes their respective objectives, the subsystem requirements that will be verified, and the test location with other needed details. These test plans will validate and verify the assembly, functionality, structural integrity, calibration, and performance of each component used in the metal 3D-printed aerospike and test stand configuration.

For the PDR and CDR document there were originally only five test plans discussed. The fifth and final test plan was separated into three separate parts but put within the same test document. This was done because the team anticipated that the team would be able to complete all three parts within the same day. However, it took much longer than expected to set-up the static fire tests. Another issue with having the three parts combined into one procedure was that the document became very long. The test reports for this also were long. It ended up just being easier to separate them. Therefore, there are now seven test procedures and reports.

Table 11: Test Plans

Test #	Test Name	Description of Test (test objectives and what physical item will be tested)	Verified Requirements	Test Location and Date	Status
01	3D Printed PLA Model and Test Stand Fitting	Validation that the aerospike design fits the test stand as designed before moving forward with metal 3D printing. It is also to validate that the test stand is correctly assembled.	SYS.01, SYS.02, SYS.05, STRUCT.04, SAF.01, SAF.02, AND SAF.05.	This test was conducted at the HSDC on 03Apr25.	Fully compliant
02	Test Stand Data Collection and Electronic System Verification	Verification that the test stand was calibrated correctly, that the sensors record and report accurate data for the force and moment, that the Python script works properly, and confirm that the control system properly integrates with the sensors.	SYS.02, SYS.05, STRUCT.04, CONTR.02, SAF.01, SAF.02, SAF.05.	This test was conducted at the HSDC on 14Apr25.	Fully compliant
03	Six A8-3 Solid Rocket Motor Configuration Test Fire with E-Match Ignitor	Validation that a singular A8-3 solid rocket motor can be lit using an MJG Firewire Initiator then further validated by lighting a six A8-3 solid rocket motor configuration simultaneously using six MJG Firewire Initiators.	SYS.02, CONTR.01, SAF.01, SAF.04, and SAF.05.	This test was conducted on private property on 24Feb25.	Fully compliant.
04	LITVC Wet Dress Rehearsal	Validation that the LITVC system is integrated and functions as designed and that the data being collected is recorded and accurate.	SYS.01, SYS.02, SYS.03, SYS.05 PROP.02, STRUCT.04, CONTR.02, CONTR.03, SAF.01, SAF.03, and SAF.05.	This test was conducted at Vaya Space on 21Apr25.	Fully compliant.
05	Fully Integrated Metal 3D-Printed Aerospike Static Fire Test	Validation that the whole system, which includes the fully assembled metal 3D-printed aerospike mounted on the test stand configuration with the calibrated electrical system, six solid rocket motors configuration with six MJG Firewire Initiators, and 75mm Classic™ Propellant Grain works together as designed as well as ignites safely and properly.	SYS.01, SYS.02, SYS.05, PROP.01, STRUCT.01, STRUCT.02, STRUCT.03, STRUCT.04, CONTR.01, CONTR.02, SAF.01, SAF.02, SAF.03, SAF.04, and SAF.05.	This test was conducted at Vaya Space on 17Apr25, 19Apr25, 21Apr25, and 22Apr25.	Fully compliant.
06	Fully Integrated Metal 3D-Printed Aerospike with Integrated LITVC System	Validation that the whole system with the integrated LITVC efficiently imposes lateral thrust, works together as designed, and ignites safely and properly.	SYS.01, SYS.02, SYS.03, SYS.05, PROP.01, PROP.02, STRUCT.01, STRUCT.02, STRUCT.03, STRUCT.04, CONTR.01, CONTR.02, CONTR.03, SAF.01, SAF.02, SAF.03, SAF.04, and SAF.05.	This test was conducted at Vaya Space on 21Apr25 and 22Apr25.	Fully compliant.
07	Fully Integrated Metal 3D-Printed Aerospike with Altitude Simulation Shroud	Validation that the whole system with the altitude simulation shroud can simulate an altitude of up to 25 [km], works together as designed and ignites safely and properly.	SYS.01, SYS.02, SYS.04, SYS.05, PROP.01, PROP.03, STRUCT.01, STRUCT.02, STRUCT.03, STRUCT.04, CONTR.01, CONTR.02, SAF.01, SAF.02, SAF.03, SAF.04, and SAF.05.	This test was conducted at Vaya Space on 21Apr25.	Fully compliant.



Test Details and Success Criteria:

01. 3D Printed PLA Model and Test Stand Fitting:

The first test will validate that the aerospike design fits within the fully assembled test stand as designed before moving forward with metal 3D-printing. It will also validate that the test stand is correctly assembled. This test procedure was executed at the L3Harris Student Design Center (HSDC) on April 3rd, 2025. *ENG-PLN-001-REV-D 3D Printed PLA Model and Test Stand Fitting Test Plan* (See Appendix C) is the detailed test procedure document that goes through the test step by step and includes photos.

To begin the test, the final aerospike design specified in the engineering drawing *REV B Final Model - Top Drawing* (See Appendix F) and the motor casing design specified in the engineering drawing *REV B Motor Casing Drawing* (See Appendix F) will be printed using PLA in the HSDC. After it has been printed, it will be visually inspected to ensure there are no cracks or other visible anomalies. Both will then be validated by completing a dimensional inspection report. Use documents *DIR-ENG-001-REV-C-Top* and *DIR-ENG-001-REV-C-Bottom* (See Appendix D) to record the specified dimensions.

Next, the test stand configuration specified in the engineering drawing *REV F Test Stand Assembly Drawing* (See Appendix F) will be assembled following the procedure written in *ENG-PLN-001-REV-D 3D Printed PLA Model and Test Stand Fitting Test Plan* (See Appendix C). After the test stand has been assembled, it will be visually verified to ensure that there are no visible gaps, misalignments, or any other anomalies. It will also be validated by completing a dimensional inspection report. Use the document *DIR-ENG-002-REV-C* (See Appendix D) to record the specified dimensions. After all three of the dimensional inspection reports are completed, the aerospike will be installed onto the test stand. It will then be visually verified to ensure that the model correctly fits the test stand as designed and has no visible gaps, misalignments, or any other anomalies.



During assembly of the test stand, impact safety glasses and steel-toed boots will be required to be worn when using hand tools, grinders, and motorized/electrical tools in case something breaks, falls, etc. When handling sharp objects and metal, protective gloves will be required. When sanding an object or performing other operations where there are potential infectious materials, a dust mask is required to protect the respiratory system.

This test will be considered successful if the 3D printed PLA aerospike model properly fits within the fully assembled test stand without any visible gaps, misalignments, cracks, or breakage. If the test stand configuration is assembled correctly, ensuring stability and balance. The system and subsystem requirements SYS.01, SYS.02, SYS.05, STRUCT.04, SAF.01, SAF.02, AND SAF.05 must be validated. Each one of these specifications must be passed to be considered successful. If one or more fails, it will only be considered a partial success or failure depending on the amount that passes.

02. Test Stand Data Collection and Electronic System Verification:

The second test will verify that the test stand configuration has been calibrated correctly and ensure that the sensors accurately record and report force and moment data that will be generated by the aerospike. Additionally, it will validate the functionality of the Python script and confirm that the control system properly integrates with the sensors. Once the system is assembled and installed in the test stand, a visual inspection will be conducted to ensure that all wiring is secure, with no loose connections or interference. This test procedure was executed at the HSDC on April 14th, 2025. Detailed step-by-step instructions, along with supporting photos, can be found in *ENG-PLN-002-REV-D Test Stand Data Collection and Electronic System Verification* (See Appendix C).

To begin the test, the DAQ box and overall electrical system needs to be set up and installed onto the test stand. The electrical schematic *ELE-ENG-001-REV-D* (See Appendix F) will be followed to create this. The installation and calibration process will be completed following the procedure written in *ENG-PLN-002-REV-C Test Stand Data Collection and Electronic System Verification* (See Appendix C). This test procedure also details how to run the Python code.



Impact safety glasses must be worn when using hand tools, grinders, motorized/electrical tools, or while soldering any electrical components. Steel-toed boots must be worn while moving or working with the calibration weights and moving the test stand. Protective gloves will be required when handling sharp objects and metal. When soldering any electrical schematics, a solder fume extractor must be used. This will be considered successful if the sensors record and report the correct data for the force and moment the aerospike generates. Success is also contingent upon the proper calibration of the test stand and sensors and the correct control system connection to both the sensors and the Python script. Additionally, the data collected from the sensors, control system, and Python script must align with the theoretical values. The system and subsystem requirements SYS.02, SYS.05, STRUCT.04, CONTR.02, SAF.01, SAF.02, SAF.05 must be verified. Each one of these specifications must be passed to be considered successful. If one or more fails, it will only be considered a partial success or failure, depending on the amount that passes.

03. Six A8-3 Solid Rocket Motor Configuration Test Fire with MJG Firewire Initiators:

The third test will validate that a singular A8-3 solid rocket motor can be lit successfully and safely using only one MJG Firewire Initiator. It will also validate that a configuration of six A8-3 solid rocket motors can be properly and safely ignited simultaneously using six MJG Firewire Initiators. This test procedure will be executed on private property on February 24th, 2025. Detailed step-by-step instructions, along with supporting photos, can be found in *ENG-PLN-003-REV-C Six A8-3 Solid Rocket Motor Configuration Test Fire with MJG Firewire Initiators* (See Appendix C).

Both the single and six A8-3 solid rocket motor configurations will be visually inspected and validated before ignition. Safety protocols will be strictly followed throughout all hot fire tests. Impact safety glasses and ear protection must be worn at all times during ignition testing. While handling the fuel grain, nitrite gloves must be worn.



The test will be considered successful if the singular A8-3 solid rocket motor properly and safely ignites using a singular MJG Firewire Initiator. If the six A8-3 solid rocket motor configuration properly and safely ignites simultaneously by using six MJG Firewire Initiators. The system and subsystem requirements SYS.02, CONTR.01, SAF.01, SAF.04, and SAF.05 must be validated. Each one of these specifications must be passed to be considered successful. If one or more fails, it will only be considered a partial success or failure depending on the amount that passes.

04. LITVC Wet Dress Rehearsal:

The fourth test will validate that the LITVC system is integrated, and functions as designed in the metal aerospike and that the thrust and deflection data being collected is being properly recorded. This test procedure was executed at Vaya Space on April 21st, 2025. Detailed step-by-step instructions, along with supporting photos, can be found in *ENG-PLN-004-REV-E LITVC Wet Dress Rehearsal* (See Appendix C).

The first part of this test procedure is to visually verify the system before continuing forward with the test. This will be done by inspecting the test stand, aerospike engine, cooling channel system, and DAQ system for any cracks, misalignments, or wiring issues. The test stand will then be installed to the test pad followed by installing the aerospike to the test stand. The test stand will then need to be calibrated by following the steps written in the procedure. Once the test stand has been calibrated, the fluid delivery system will be set up and tested following the test procedure. The LITVC will then be tested on its functionality. This will be done by running water through the LITVC system, observing the ejection pattern, and checking for leaks after shutdown.

The test will be considered successful if nothing blocks the water flow and the water is able to flow properly through the integrated LITVC as designed. The system and subsystem requirements SYS.01, SYS.02, SYS.03, SYS.05 PROP.02, STRUCT.04, CONTR.02, CONTR.03, SAF.01, SAF.03, and SAF.05 must be validated. Each one of these specifications must be passed to be considered successful. If one or more fails, it will only be considered a partial success or failure depending on the amount that passes.

05. Fully Integrated Metal 3D-Printed Aerospike Static Fire Test:

The fifth test will validate the whole system, which includes the fully assembled metal 3D-printed aerospike mounted on the test stand configuration with the calibrated electrical system, six solid rocket motors configuration with six MJG Firewire Initiators, 75mm Classic™ Propellant Grain, and a water-cooling subsystem controlled via a manifold and pump. This test procedure was executed at Vaya Space on April 17th, 19th, 21st, and 22nd 2025. Detailed step-by-step instructions, along with supporting photos, can be found in *ENG-PLN-005-REV-E Fully Integrated Metal 3D Printed Aerospike* (See Appendix C).

Before each part of the test and before every static firing, visual verification of the test stand, aerospike engine, propellant grain, and DAQ system will be conducted. It will be visually verified that the aerospike engine fits securely in the test stand without visible gaps and that all wiring connections are secure and free of interference. Additionally, each propellant grain is checked for any cracks or defects that could impact performance or safety. Throughout the duration of all static fire tests, earplugs must be worn. While handling the fuel grain, rocket candy, or ignitors nitrite gloves must be worn. This test will be a static fire test with the fully assembled test stand and metal 3D-printed aerospike configuration. The DAQ system will be configured to record thrust vectoring data in real time.

The first part of the test procedure is to secure pieces of rocket candy with masking tape to the ignitor side of the e-matches then feed them through the engine and tape it to the fuel grain. A vermiculite gasket will then be placed in between the bottom of the metal 3D-printed aerospike and the top of the motor casings. The cooling system used in *ENG-PLN-004-REV-E LITVC Wet Dress Rehearsal* (See Appendix C) will be set up for heat management. The ignitor wires will then be installed to the battery-powered ignition box where they will then be checked with a multimeter to verify connection.



The entire configuration will then be visually inspected for any anomalies. Once verified, the first test firing can commence. Multiple cameras will then be set up around the aerospike to record each firing. Next, connect the positive and negative wires from the bottom of the ignition box to the positive and negative leads of the battery. Now set up the DAQ system and Python script to record the three-dimensional thrust vector. Once the cameras have started recording and all personal have moved behind the concrete wall, start the fluid delivery system. Now turn on the power to the ignition box. It is very important that this is done last before ignition. Once all of these steps have been completed, the ignition switch can be pressed to conduct the first test run.

After the test fire is complete, turn off the water pump, close the designated valves, and click the “Stop” button, which will automatically save a file with all the relevant data required for post processing. Allow the engine to cool completely before interacting with it. Repeat this process two times for a total of three test runs, conducting visual inspections between each test run to verify that no anomalies have occurred. Also ensure that the data is being properly recorded and saved from each test firing.

The test will be considered successful if the prototype and system components function as designed, operating seamlessly as an integrated system. If the system ignites properly and safely with six MJG Firewire Initiators and 75mm Classic™ Propellant Grain. If the system functions properly and safely with the calibrated sensors, electrical configuration, and the Python script. The system and subsystem requirements SYS. 01, SYS.02, SYS.05, PROP.01, STRUCT.01, STRUCT.02, STRUCT.03, STRUCT.04, CONTR.01, CONTR.02, SAF.01, SAF.02, SAF.03, SAF.04, and SAF.05.

06. Fully Integrated Metal 3D-Printed Aerospike with Integrated LITVC Static Fire Test:

The sixth test will validate the whole system, which includes the fully assembled metal 3D-printed aerospike mounted on the test stand configuration with the calibrated electrical system, six solid rocket motors configuration with six MJG Firewire Initiators, 75mm Classic™ Propellant Grain, and a water-cooling subsystem controlled via a manifold and pump with the integrated LITVC. This test procedure was executed at Vaya Space on April 21st and 22nd 2025. Detailed step-by-step instructions, along with supporting photos, can be found in *ENG-PLN-006-REV-E LITVC System* (See Appendix C).

Before each part of the test and before every static firing, visual verification of the test stand, aerospike engine, propellant grain, and DAQ system will be conducted. It will be visually verified that the aerospike engine fits securely in the test stand without visible gaps and that all wiring connections are secure and free of interference. Additionally, each propellant grain is checked for any cracks or defects that could impact performance or safety. Throughout the duration of all static fire tests, earplugs must be worn. While handling the fuel grain, rocket candy, or ignitors nitrite gloves must be worn. This test will be a static fire test with the integrated LITVC system, fully assembled test stand, and metal 3D-printed aerospike configuration. The main focus of this test will be on LITVC and if it efficiently imposes lateral thrust for the aerospike by using the same fluid delivery system used in *ENG-PLN-004-REV-E LITVC Wet Dress Rehearsal* (See Appendix C).

The first part of the test procedure is to attach a brass hose barb and hose to the LITVC port of the metal 3D-printed aerospike. Next, secure pieces of rocket candy with masking tape to the ignitor side of the e-matches then feed them through the engine and tape it to the fuel grain. A vermiculite gasket will then be placed in between the bottom of the metal 3D-printed aerospike and the top of the motor casings. The cooling system used in *ENG-PLN-004-REV-E LITVC Wet Dress Rehearsal* (See Appendix C) will be set up for heat management. The ignitor wires will then be installed to the battery-powered ignition box where they will then be checked with a multimeter to verify connection.



The entire configuration will then be visually inspected for any anomalies. Once verified, the first test firing can commence. Multiple cameras will then be set up around the aerospike to record each firing. Next, connect the positive and negative wires from the bottom of the ignition box to the positive and negative leads of the battery. Now set up the DAQ system and Python script to record the three-dimensional thrust vector. Once the cameras have started recording and all personal have moved behind the concrete wall, start the fluid delivery system. Right before turning the power to the ignition box on, open the valve that controls the LITVC. Now turn on the power to the ignition box. It is very important that this is done last before ignition. Once all of these steps have been completed, the ignition switch can be pressed to conduct the first test run.

After the test fire is complete, turn off the water pump, close the designated valves, and click the “Stop” button, which will automatically save a file with all the relevant data required for post processing. Allow the engine to cool completely before interacting with it. Repeat this process two times for a total of three test runs, conducting visual inspections between each test run to verify that no anomalies have occurred. Also ensure that the data is being properly recorded and saved from each test firing.

The test will be considered successful if nothing blocks the water flow and the water is able to flow properly through the integrated LITVC as designed and if it efficiently imposes lateral thrust for the aerospike by using the same fluid delivery system used in the wet dress rehearsal. The system and subsystem requirements SYS. 01, SYS.02, SYS.03, SYS.05, PROP.01, PROP.02, STRUCT.01, STRUCT.02, STRUCT.03, STRUCT.04, CONTR.01, CONTR.02, CONTR.03, SAF.01, SAF.02, SAF.03, SAF.04, and SAF.05 must be validated. Each one of these specifications must be passed to be considered successful. If one or more fails, it will only be considered a partial success or failure depending on the amount that passes.



07. Fully Integrated Metal 3D-Printed Aerospike with Altitude Simulation Shroud Static Fire Test:

The seventh test will validate the whole system, which includes the fully assembled metal 3D-printed aerospike mounted on the test stand configuration with the calibrated electrical system, six solid rocket motors configuration with six MJG Firewire Initiators, 75mm Classic™ Propellant Grain, and a water-cooling subsystem controlled via a manifold and pump with the altitude simulation shroud. This test procedure was executed at Vaya Space on April 21st 2025. Detailed step-by-step instructions, along with supporting photos, can be found in *ENG-PLN-007-REV-E Altitude Simulation Shroud* (See Appendix C).

Before each part of the test and before every static firing, visual verification of the test stand, aerospike engine, propellant grain, and DAQ system will be conducted. It will be visually verified that the aerospike engine fits securely in the test stand without visible gaps and that all wiring connections are secure and free of interference. Additionally, each propellant grain is checked for any cracks or defects that could impact performance or safety. Throughout the duration of all static fire tests, earplugs must be worn. While handling the fuel grain, rocket candy, or ignitors nitrite gloves must be worn. This test will be a static fire test with the altitude simulation shroud, metal 3D-printed aerospike configuration, and the test stand. The main focus of this test will be on the altitude simulation shroud.

The first part of the test procedure is to secure pieces of rocket candy with masking tape to the ignitor side of the e-matches then feed them through the engine and tape it to the fuel grain. A vermiculite gasket will then be placed in between the bottom of the metal 3D-printed aerospike and the top of the motor casings. The cooling system used in *ENG-PLN-004-REV-E LITVC Wet Dress Rehearsal* (See Appendix C) will be set up for heat management. Next the altitude simulation shroud test stand, bottom plate, sensor, and tube will be set up. The ignitor wires will then be installed to the battery-powered ignition box where they will then be checked with a multimeter to verify connection.



The entire configuration will then be visually inspected for any anomalies. Once verified, the first test firing can commence. Multiple cameras will then be set up around the aerospike to record each firing. Next, connect the positive and negative wires from the bottom of the ignition box to the positive and negative leads of the battery. Now set up the DAQ system and Python script to record the three-dimensional thrust vector. Once the cameras have started recording and all personal have moved behind the concrete wall, start the fluid delivery system. Now turn on the power to the ignition box. It is very important that this is done last before ignition. Once all of these steps have been completed, the ignition switch can be pressed to conduct the first test run.

After the test fire is complete, turn off the water pump, close the designated valves, and click the “Stop” button, which will automatically save a file with all the relevant data required for post processing. Allow the engine to cool completely before interacting with it. Repeat this process two times for a total of three test runs, conducting visual inspections between each test run to verify that no anomalies have occurred. Also ensure that the data is being properly recorded and saved from each test firing.

The test will be considered successful if the prototype and system components function as designed, operating seamlessly as an integrated system. If the system ignites properly and safely with six MJG Firewire Initiators and 75mm Classic™ Propellant Grain. If the system functions properly and safely with the calibrated sensors, electrical configuration, and the Python script. The altitude shroud simulation must successfully record thrust data at simulated altitudes of up to 25 [km]. The system and subsystem requirements SYS. 01, SYS.02, SYS.04, SYS.05, PROP.01, PROP.03, STRUCT.01, STRUCT.02, STRUCT.03, STRUCT.04, CONTR.01, CONTR.02, SAF.01, SAF.02, SAF.03, SAF.04, and SAF.05.

9.2 Test Results (Smith)

01. 3D Printed PLA Model and Test Stand Fitting:

On April 3rd, 2025, *ENG-PLN-001-REV-D 3D-Printed PLA Model and Test Stand Fitting* (See Appendix C) was conducted. The objectives of this test were to validate that the aerospike design fits the test stand as designed before moving forward with metal 3D-printing. It is also to validate that the test stand is correctly assembled. This will be done by visually inspecting it as well as completing a dimension inspection report. *Table 12*, shown below shows the accuracy range that was used to determine if the measurements documented were considered to be accurate to the engineering drawings.

As shown below in Table 13 - Table 18, all of the success criteria was met. This includes that the PLA model fits as designed within the fully assembled test stand. That there no visual gaps, misalignments, cracking, or breakage. That the test stand configuration is sturdy and balanced. It validated the system and subsystem requirements SYS.01, SYS.02, SYS.05, STRUCT.04, SAF.01, SAF.02, and SAF.05.

Table 12: Accuracy Range used for DIRs.

Accuracy Range:	
Accurate	≥ 90%
Borderline	70% - 89.99%
Not Accurate	< 70%

Table 13: Recorded measurements from DIR-ENG-001-REV-C-Top.

Measurements:		
Specified Measurement:	Dimensions on Drawing (mm):	Measured Dimensions (mm):
Measurement 1	185.99	188.05
Measurement 2	273.63	269.79
Measurement 3	64.96	62.7
Measurement 4	12	11.37
Measurement 5	120	108.88
Measurement 6	207.85	196.03
Measurement 7	240	228.64

Table 14: Error Calculations from DIR-ENG-001-REV-C-Top.

Error Calculations:				
Specified Measurement:	Difference (mm):	Error Percentage (%):	Accuracy Percentage (%):	Classification:
Measurement 1	-2.060	1.107586429	98.89241357	Accurate
Measurement 2	3.840	1.403354895	98.5966451	Accurate
Measurement 3	2.260	3.479064039	96.52093596	Accurate
Measurement 4	0.630	5.25	94.75	Accurate
Measurement 5	11.120	9.266666667	90.73333333	Accurate
Measurement 6	11.820	5.686793361	94.31320664	Accurate
Measurement 7	11.360	4.733333333	95.26666667	Accurate

Table 13 shows what the specified measurement value was on the engineering drawing *REV B Final Model - Top Drawing* (See Appendix F) compared to the dimensions that were measured with calipers in *DIR-ENG-001-REV-C-Top* (See Appendix D). From this, you can see that the recorded dimensions are a little off compared to the dimensions specified on the engineering drawing. The majority of the measurements are smaller than the CAD drawing. Measurement 1 is the only one what is larger.

This is because to successfully 3D-print the aerospike using PLA, the team had to use a lower resolution which resulted in the plastic to shrink. Regardless of this, all of the measurements are considered to be accurate as shown above in Table 14. Table 14 shows each of the measurements difference then it's calculated error and accuracy percentage.

Table 15: Recorded measurements from DIR-ENG-001-REV-C-Bottom.

Measurements:		
Specified Measurement:	Dimensions on Drawing (mm):	Measured Dimensions (mm):
Measurement 1	295	294.93
Measurement 2	137.83	141.97
Measurement 3	12	12.29
Measurement 4	9	4.38
Measurement 5	44	43.89
Measurement 6	64.95	64.57
Measurement 7	120	118.84
Measurement 8	207.85	206.56
Measurement 9	240	236.44
Measurement 10	77.94	77.18
Measurement 11	38.97	38.52
Measurement 12	90	88.59
Measurement 13	45	44.56

Table 16: Error Calculations from DIR-ENG-001-REV-C-Bottom.

Error Calculations:				
Specified Measurement:	Difference (mm):	Error Percentage (%):	Accuracy Percentage (%):	Classification:
Measurement 1	0.070	0.023728814	99.97627119	Accurate
Measurement 2	-4.140	3.00370021	96.99629979	Accurate
Measurement 3	-0.290	2.416666667	97.58333333	Accurate
Measurement 4	4.620	51.33333333	48.66666667	Not Accurate
Measurement 5	0.110	0.25	99.75	Accurate
Measurement 6	0.380	0.585065435	99.41493457	Accurate
Measurement 7	1.160	0.966666667	99.03333333	Accurate
Measurement 8	1.290	0.620639885	99.37936012	Accurate
Measurement 9	3.560	1.483333333	98.51666667	Accurate
Measurement 10	0.760	0.975109058	99.02489094	Accurate
Measurement 11	0.450	1.154734411	98.84526559	Accurate
Measurement 12	1.410	1.566666667	98.43333333	Accurate
Measurement 13	0.440	0.977777778	99.02222222	Accurate

Table 15 shows what the specified measurement value was on the engineering drawing *REV B Motor Casing Drawing* (See Appendix F) compared to the dimensions that were measured with calipers in *DIR-ENG-001-REV-C-Bottom* (See Appendix D). From this, it is shown that Measurement 4 is off by a large amount compared to the other values. The rest of the values are very close to the specified dimensions.

This could be due to human error or how the plastic settled after being 3D-printed like what occurred in *DIR-ENG-001-REV-C-Top*. The top and bottom portions fit within the test stand without any anomalies regardless of this. *Table 16* shows each of the measurements difference then it's calculated error and accuracy percentage.

Table 17: Recorded measurements from DIR-ENG-002-REV-C.

Measurements:		
Specified Measurement:	Dimensions on Drawing (mm):	Measured Dimensions (mm):
Measurement 1	228.54	240.59
Measurement 2	12	11.49
Measurement 3	120	118.07
Measurement 4	207.84	205.8
Measurement 5	240	236.91

Table 18: Error Calculations from DIR-ENG-002-REV-C.

Error Calculations:				
Specified Measurement:	Difference (mm):	Error Percentage (%):	Accuracy Percentage (%):	Classification:
Measurement 1	-12.050	5.272599982	94.72740002	Accurate
Measurement 2	0.510	4.25	95.75	Accurate
Measurement 3	1.930	1.608333333	98.39166667	Accurate
Measurement 4	2.040	0.981524249	99.01847575	Accurate
Measurement 5	3.090	1.2875	98.7125	Accurate



Table 17 shows what the specified measurement value was on the engineering drawing *REV F Test Stand Assembly Drawing* (See Appendix F) compared to the dimensions that were measured with calipers in *DIR-ENG-002-REV-C* (See Appendix D). From this, it is shown that Measurement 1 is off by a large amount compared to the other values. The rest of the values are very close to the specified dimensions.

This could be due to human error while recording the measurements. The top and bottom portions fit within the test stand without any anomalies regardless of this. Regardless of this, the measurement is still considered to be accurate. The top and bottom portions fit within the test stand without any anomalies regardless of this. Table 18 shows each of the measurements difference then it's calculated error and accuracy percentage.

Overall, the dimensions recorded in *DIR-ENG-001-REV-C-Top*, *DIR-ENG-001-REV-C-Bottom*, and *DIR-ENG-002-REV-C* are accurate to the engineering drawings. As discussed above, the dimensions recorded in *DIR-ENG-001-REV-C-Top* are smaller than the dimensions specified on the CAD drawing. This is because to successfully 3D-print the aerospike using PLA, the team had to use a lower resolution which resulted in the plastic to shrink. Measurement 4 in *DIR-ENG-001-REV-C-Bottom* is off by a large amount. This could be due to human error or how the plastic settled after being 3D-printed like what occurred in *DIR-ENG-001-REV-C-Top*. The top and bottom portions fit within the test stand without any anomalies regardless of this. Measurement 1 in *DIR-ENG-002-REV-C* is off by a large amount. This could be due to human error while recording the measurements. The top and bottom portions fit within the test stand without any anomalies regardless of this. The detailed test report of this is in the document *ENG-RPT-001-REV-D 3D-Printed PLA Model and Test Stand Fitting* (See Appendix C).

02. Test Stand Data Collection and Electronic System Verification:

On April 14th, 2025, *ENG-PLN-002-REV-D Test Stand Data Collection and Electronic System Verification* (See Appendix C) was conducted. The objectives of this test were to verify that the test stand was calibrated correctly and that the sensors being used record and report accurate data for the force and moment that will be generated by the aerospike. It will also validate the functionality of the Python script and confirm that the control system properly integrates with the sensors.

As shown below in Table 19, all success criteria was met. This includes that the test stand sensors were calibrated correctly, the electrical configuration powered the sensors, circuit boards, and all the wiring as designed, and that the electrical configuration is compatible with the Python code. It also validated that the code used produces three separate graphs representing the data collected, the sensors were able to record the force and moment that is generated, and that the data that was recorded is accurate to the theoretical calculations. It verified the system and subsystem requirements SYS.02, SYS.05, STRUCT.04, CONTR.02, SAF.01, SAF.02, and SAF.05.

Table 19: Values Recorded from Calibrating the Test Stand.

Calibration Matrix Values:					
Channel	F_x	F_y	F_z	M_x	M_y
LC1	-17861.512	-61255.088	-36403.8	163909.443	-35557.918
LC3	-15393.024	59578.6974	-43429.669	-171250.87	195064.975
LC4	-16750.293	-3275.441	78053.7591	-29578.429	179314.3
LC5	-14444.439	4649.25373	71139.0461	-16566.55	-155940.07
LC6	-16199.756	-59517.639	-37919.968	-195514.69	-206647.18

The table above shows the values that were calculated from calibrating the test stand. These values are acquired by getting the slope of the output response of the load cells when applying a load, saving the values for each load cell required and then this table will be inverted. This inverted matrix is then dotted with the load cell values to get the force readings in the x, y, and z directions. This matrix cannot be hand calculated because it is based on the live reading of the load cells which is not getting recorded.

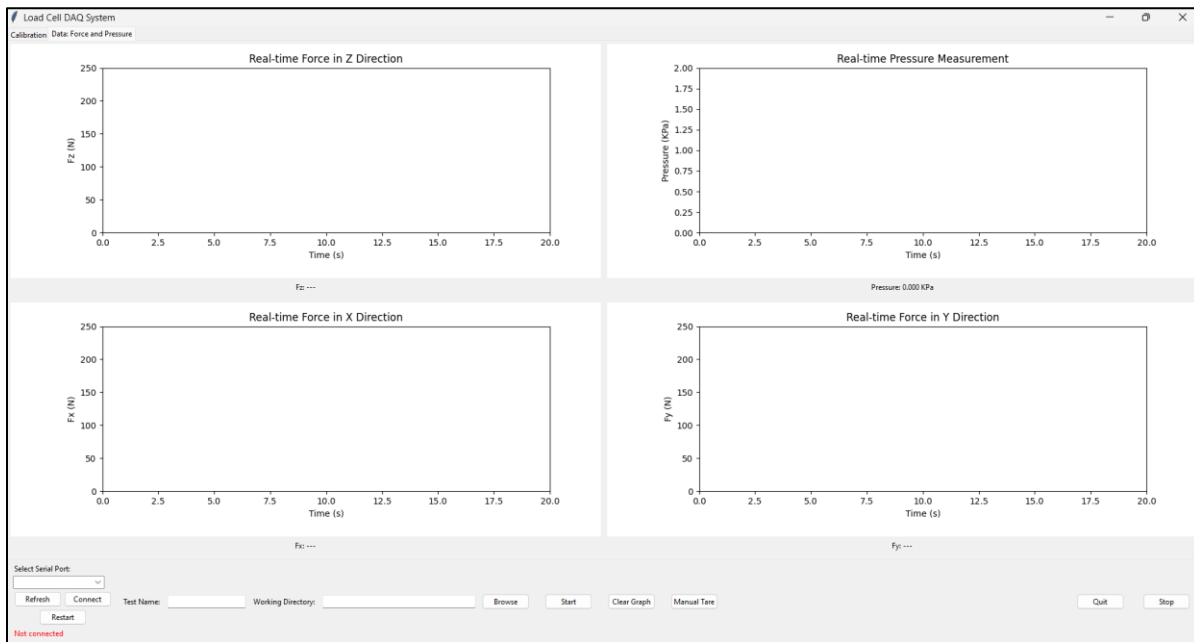


Figure 127: Data Tab with Three Separate Plots for a Thrust Vector.

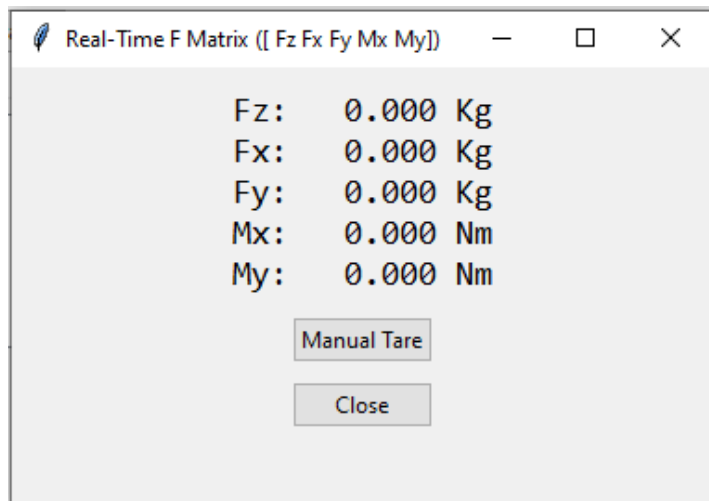


Figure 130: Live Mass Reading Window.



Figure 129 displayed above, shows the “*Data Tab*” in the Python program where a user can start a test after loading or creating a proper calibration matrix. After starting, the data is collected and presented in real time, based on the linear equation setup in *Appendix E - Test Stand (Stewart platform) Calculations*. In total there are four plots: Fz/Fy/Fx vs. Time and an additional pressure plot vs. time, which is only functional for the altitude simulating shroud test.

For this test, there was no need to do an extensive number of recorded plots from applying forces. Instead, weights were applied onto every axis in a controlled manner, step by step while simultaneously observing the Real Time F Matrix for validation. In this pop-up window, the forces in each axis are set as a mass, instead of a Newton force – done for ease of use. This accommodation allowed for several known masses to be applied and compared. Generally, there is a small noticeable error of ± 200 [g] ; equating to a 33 [g] uncertainty for each load cell, primarily caused by load cell sensitivity and drift. Expecting to record thrust values up to 1500 [N], this error is insignificant only being ± 2 [N].

From the data shown above in *Table 19*, the test stand was calibrated correctly. This test also successfully showed that the DAQ system, Python script, sensors, and the overall electrical system works as designed. The test successfully produced a calibration matrix, and which was able to be reloaded and created accurate (± 200 [g]) live readings of mass in all directions. The detailed test report of this is in the document *ENG-RPT-002-REV-D Test Stand Data Collection and Electronic System Verification* (See Appendix C).

03. Six A8-3 Solid Rocket Motor Configuration Test Fire with MJG Firewire Initiators:

On February 24th, 2025, *ENG-PLN-003-REV-B Six A8-3 Solid Rocket Motor Configuration Test Fire with E-Match Ignitor* (See Appendix C) was conducted. The objectives of this test were to validate that a singular A8-3 motor could be ignited using one MJG Firewire Initiator as well as that six A8-3 motors could be ignited simultaneously using six MJG Firewire Initiators. As shown below in *Figure 131*, a singular A8-3 motor was successfully and safely ignited using a singular MJG Firewire Initiator. This test was further validated by safely and properly igniting six of the A8-3 motors using six MJG Firewire Initiators, as shown below in *Figure 132*.

Both the singular and six A8-3 motor configurations were successful in initiating the engine start sequence remotely, which fulfills subsystem requirement CONTR.01. The team also met all the safety requirements regarding safety training, PPE, hazardous material handling, and hot firing, which fulfills subsystem requirements SAF.01, SAF.04, and SAF.05. The detailed test report of this is in the document *ENG-RPT-002-REV-D Test Stand Data Collection and Electronic System Verification* (See Appendix C).

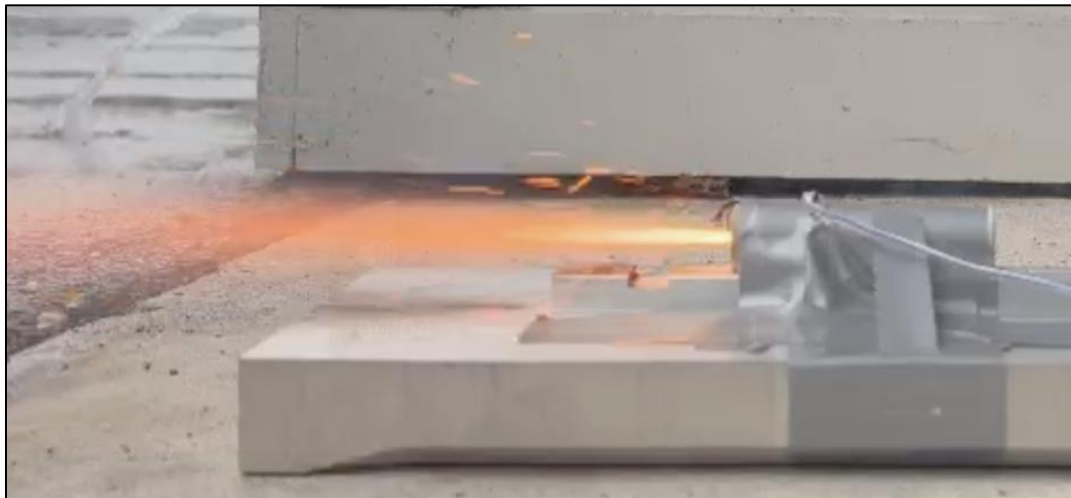


Figure 131: Singular A8-3 Motor ignited using a singular MJG Firewire Initiator



Figure 132: six A8-3 motors ignited using six MJG Firewire Initiators

04. LITVC Wet Dress Rehearsal:

On April 23rd, 2025, *ENG-PLN-004-REV-E LITVC Wet Dress Rehearsal* (See Appendix C) was conducted. The objectives of this test were to validate that the LITVC system is integrated, and functions as designed in the metal aerospike, as well as that the thrust and deflection data being collected is being properly recorded. As shown below in *Figures 136 and 137*, all success criteria were met. This includes that nothing blocked the water flow through the integrated LITVC, and the water was able to flow properly through the integrated LITVC as designed. It validated the system and subsystem requirements SYS.01, SYS.02, SYS.03, SYS.05, PROP.02, STRUCT.04, CONTR.02 CONTR.03, SAF.01, SAF.03, and SAF.05.

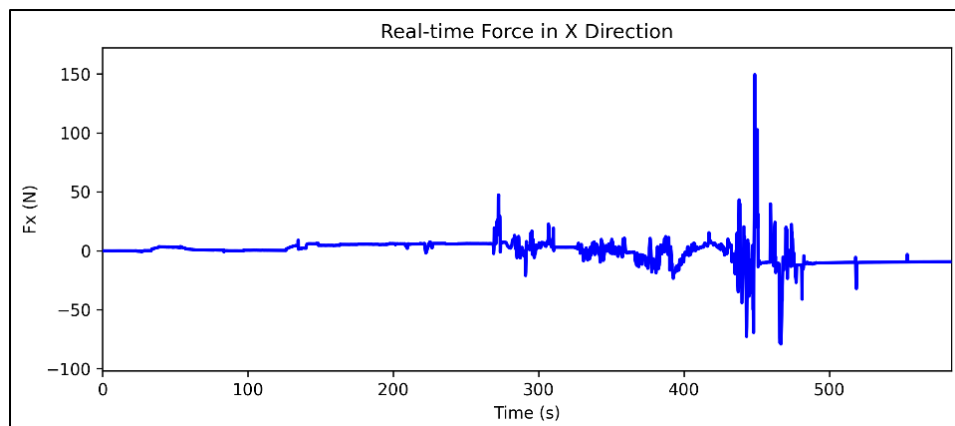


Figure 133: Graph of the real-time force in the x-direction for test run 1.

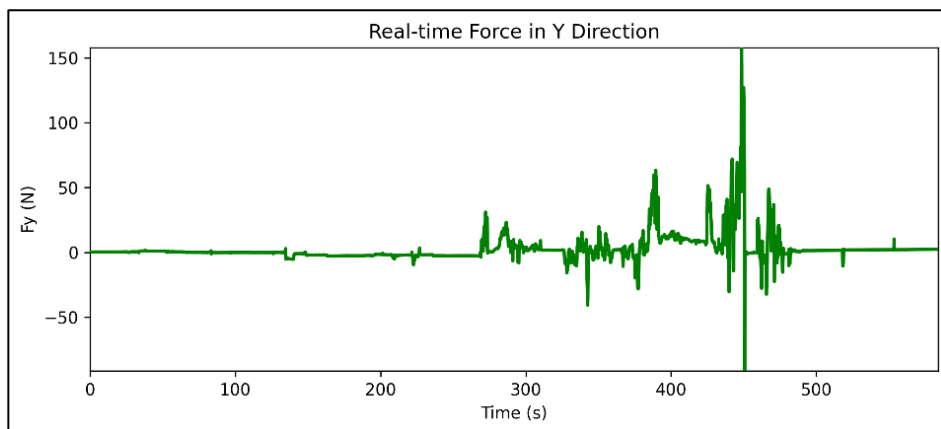


Figure 134: Graph of the real-time force in the y-direction for test run 1.

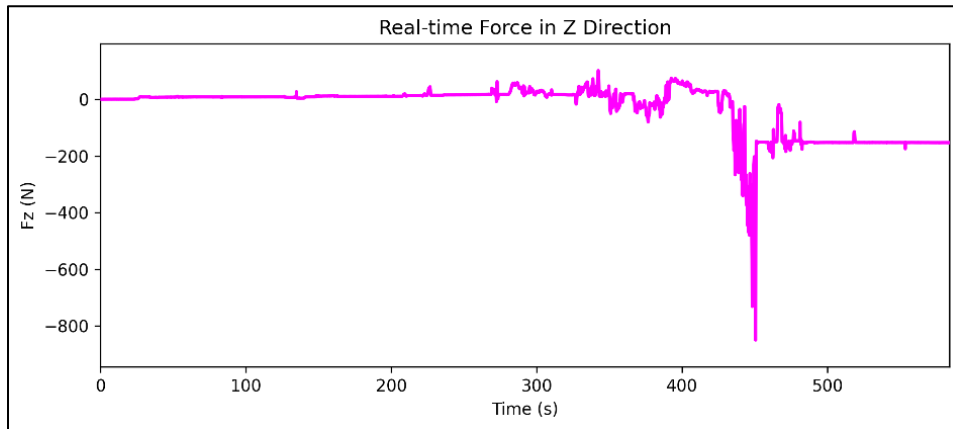


Figure 135: Graph of the real-time force in the x-direction for test run 1.

The test proves that because of the high flux of water across all the manifolds, there are some extra forces that are applied onto the test stand. While data was recorded for this test, it was not used in the result calculations for any of the tests as the data collection system was always manually tared at operational conditions (full flowing water in the system) before firing.

The graphs shown above do not show accurate results as there is not only water flowing in the cooling pipes but also the hose that is being attached to the LITVC port is turned manually. Additionally, the data collected is only relevant to the 300 second mark, after which the data collection was still running while actively removing the test stand resulting in a sharp spike in forces.



Figure 136: Water flowing through the LITVC ports of the metal 3D-printed aerospike.



Figure 137: Water flowing through the LITVC ports of the metal 3D-printed aerospike.



As shown in the *Figures 136 and 137* above, the water and fluid delivery system successfully flowed through the LITVC port and metal 3D-printed aerospike. The aerospike used in this test had some left-over support structures from the manufacturing process. To allow water to properly flow through, the team had to use a small Dremel and cut out the extra material. After that, there were no other anomalies. The detailed test report of this is in the document *ENG-RPT-004-REV-E LITVC Wet Dress Rehearsal* (See Appendix C).



05. Fully Integrated Metal 3D-Printed Aerospike Static Fire Test:

On the dates of April 17th, 19th, 21st, and 22nd 2025, *ENG-PLN-005-REV-E Fully Integrated Metal 3D Printed Aerospike Static Fire Test* (See Appendix C) was conducted. The objectives of this test were to validate the whole system, which includes the fully assembled metal 3D-printed aerospike mounted on the test stand configuration with the calibrated electrical system, six solid rocket motors configuration with six MJG Firewire Initiators, 75mm Classic™ Propellant Grain, and a water-cooling subsystem controlled via a manifold and pump.

As shown below in the figures and discussion, all the success criteria were met. This includes that the prototype and systems components worked together as designed. It validated the system and subsystem requirements the system and subsystem requirements SYS. 01, SYS.02, SYS.05, PROP.01, STRUCT.01, STRUCT.02, STRUCT.03, STRUCT.04, CONTR.01, CONTR.02, SAF.01, SAF.02, SAF.03, SAF.04, and SAF.05. *Table 12*, shown above was used to determine if the data values that were collected were considered to be accurate to the analysis.

Test Run 1 Data:

Table 20: Force and Moment Values from Test Run 1.

Data Type	F_x (N)	F_y (N)	F_z (N)	M_x (Nm)	M_y (Nm)
Experimental	29.442	51.779	755.760	0.5714	0.3341
Theoretical	0	0	1334	0	0

Table 21: Error Calculation Results from Test Run 1.

Error Calculations:				
Specified Measurement:	Difference (N):	Error Percentage (%):	Accuracy Percentage (%):	Classification:
F_x (N)	29.442	N/A	N/A	N/A
F_y (N)	51.779	N/A	N/A	N/A
F_z (N)	-578.240	43.34633712	56.65366288	Not Accurate
M_x (Nm)	0.571	N/A	N/A	N/A
M_y (Nm)	0.334	N/A	N/A	N/A

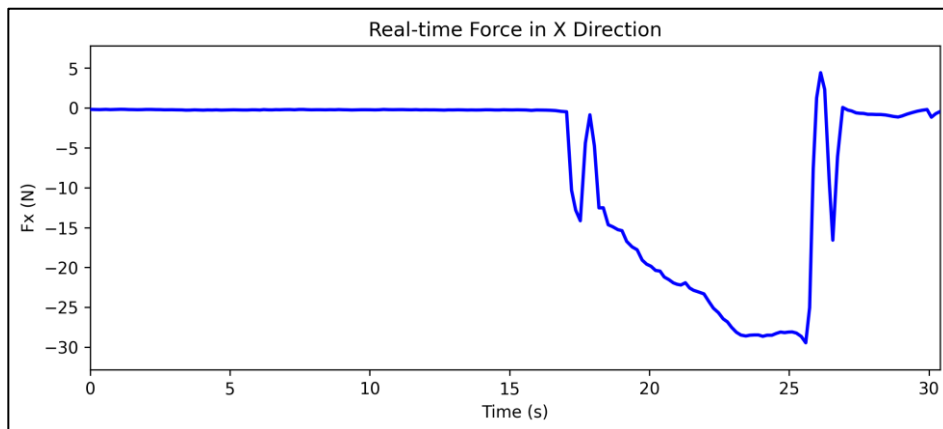


Figure 138: Graph of the real-time force in the x-direction for test run 1.

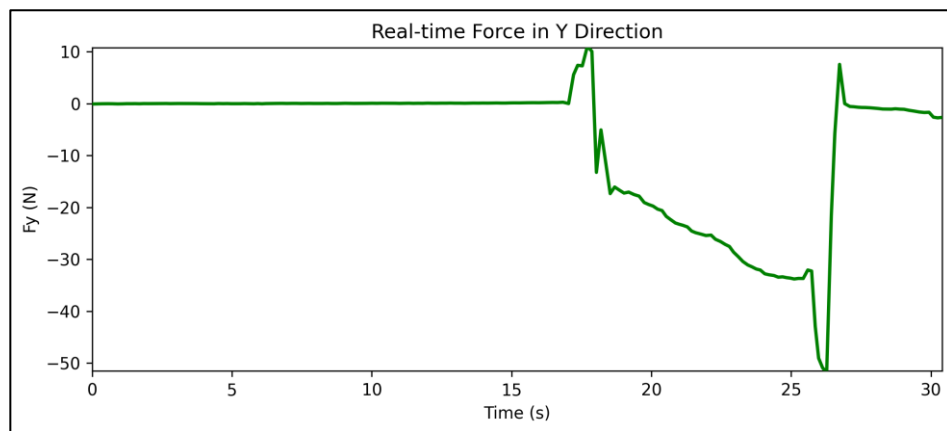


Figure 139: Graph of the real-time force in the y-direction for test run 1.

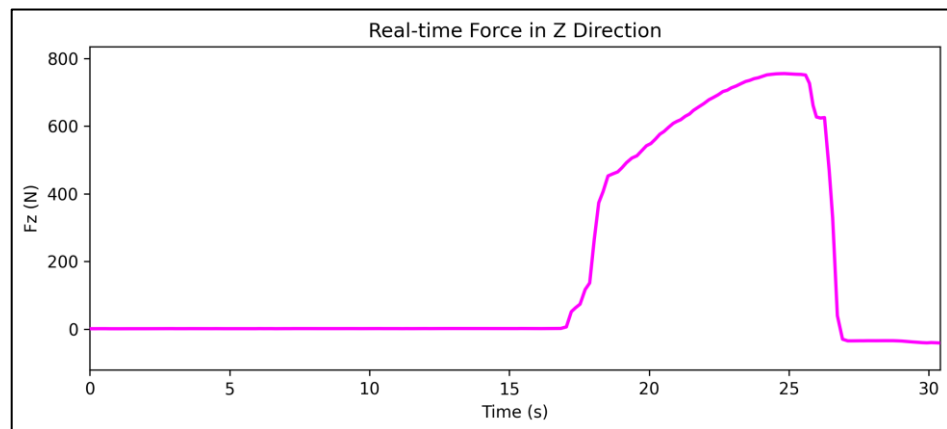


Figure 140: Graph of the real-time force in the z-direction for test run 1.

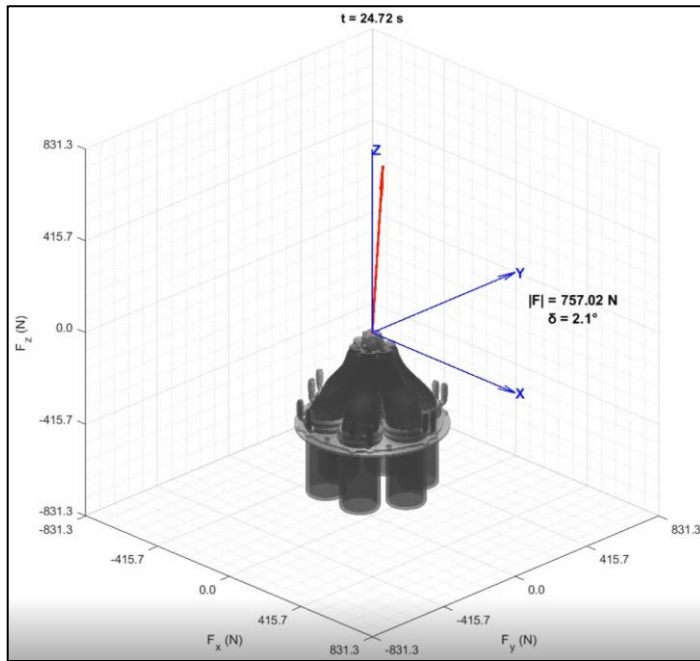


Figure 141: Diagram of the plume created with the data collected from test run 1.

Table 20 shows the force and moment values that were recorded from test run 1 compared to the theoretical values from the analysis. *Table 21* shows each of the measurements difference then it's calculated error and accuracy percentage. The thrust that was achieved in the first test run is not accurate to what the analysis predicted as shown above in *Table 21*. This is due to the gaskets the team used, causing leakage which caused the pressure drop in the combustion chamber. At a lower combustion pressure, the fuel burns longer while also producing less thrust. From the burn sim analysis, the firing should have an estimate duration of 4.61 seconds, instead it produced slightly over half the thrust while also burning twice as long – overall showing that it aligns properly with the burn sim. If the system had maintained full combustion pressure as intended, the burn duration and thrust would have aligned with some slight error to the predictions. For this test the team used 1 vermiculite gasket. *Figure 140* graphs the thrust that the aerospike produced during this test run.

Test Run 2 Data:

Table 22: Force and Moment Values from Test Run 2.

Data Type	F_x (N)	F_y (N)	F_z (N)	M_x (Nm)	M_y (Nm)
Experimental	29.688	52.124	505.241	0.1978	0.3280
Theoretical	0	0	1334	0	0

Table 23: Error Calculation Results from Test Run 2.

Error Calculations:				
Specified Measurement:	Difference (N):	Error Percentage (%):	Accuracy Percentage (%):	Classification:
F_x (N)	29.688	N/A	N/A	N/A
F_y (N)	52.124	N/A	N/A	N/A
F_z (N)	-828.759	62.12585342	37.87414658	Not Accurate
M_x (Nm)	0.198	N/A	N/A	N/A
M_y (Nm)	0.328	N/A	N/A	N/A

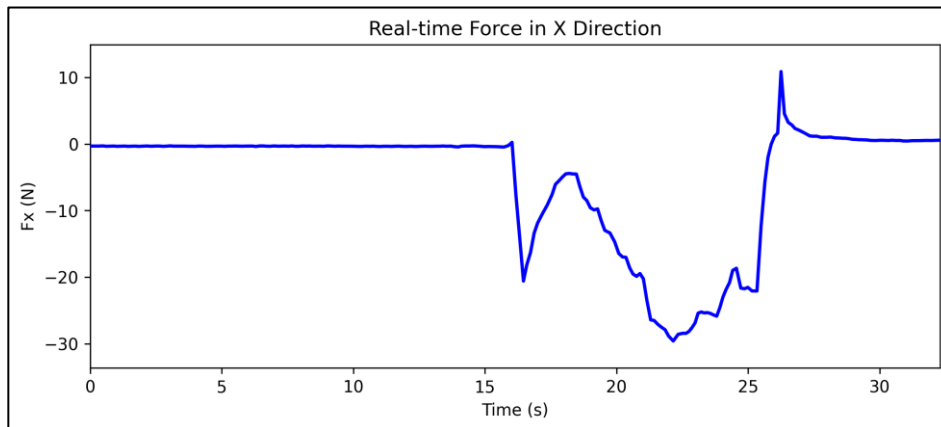


Figure 142: Graph of the real-time force in the x-direction for test run 2.

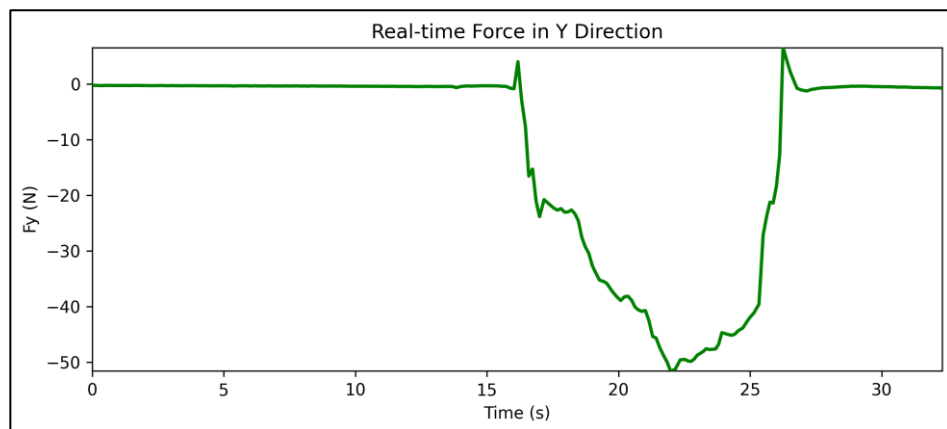


Figure 143: Graph of the real-time force in the y-direction for test run 2.

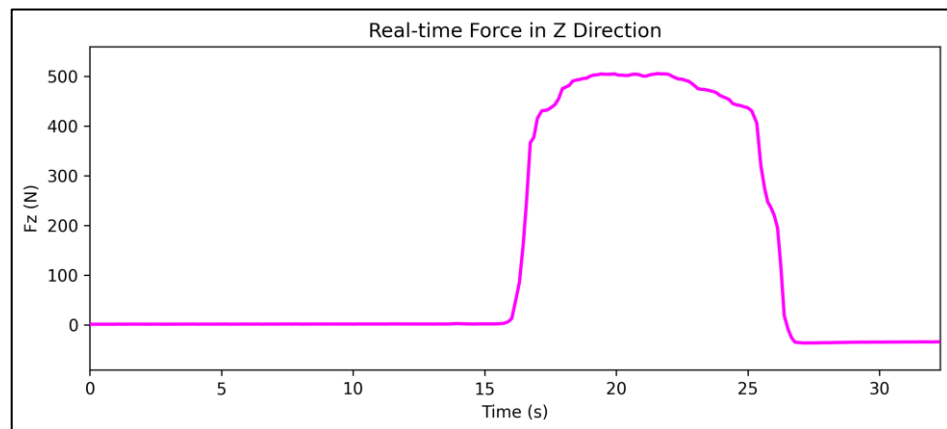


Figure 144: Graph of the real-time force in the z-direction for test run 2.

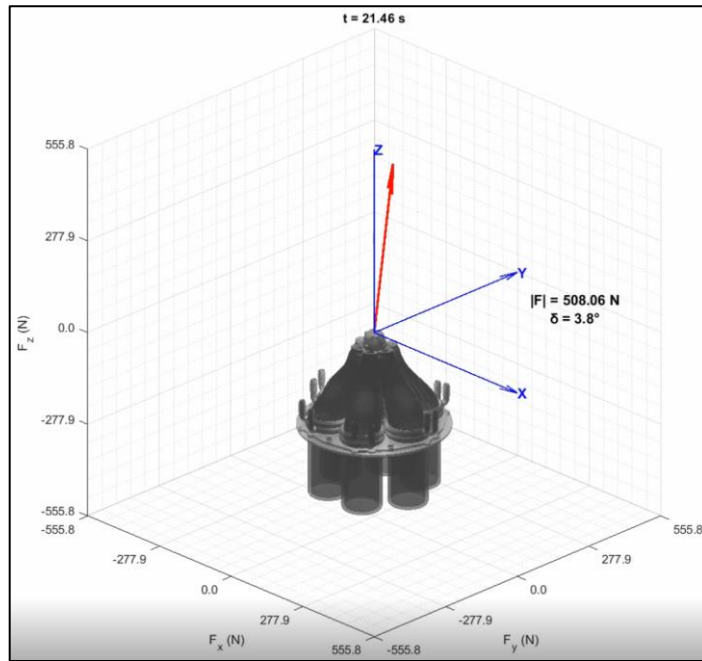


Figure 145: Diagram of the plume created with the data collected from test run 2.

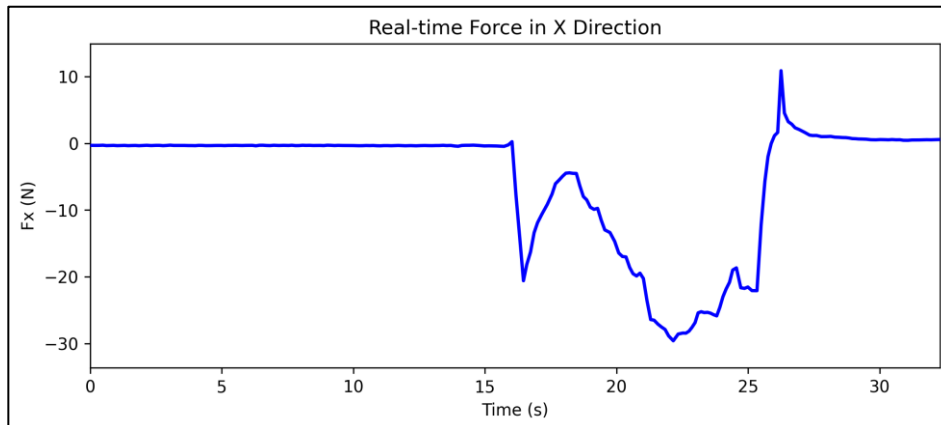
Table 22 shows the force and moment values that were recorded from test run 1 compared to the theoretical values from the analysis. *Table 23* shows each of the measurements difference then it's calculated error and accuracy percentage. Once again, the thrust that was achieved in the second test run is not accurate to what the analysis predicted as shown above in *Table 23*. This is again due to the gaskets causing leakage. For this test run, the team coated the bottom of the 3D-printed metal aerospike with high-temperature red RTV silicone gasket maker. As you can see from the values, only applying a barrier of RTV caused more leakage which resulted in a lower thrust than the first test run with the vermiculite gasket. *Figure 144* graphs the thrust that the aerospike produced during this test run.

Test Run 3 Data:*Table 24: Force and Moment Values from Test Run 3.*

Data Type	F_x (N)	F_y (N)	F_z (N)	M_x (Nm)	M_y (Nm)
Experimental	92.634	78.613	989.605	0.2554	0.6220
Theoretical	0	0	1721	0	0

Table 25: Error Calculation Results from Test Run 3.

Error Calculations:				
Specified Measurement:	Difference (N):	Error Percentage (%):	Accuracy Percentage (%):	Classification:
F_x (N)	92.634	N/A	N/A	N/A
F_y (N)	78.613	N/A	N/A	N/A
F_z (N)	-731.395	42.50	57.50	Not Accurate
M_x (Nm)	0.255	N/A	N/A	N/A
M_y (Nm)	0.622	N/A	N/A	N/A

*Figure 146: Graph of the real-time force in the x-direction for test run 3.*

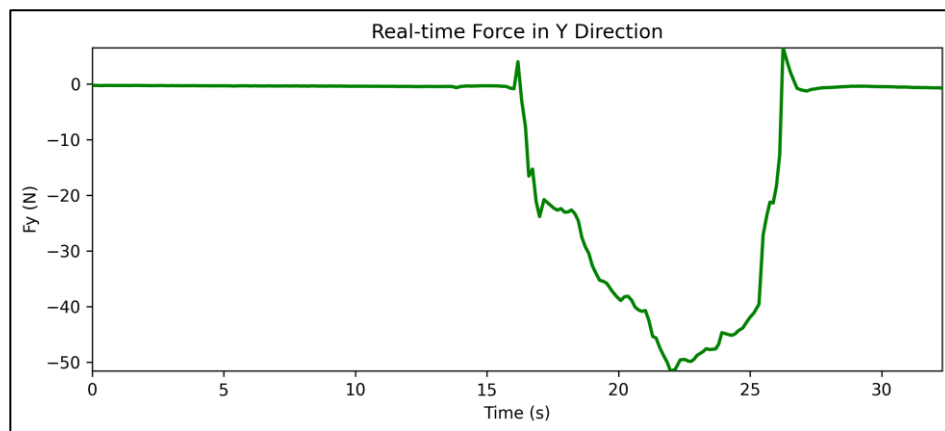


Figure 147: Graph of the real-time force in the y-direction for test run 3.

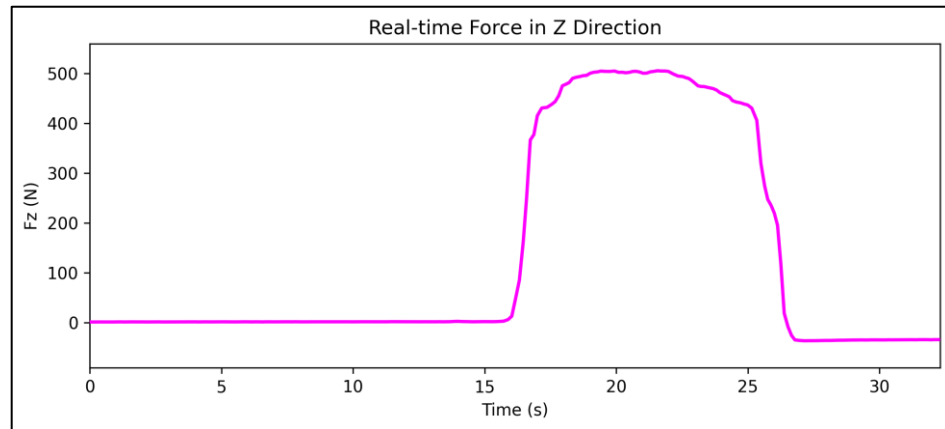


Figure 148: Graph of the real-time force in the z-direction for test run 3.

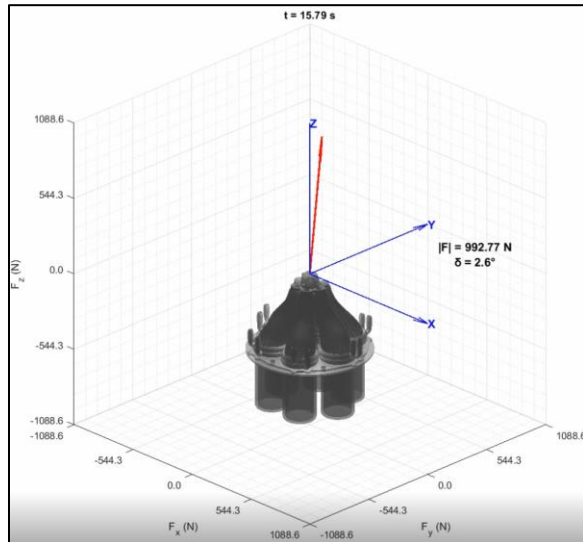


Figure 149: Diagram of the plume created with the data collected from test run 3.

Table 24 shows the force and moment values that were recorded from test run 3 compared to the theoretical values from the analysis. *Table 25* shows each of the measurements difference then it's calculated error and accuracy percentage. The thrust achieved in this test run was higher than in the previous tests. This increase is primarily due to the use of a different fuel grain known as "Redline," which is more energetic than the standard grains used in the previous two static firings. Because the regular grains were limited and reserved for planned tests, the Redline grains, compatible with the motor casing, were used for this experimental run as a throwaway test. This allowed us to evaluate a new sealing method without depleting the main propellant grains.

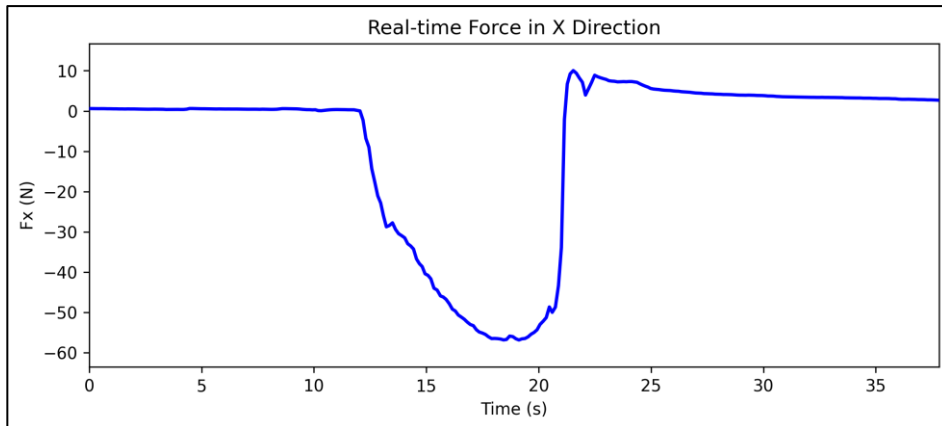
To address pressure leakage, RTV sealant was applied to the metal 3D-printed aerospike, followed by the placement of a vermiculite gasket and a second layer of RTV along the motor casing interface. However, this method proved ineffective, the pressure still leaked at similar levels as before, but with even more damaging consequences discussed in p.224. The combined effect of continued leakage and erosion led to the conclusion that using Redline grains for throwaway tests posed too high a risk, and the approach was ultimately abandoned. *Figure 148* graphs the thrust that the aerospike produced during this test run.

Test Run 4 Data:*Table 26: Force and Moment Values from Test Run 4.*

Data Type	F_x (N)	F_y (N)	F_z (N)	M_x (Nm)	M_y (Nm)
Experimental	56.841	57.752	597.577	0.0779	0.2530
Theoretical	0	0	1334	0	0

Table 27: Error Calculation Results from Test Run 4.

Error Calculations:				
Specified Measurement:	Difference (N):	Error Percentage (%):	Accuracy Percentage (%):	Classification:
F_x (N)	56.841	N/A	N/A	N/A
F_y (N)	57.752	N/A	N/A	N/A
F_z (N)	-736.423	55.20415015	44.79584985	Not Accurate
M_x (Nm)	0.078	N/A	N/A	N/A
M_y (Nm)	0.253	N/A	N/A	N/A

*Figure 150: Graph of the real-time force in the x-direction for test run 4.*

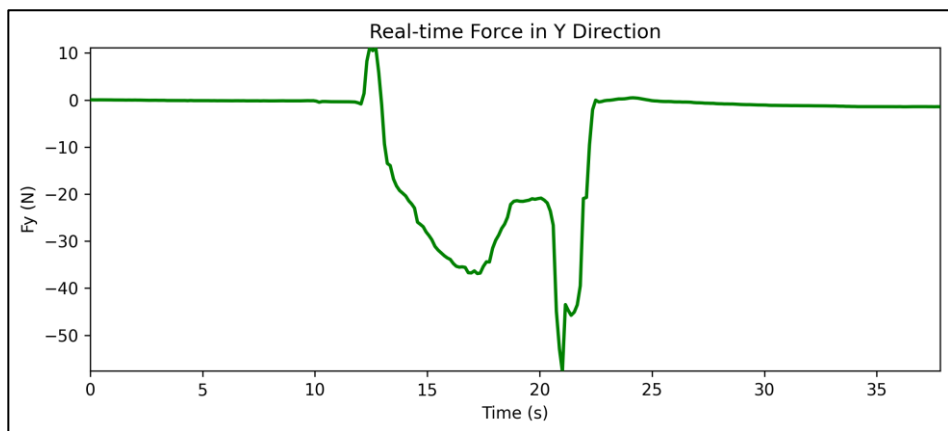


Figure 151: Graph of the real-time force in the y-direction for test run 4.

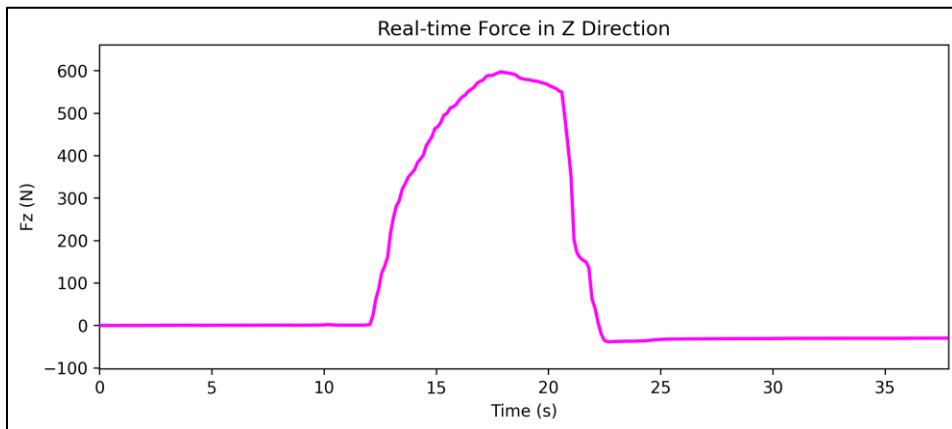


Figure 152: Graph of the real-time force in the z-direction for test run 4.

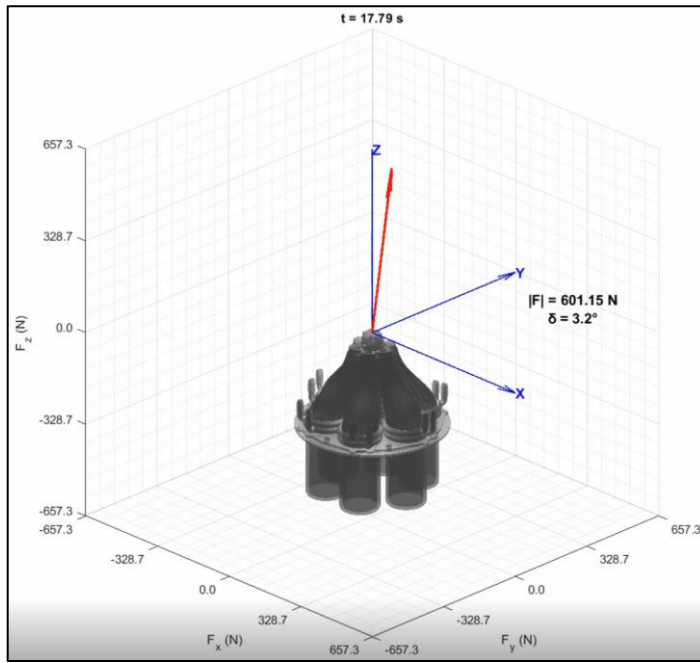


Figure 153: Diagram of the plume created with the data collected from test run 4.

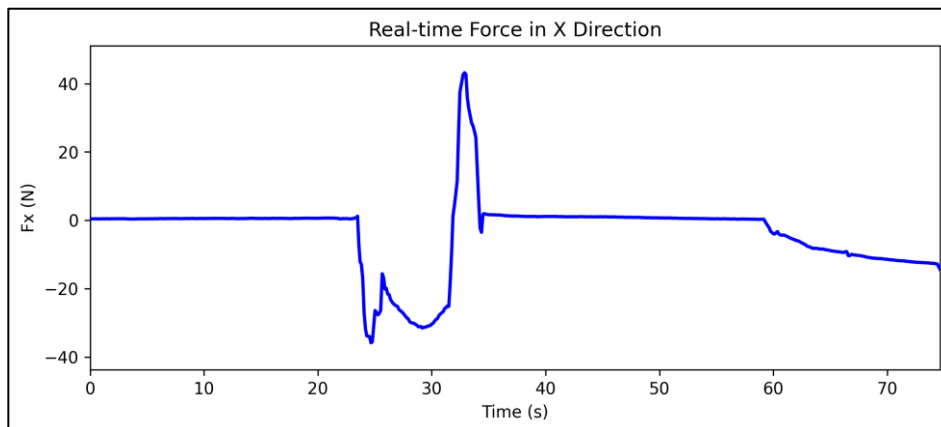
Table 26 shows the force and moment values that were recorded from test run 1 compared to the theoretical values from the analysis. Table 27 shows each of the measurements difference then it's calculated error and accuracy percentage. The thrust produced in this test run was once again lower than the predicted value and is still due to the gasket leakage. For this test run, the team once again put RTV on the metal 3D-printed aerospike then put the vermiculite gasket on and applied more RTV on the motor casings. The team also added six c-clamps around the outside of the aerospike to seal the gasket further. Doing this stopped the pressure leak on the outer casing, however the built-up pressure was forced toward the inner section of the 3D print, discussed further in p.224. Figure 152 graphs the thrust that the aerospike produced during this test run.

Test Run 5 Data:*Table 28: Force and Moment Values from Test Run 5.*

Data Type	F_x (N)	F_y (N)	F_z (N)	M_x (Nm)	M_y (Nm)
Experimental	43.179	41.282	756.542	0.3881	0.5878
Theoretical	0	0	1334	0	0

Table 29: Error Calculation Results from Test Run 5.

Error Calculations:				
Specified Measurement:	Difference (N):	Error Percentage (%):	Accuracy Percentage (%):	Classification:
F_x (N)	43.179	N/A	N/A	N/A
F_y (N)	41.282	N/A	N/A	N/A
F_z (N)	-577.458	43.28767712	56.71232288	Not Accurate
M_x (Nm)	0.388	N/A	N/A	N/A
M_y (Nm)	0.588	N/A	N/A	N/A

*Figure 154: Graph of the real-time force in the x-direction for test run 5.*

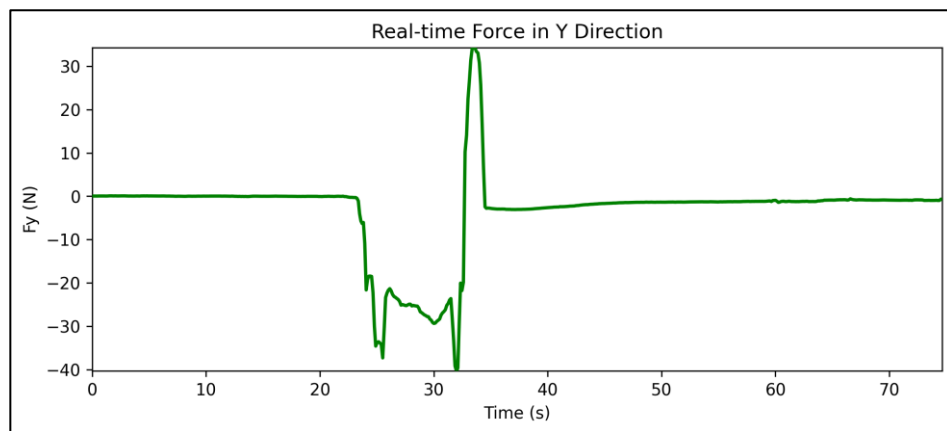


Figure 155: Graph of the real-time force in the y-direction for test run 5.

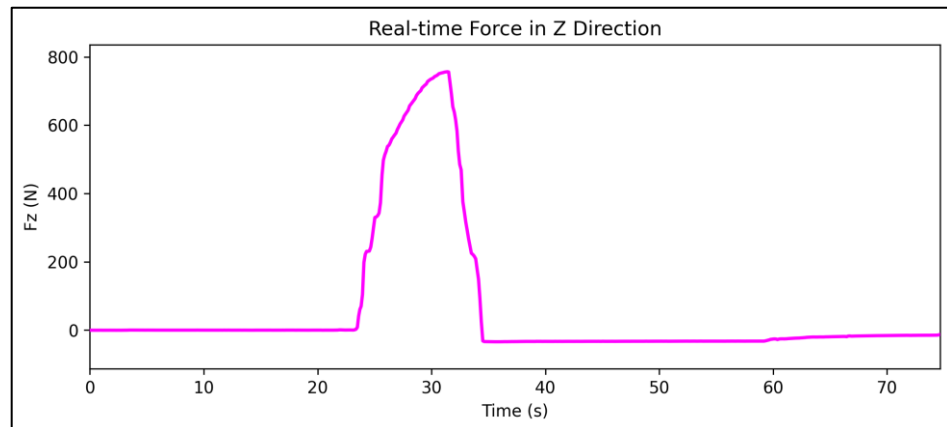


Figure 156: Graph of the real-time force in the z-direction for test run 5.

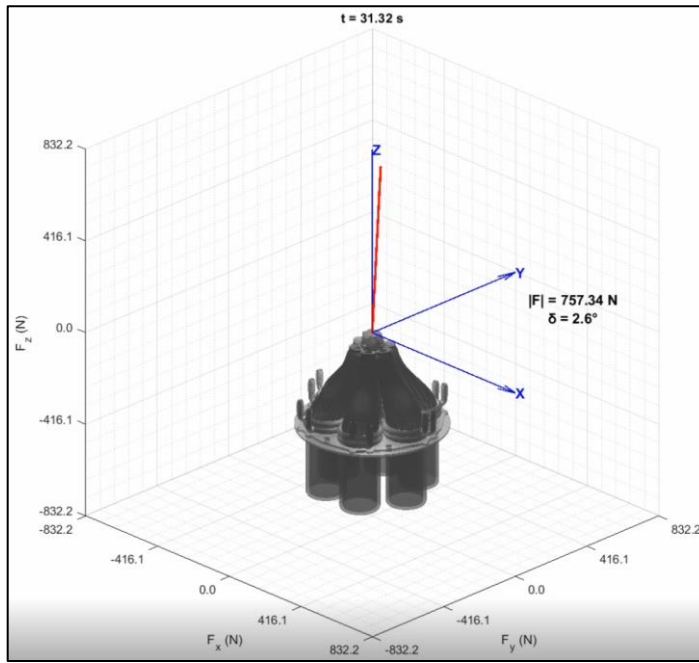


Figure 157: Diagram of the plume created with the data collected from test run 5.

Table 28 shows the force and moment values that were recorded from test run 1 compared to the theoretical values from the analysis. Table 29 shows each of the measurements difference then it's calculated error and accuracy percentage. The thrust that was achieved in the fifth test run is very similar to what was achieved in the first static fire test. This is because the configuration was set up the same, the only difference being that a vermiculite gasket was combined with a c-clamp setup. It is once again not accurate to what the analysis predicted and is due to the gaskets causing leakage which made the pressure drop. Figure 157 graphs the thrust that the aerospike produced during this test run.

Table 30: The Max Force and Moment Values from Test Runs 1, 2, 3, 4, and 5.

Max Values from Test Runs 1 – 5:					
Test Run:	Thrust (N):	Difference (N):	Error Percentage (%):	Accuracy Percentage (%):	Classification:
1	755.760	578.240	43.34633712	56.65366288	Not Accurate
2	505.241	828.759	62.12585342	37.87414658	Not Accurate
3	989.605	731.395	42.50	57.50	Not Accurate
4	597.577	736.423	55.20415015	44.79584985	Not Accurate
5	756.542	577.458	43.28767712	56.71232288	Not Accurate

Table 31: The Overall Max Force and Moment Values from Test Runs 1 - 5.

Overall Max Values from Test Runs 1 - 5:					
Data Type	F_x (N)	F_y (N)	F_z (N)	M_x (Nm)	M_y (Nm)
Experimental	92.634	78.613	989.605	0.571	0.425
Theoretical	0	0	1721	0	0

Table 32: Error Calculations for the Overall Max Force and Moment from Test Runs 1 - 5.

Error Calculations:				
Specified Measurement:	Difference (N):	Error Percentage (%):	Accuracy Percentage (%):	Classification:
F_x (N)	92.634	N/A	N/A	N/A
F_y (N)	78.613	N/A	N/A	N/A
F_z (N)	-731.395	42.50	57.50	Not Accurate
M_x (Nm)	0.571	N/A	N/A	N/A
M_y (Nm)	0.622	N/A	N/A	N/A

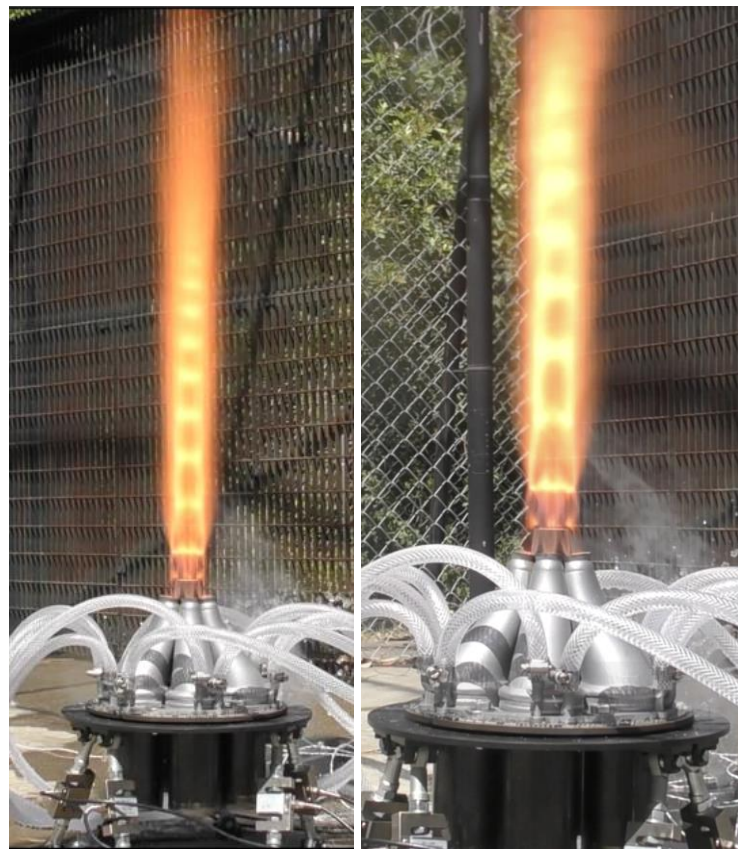
Test Run 1 Footage:

Figure 158: Still frames of Test Run 1.

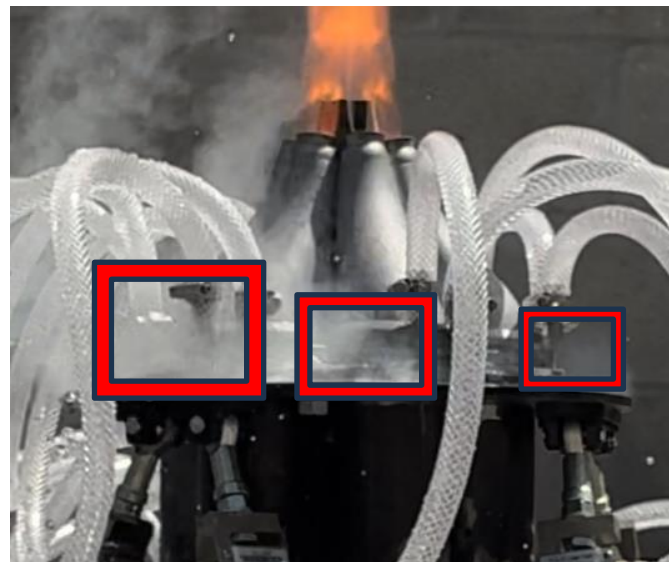


Figure 159: Close up of gasket leakage from Test Run 1.

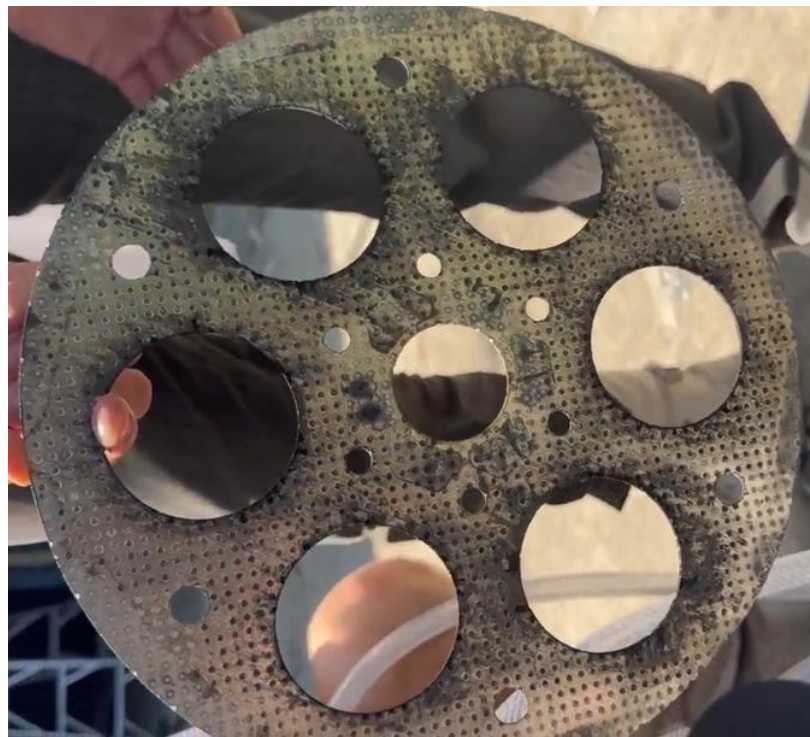


Figure 160: Image of the top of the gasket after firing from Test Run 1.

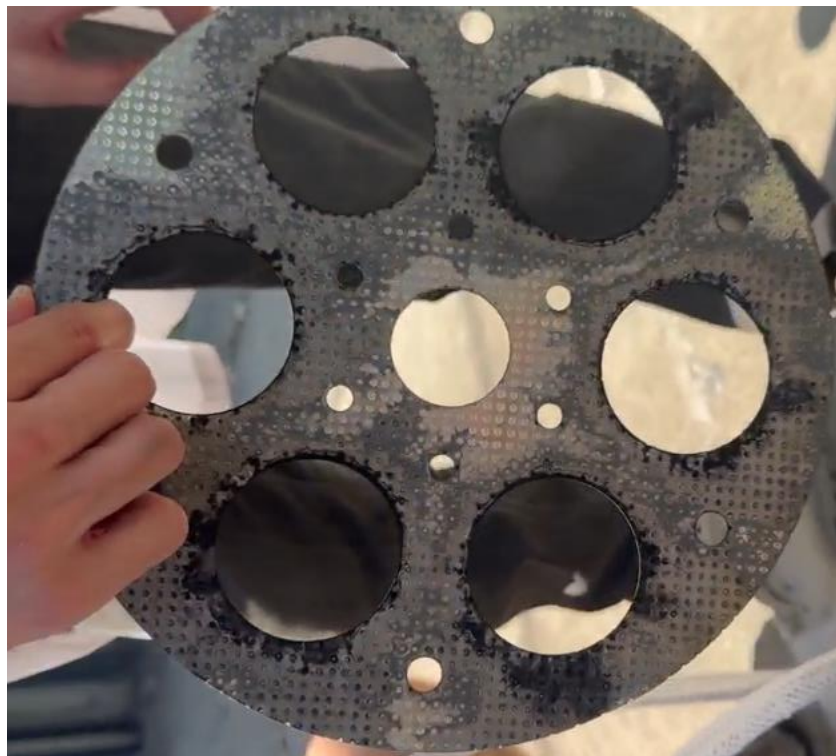


Figure 161: Image of the bottom of the gasket after firing from Test Run 1.

Test Run 2 Footage:

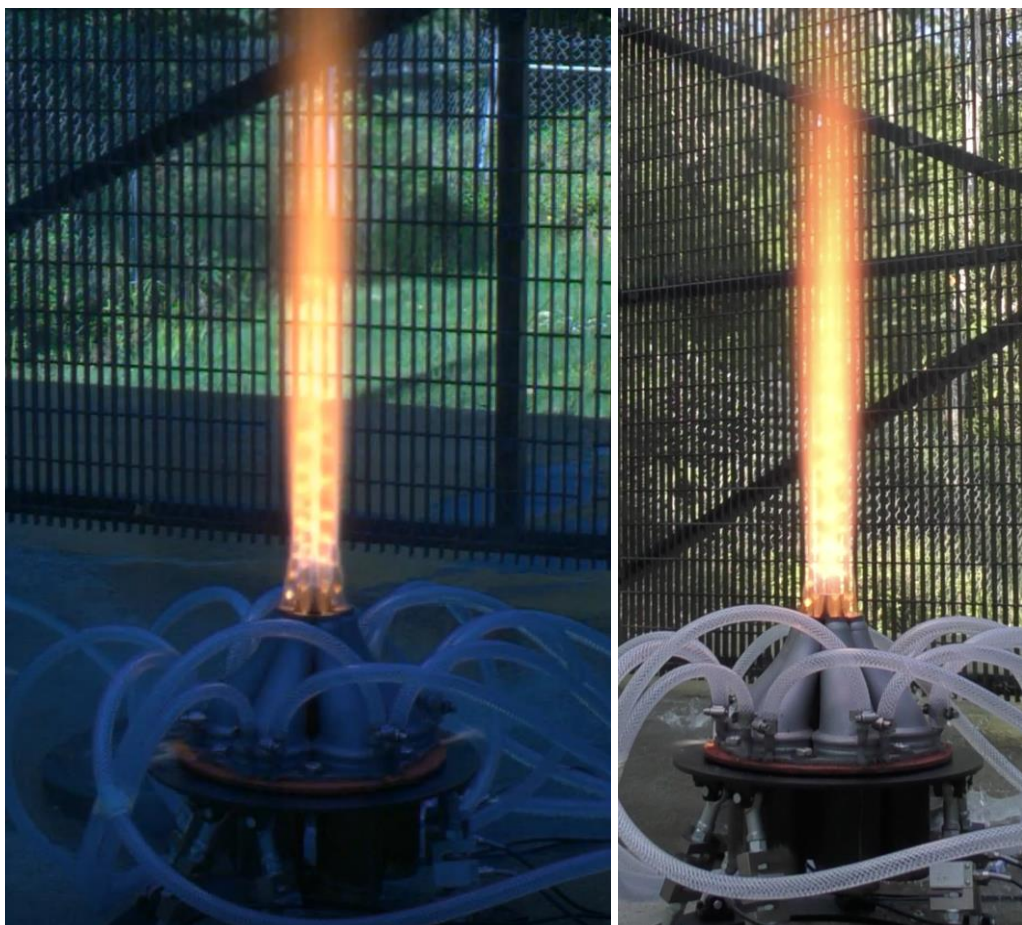


Figure 162: Still frames of Test Run 2.



Figure 163: Close up of gasket leakage from Test Run 2.



Figure 164: Image of the bottom of the aerospike after firing from Test Run 2.



Figure 165: Image of the motor casings after firing from Test Run 2.

Test Run 3 Footage:

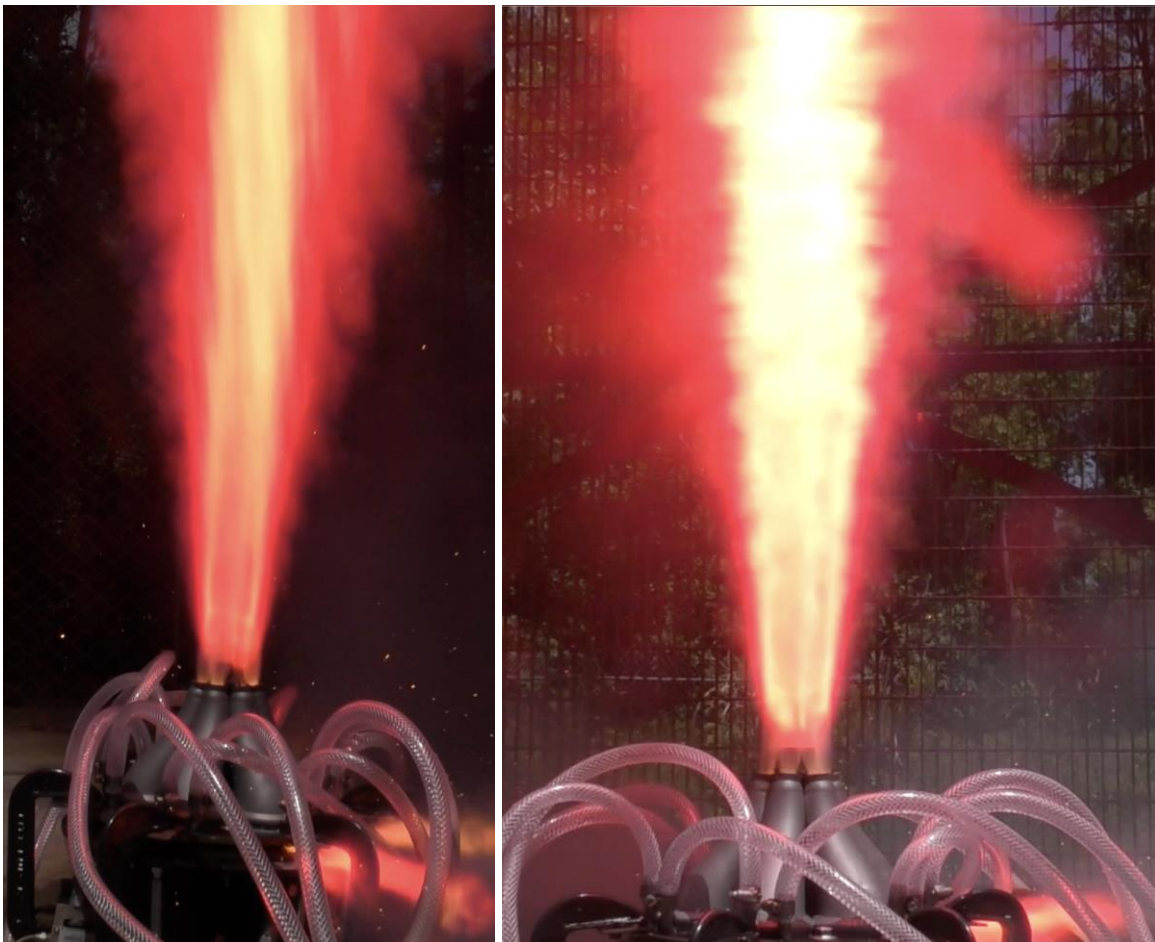


Figure 166: Still frames of Test Run 3.

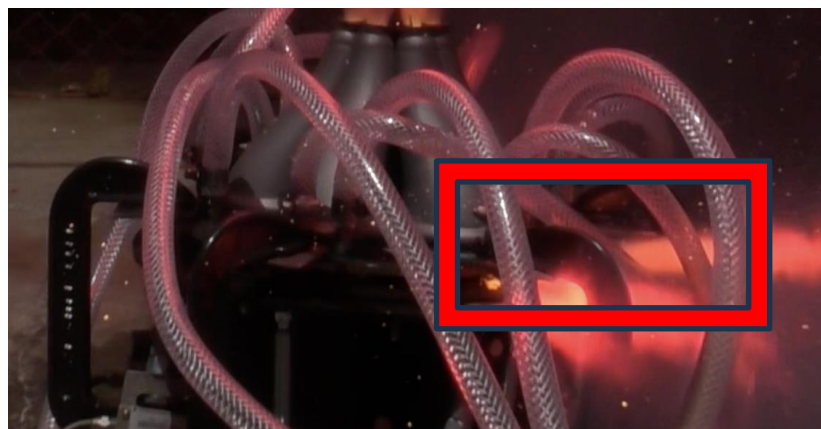


Figure 167: Close up of gasket leakage from Test Run 3.



Figure 168: Image of the tip of the aerospike after firing from Test Run 3.



Figure 169: Image of gasket on the motor casing after firing from Test Run 3.



Figure 170: Image of gasket on the motor casing after firing from Test Run 3.



Figure 171: Image of gasket on the motor casing after firing from Test Run 3.



Figure 172: Image of the motor casing after firing from Test Run 3.



Figure 173: Image of gasket and motor casing after firing from Test Run 3.



Figure 174: Image of gasket and motor casing after firing from Test Run 3.

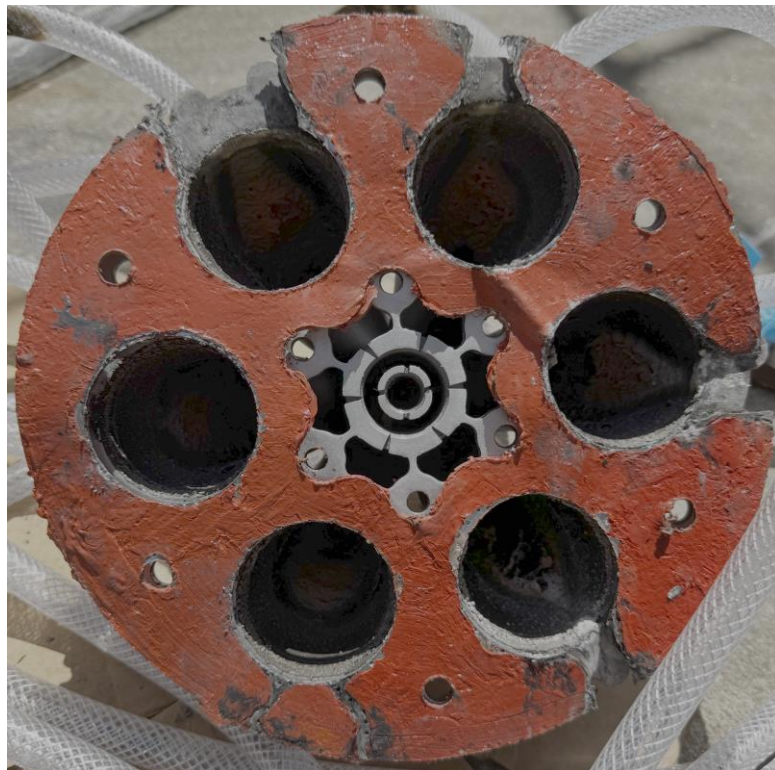


Figure 175: Image of gasket on the aerospike after firing from Test Run 3.



Figure 176: Image of the bottom of the aerospike after firing from Test Run 3.



Figure 177: Image of the inside of a nozzle of the aerospike after firing from Test Run 3.



Figure 178: Image of the aluminum chlorohydrate that was created inside the aerospike's nozzle during Test Run 3.

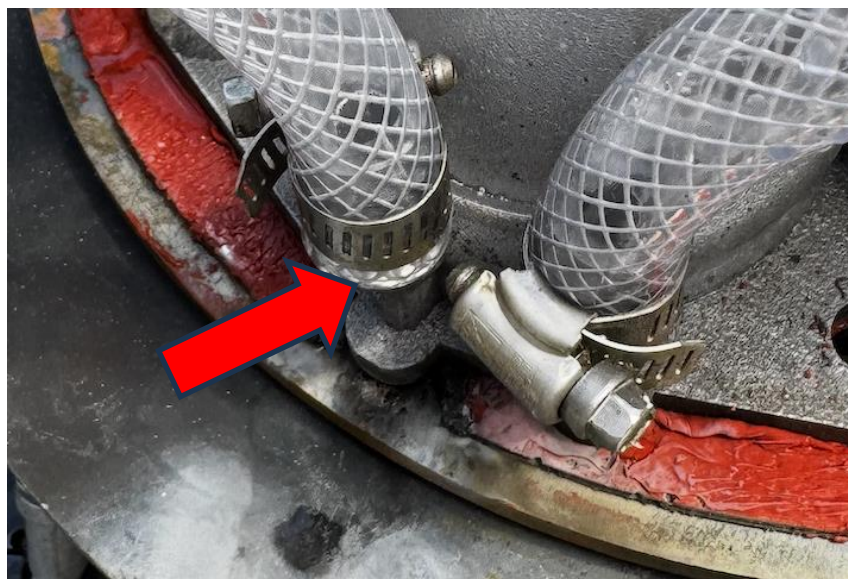


Figure 179: Image of where the leakage occurred from Test Run 3.



Figure 180: Image of where the leakage occurred from Test Run 3.



Figure 181: Image of where the leakage occurred from Test Run 3.



Figure 182: Image of where the leakage occurred from Test Run 3.

Test Run 4 Footage:

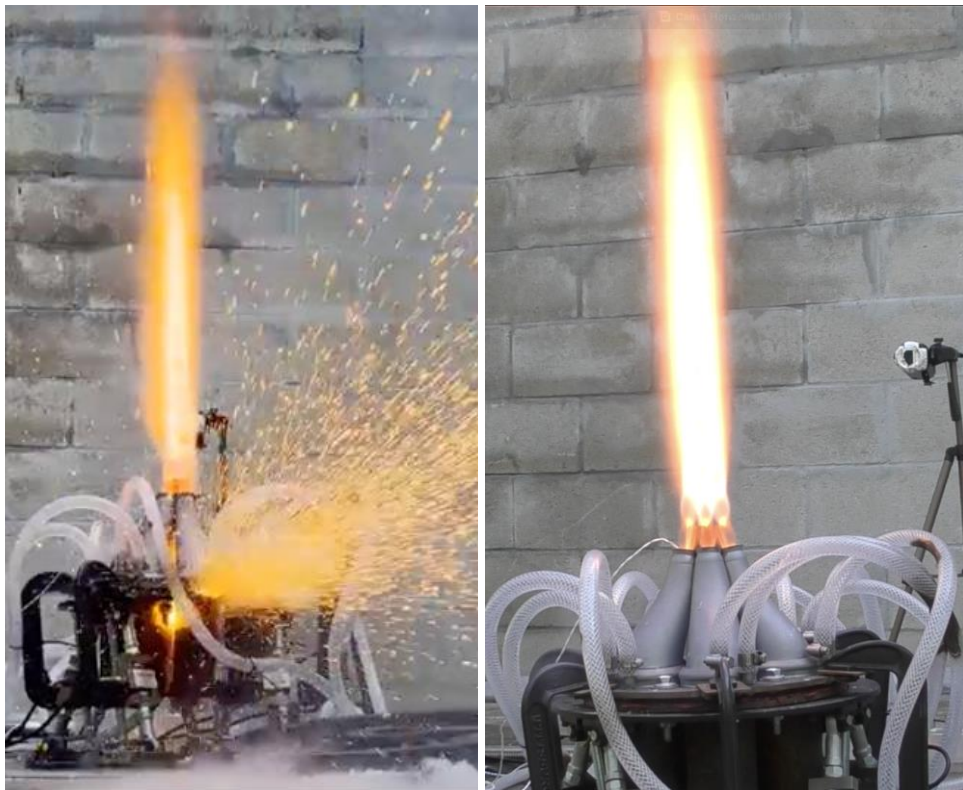


Figure 183: Still frames of Test Run 4.



Figure 184: Close up of gasket leakage from Test Run 3.

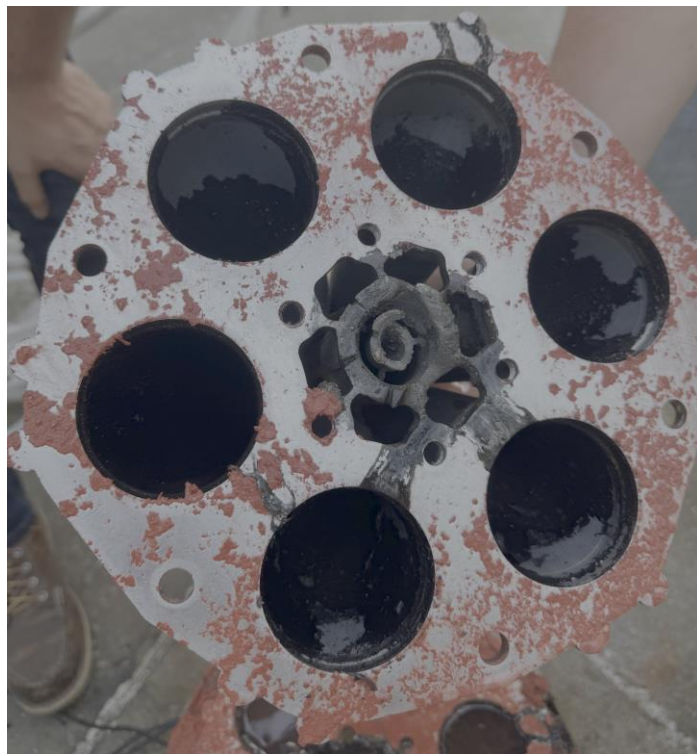


Figure 185: Image of the bottom of the aerospike after firing from Test Run 4.



Figure 186: Image of the motor casings after firing from Test Run 4.



Figure 187: Image that shows where some of the leakage occurred after firing from Test Run 4.



Figure 188: Image of the top of the gasket after firing from Test Run 4.



Figure 189: Image of the bottom of the gasket after firing from Test Run 4.



Figure 190: Image of the hose attached to the bottom of the aerospike after firing from Test Run 4.

Test Run 5 Footage:



Figure 191: Still frames of Test Run 5.

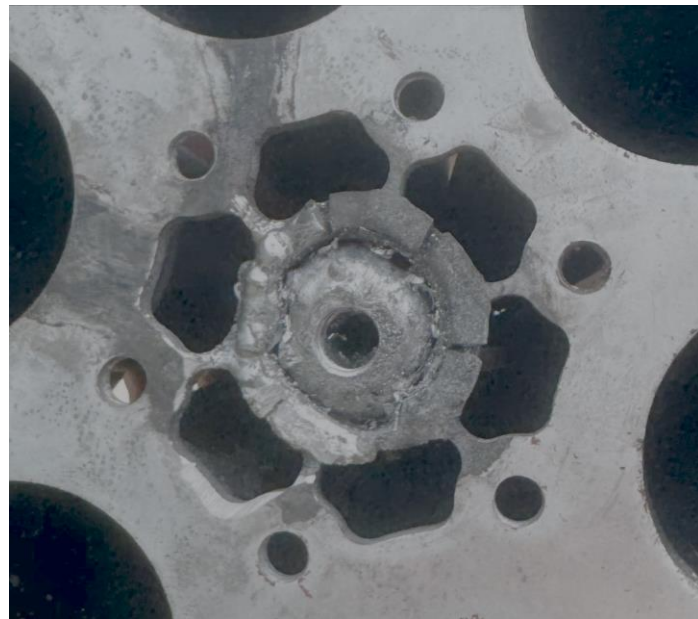


Figure 192: Image of the bottom of the aerospike after welding before Test Run 5.



Figure 193: Image of the bottom of the aerospike after firing from Test Run 5.



Figure 194: Close up image of the bottom of the aerospike after firing from Test Run 5.



Figure 195: Image of the inside of a nozzle of the aerospike after firing from Test Run 5.

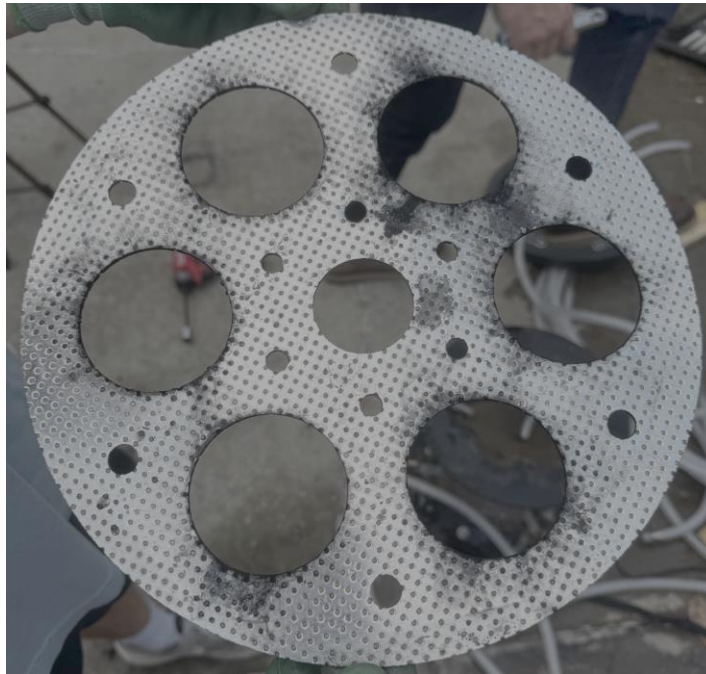


Figure 196: Image of the top of the gasket after firing from Test Run 5.



Figure 197: Image of the bottom of the gasket after firing from Test Run 5.

From the recorded values shown above in *Tables 31* and *32*, the overall maximum thrust that was achieved among test runs 1 to 5 was 989.605 [N], however this is for the redline grains where the predicted thrust should be even higher at around 1721 [N]. The highest thrust achieved using the 75mm Classic™ Propellant Grain, occurred in static fire tests 1 and 5, where the thrust reached 755.760 and 756.542 [N]. Since these two tests were nearly identical in their results, the LITVC tests will be setup using the same configuration for comparing the calculated deflection.

This was due to leakage that was created by the vermiculite gaskets that were used. *Table 30* displays the maximum thrust that was recorded for each test run as well as the calculated difference between the experimental and theoretical values, error percentage, accuracy percentage, and whether the measurement is accurate, borderline, or not accurate.

During the third and fourth test run, both metal 3D-printed aerospikes were damaged from firing. Instead of using the specified fuel grain, 75mm Classic™ Propellant Grain, which is an ammonium perchlorate composite propellant, the team used a fuel grain known as 75mm Redline™ Propellant Grain. This fuel grain was given to the team to use in case the team ran out of fuel. The redline fuel contained more aluminum and is more powerful than the selected fuel grain. During the test fire, the cooling channels ended up cooling the fuel grain which created

aluminum chlorohydrate. The aluminum chlorohydrate that was created was being shot through the nozzles of the aerospike at high speeds, essentially sandblasting the tip of the spike as shown in *Figure 168*. It also left physical pieces of aluminum chlorohydrate within the actual nozzle itself, as shown above in *Figures 177* and *178*.

To try and fix the issue with the gasket leaks, the team used high-temperature red RTV silicone gasket maker with a vermiculite gasket clamped down with six C-clamps. When doing this, it sealed the outside completely, but the center/inside area of the aerospike was not sealed completely. This resulted in a leak right at the center of the aerospike which exposed it to high temperatures for the duration of test run 4. Due to this leak, the LITVC portion of the aerospike was partially melted as shown above in *Figures 185* and *187*. It also melted the vinyl tuning in multiple spots as well as the brass hose barb shown above *Figure 190* which resulted in the sparks that are shown in *Figure 183*.

In order to be able to keep testing, the team needed to clean and try to repair the aerospikes. The aerospike used in the third test run was cleaned and had the aluminum chlorohydrate scrubbed out. The team were not able to get all of it out, but most of it was extracted. The rest of it was burned out in the following test fires. For the aerospike used in the fourth test run, it was a bit more complicated and difficult to repair. This one was given to Vaya Space's welder where they welded the bottom of the aerospike to close the LITVC port as shown above in *Figure 192*. The team then drilled and threaded a hole to create the LITVC port. Although this worked, after the test run, the weld began to diminish as shown above in *Figures 193* and *194*.

The welded aerospike from the fourth test run was used for the fifth test run. As shown above in *Table 28*, the newly repaired aerospike produced a maximum thrust of 756.542 [N] which is almost identical to the thrust that was produced in the first test run. The detailed test report of this is in the document *ENG-RPT-005-REV-A Fully Integrated Metal 3D Printed Aerospike Static Fire Test* (See Appendix C).

06. Fully Integrated Metal 3D-Printed Aerospike with Integrated LITVC Static Fire Test:

On the dates of April 21st and 22nd 2025, *ENG-PLN-006-REV-A Fully Integrated Metal 3D Printed Aerospike with LITVC Static Fire Test* (See Appendix C) was conducted. The objectives of this test were to validate the whole system, which includes the fully assembled metal 3D-printed aerospike mounted on the test stand configuration with the calibrated electrical system, LITVC integration, six solid rocket motors configuration with six MJG Firewire Initiators, 75mm Classic™ Propellant Grain and a water-cooling subsystem controlled via a manifold and pump. It will validate that the integrated LITVC system efficiently imposes lateral thrust for the aerospike by using the same fluid delivery system used in the test plan document *ENG-PLN-004-REV-D LITVC Wet Dress Rehearsal*.

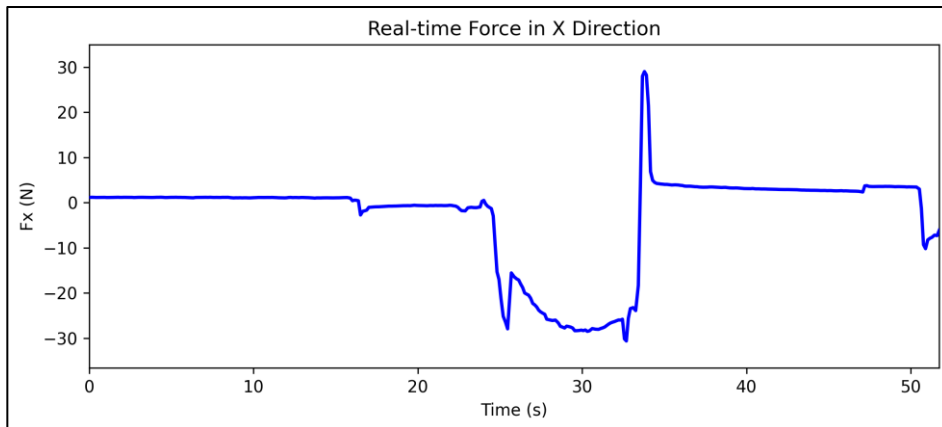
As shown below in the figures and discussion, all the success criteria were met. This includes that the prototype and systems components worked together as designed. It validated the system and subsystem requirements SYS. 01, SYS.02, SYS.03, SYS.05, PROP.01, PROP.02, STRUCT.01, STRUCT.02, STRUCT.03, STRUCT.04, CONTR.01, CONTR.02, CONTR.03, SAF.01, SAF.02, SAF.03, SAF.04, and SAF.05. *Table 12*, shown above, was used to determine if the data values that were collected were considered to be accurate to the analysis.

Test Run 1 Data:*Table 32: Force and Moment Values from Test Run 1.*

Data Type	F_x (N)	F_y (N)	F_z (N)	M_x (Nm)	M_y (Nm)	θ (°)
Experimental	30.643	68.724	753.295	0.0797	0.3409	3.7
Desired	0	69.816	1332.172	0	0	3

Table 33: Error Calculation Results from Test Run 1.

Error Calculations:				
Specified Measurement:	Difference:	Error Percentage (%):	Accuracy Percentage (%):	Classification:
F_x (N)	30.643	N/A	N/A	N/A
F_y (N)	-1.092	1.563756999	98.436243	Accurate
F_z (N)	-578.877	43.453602	56.546398	Not Accurate
Deflection Angle (°)	-0.7	90.14505153	9.854948466	Not Accurate

*Figure 198: Graph of the real-time force in the x-direction for test run 1.*

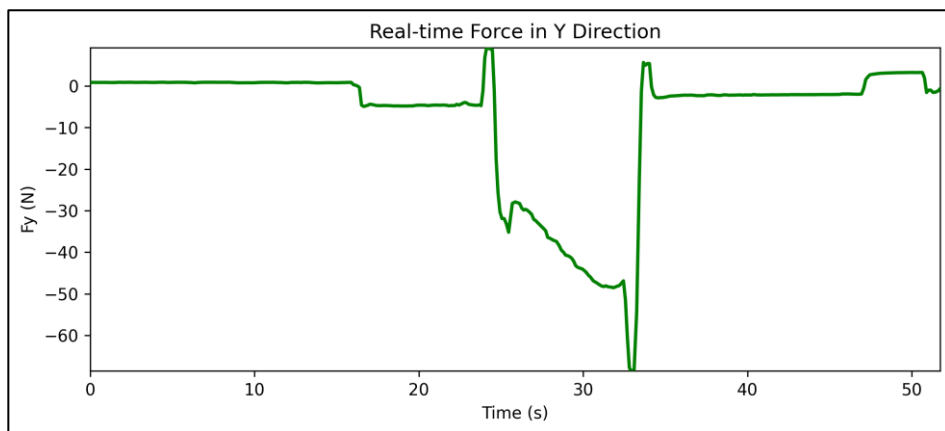


Figure 199: Graph of the real-time force in the y-direction for test run 1.

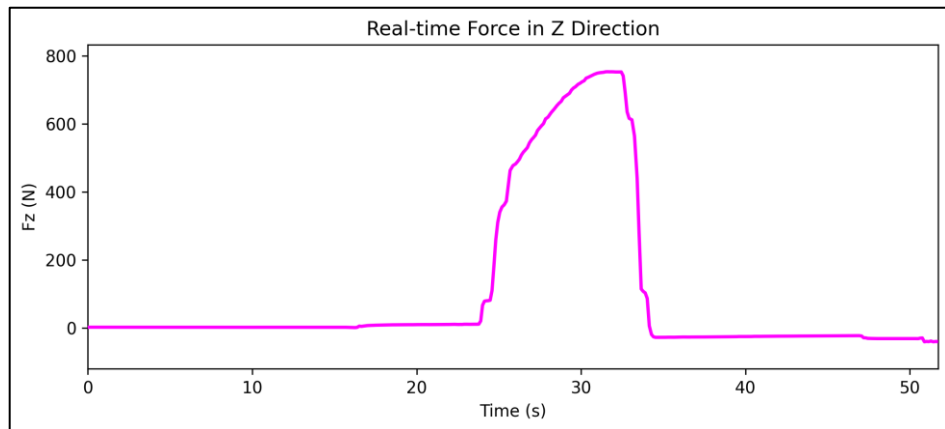


Figure 200: Graph of the real-time force in the z-direction for test run 1.

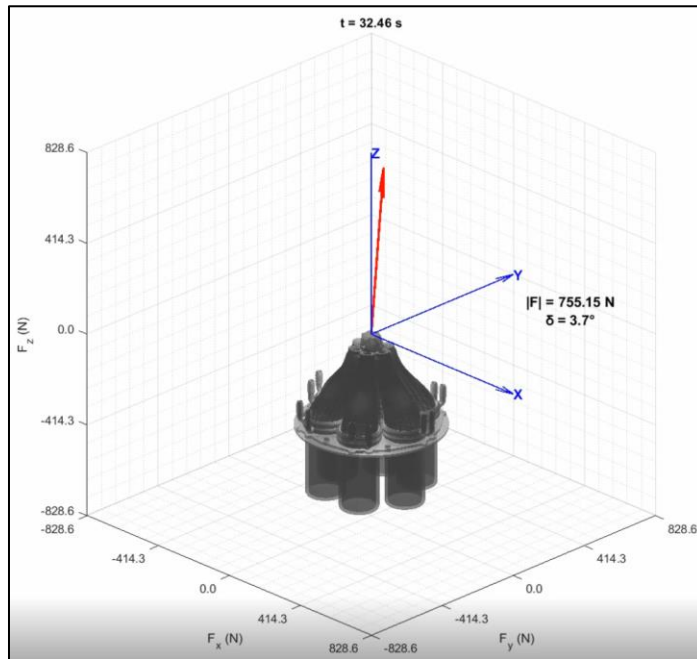


Figure 201: Diagram of the plume created with the data collected from test run 1.

The thrust that was achieved in the first test run is not accurate to what the analysis predicted. This is due to the gaskets the team used causing a visible leakage which made the pressure drop drastically. For this test the team used 1 vermiculite gasket.

Note: All deflection angles going forward are recorded at the peak thrust magnitude.

Test Run 2 Data:

Table 34: Force and Moment Values from Test Run 2.

Data Type	F_x (N)	F_y (N)	F_z (N)	M_x (Nm)	M_y (Nm)	θ (°)
Experimental	33.854	47.410	773.642	0.3975	0.2593	4.0
Desired	0	69.816	1332.172	0	0	3

Table 35: Error Calculation Results from Test Run 2.

Error Calculations:				
Specified Measurement:	Difference:	Error Percentage (%):	Accuracy Percentage (%):	Classification:
F_x (N)	33.854	N/A	N/A	N/A
F_y (N)	-22.406	32.09282468	67.90717532	Not Accurate
F_z (N)	-558.530	41.92629135	58.07370865	Not Accurate
Deflection Angle (°)	-1.0	43.54483565	56.45516435	Not Accurate

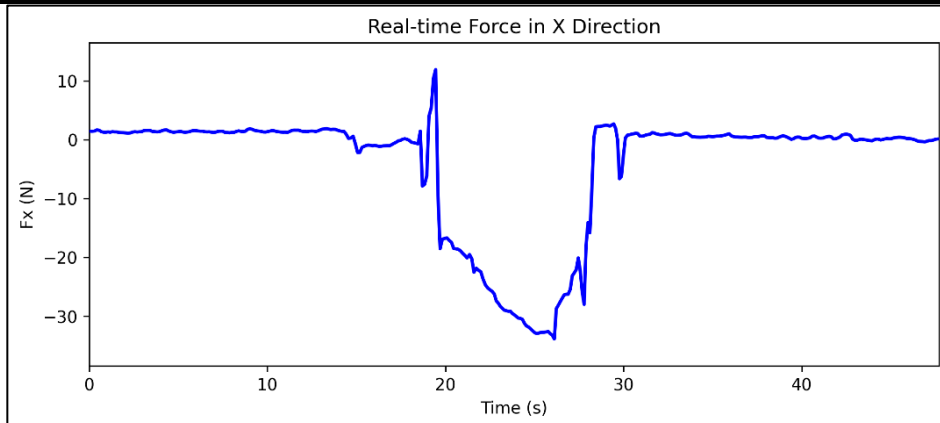


Figure 202: Graph of the real-time force in the x-direction for test run 2.

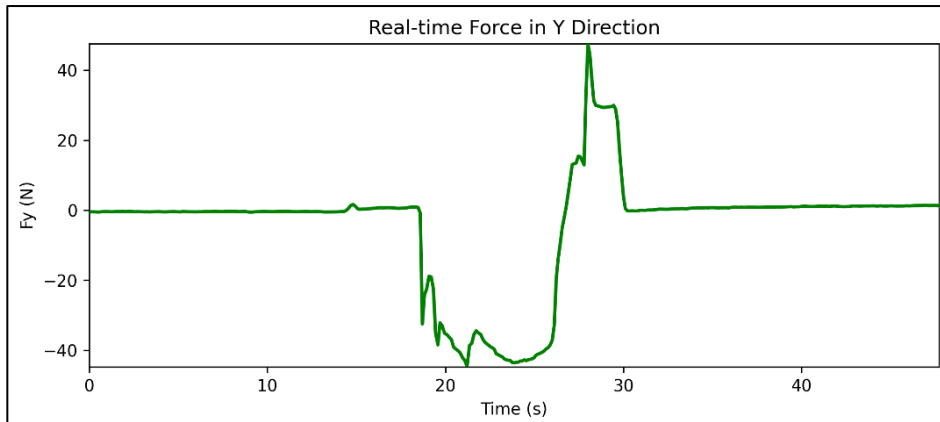


Figure 203: Graph of the real-time force in the y-direction for test run 2.

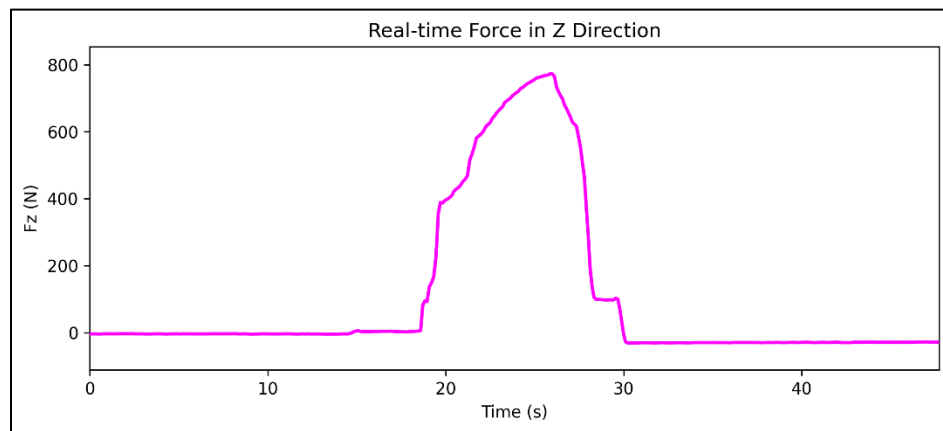


Figure 204: Graph of the real-time force in the z -direction for test run 2.

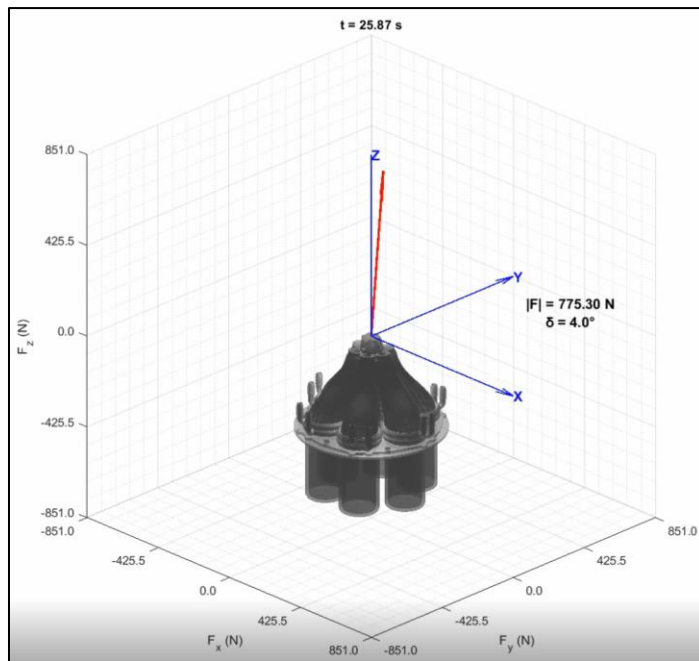


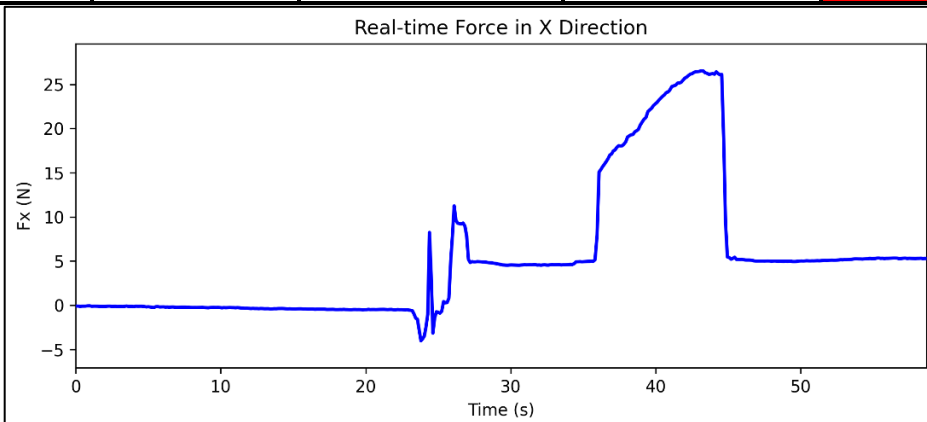
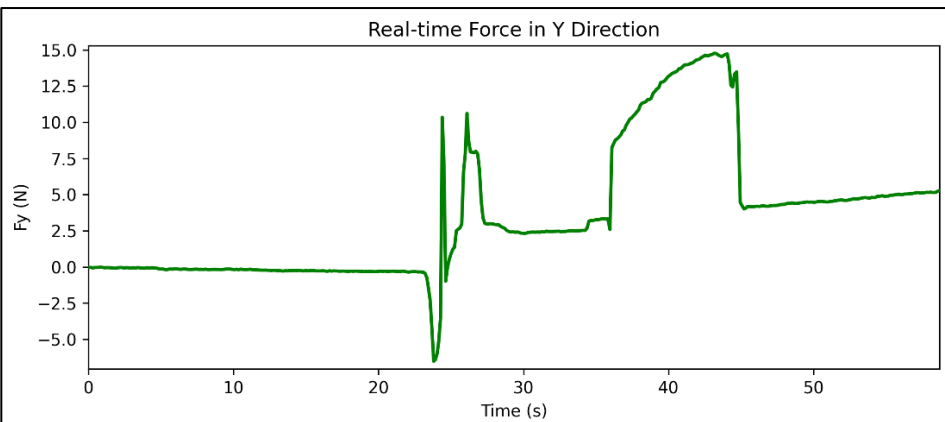
Figure 205: Diagram of the plume created with the data collected from test run 2.

Test Run 3 Data:*Table 36: Force and Moment Values from Test Run 1.*

Data Type	F_x (N)	F_y (N)	F_z (N)	M_x (Nm)	M_y (Nm)	θ (°)
Experimental	26.916	14.832	113.187	0.538	0.350	15.19
Desired	0	69.816	1332.172	0	0	3

Table 37: Error Calculation Results from Test Run 1.

Error Calculations:				
Specified Measurement:	Difference:	Error Percentage (%):	Accuracy Percentage (%):	Classification:
F_x (N)	26.916	N/A	N/A	N/A
F_y (N)	-54.984	78.755	21.244	Not Accurate
F_z (N)	-1218.985	91.505	8.496	Not Accurate
Deflection Angle (°)	12.191	406.356	-306.356	Not Accurate

*Figure 206: Graph of the real-time force in the x-direction for test run 3.**Figure 207: Graph of the real-time force in the y-direction for test run 3.*

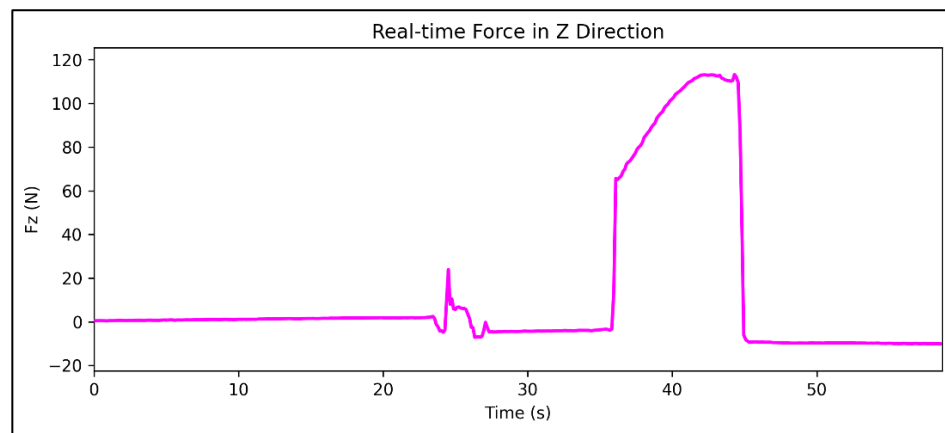


Figure 208: Graph of the real-time force in the z-direction for test run 3.

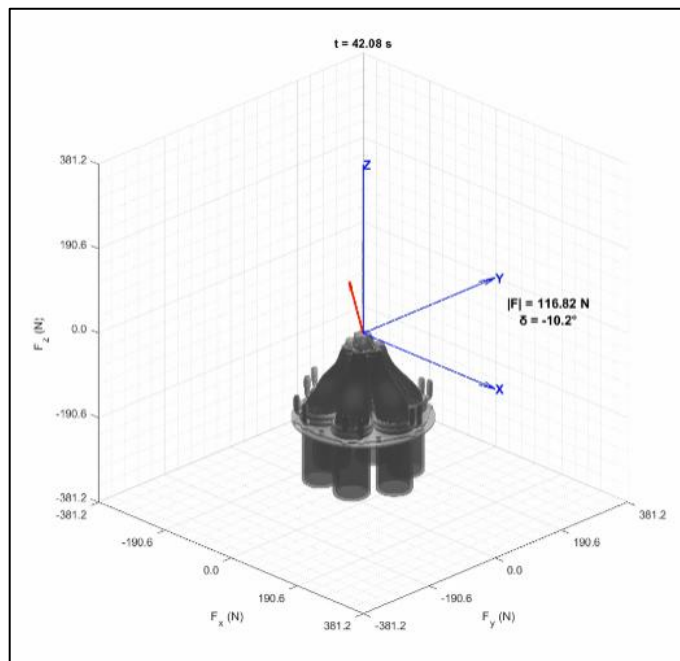


Figure 209: Diagram of the plume created with the data collected from test run 3.

Test Run 1 Footage:

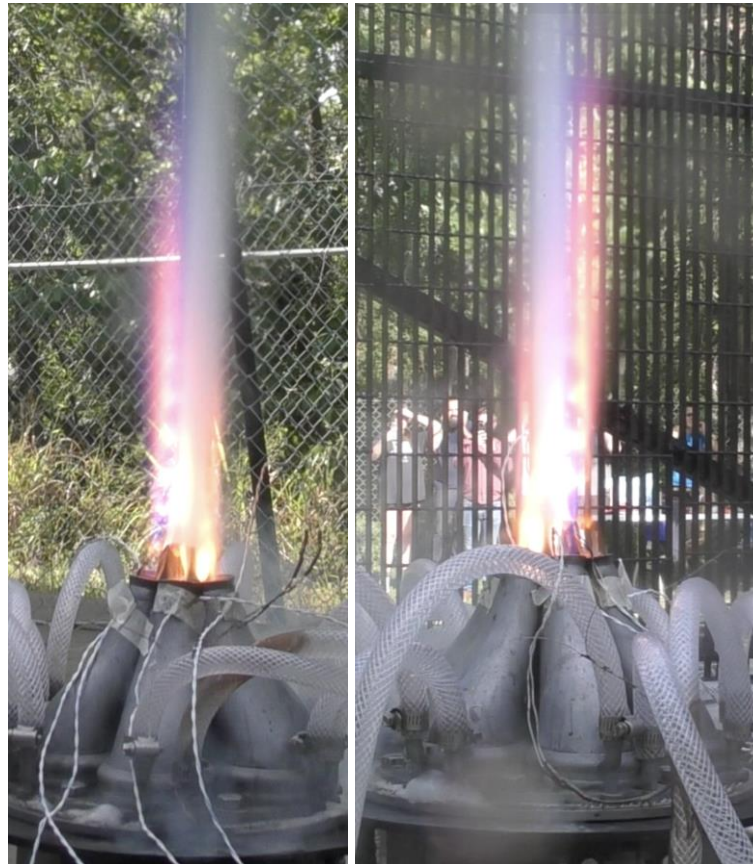


Figure 210: Still frames of Test Run 1.



Figure 211: Top of the aerospike after firing.

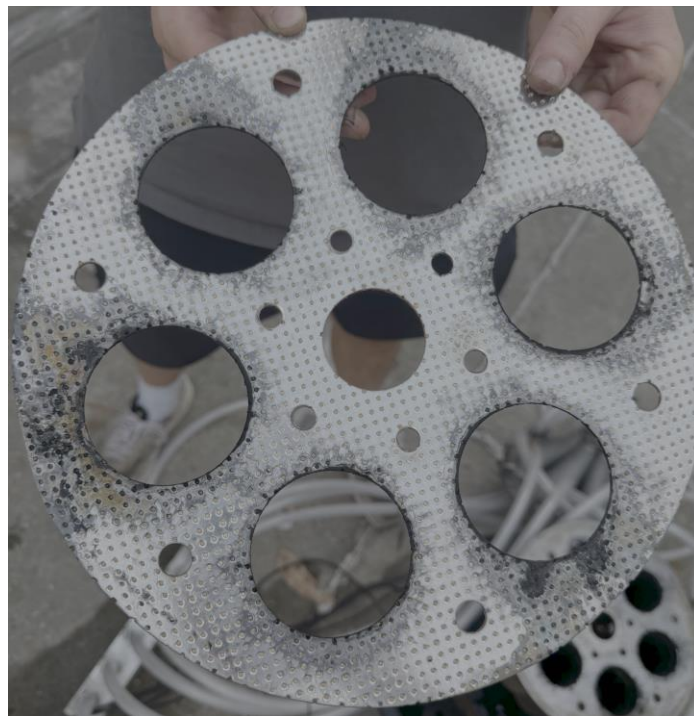


Figure 212: Image of the top of the gasket after firing.



Figure 213: Image of the top of the motor casings after firing.



Figure 214: Image of where the leakage occurred from Test Run 1.

Test Run 2 Footage:



Figure 215: Still frames of Test Run 2.



Figure 216: Top of the aerospike after firing.

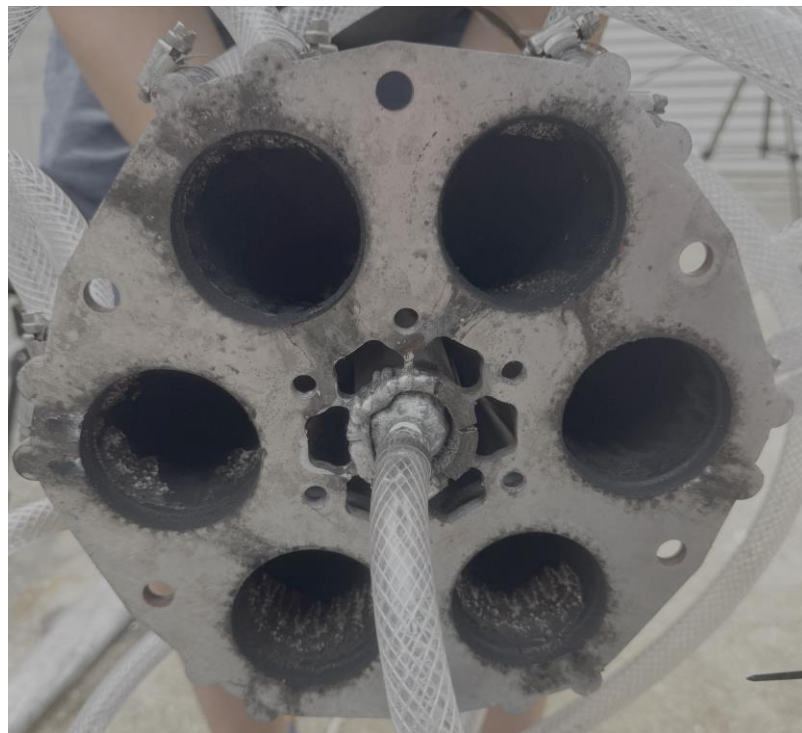


Figure 217: Bottom of the aerospike after firing.



Figure 218: Motor casings after firing.



Figure 219: Image of the top of the gasket after firing.



Figure 220: Image of the bottom of the gasket after firing.

Test Run 3 Footage:

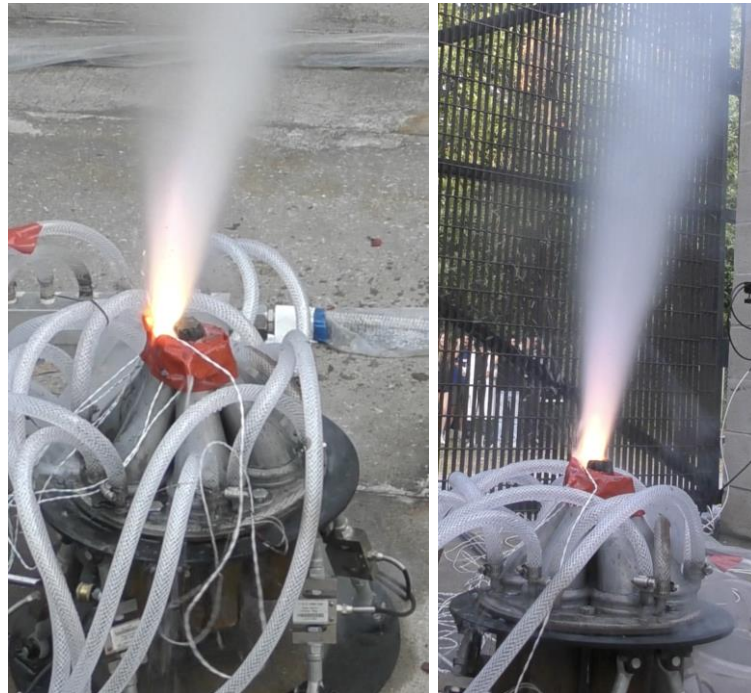


Figure 221: Still frames of Test Run 3.

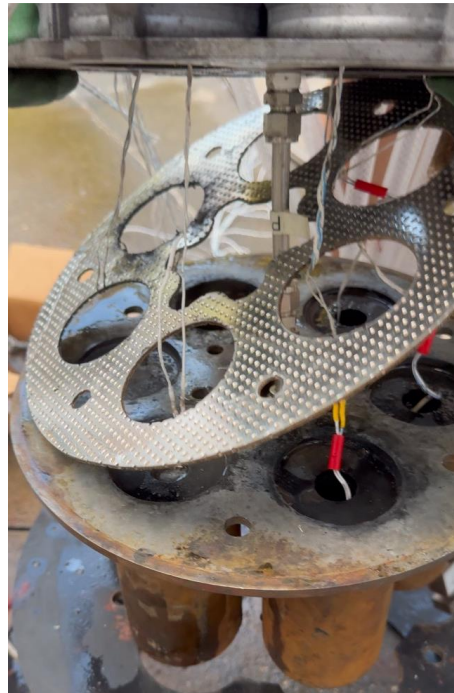


Figure 222: Motor casing and aerospike configuration after firing.



Figure 223: Motor casings after firing.



Figure 224: Top of the gasket after firing.

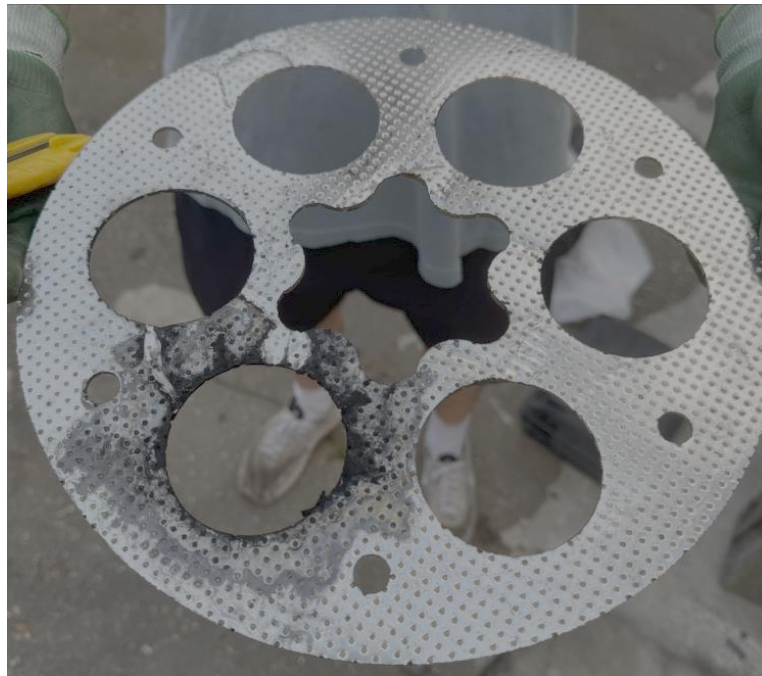


Figure 225: Bottom of the gasket after firing.

As shown above in *Tables 32 and 34*, the LITVC was able to produce a deflection angle of 3.7° at the peak value of generated thrust during the first test run and a deflection angle of 4.0° at the peak value of generated thrust during the second test run. This results in an average deflection angle of 3.9° . Test run 3 data was scrapped due to a misfire. The data was deemed unusable due to only one solid motor going off. For LITVC to produce a measurable and meaningful deflection, all 6 motors need to fire.

Despite technically reaching the desired value, there is an associated error of $\pm 2.4^\circ$ that arises from the regular static fire tests. Static fire tests 1 and 5 were the only controlled static firings from *ENG-RPT-005-REV-A Fully Integrated Metal 3D Printed Aerospike Static Fire Test*. Test runs 1 and 5 from this report reached a deflection angle of 2.1° and 2.7° , respectively. Although there should be relatively no vectoring during those tests, the average deflection is 2.4° which is primarily caused by the slight deviations in the ignition system. Since all propellant grains are not perfectly firing, each is behaving on a different pressure curve which is creating enough thrust to have some deflection produced.



Nonetheless, there is a noticeable and consistent difference between the two types of firings. For the LITVC firings, the team can say that the deflection angle achieved was $3.9^\circ \pm 2.4^\circ$, so a minimum of 1.5° and a maximum of 6.3° . Although this uncertainty doesn't cover the minimum desired angle deflection angle of 3° , the data does prove the exit plume was deflected to an extent higher than the static tests and does fulfill the PROP.02 requirement of providing a deflection of at least 3 [deg]. The detailed test report of this is in the document *ENG-RPT-006-REV-A Fully Integrated Metal 3D Printed Aerospike with LITVC Static Fire Test* (See Appendix C).



07. Fully Integrated Metal 3D-Printed Aerospike with Altitude Simulation Shroud Static Fire Test:

On April 21st, 2025, *ENG-PLN-007-REV-A Fully Integrated Metal 3D Printed Aerospike with Altitude Simulation Shroud Static Fire Test* (See Appendix C) was conducted. The objectives of this test were to validate the whole system, which includes the fully assembled metal 3D-printed aerospike mounted on the test stand configuration with the calibrated electrical system, six solid rocket motors configuration with six MJG Firewire Initiators, 75mm Classic™ Propellant Grain, a water-cooling subsystem controlled via a manifold and pump with an altitude simulation shroud. It will also validate that the altitude that the shroud is simulating records the thrust at an altitude of up to 25 [km].

As shown below in the figures and discussion, all the success criteria were met. This includes that the prototype and systems components worked together as designed and the altitude shroud that is being simulated recorded the thrust at an altitude of up to 25 km. It validated the system and subsystem requirements SYS. 01, SYS.02, SYS.04, SYS.05, PROP.01, PROP.03, STRUCT.01, STRUCT.02, STRUCT.03, STRUCT.04, CONTR.01, CONTR.02, SAF.01, SAF.02, SAF.03, SAF.04, and SAF.05. *Table 12*, shown above, was used to determine if the data values that were collected were considered to be accurate to the analysis.

Test Run 1 Data:

Table 38: Force, Moment, and Pressure Values from Test Run 1.

Data Type	F_x (N)	F_y (N)	F_z (N)	M_x (Nm)	M_y (Nm)	Pressure (kPa)
Experimental	96.193	116.880	520.649	0.7266	2.884	65.042
Theoretical	0	0	1334	0	0	10.00

Table 39: Error Calculation Results from Test Run 1.

Error Calculations:				
Specified Measurement:	Difference (N):	Error Percentage (%):	Accuracy Percentage (%):	Classification:
F_x (N)	96.193	N/A	N/A	N/A
F_y (N)	116.880	N/A	N/A	N/A
F_z (N)	-813.351	60.97082095	39.02917905	Not Accurate
M_x (Nm)	0.727	N/A	N/A	N/A
M_y (Nm)	2.884	N/A	N/A	N/A
Pressure (kPa)	55.042	84.63	15.37	Not Accurate

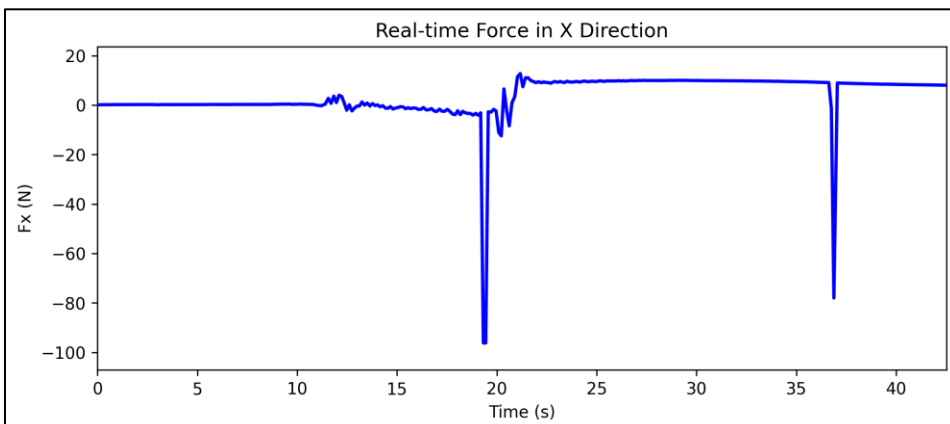


Figure 226: Graph of the real-time force in the x-direction for test run 1.

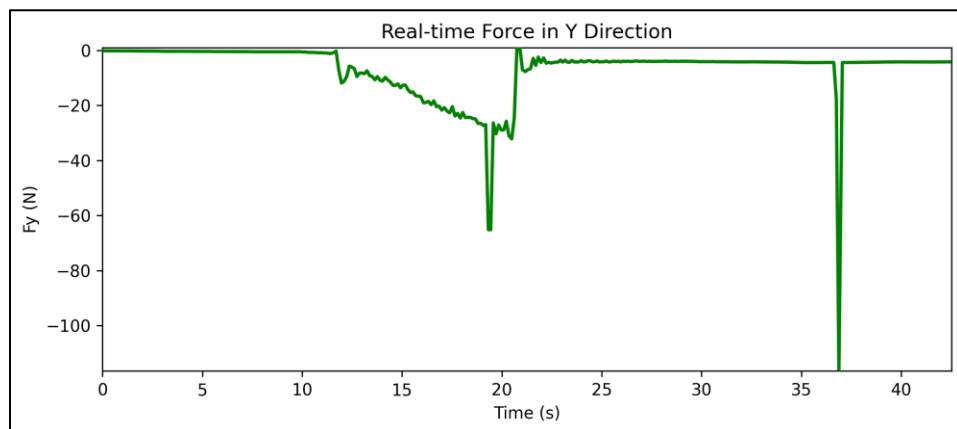


Figure 227: Graph of the real-time force in the y-direction for test run 1.

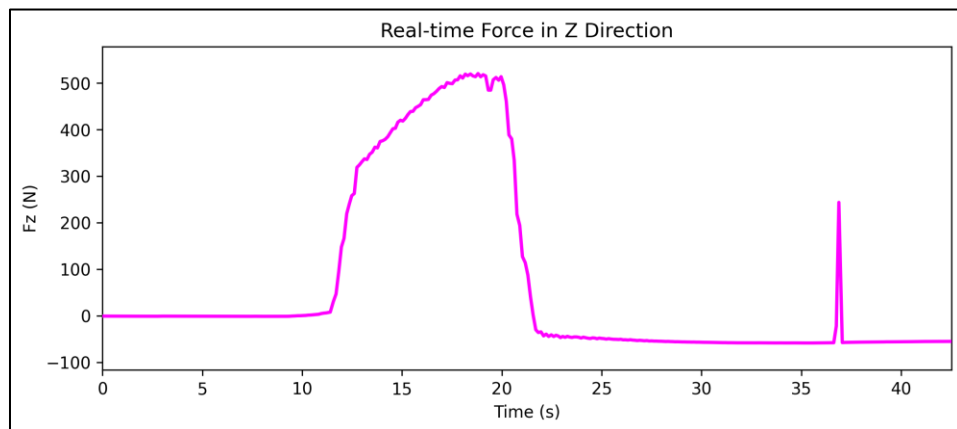


Figure 228: Graph of the real-time force in the z-direction for test run 1.

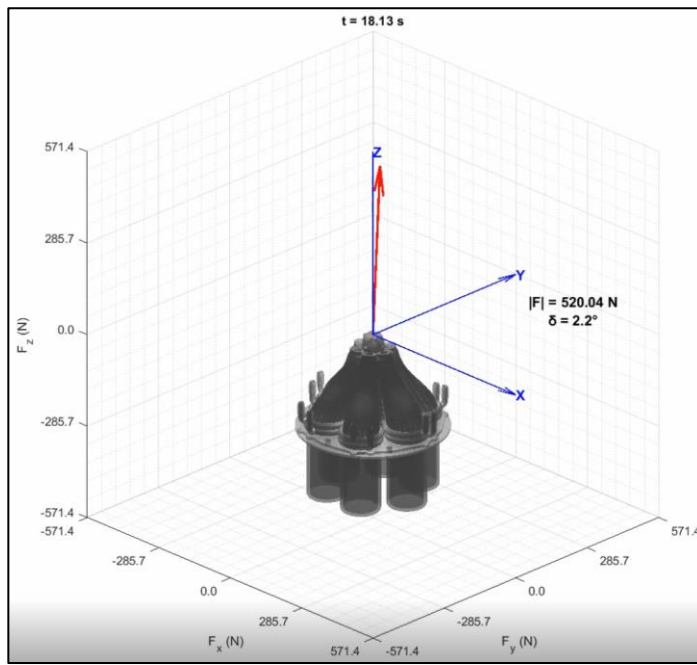


Figure 229: Diagram of the plume created with the data collected for test run 1.

The thrust that was achieved in the first test run is not accurate to what the analysis predicted. This is due to the gaskets the team used causing leakage which made the pressure drop drastically. For this test the team used 1 vermiculite gasket. The requirement that drove the altitude simulating shroud stated that the system shall be able to simulate altitudes up to 25 km, whereas for this test, an altitude of roughly 3.59 km was simulated.

Test Run 1 Footage:

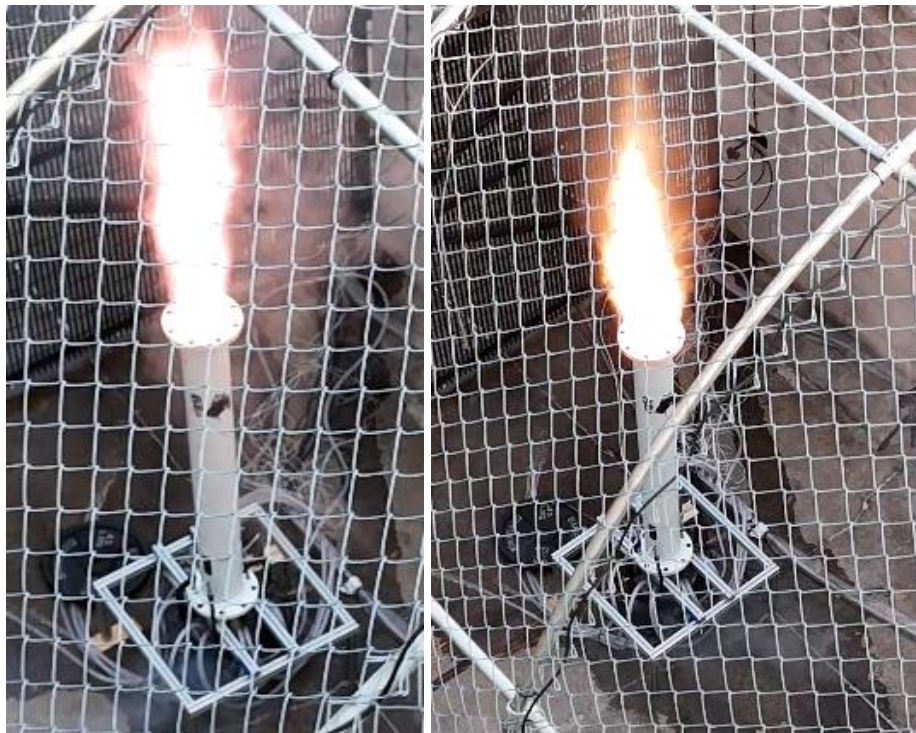


Figure 230: Still frame of Test Run 1.

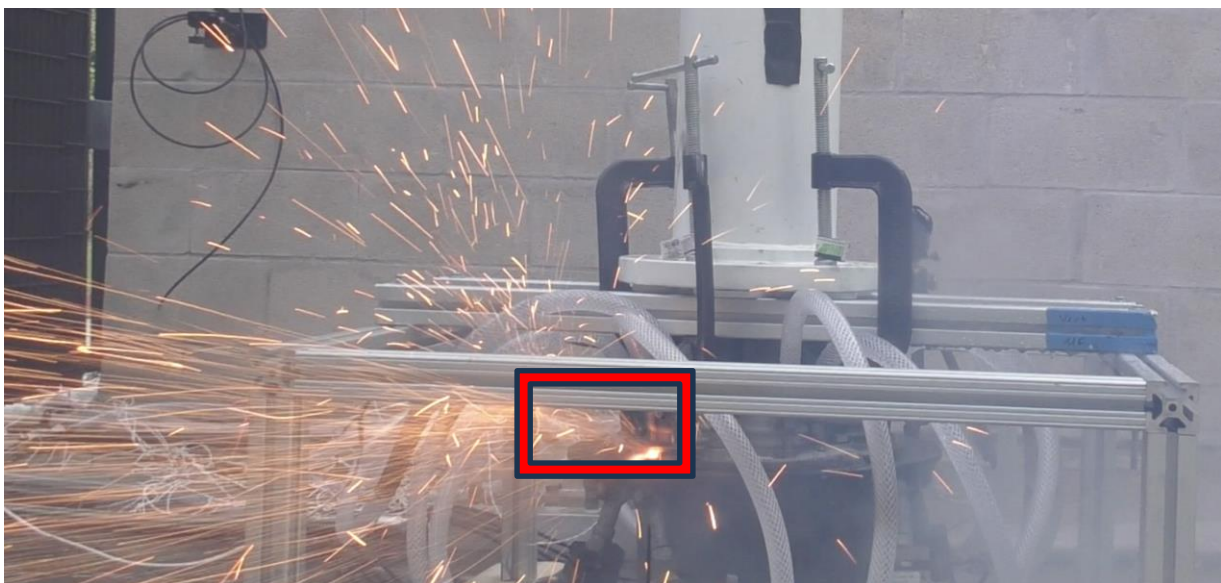


Figure 231: Close up of gasket leakage.

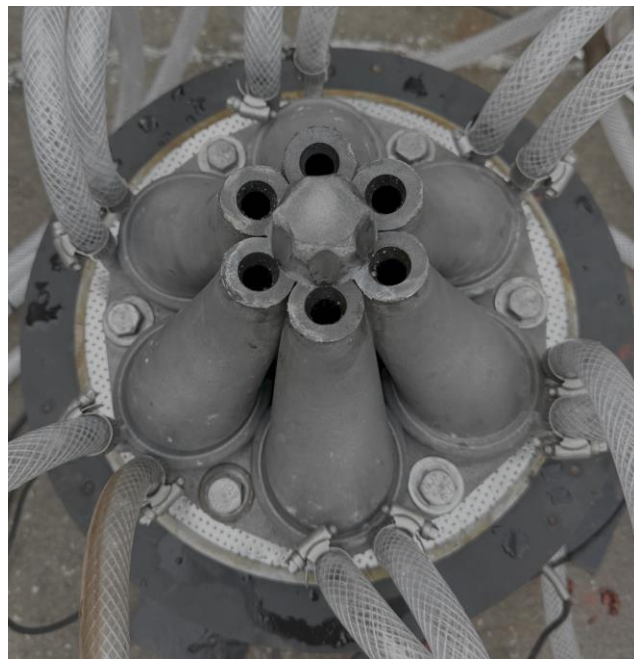


Figure 232: Top view of the aerospike after firing.



Figure 233: Close up of the aerospike after firing.



Figure 234: Inside view of the altitude simulating shroud.

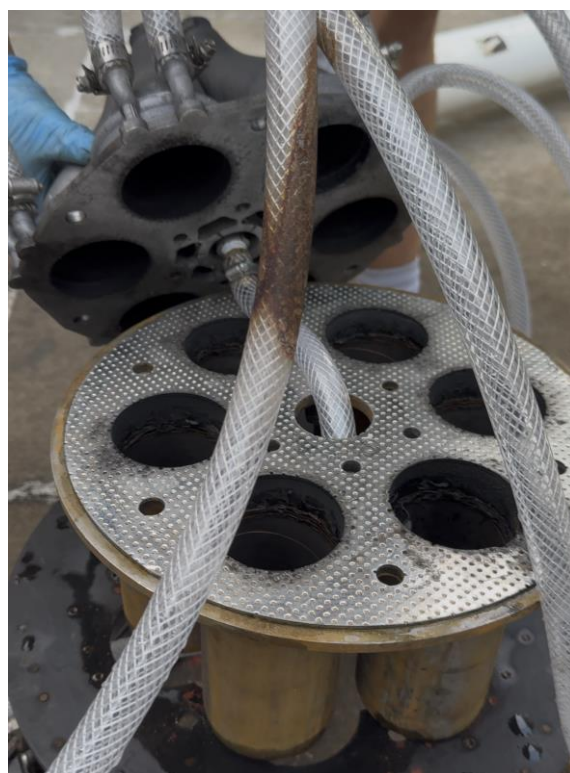


Figure 235: Aerospike, gasket, and motor casing after test firing.



Figure 236: Gasket after test firing.



Figure 237: Gasket after test firing.



Figure 238: Image of the top of the gasket after firing.



Figure 239: Image of the bottom of the gasket after firing.



Figure 240: Image of the motor casings after firing.

The altitude simulation shroud static fire test yielded valuable insights into system performance and areas for refinement. While the recorded thrust was lower than theoretical predictions, the test successfully demonstrated the main functionality of the integrated altitude simulation shroud system. The shroud was able to reduce the local ambient pressure around the aerospike to 65,042 [Pa], simulating an altitude of 3.59 [km], confirming the feasibility of local ambient pressure reduction using the current design. In the original CFD analysis, the system should have produced an ambient pressure of 10 [kPa] simulating an altitude of 16 [km] however, this analysis accounts for the combustion pressure being 1.724 [Mpa] (or 250 [psia]) not the reduced value caused by the leak. The Post-Test Analysis Section on p.265 addresses this issue and simulates the CFD analysis at an estimated combustion pressure that was experienced during the firing.

A completely simulated 25 km test was largely unrealistic. A better system could be implemented to better reduce the pressure inside the shroud by utilizing a pump that could suck



out the air inside the shroud from behind the exit of the nozzles themselves. This could be monitored and controlled to accurately simulate any altitude that was required under the capabilities of the pump.

Note that the significant pressure losses experienced during the static fires of this system also impacted the results of this test; lower chamber pressure means lower exhaust velocity. Due to the pressure leak, the ambient pressure was not able to decrease to the expected 10 [Kpa] but instead to the higher ambient pressure proven by the new simulation. The test setup validated numerous system and subsystem requirements, including structural integrity, burn duration, remote ignition, thrust data acquisition, and compliance with safety protocols. Key challenges identified include improving aerospike to motor casing sealing, shroud to aerospike interface, and test setup turnaround time. The detailed test report of this is in the document *ENG-RPT-007-REV-A Fully Integrated Metal 3D Printed Aerospike with Altitude Simulation Shroud Static Fire Test* (See Appendix C).



10 RISK MANAGEMENT (SMITH)

Since the team will be metal 3D printing the aerospike nozzle and using solid rocket motors, there are multiple potential risks that could occur. These risks have been categorized into technical, operational, schedule, and financial risks. Identifying these potential risks helps to prevent possible failures, injuries, schedule delays, and cost overruns.

The risks have been categorized and organized into four risks matrices, which are shown below in *Tables 45, 46, 48, 49, 51, 52, 54, and 55*. These risks have been organized from the highest risk priority number (RPN) to the lowest. The values for each RPN were calculated by multiplying its severity level, occurrence level, and detection level. In order to determine what each risk's severity, occurrence, and detection level were, an action priority table, displayed below in *Table 43*, was created. This type of risk matrix is a failure modes and effects analysis (FMEA). After each risk was identified, mitigation strategies for each risk were created to help lower the potential risk level and its effects.

Table 40: Severity Levels [11]

Severity (1-10)	Meaning
1 - 2	Minor effect on performance
3 - 4	Moderate effect, possible inconvenience
5 - 6	Significant impact, could degrade function
7 - 8	Serious, could cause loss of function or safety issues
9 - 10	Critical failure, system-level hazard

Table 41: Occurrence Levels [11]

Occurrence (1-10)	Meaning
1 - 2	Unlikely to occur
3 - 4	Low probability of occurrence
5 - 6	Moderate likelihood of occurrence
7 - 8	High likelihood of occurrence
9 - 10	Very likely to occur

Table 42: Detection Levels [11]

Detection (1-10)		Meaning	
1 - 2		Almost certain to detect	
3 - 4		Likely to detect	
5 - 6		Moderate chance of detection	
7 - 8		Low chance of detection	
9 - 10		Very unlikely to detect	

Table 43: Action Priority Table

		Occurrence					Detection
		1-2	3-4	5-6	7-8	9-10	
Severity	1-2	L	L	L	L	L	1-3
	1-2	L	L	L	L	L	4-7
	1-2	L	L	L	L	L	8-10
	3-4	L	L	L	L	L	1-3
	3-4	L	L	L	L	M	4-7
	3-4	L	L	L	M	M	8-10
	5-6	L	L	M	M	M	1-3
	5-6	L	M	M	M	H	4-7
	5-6	L	M	M	M	H	8-10
	7-8	L	M	M	M	H	1-3
	7-8	L	M	M	H	H	4-7
	7-8	L	M	H	H	H	8-10
9-10	9-10	L	H	H	H	H	1-3
	9-10	L	H	H	H	H	4-7
	9-10	L	H	H	H	H	8-10
Action Priority Table							

10.1 Team Technical Risks (Smith)

Table 44: Technical Risks

Failure Mode	Effect	Mitigation
1.) Student Ansys Software Limitation	Inaccurate simulation models of aerospike and test stand.	Get second opinions from the engineers at Vaya as well as various professors at Florida Tech. While testing ensure all safety procedures are being followed in case the models were inaccurate to prevent injuries.
2.) Vibration-Induced Fatigue	Prototype failure/breakage during test.	Eliminate as much vibration as possible along with creating an S-N chart to help predict when failure could occur. Also having bystanders wear PPE like safety glasses.
3.) LITVC Failure	Incorrect data and improper flow.	All remote operations tested in a safe environment; use of emergency shutdown mechanisms
4.) Thermal Stress Failure	Incorrect data and prototype failure during testing.	Monitor printing temperatures to ensure minimal thermal stress as well as everyone in the area is required to wear PPE such as safety glasses. Additionally, the printed geometry could be designed with warping in mind for the specific printer used, reducing the risk of warping further
5.) Material Failure	Prototype failure/breakage during test.	Test area will be viewed at further distance and everyone in the area is required to wear PPE such as safety glasses
6.) Anisotropic Properties Failure	Prototype failure/breakage during test.	Quality control on each part that is manufactured to ensure each part is evenly printed in the same direction, and have bystanders wear PPE like safety glasses.
7.) Residual Stress Failure	Premature cracks and warping that will lead to prototype failure.	Do quality control on each component that is 3D to check for any visible cracks or warping of the part. Also having bystanders wear PPE like safety glasses.
8.) Layer Delamination	Prototype failure or inaccurate data.	Do quality control on each component that is 3D to check for any visible signs of delamination. Also having bystanders wear PPE like safety glasses.

Table 45: Technical Risks Before Mitigation

Failure Mode	Severity (1-10)	Occurrence (1-10)	Detection (1-10)	Old RPN	Risk Level:
1.) Student Ansys Software Limitation	9	8	6	432	High
2.) Vibration-Induced Fatigue	8	6	6	288	Medium
3.) LITVC Failure	6	5	9	270	Medium
4.) Thermal Stress Failure	8	4	8	256	Medium
5.) Material Failure	8	5	3	120	Medium
6.) Anisotropic Properties Failure	8	5	3	120	Medium
7.) Residual Stress Failure	8	3	3	72	Medium
8.) Layer Delamination	9	2	3	54	Low

Table 46: Technical Risks After Mitigation

Failure Mode	Severity (1-10)	Occurrence (1-10)	Detection (1-10)	New RPN	Risk Level:
1.) Student Ansys Software Limitation	7	4	3	84	Medium
2.) Vibration-Induced Fatigue	7	4	3	84	Medium
3.) LITVC Failure	5	5	5	125	Medium
4.) Thermal Stress Failure	4	5	3	60	Low
5.) Material Failure	2	5	2	20	Low
6.) Anisotropic Properties Failure	4	2	1	8	Low
7.) Residual Stress Failure	4	2	1	8	Low
8.) Layer Delamination	4	2	1	8	Low

10.2 Team Operational Risks (Smith)

Table 47: Operational Risks

Failure Mode	Effect	Mitigation
1.) Structural Failure (Test Stand)	Loss of testing.	Secure mounting with structural inspection prior to testing.
2.) Manufacturing Inconsistency	Inaccurate data, premature failure of prototype, schedule delay.	Ensure that the values from the CAD drawings and previous dimensional inspection reports line up accordingly or are similar as well as visually check each part for any sort of flaws or issues. If inconsistencies are discovered, find a new manufacturer to print 3D parts.
3.) Material Corrosion	Oxidation or corrosion which could lead to failure.	Ensuring that the parts printed are kept in a dry, temperature control area to prevent rusting.

Table 48: Operational Risks Before Mitigation

Failure Mode	Severity (1-10)	Occurrence (1-10)	Detection (1-10)	Old RPN	Risk Level:
1.) Structural Failure (Test Stand)	10	5	4	200	High
2.) Manufacturing Inconsistency	8	4	2	64	Medium
3.) Material Corrosion	6	1	1	6	Low

Table 49: Operational Risks After Mitigation

Failure Mode	Severity (1-10)	Occurrence (1-10)	Detection (1-10)	New RPN	Risk Level:
1.) Structural Failure (Test Stand)	5	3	2	30	Low
2.) Manufacturing Inconsistency	4	3	1	12	Low
3.) Material Corrosion	3	1	1	3	Low

10.3 Team Schedule Risks (Smith)

Table 50: Schedule Risks

Failure Mode	Effect	Mitigation
1.) 3D Printing Failure	Schedule delay.	Have print monitoring measures set in place by the manufacturer based on what safety standard they are using as a company.
2.) Design Failure	Schedule delay.	Have multiple people work on the design as well as have the industry mentors look over it to ensure that the team did not miss something.
3.) Supply Chain Issues (3D Printing)	Schedule delay.	Order what material the team need immediately after deciding on it as well as send in design specifications to the manufacturer for immediate manufacturing.
4.) Supply Chain Issues (Solid Rocket Motors)	Schedule delay.	Order solid rocket motors as soon as possible as well as a larger quantity in case failure occurs with the motors.

Table 51: Schedule Risks Before Mitigation

Failure Mode	Severity (1-10)	Occurrence (1-10)	Detection (1-10)	Old RPN	Risk Level:
1.) 3D Printing Failure	7	8	8	448	High
2.) Design Failure	10	5	8	400	High
3.) Supply Chain Issues (3D Printing)	9	8	3	216	High
4.) Supply Chain Issues (Solid Rocket Motors)	9	8	3	216	High

Table 52: Schedule Risks After Mitigation

Failure Mode	Severity (1-10)	Occurrence (1-10)	Detection (1-10)	New RPN	Risk Level:
1.) 3D Printing Failure	6	5	3	90	Medium
2.) Design Failure	7	5	4	140	Medium
3.) Supply Chain Issues (3D Printing)	4	5	2	40	Low
4.) Supply Chain Issues (Solid Rocket Motors)	4	5	2	40	Low

10.4 Team Financial Risks (Smith)

Table 53: Financial Risks

Failure Mode	Effect	Mitigation
1.) 3D Printing Failure	Spending more money to reprint design.	Set aside some money in the budget to use as a fallback as well as ensure that the 3D printer is set up to the design's needs and specifications.
2.) Cost of Large Quantity of Motors	A large amount of the budget will be put towards motors and not other items that will also be needed.	Inquire about donations and/or sponsorship from Rocket Motor Components (RCS).
3.) Shipping and Taxes	More money spent than planned for.	Include shipping and taxes in the budget to plan accordingly.

Table 54: Financial Risks Before Mitigation

Failure Mode	Severity (1-10)	Occurrence (1-10)	Detection (1-10)	Old RPN	Risk Level:
1.) 3D Printing Failure	5	8	5	200	Medium
2.) Cost of Large Quantity of Motors	5	7	1	35	Medium
3.) Shipping and Taxes	4	5	1	20	Low

Table 55: Financial Risks After Mitigation

Failure Mode	Severity (1-10)	Occurrence (1-10)	Detection (1-10)	New RPN	Risk Level:
1.) 3D Printing Failure	2	3	1	6	Low
2.) Cost of Large Quantity of Motors	1	1	1	1	Low
3.) Shipping and Taxes	2	2	1	6	Low

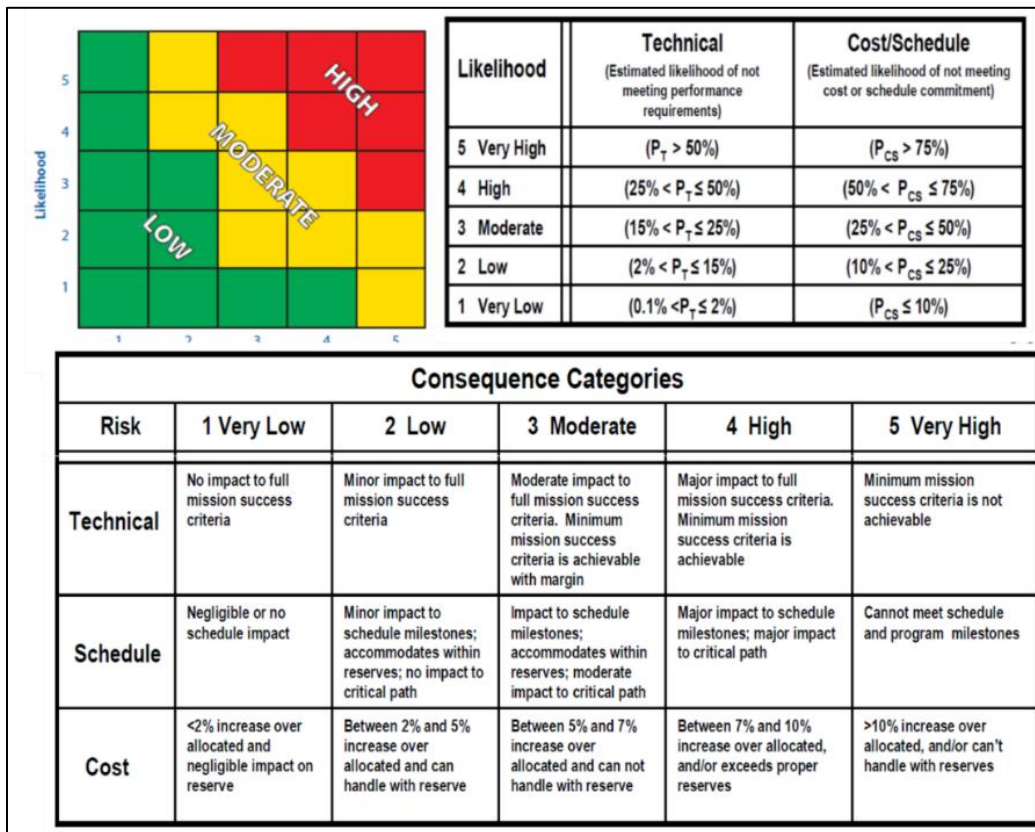


Figure 241: Risk Categorization example from GSFC-STD-0002, "Technical Risk Reporting"

11 POST-CDR ANALYSIS (VALLIERE)

With AlSi10Mg being the final material choice for the aerospike print, another thermo-structural analysis must be done to verify the aerospike's survivability during predicted testing conditions. The setup for this analysis is essentially identical to the one seen in Figure 100 and Figure 104, the only difference being the material model used for AlSi10Mg has a much higher fidelity, specifically regarding the material's plasticity. Thermal analysis results can be seen in Figure.

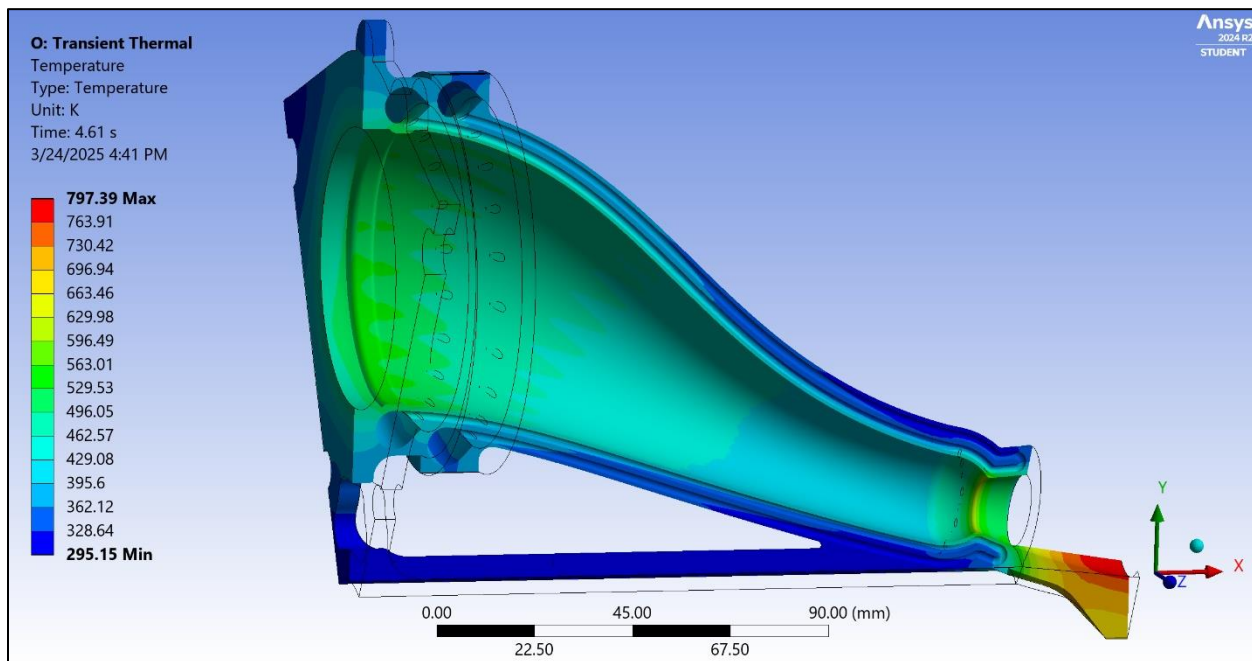


Figure 242: AlSi10Mg – Thermal Results

The highest temperatures occur directly under the manifold, where the velocity of the coolant is at a minimum, at the throat which is caused by the increased heat flux in that section, and at the end of the spike where there is no active cooling. The melting point of AlSi10Mg is 843.15 [K], however, the maximum temperature reached from the simulation is 797.39 [K]. Although no material reaches the melting point, this increase in temperature will lead to a softening of the material and thermal stresses in places where thermal expansion is constrained.

Because yielding is expected in the nozzle due to the high temperatures and resulting thermal stresses, a plastic model of AlSi10Mg will need to be implemented in Ansys to simulate that yielding behavior. The following three-component Chaboche kinematic hardening model for additively manufactured AlSi10Mg was used for this [29]:

Table 19: AlSi10Mg Chaboche Parameters

Temp (°C)	Y ₀ (MPa)	C ₁ (MPa)	γ ₁	C ₂ (MPa)	γ ₂	C ₃ (MPa)	γ ₃
20	143.9	527169.0	16433.6	150506.5	2134.4	9915.1	34.6
50	157.1	138051.3	3243.4	138047.9	3553.2	10546.4	46.6
100	126.1	434307.4	11596.0	131448.4	1959.3	7340.9	47.6
150	108.6	193335.3	8620.6	130294.7	1826.3	5421.5	51.5
200	99.9	299530.9	10546.0	88890.2	1619.5	4223.5	69.2
320	41.4	47878.4	5805.9	41018.1	2337.5	9395.1	736.5
370	15.4	14796.1	3642.5	14758.9	3628.1	8344.7	715.4
440	6.8	2756.5	1878.8	2756.4	1883.4	1403.5	428.8

This data can be used to plot stress-strain curves and compare them to the bilinear elasto-plastic models for AlSi10Mg provided by Ansys in the additive manufacturing materials library to ensure the data is realistic. This is done in MATLAB (see Appendix A.6) and the results are shown in Figure 242; the two models appear to agree quite well.

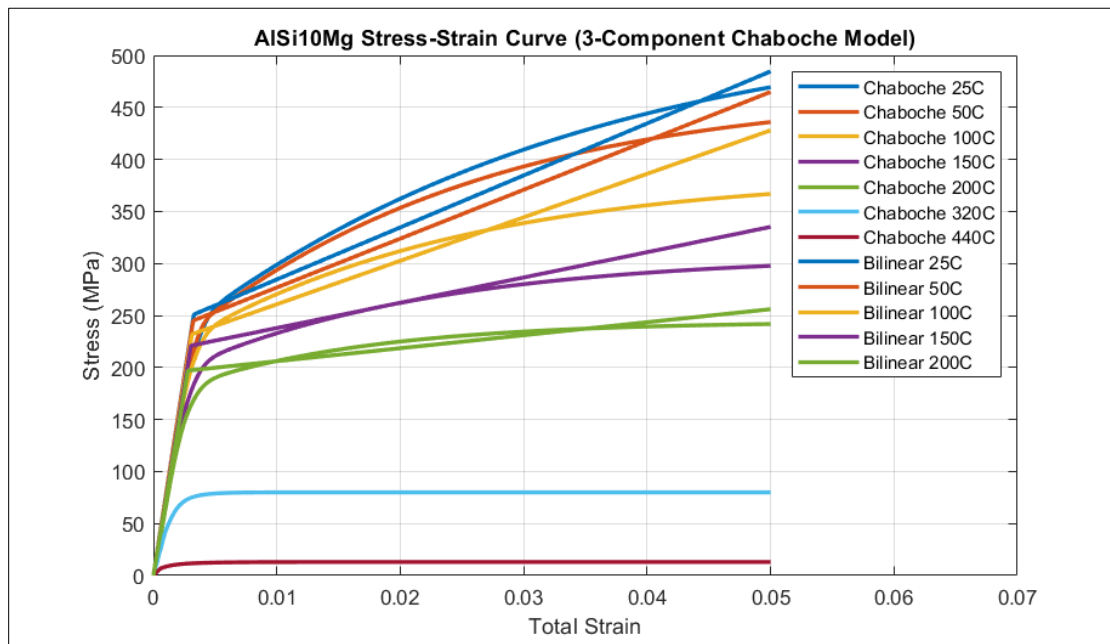


Figure 243: AlSi10Mg Chaboche vs Bilinear

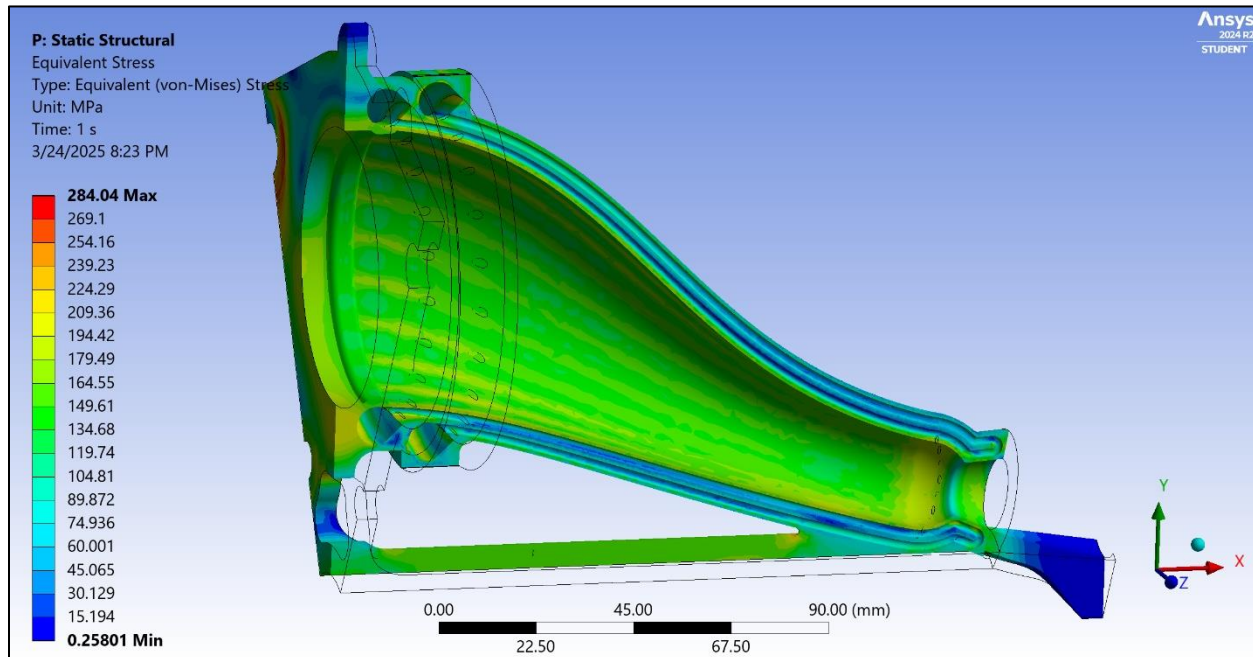


Figure 243: AlSi10Mg – Equivalent Stress

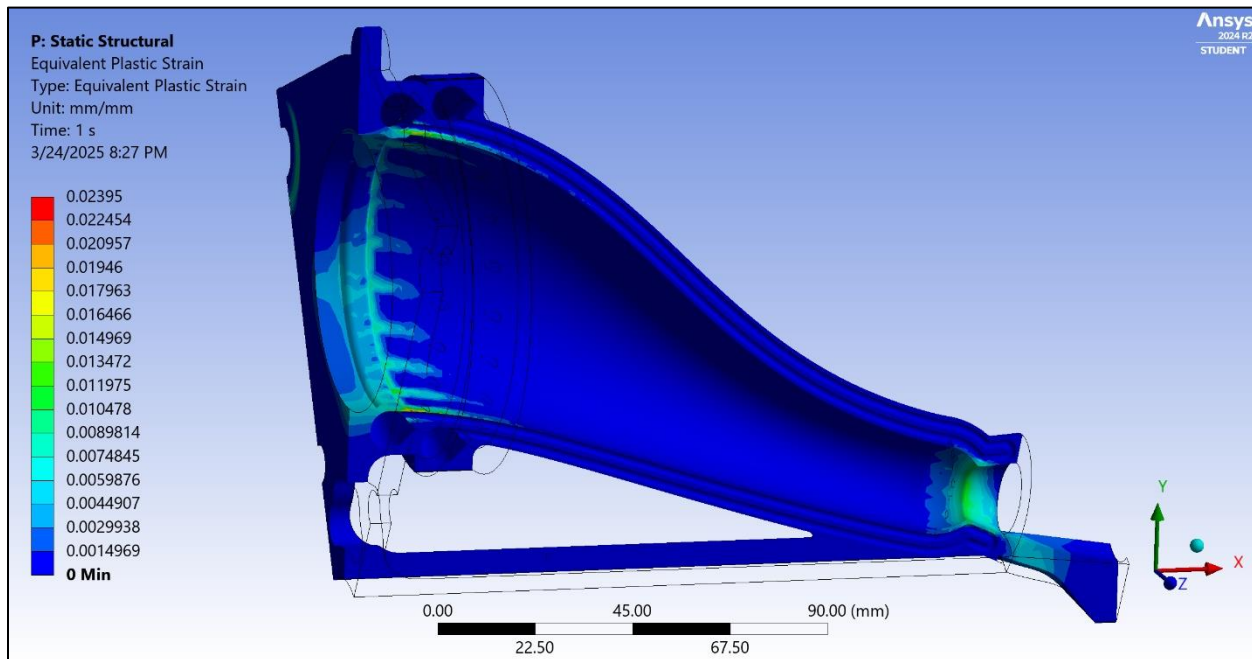


Figure 244: AlSi10Mg – Plastic Strain

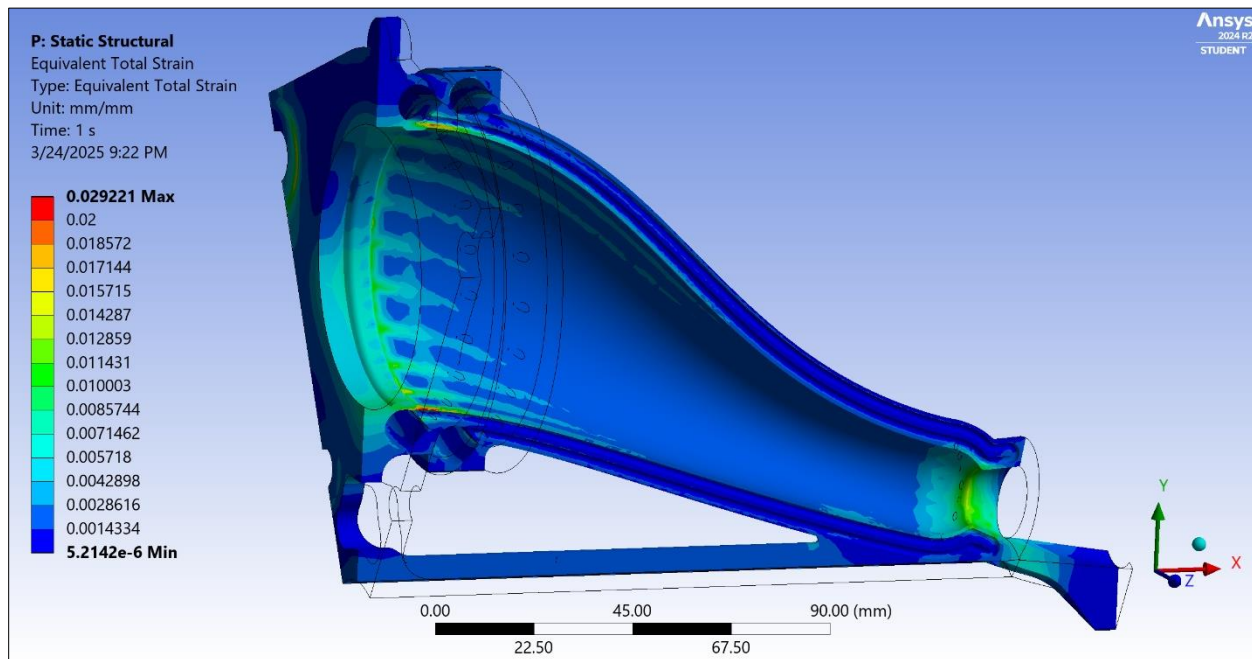


Figure 245: AlSi10Mg – Total Strain

The plastic strain plot in Figure 244 indicates where yielding is expected to occur and the total strain plot in Figure 245 presents the total magnitude of expected strain which can be compared to the expected fracture strain of 4.4% [30]. When exporting the nodal total strain results to excel and filtering the data in a table, it is seen that out of the 996,497 nodes, only 46 of them are at >2% total strain with the max strain being 2.9%. The locations of these nodes are at the inlet of the cooling channels in the wall between the cooling channel and thrust chamber, as seen in Figure 246.

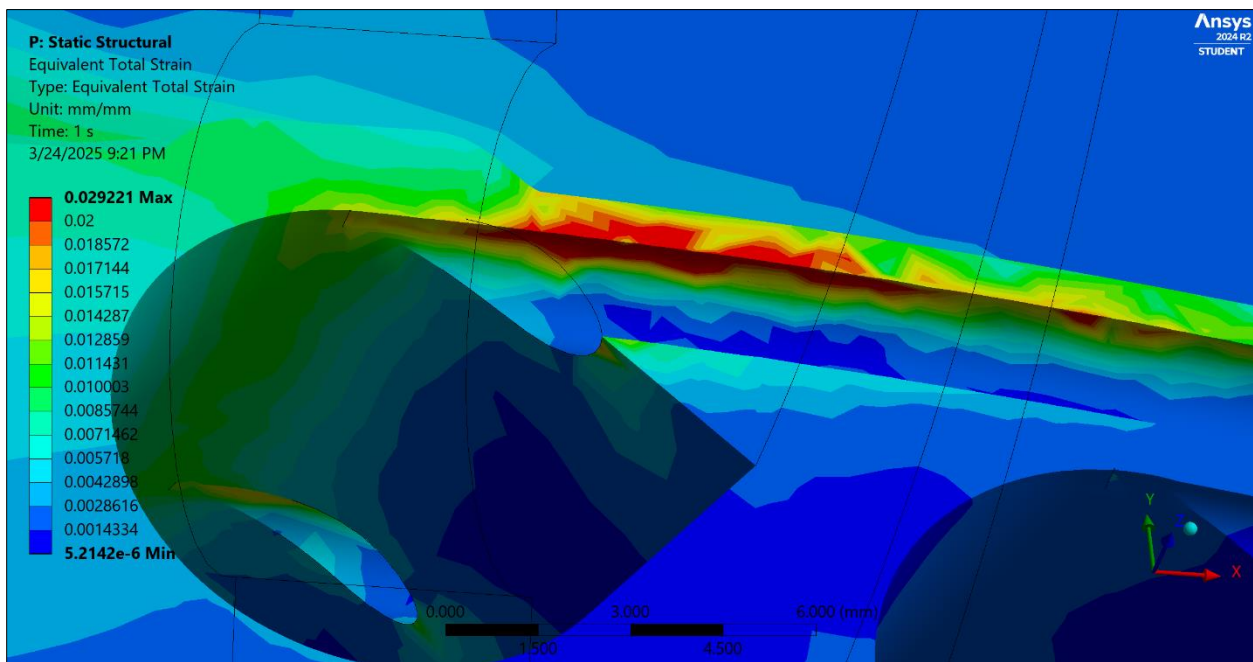


Figure 246: High Strain Area

12 POST-TEST ANALYSIS (VALLIERE)

12.1 Propulsion Analysis

Thrust being the only quantity measured during the static fire tests makes it difficult to predict with confidence what the chamber pressure inside the thrust chamber was during firing. Therefore, the easiest and most simple method of relating thrust and chamber pressure by a factor was used. The results from the fuel burn analysis gives a theoretical prediction of chamber pressure and thrust throughout the duration of the burn, which is seen in Figure 55. Dividing chamber pressure in psia by thrust in lbf, gives an array of factors used to relate the two quantities, seen in Figure 247. Because the fuel is assumed to be identical across analysis and testing, relating its combustion behavior in this oversimplified way is sufficient enough to make a guess of the chamber pressure during testing.

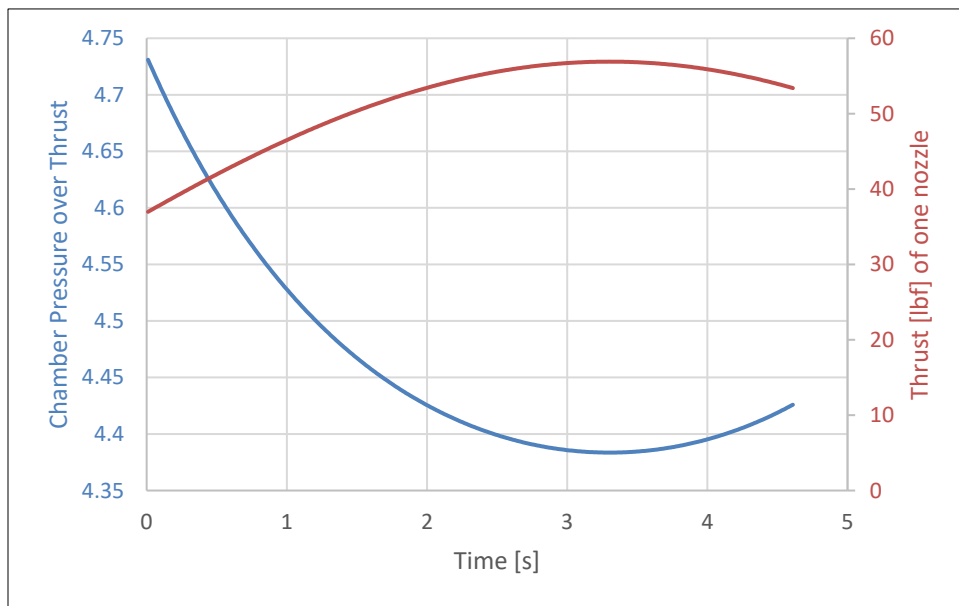


Figure 247: Chamber Pressure-Thrust Relation Factor

It can be seen that the relation factor follows an inverse relationship with thrust; the higher the thrust, the lower the relation factor. Since all CFD simulations of the aerospike are steady-state and done using the max chamber pressure condition of the burn, the minimum relation factor will be used to determine the chamber pressure of static fire test 1. As seen Figure 248, the max thrust

of static test fire 1 was 169.9 [lbf]. Using the relation factor that correlates to max thrust, 4.383, the max chamber pressure during static fire test 1 was 124.1 [psia].

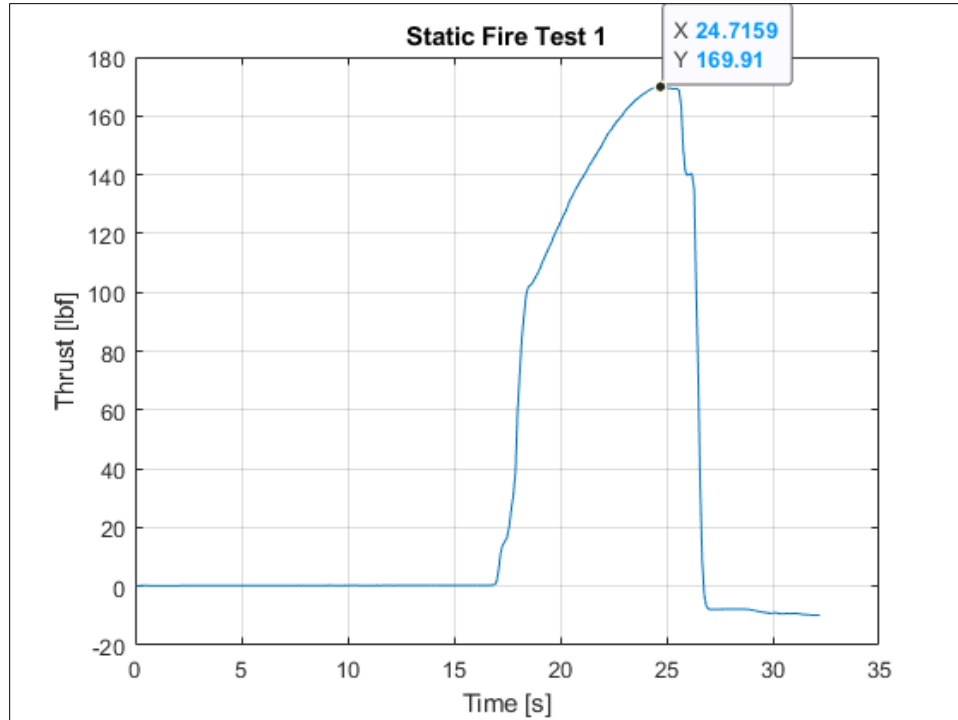


Figure 248: Static Fire Test 1 Thrust Data in z-direction

Going back to Ansys Fluent, an identical simulation to the one represented by Figures 59-61 was done to compare results with test footage, only using different boundary conditions reflecting test conditions. The case setup is as follows:

User defined fluid:

- Density set to ideal gas
- $c_p = 1,874.7 \text{ [J/kg}\cdot\text{K]}$
- Viscosity set to Sutherland's Law
 - Reference viscosity (μ_0): $1.30\text{e-}05 \text{ [Pa}\cdot\text{s]}$
 - Reference temperature (T_0): 283.60 [K]
 - Sutherland Constant (S): 107.90 [K]
- k- ϵ Realizable viscous model

- Molecular weight = 24.145 [g/mol]

Pressure Inlet:

- $P_0 = 885,802 \text{ [Pa]}$ (124.1 [psia])
- $T_0 = 2,500 \text{ [K]}$

Pressure Far-field:

- Pressure = 101,325 [Pa]
- Mach = 0.01 in x-direction
- Temperature = 300 [K]

Pressure Outlet:

- Pressure = 101,325 [Pa]
- Temperature = 300 [K]

A 3D volume rendering of the results show similarity with the footage from static fire test 1, as seen in Figures 251-252. The first Mach diamond, in the footage and CFD results, is located just after the end of the spike. The flow expansion immediately following the bell nozzle exit is also visually similar. Furthermore, the distance from the nozzle to the first Mach diamond can be approximated by:

$$x = 0.67D_0 \sqrt{\frac{P_0}{P_1}}$$

where:

x is distance from nozzle to first Mach diamond in [m]

D_0 is nozzle diameter in [m]

P_0 is chamber pressure in [Pa]

P_1 is ambient pressure in [Pa]

Therefore, given that the bell nozzle exit diameter is 16.8 [mm], the estimated chamber pressure from before is 885,802 [Pa], and ambient pressure is 101,325 [Pa], the distance of the first Mach diamond can be estimated:

$$x = 0.67(0.0168) \sqrt{\frac{885802}{101325}} = 0.03328 \text{ m}$$

Drawing a line 33.28 [mm] from the exit plane of one of the bell nozzles in Fusion, it can be seen (Figure 249) that this is very close to where the first Mach diamond appears in the test footage and in the CFD results.

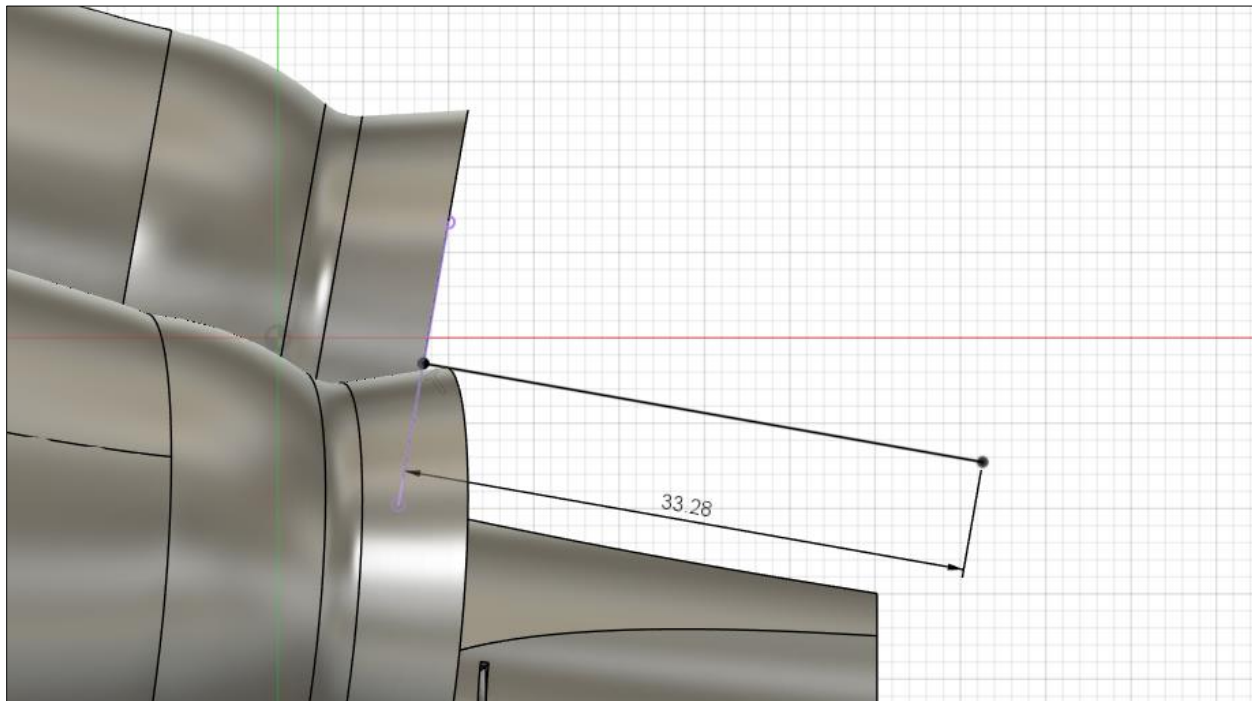


Figure 249: Estimation of Location of First Mach Diamond in Fusion



Figure 250: Image from Static Test Fire 1 at Max Thrust Instance

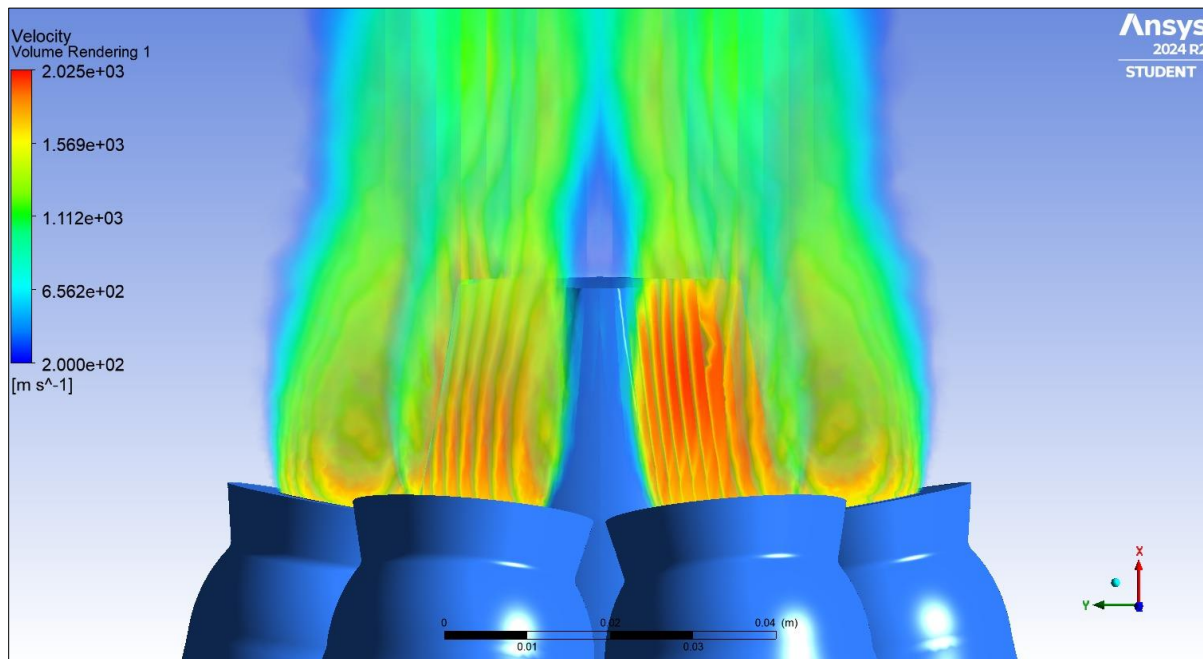


Figure 251: 3D Volume Rendering of Post-Test CFD Analysis

As for the altitude simulating shroud, the pressure sensor fixed to the base plate of the shroud produced data showing the minimum local pressure experienced during the test was 65,042 [Pa]. This ambient pressure correlates to an altitude of 3.59 [km], meeting PROP.03 which requires that the shroud simulates an altitude of up to 25 [km]. The real time pressure data measured by the pressure sensor during the shroud test can be seen in Figure 252.

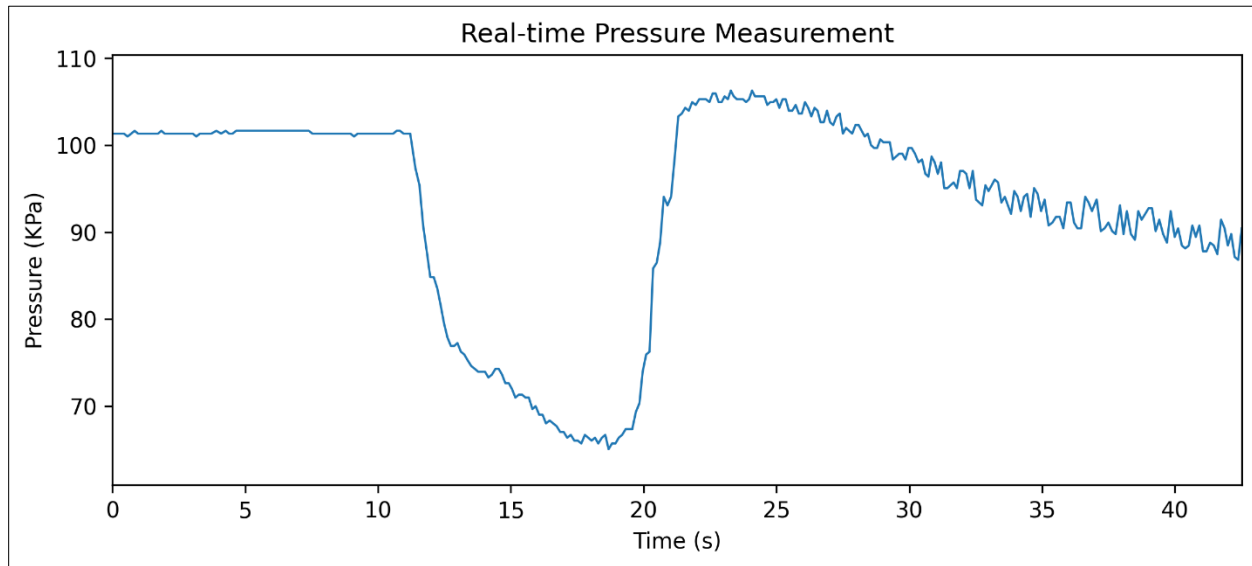


Figure 252: Pressure Sensor Data

Another CFD simulation was done to compare results with test data in an attempt to further validate the model and the system's real-world performance. A fluid domain similar to the one in Figure 59 but with a total fluid domain diameter of 6 [in] was used to simulate the internal volume of the shroud, as well as the base plate of the shroud being represented by a wall boundary instead of a pressure far-field. This slightly modified fluid domain, due to its overall reduced volume and having the same amount of mesh elements, is somewhat finer which should lead to a higher fidelity result. At the end of the simulation, the area-weighted average for static pressure over the shroud base where the pressure sensor was located was 65155 [Pa]. This strongly agrees with the test data; the percent error is only 0.174%. A pressure contour constrained from 0-1 [atm] and a velocity contour of this simulation in the xy-plane of the fluid domain can be seen in Figure 253 and Figure 254 respectively.

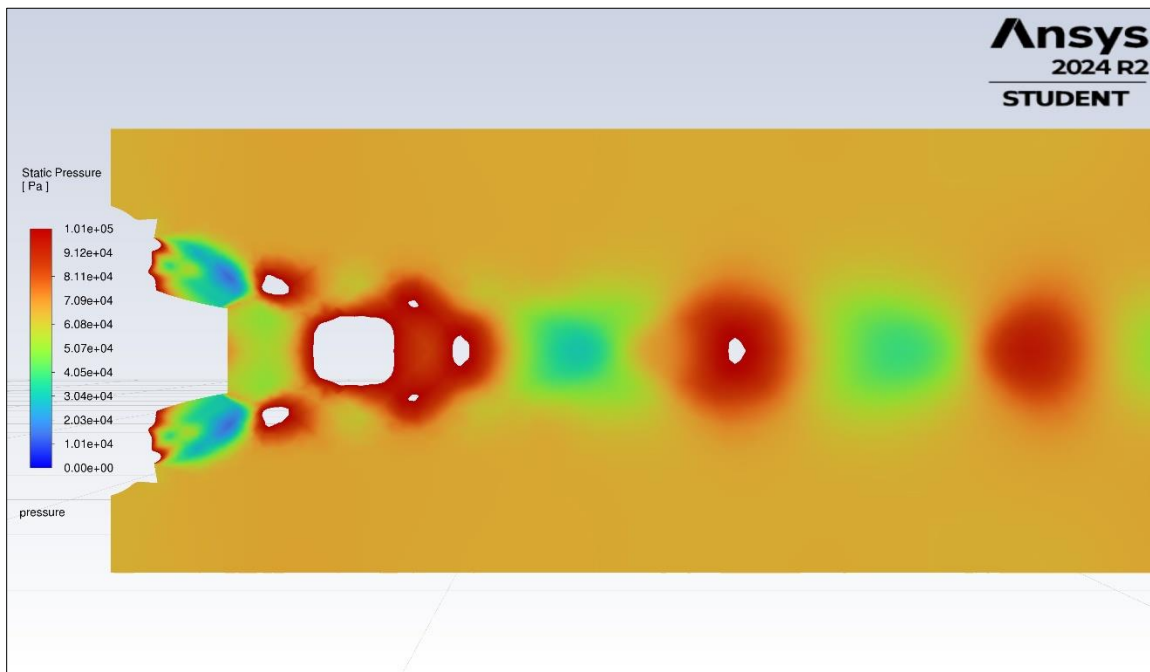


Figure 253: Shroud Simulation Pressure Contour

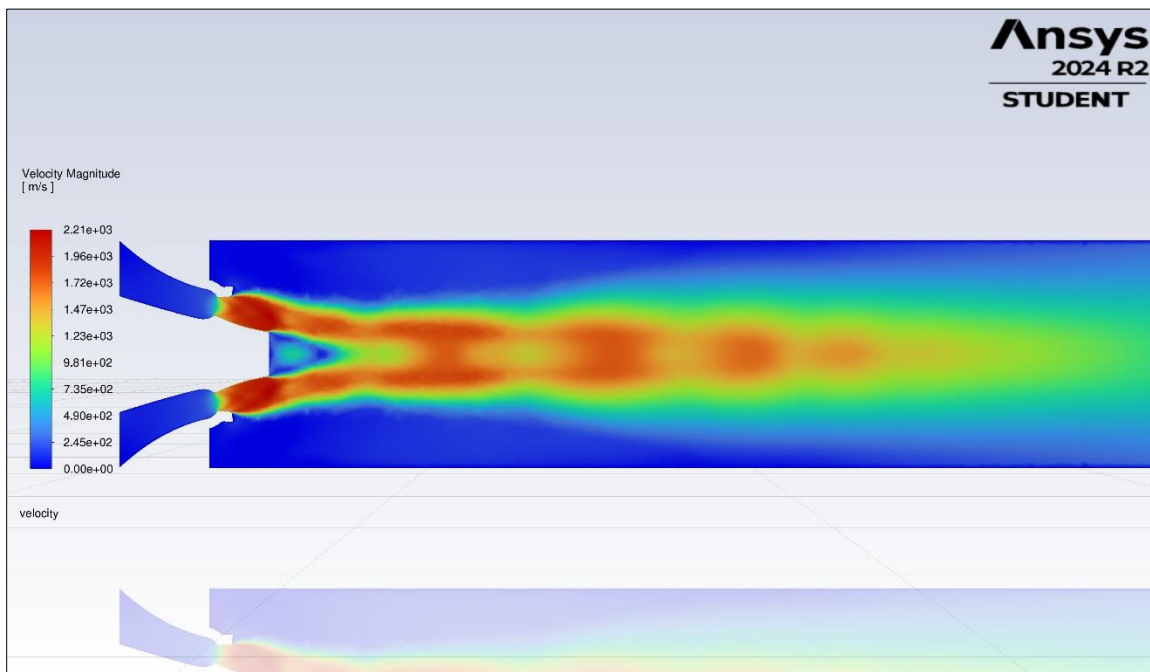


Figure 254: Shroud Simulation Velocity Contour

12.2 Structural Analysis

Repeating the thermal analysis using the heat transfer data pulled from the CFD simulation done in section 12.1, it is apparent in Figure that the temperatures inside the thrust chamber are much lower because lower chamber pressure means lower chamber temperature and lower density, which convection coefficient is a function of. However, the temperature in the spike is higher as the burn time of the test was longer and the spike has no active cooling. During testing, however, the spike was anodized, so the heat transfer seen by those surfaces would have been much lower. Nonetheless, 823.43 [K] is still below the melting point of AlSi10Mg, and outside of erosion experienced by one of the spikes during testing with a more violent burning fuel with higher aluminum content, there was no sign of melting on any thrust surface.

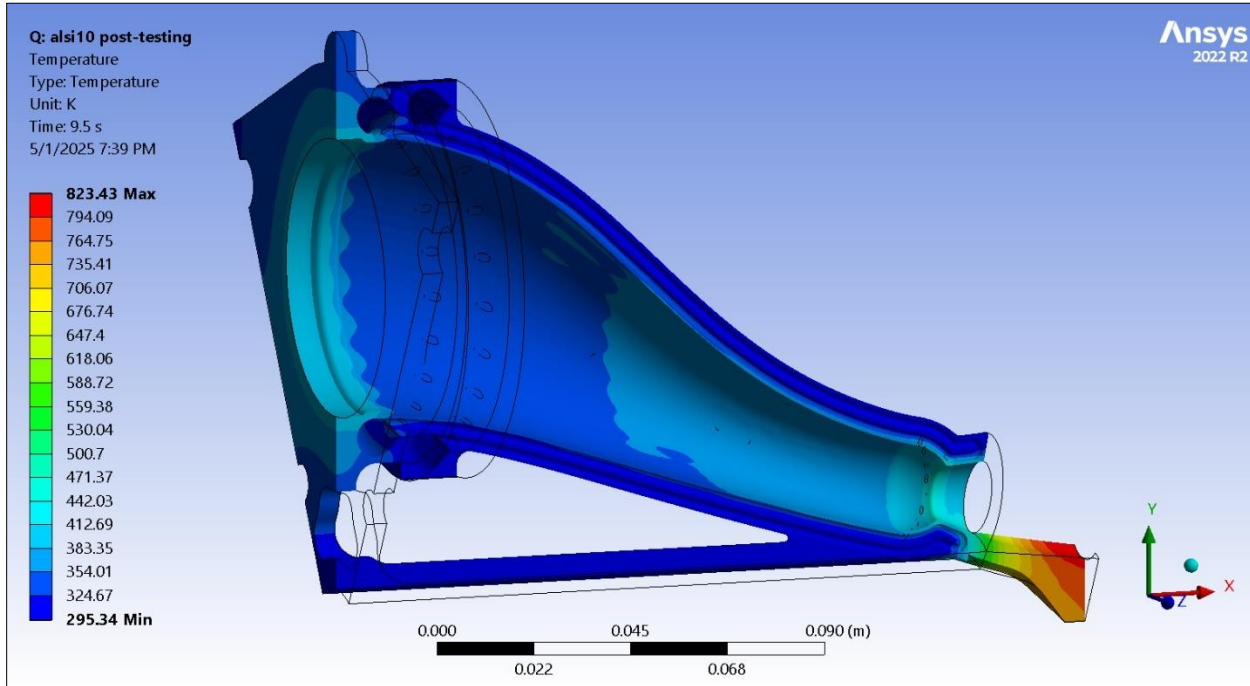


Figure 255: Post-Test Analysis of AlSi10Mg – Thermal Results

Repeating the structural analysis using the pressure data also pulled from the CFD simulation done in section 12.1 and the thermal data from the previous thermal analysis, it is apparent in Figure 256 that the total strain is significantly lower now that the temperature and chamber pressure is much lower. Of the 996,457 nodes in the model, less than 200 of them

experience total strain higher than 0.5%, and only one node is above 1%. The final factor of safety with respect to the assumed 4.4% fracture strain is 4.15.

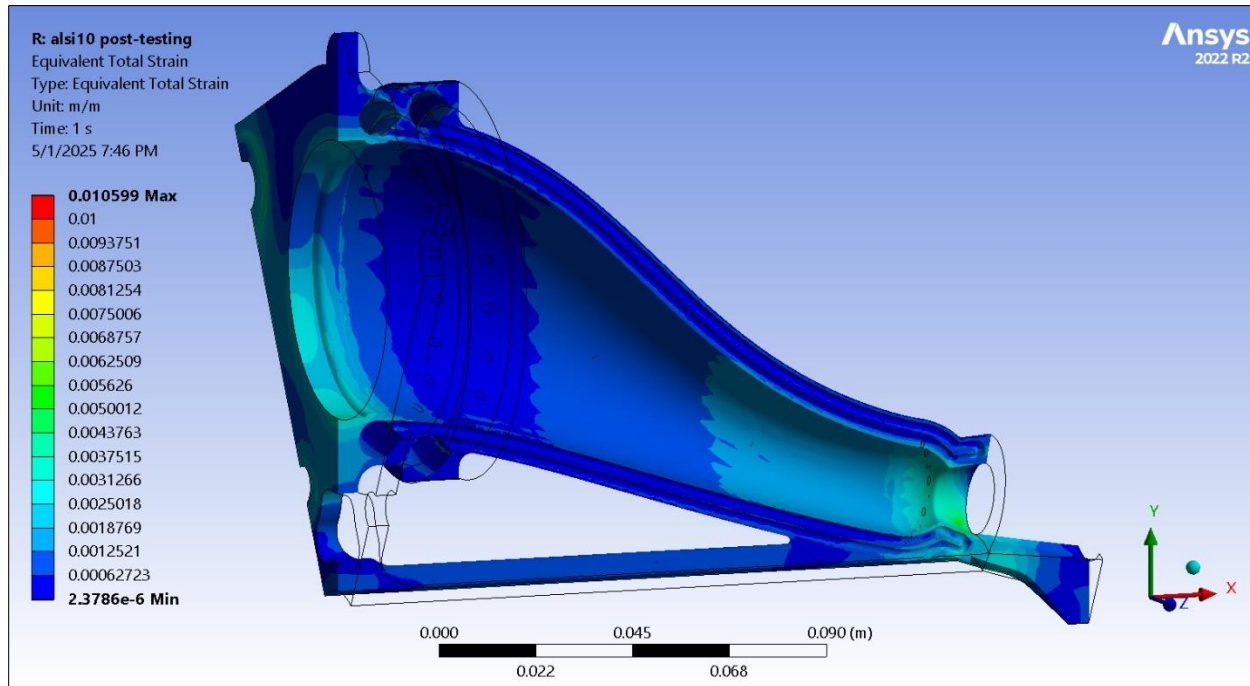


Figure 256: Post-Test Analysis of AlSi10Mg – Total Strain



13 CONCLUSIONS AND PLANS FOR FORWARD WORK (LEITA)

13.1 Conclusion

Project Vulcan has successfully evolved from a conceptual propulsion architecture into a fully realized and experimentally validated system. By achieving 100% of its Level 1 and Level 2 system requirements, the team demonstrated comprehensive fulfillment of technical, performance, and stakeholder-defined objectives. Through a combination of rigorous design processes, lean manufacturing strategies, and agile project execution, the team advanced a novel, metal 3D-printed toroidal aerospike engine integrated with a Liquid-Injected Thrust Vector Control (LITVC) system.

Every project milestone, from initial design validation through fabrication, integration, and testing, was executed on schedule and within budget, with 99.92% of the allocated funding strategically utilized. Following a two-day integration Work-A-Thon, the system underwent nine static fire tests at the Vaya Space test facility. These tests provided critical performance data across thrust generation, LITVC responsiveness, thermal resilience, and sensor/data acquisition integrity.

The ability to transition from preliminary analysis to empirical performance verification represents a rare achievement in academic propulsion projects. Moreover, the collaboration with industrial partners, the successful management of high-risk components (including combustion chambers and actuation hardware), and the iterative learning from each test cycle firmly establish Project Vulcan as a model of student-led aerospace innovation.

13.2 Future Work

Although Project Vulcan met all functional and experimental validation goals, the static fire campaign revealed a key limitation in the combustion chamber sealing methodology that warrants redesign.

The biggest area of concern during the test firings was the gasket leak in between the bolted flange system connecting the top aerospike section to the motor casings. The initial design called for O-ring cutouts to be made in the motor casing section. The O-rings would be placed at each of the motors and squished between the flanges using high-torqued bolts to seal the entire combustion within the combustion chamber. Due to manufacturing problems, the O-ring cutouts could not be implemented, so a different approach, using ultra high-temperature steel-clad vermiculite gaskets, was used in an attempt to seal the combustion. This method did not successfully seal the entirety of the high-pressure combustion, causing the thrust values to be lower than the expected values found using prior analysis.

Solving this problem will require returning to the aerospike's design by removing the bolted flange system entirely. While this is an effective method for sealing the combustion, it makes test setup impractical due to the need to open the system for motor insertion before each firing. Using the new threaded twist-lock end caps on each of the motor casing's tubes, an easy and simple fire setup can still be completed.

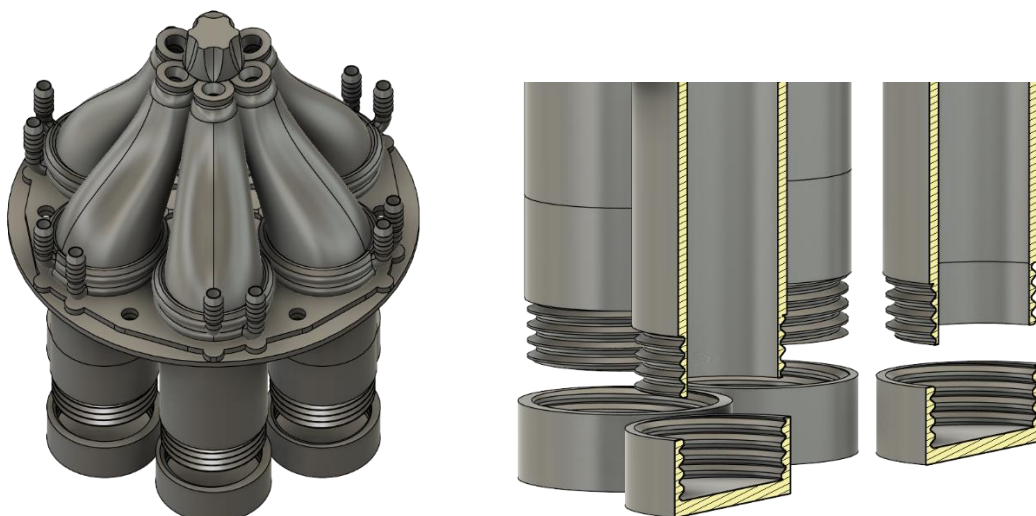


Figure 258: Twist-lock Threaded End Caps Expanded/Cross Section

This re-engineering effort would eliminate a known leakage path, improving combustion containment and restoring expected thrust output. The threaded end cap solution enhances sealing performance and supports operational efficiency by allowing faster reloading and reducing the likelihood of gasket misalignment or degradation between firings. Unlike the bolted flange system, which imposed strict torque requirements and offered little tolerance for manufacturing variance, the twist-lock system introduces repeatable modularity and streamlined workflow.



Figure 259: Twist-lock Threaded End Caps Integrated

In future development phases, the team also intends to explore optimizations to injector configuration symmetry, LITVC control algorithms, and thermal management within the aerospike body. These refinements and the proposed mechanical redesign aim to elevate the propulsion system's repeatability, peak efficiency, and readiness for potential flight-scaled applications. As such, Project Vulcan continues to serve as a platform for innovation and for maturing real-world design solutions applicable to next-generation aerospace propulsion.



14 REFERENCES (BEDELBAEV)

- [1] *75MM ClassicTM Propellant Grain.* the RCS Store. (2024).
https://www.rocketmotorparts.com/details/p1577809_20050157.aspx
- [2] *Additive manufacturing building the future Spotlight.* U.S. Department of Energy. (2019, April). https://www.energy.gov/sites/prod/files/2019/07/f64/2019-OTT-Additive-Manufacturing-Spotlight_0.pdf
- [3] *Altitude compensation.* Aerospaceweb.org | Aerospike Engine - Altitude Compensation. (n.d.). <https://aerospaceweb.org/design/aerospike/compensation.shtml>
- [4] Berrier, B. L., & Mason, M. L. (1988). *Static performance of an axisymmetric nozzle with post-exit vanes for Multiaxis Thrust vectoring.* National Aeronautics and Space Administration, Scientific and Technical Information Division ; For sale by the National Technical Information Service.
- [5] Bestelink, M., Baker, A., & Heywood, M. (2010, October). *Wordpress.* World Press.
https://wilocalfood.wordpress.com/wp-content/uploads/2014/10/youth-engagement-in-building-thriving-and-resilient-food-systems_presentation1.pdf
- [6] Blakey-Milner, B., Gradl, P., Snedden, G., Brooks, M., Pitot, J., Lopez, E., Leary, M., Berto, F., & du Plessis, A. (2021). Metal Additive Manufacturing in Aerospace: A Review. *Materials & Design, 209, 110008.* <https://doi.org/10.1016/j.matdes.2021.110008>
- [7] Florida Tech. (2024). *L3harris Student Design Center: Florida tech.* L3Harris Student Design Center | Florida Tech. <https://www.fit.edu/engineering-and-science/about/facilities/l3harris-student-design-center>
- [8] Fossà, L. (2021, January). *Axisymmetric minimum length nozzle design tool.* Axisymmetric Minimum Length Nozzle Design Tool - File Exchange - MATLAB Central.
<https://www.mathworks.com/matlabcentral/fileexchange/85253-axisymmetric-minimum-length-nozzle-design-tool>

- [9] Gallagher, D. W., Green, D. L., & Andrews, H. (1993). *Interpreted cooper-harper for broader use - NASA technical reports server (NTRS)*. NASA. <https://ntrs.nasa.gov/citations/19940008836>
- [10] Gudenkauf, J. (2017, July 10). *NASA Technical Reports Server (NTRS) 20170008979: Simulation of liquid injection thrust vector control for Mars ascent vehicle : NASA Technical Reports Server (NTRS) : Free download, Borrow, and streaming*. Internet Archive. https://archive.org/details/NASA_NTRS_Archive_20170008979
- [11] Irmak, F. (2024). *Senior Design Class Presentations*.
- [12] Jain, U., Shukla, H., Kapoor, S., Pandey, A., & Nirwal, H. (2020). Design and analysis of 2-Axis Rocket Motor Stand for thrust vectoring. *AIAA Propulsion and Energy 2020 Forum*. <https://doi.org/10.2514/6.2020-3920>
- [13] Ji, W., Zhou, R., Vivegananthan, P., See Wu, M., Gao, H., & Zhou, K. (2023). Recent progress in gradient-structured metals and alloys. *Progress in Materials Science*, 140, 101194. <https://doi.org/10.1016/j.pmatsci.2023.101194>
- [14] Jin, J., Park, Y., Lee, C., Jeong, S., Lee, J., & Baek, C. (2021). Design of a thrust stand using flexure. *Journal of the Korean Society for Aeronautical & Space Sciences*, 49(3), 205–212. <https://doi.org/10.5139/jksas.2021.49.3.205>
- [15] Miloš. (2015). A novel 6 dof thrust vector control test stand. *Tehnicki Vjesnik - Technical Gazette*, 22(5). <https://doi.org/10.17559/tv-20140621064603>
- [16] Modlin, C. T., & Zipay, J. J. (2014, January). *The 1.5 & 1.4 Ultimate Factors of Safety for Aircraft & Spacecraft – History, Definition and Applications*. NASA. <https://ntrs.nasa.gov/api/citations/20140011147/downloads/20140011147.pdf>
- [17] Paris, H., Mokhtarian, H., Coatanéa, E., Museau, M., & Ituarte, I. F. (2016). Comparative environmental impacts of additive and subtractive manufacturing technologies. *CIRP Annals*, 65(1), 29–32. <https://doi.org/10.1016/j.cirp.2016.04.036>

- [18] *Polaris Raumflugzeuge - Aerospike Engines.* POLARIS Raumflugzeuge - Aerospike Engines. (2024). <https://www.polaris-raumflugzeuge.de/Technology/Aerospike-Engines>
- [19] *Products.* Pangea Aerospace. (2024, July 1). <https://pangeaaerospace.com/products/>
- [20] Rezende, R. N., Alves, L. R., Mishra, A., Shukla, H., Varshney, H., Dhawan, H., Kapoor, S., Jain, U., & Mendonsa, R. (2021). Designing a thrust vector test stand for the turborocket. *AIAA Propulsion and Energy 2021 Forum*. <https://doi.org/10.2514/6.2021-3350>
- [21] RS-25 Propulsion System. (2024, July). <https://www.l3harris.com/sites/default/files/2024-07/l3harris-ar-rs-25-spec-sheet.pdf>
- [22] Rutherford, J. W., Bass, S. M., & Larsen, S. D. (1993). Canard rotor/wing: A revolutionary high-speed rotorcraft concept. *Aerospace Design Conference*. <https://doi.org/10.2514/6.1993-1175>
- [23] Shishko, R., Aster, R., & Cassingham, R. C. (1995). *NASA Systems Engineering Handbook*. National Aeronautics and Space Administration.
- [24] Sung, H.-G., Yeom, H.-W., Yoon, S., Kim, S.-J., & Kim, J. (2010). Investigation of rocket exhaust diffusers for altitude simulation. *Journal of Propulsion and Power*, 26(2), 240–247. <https://doi.org/10.2514/1.46226>
- [25] Taiwo, O. (2024, July 24). *Home Page.* Solideon. <https://solideon.com/>
- [26] Werner, D. (2023, January 23). *Firefly aims to build the “Model t of rockets.”* SpaceNews. <https://spacenews.com/building-the-model-t-of-rockets/>
- [27] *What is directed energy deposition (ded)?.* Markforged. (2024). <https://markforged.com/resources/learn/3d-printing-basics/3d-printing-processes/what-is-directed-energy-deposition-ded>
- [28] NASA. (1988). Information content from the NSTS Shuttle Reference Manual. Main Propulsion System.

<https://web.archive.org/web/20211123164917/https://science.ksc.nasa.gov/shuttle/technology/sts-newsref/sts-mps.html>

[29] Brenner, S., & Nedeljkovic-Groha, V. (2025, February 28). *Experimental and numerical study on the temperature-dependent tensile properties of alsi10mg fabricated by laser-based powder bed fusion*. SpringerLink. https://link.springer.com/chapter/10.1007/978-3-031-77403-4_11

[30] Lupi, G., de Menezes, J. T., Belotti, F., Bruzzo, F., López, E., Volpp, J., Castrodeza, E. M., & Casati, R. (2023). Fracture toughness of alsi10mg alloy produced by direct energy deposition with different crack plane orientations. *Materials Today Communications*, 37. <https://doi.org/10.1016/j.mtcomm.2023.107460>